

High Sensitivity Nucleic Acid Detection Using Metal Nanowires and Nanotubes

Andrea McCooey BSc. (Hons)

Thesis submitted for the award of PhD

School of Chemical Sciences
Dublin City University

Supervisor:
Prof Robert J. Forster

September 2015

Declaration

I hereby certify that this material, which I now submit for assessment on the programme of study leading to the award of Doctor of Philosophy is entirely my own work, and that I have exercised reasonable care to ensure that the work is original, and does not to the best of my knowledge breach any law of copyright, and has not been taken from the work of others save and to the extent that such work has been cited and acknowledged within the text of my work.

Signed:_____ ID No:_____ Date:_____

Table of Contents

Declaration	i
List of Figures	vii
List of Abbreviations	xxi
Abstract	xxv
Publications and Presentations	xxvii
1. SURVEY OF LITERATURE	1
1.1 Introduction	2
1.2 Template materials	8
1.2.1 Other materials	9
1.3 Template synthetic techniques	10
1.3.1 Electrochemical deposition	10
1.3.2 Electroless deposition	12
1.4 Synthesis of nanomaterials	13
1.4.1 Gold Nanowires	13
1.4.2 Copper nanowires	21
1.4.3 Potentiostatic deposition vs. galvanostatic deposition	25
1.5 Core shell nanowires	26
1.6 Summary	30
1.7 Applications	31
1.7.1 Gold Nanowires	32
1.7.2 Core:Shell Nanowires	43
1.8 Conclusion	48
2. EXPERIMENTAL PROCEDURES	56
2.1 Materials	57

2.2	Electrochemistry	59
2.3	Sample preparation	59
2.4	Spectroscopic Techniques	60
2.4.1	Raman Spectroscopy	60
2.4.2	EDX Spectroscopy	60
2.5	Microscopic Techniques	61
2.5.1	Scanning Electron Microscopy	61
2.5.2	Field-Emission Scanning Electron Microscopy (FE-SEM)	61
2.6	ICP-MS	61
2.7	Calculation of Electrochemical Area and Surface Roughness of a bare gold electrode	62
2.8	Capacitance of gold electrodes	65
2.9	Experimental Procedures	67
2.9.1	Synthesis of gold nanowires and nanotubes	67
2.9.2	DNA modification of the gold nanowires/nanotubes	67
2.9.3	DNA Hybridisation	68
2.9.4	Electrochemical detection of <i>S. aureus</i> ss-DNA target by solid gold nanowires and hollow gold nanotubes	68
2.9.5	Regeneration of gold electrodes following modification with DNA monolayer and nanowire-labelled probe DNA	70
2.9.6	Optimal conditions used to synthesise core:shell nanowires	70
2.9.7	Functionalisation of hollow nanotubes and core:shell nanowires with $[(\text{Ru}(\text{bpy})_2(\text{Qbpy}))^{2+} (\text{ClO}_4)_2]$	71
2.9.8	Electrochemical detection of <i>S. aureus</i> ss-DNA target by gold:copper core:shell nanowires	72
2.10	Conclusion	73

2.11	References	74
3.	SYNTHESIS AND CHARACTERISATION OF GOLD NANOWIRES AND NANOTUBES	75
3.1	Introduction	76
3.2	Results and Discussion	78
3.2.1	Substrate used for electrochemical deposition of nanowires and nanotubes	78
3.2.2	Potentiostatic deposition of gold nanowires	79
3.2.3	SEM images of nanowires after release from the membrane	85
3.2.4	Electrochemical characterisation of nanowire – modified carbon electrodes	92
3.2.4.1	Cyclic Voltammetry	92
3.2.4.2	Capacitance	98
3.2.5	Mass of gold deposited during deposition of nanowires	103
3.2.6	Concentration of Nanowires	107
3.2.7	Potentiostatic deposition of gold nanotubes	108
3.2.8	SEM images of nanotubes after release from the membrane	111
3.2.9	Electrochemical characterisation of nanotube - modified carbon electrodes	114
3.2.9.1	Cyclic Voltammetry	114
3.2.9.2	Capacitance	116
3.2.10	Mass of gold deposited during deposition of nanotubes	121
3.2.11	Concentration of Nanotubes	124
3.3	Conclusion	128
3.4	References	130
4.	SYNTHESIS AND CHARACTERISATION OF GOLD:COPPER CORE:SHELL NANOWIRES	133
4.1	Introduction	134
4.2	Results and Discussion	136

4.2.1	Substrate used as template for nanostructure deposition	136
4.2.2	Galvanostatic deposition of copper	138
4.2.3	SEM analysis following copper deposition	142
4.2.4	Potentiostatic deposition of gold	147
4.2.5	Mass of deposited gold	150
4.2.6	SEM analysis following gold deposition	152
4.2.7	Fe-SEM analysis	155
4.2.8	EDX spectroscopy	157
4.2.9	Cyclic Voltammetry	159
4.2.10	Raman Spectroscopy	165
4.3	Conclusion	170
4.4	References	172

5. DETECTION OF NUCLEIC ACIDS USING FUNCTIONALISED GOLD NANOWIRES, NANOTUBES, AND GOLD:COPPER CORE:SHELL NANOWIRES

176

5.1	Introduction	177
5.2	Results and Discussion	181
5.2.1	Application of gold nanowires to label-free, amplification free, detection of target DNA	181
5.2.1.1	Characterisation of gold nanowire/nanotube biosensor response	183
5.2.1.2	Calibration plot for gold nanowire response	185
5.2.2	Application of hollow gold nanotubes to label-free, amplification-free detection of target DNA	188
5.2.2.1	Calibration plot for gold nanotube response	189
5.2.2.2	Control Study	192

5.2.3	Application of gold:copper core:shell nanowires to label-free, amplification-free detection of target DNA	200
5.2.3.1	Characterisation of core:shell nanowire biosensor response	201
5.2.3.2	Theoretical charge produced by selective oxidation of copper shell	204
5.2.3.3	Theoretical charge produced by reduction of thiol bonds	206
5.2.3.4	Selective reduction of thiol bonds	208
5.2.4	Detection of DNA Approach 1 – Reduction of thiol bonds	213
5.2.4.1	Control Study	219
5.2.5	Selectivity of the Assay using 1 and 3 Base Mismatches	222
5.2.5.1	1 Base Mismatch	222
5.2.5.2	3 Base Mismatch	225
5.2.6	Detection of DNA Approach 2 – Selective oxidation of Copper shell	230
5.3	Conclusion	236
5.4	References	240
6.	CONCLUSIONS AND FUTURE WORK	243
6.1	Summary	244

List of Figures

Figure 1.1: <i>Schematic diagram of nanostructures formed within a membrane template; and the structures after removal of the template [reproduced from S. Barth, F. Hernandez-Ramirez, J. D. Holmes and A. Romano-Rodriguez, <i>Progress in Materials Science</i>, 2010, 55, 563-627]</i>	11
Figure 1.2: <i>SEM image of the Ni nanowires obtained after the dissolution of the polycarbonate membrane. Electrodeposition has been stopped before the transition to bulk growth can occur. [Adapted from C. Schönenberger, B. vanderZande, L. Fokkink, M. Henny, C. Schmid, M. Kruger, A. Bachtold, R. Huber, H. Birk and U. Staufer, <i>J Phys Chem B</i>, 1997, 101, 5497-5505]</i>	14
Figure 1.3: <i>SEM images of Ni deposited in 80nm porous membranes obtained after dissolution of the membrane. Electrodeposition has been stopped at the transition to bulk growth and long afterwards for (a) and (b) respectively. [Reproduced from C. Schönenberger, B. vanderZande, L. Fokkink, M. Henny, C. Schmid, M. Kruger, A. Bachtold, R. Huber, H. Birk and U. Staufer, <i>J Phys Chem B</i>, 1997, 101, 5497-5505]</i>	16
Figure 1.4: <i>(a) SEM micrograph of the gold nanowires following dissolution of the polycarbonate membrane in dichloromethane for 2h. (b) TEM image of a single nanowire dispersed in chitosan solution. [Reproduced from Y. Lu, M. Yang, F. Qu, G. Shen and R. Yu, <i>Bioelectrochemistry</i>, 2007, 71, 211-216]</i>	17
Figure 1.5: <i>SEM micrograph of 160 nm diameter AuNWs. Inset: end sections of wires. [Adapted from S. Karim, M. E. Toimil-Molares, F. Maurer, G. Mieke, W. Ensinger, J. Liu, T. W. Cornelius and R. Neumann, <i>Applied Physics A-Materials Science & Processing</i>, 2006, 84, 403-407]</i>	18
Figure 1.6: <i>HRSEM of a 25 nm nanowire. [Adapted from S. Karim, M. E. Toimil-Molares, F. Maurer, G. Mieke, W. Ensinger, J. Liu, T. W. Cornelius and R. Neumann, <i>Applied Physics A-Materials Science & Processing</i>, 2006, 84, 403-407]</i>	19

Figure 1.7: <i>Current–time transients for Au electrodeposition in membranes with 70 nm diameter pores for different potentiostatic voltages at 65°C. Arrows indicate the end of zone II, i.e., the point at which the current starts to increase [reproduced from S. Karim, M. E. Toimil-Molares, F. Maurer, G. Mische, W. Ensinger, J. Liu, T. W. Cornelius and R. Neumann, <i>Applied Physics A-Materials Science & Processing</i>, 2006, 84, 403-407]</i>	20
Figure 1.8: <i>Cross sectional view of electrodeposited CuNWs. [Reproduced from M. I. Irshad, F. Ahmad, N. M. Mohamed and M. Z. Abdullah, <i>International Journal of Electrochemical Science</i>, 2014, 9, 2548-2555]</i>	21
Figure 1.9: <i>Current density profile of Cu nanowire deposition. The three stages of growth are indicated by the arrows: Stage 1: decrease in current density showing pores are empty before deposition, Stage 2: density increases as nanowires begin to grow, and Stage 3: current density becomes constant as growth transitions to a bulk film. [Reproduced from M. I. Irshad, F. Ahmad, N. M. Mohamed and M. Z. Abdullah, <i>International Journal of Electrochemical Science</i>, 2014, 9, 2548-2555]</i>	22
Figure 1.10: <i>Cross-section views of anodic alumina membranes filled with Cu nanowires obtained by continuous deposition. ((a) and (b)) –0.3 V(SCE) after (a) 1 h and (b) 3 h. ((c) and (d)) –0.6 V(SCE) after 1 h of electrodeposition in central part of the cross-section (c) and in proximity of the template surface (d) [Reproduced from R. Inguanta, S. Piazza and C. Sunseri, <i>Appl. Surf. Sci.</i>, 2009, 255, 8816-8823]</i>	23
Figure 1.11: <i>Images of TiO₂ templates after filling with Cu: SEM images of top view (a,b), TEM image of cross section (c), and XRD spectrum (d). [Adapted from D. Fang, K. Huang, S. Liu and D. Qin, <i>Electrochemistry Communications</i>, 2009, 11, 901-904]</i>	24
Figure 1.12: <i>The schematic illustration of formation process of Cu nanowires inside the porous anodic titania template. [Adapted from D. Fang, K. Huang, S. Liu and D. Qin, <i>Electrochemistry Communications</i>, 2009, 11, 901-904]</i>	25

Figure 1.13 SEM of Cu nanotubes plated from the CoNiCu bath at -0.325 V. Cu EDX spectrum shown on lower right. [Reproduced from D. M. Davis and E. J. Podlaha, <i>Electrochemical and Solid State Letters</i> , 2005, 8, D1-D4].....	27
Figure 1.14: EDX spectrum of CoNiCu nanotubes deposited for 60 min at -1 V from CoNiCu electrolyte. [Adapted from D. M. Davis and E. J. Podlaha, <i>Electrochemical and Solid State Letters</i> , 2005, 8, D1-D4]	28
Figure 1.15: SEM of core:shell wires obtained by filling CoNiCu tubes with Cu from a concentrated Cu electrolyte. ESX spectrum is shown on the right. [Reproduced from D. M. Davis and E. J. Podlaha, <i>Electrochemical and Solid State Letters</i> , 2005, 8, D1-D4]	29
Figure 1.16: Schematic illustration of (a) Synthesis of AuNWs and (b) fabrication of the DNA biosensor electrodes. (WE-working electrode, RE-reference electrode, CE-counter electrode) [Reproduced from T. S. Ramulu, R. Venu, B. Sinha, B. Lim, S. J. Jeon, S. S. Yoon and C. G. Kim, <i>Biosens. Bioelectron.</i> , 2013, 40, 258-264].....	32
Figure 1.17: Cyclic voltammograms of AuNW (i), AuNW/thiolated probe-DNA (ii) AuNW/thiolated probe-DNA/complementary target-DNA (iii) electrodes in 0.05 M PBS (pH 7.4, 0.15 M NaCl) containing 5 mM $[Fe(CN)_6]^{3-/4-}$ [Reproduced from T. S. Ramulu, R. Venu, B. Sinha, B. Lim, S. J. Jeon, S. S. Yoon and C. G. Kim, <i>Biosens. Bioelectron.</i> , 2013, 40, 258-264].....	34
Figure 1.18: (a) Differential pulse voltograms of (i) AuNWsA/t-DNA (ii) AuNWsA/t-DNA/c-DNA (iii) AuNWsA/t-DNA/nc-DNA(iv) AuNWsA/t-DNA/m-DNA electrodes; (b) DPV measurements of AuNWsA/t-DNA electrode after hybridization with different concentrations of complimentary sequence in 0.05 M PBS (pH 7.4, 0.15 M NaCl) containing 20 μ M methylene blue and (c) ΔI_p as a function of $\ln(\text{target DNA concentration})$ of (i) bare Au electrode (ii) and AuNWsA electrode. [Reproduced from T. S. Ramulu, R. Venu, B. Sinha, B. Lim, S. J. Jeon, S. S. Yoon and C. G. Kim, <i>Biosens. Bioelectron.</i> , 2013, 40, 258-264]	35
Figure 1.19: Scanning electron micrograph and schematic illustration of 3D nanoelectrode ensemble. [Reproduced from Gasparac, R.; Taft, B. J.; Lapierre-	

Devlin, M. A.; Lazareck, A. D.; Xu, J. M.; Kelley, S. O. *J. Am. Chem. Soc.* **2004**, *126*, 12270-12271]36

Figure 1.20: *Representative cyclic voltammograms for 18-mer duplex DNA modified macroelectrode (a), and NEE (b) collected in solutions containing 2 mM [Fe(CN)₆]³⁻ and 10 (blue), 20 (red), and 80 μM (black) [Ru(NH₃)₆]³⁺ [Reproduced from M. A. Lapierre-Devlin, C. L. Asher, B. J. Taft, R. Gasparac, M. A. Roberts and S. O. Kelley, *Nano Letters*, 2005, **5**, 1051-1055].....37*

Figure 1.21: *Representative cyclic voltammograms of (a) 3 mM [Ru(NH₃)₆]³⁺ at a bare NEE, (b) 27 μM [Ru(NH₃)₆]³⁺ at a NEE modified with 30-mer duplex DNA, (c) 27 μM [Ru(NH₃)₆]³⁺ and 2mM [Fe(CN)₆]³⁻ at a NEE modified with 30-mer duplex DNA, (d) 3 mM [Ru(NH₃)₆]³⁺ at a bare Au macroelectrode, (e) 27 μM [Ru(NH₃)₆]³⁺ at a macroelectrode modified with 30-mer duplex DNA, (f) 27 μM [Ru(NH₃)₆]³⁺ and 2mM [Fe(CN)₆]³⁻ at a macroelectrode modified with 30-mer duplex DNA [Reproduced from M. A. Lapierre-Devlin, C. L. Asher, B. J. Taft, R. Gasparac, M. A. Roberts and S. O. Kelley, *Nano Letters*, 2005, **5**, 1051-1055]..38*

Figure 1.22: *Effect of potential on the response of the gold nanowire modified electrode towards 1 mM hydrogen peroxide in 0.06 M PBS. [Reproduced from Y. Lu, M. Yang, F. Qu, G. Shen and R. Yu, *Bioelectrochemistry*, 2007, **71**, 211-216]39*

Figure 1.23: *Current-time transient obtained at the conventional gold electrode (a) and the gold nanowire modified electrode (b) upon increasing the concentration of hydrogen peroxide in steps of 1 mM at -0.2 V vs. SCE in 0.06 M PBS. [Reproduced from Y. Lu, M. Yang, F. Qu, G. Shen and R. Yu, *Bioelectrochemistry*, 2007, **71**, 211-216].....40*

Figure 1.24: *Current time transient of GOx modified biosensor for the successive addition of 0.5 mM glucose at -0.2 V vs. SCE. Inset: Calibration curve of current response over range of glucose concentrations. [Reproduced from Y. Lu, M. Yang, F. Qu, G. Shen and R. Yu, *Bioelectrochemistry*, 2007, **71**, 211-216].....42*

Figure 1.25: *Schematic representation of formation of bimetallic Ag:Cu core:shell nanowire modified glassy carbon electrode [Reproduced from J. S. Easow and T. Selvaraju, *Electrochim. Acta*, 2013, **112**, 648-654].....43*

Figure 1.26: SEM image of Ag:Cu bimetallic nanowires grown on glass substrates for SEM analysis. [Reproduced from J. S. Easow and T. Selvaraju, <i>Electrochim. Acta</i> , 2013, 112 , 648-654]	44
Figure 1.27: Cyclic voltammetric response of (a) bare GC, (b) GC/Nf/Ag _{seed} , and (c) bimetallic GC/Nf/Ag:CuNW electrodes in the presence of 0.2 mM H ₂ O ₂ . The supporting electrolyte was 0.01 M PBS (pH 7.2). [Reproduced from J. S. Easow and T. Selvaraju, <i>Electrochim. Acta</i> , 2013, 112 , 648-654]	45
Figure 1.28: Chronoamperometric response of bimetallic GC/Nf/Ag:Cu NWs electrode toward different concentrations of H ₂ O ₂ in PBS (pH 7.2) The electrode potential is fixed at -0.6 V vs. Ag/AgCl. Inset: Current correlation vs. H ₂ O ₂ concentration. [Reproduced from J. S. Easow and T. Selvaraju, <i>Electrochim. Acta</i> , 2013, 112 , 648-654]	46
Figure 2.1: Cyclic voltammogram of a 2 mm diameter gold electrode in 0.1 M H ₂ SO ₄ with a surface roughness factor of 1.5. The counter electrode was a platinum wire and the reference electrode was Ag/AgCl in 3M KCl. The scan rate is 100 mVs ⁻¹ . The sixth scan is presented.	63
Figure 2.2: Cyclic voltammogram demonstrating capacitance of a bare gold electrode in 0.1M LiClO ₄ in ACN. The potential was swept from 0 to 0.6V with a scan rate of 100mVs ⁻¹ .The reference electrode was Ag/AgCl in 3 M KCl. The sixth scan is presented.	66
Figure 2.3: Schematic representation of the synthesis of gold nanowires/nanotubes within the pores of a polycarbonate membrane, and their subsequent incorporation into a DNA biosensor. Step 1: Metal deposition through the pores of a metal sputtered polycarbonate membrane results in nanowires or nanotubes of gold. These nanostructures are then functionalised with probe strand DNA that is complementary to a section of the target of interest, <i>S. aureus mastitis</i> . Following functionalisation, the membrane is removed and the wires are suspended in solution, creating a solution of free wires that are functionalised on one end with probe DNA. Step 2: Separately, on a gold disk electrode, thiol modified capture DNA is functionalised to the electrode surface. This capture DNA strand is complementary to a section of the	

target of interest. Following complete coverage of the electrode with a monolayer of capture DNA, the electrode is immersed in a solution of the target DNA, where it hybridises with the capture strand. The electrode is then immersed in the previously labelled gold nanowire solution, and the section of the target that is not already bound to capture DNA will bind to the probe DNA present on the nanowire surface. This electrode is now fully hybridised, and the target DNA can be detected due to the presence of the gold nanowires.69

Figure 2.4: Structure of $[(Ru(bpy)_2(Qbpy))]^{2+}$ dye.71

Figure 3.1: SEM image of a commercial PC membrane. A 20 nm thick gold layer has been sputtered on the membrane surface and the membrane has been mounted on a carbon tab for SEM analysis. Accelerating voltage was 20 kV.78

Figure 3.2: Current-time transient for growth of gold nanowires through a porous polycarbonate membrane mounted on FDTO. The potential applied was -0.273 V vs. Ag/AgCl in 3 M KCl for 1800 seconds. The membrane had been sputter coated with a ~300 nm thick layer prior to electrodeposition.80

Figure 3.3: Current density vs. $t^{0.5}$ for copper electrodeposition within the pores of a polycarbonate membrane. [Reproduced from I. U. Schuchert, M. E. Toimil-Molares, D. Dobrev, J. Vetter, R. Neumann and M. Martin, J. Electrochem. Soc., 2003, 150, C189-C194]82

Figure 3.4: Diffusion processes during pore filling: (a) linear diffusion inside the pore, (b) radial diffusion toward the pore opening, and (c) linear diffusion toward the whole membrane surface. [Reproduced from I. U. Schuchert, M. E. Toimil-Molares, D. Dobrev, J. Vetter, R. Neumann and M. Martin, J. Electrochem. Soc., 2003, 150, C189-C194]83

Figure 3.5: SEM images of Au nanowires after dissolution of polycarbonate membrane, sonication to remove sputtered gold layer and suspension dropcast for analysis. Deposition times are: (A) 10 min, (B) 20 min, (C) 30 min, (D) 40 min, (E) 50 min, (F) 60 min, (G) 2 hours, (H) 3 hours, (I) 4 hours, (J) 5 hours, (K) 6 hours, (L) 7 hours, (M) 8 hours, (N) 9 hours, (O) 10 hours, (P) 11 hours, and (Q) 12 hours. Accelerating voltages are 5 – 20 kV.....86

Figure 3.6: <i>Plot of average wire length from SEM analysis vs. deposition time for solid gold nanowires.</i>	90
Figure 3.7: <i>Cyclic voltammogram of a 50 min Au nanowire modified carbon electrode in 0.01 M H₂SO₄ with a surface roughness factor of 1.95 (solid line) vs. a cyclic voltammogram of a bare carbon electrode in 0.1M H₂SO₄ (dashed line). The reference electrode is Ag/AgCl in 3 M KCl. The scan rate is 100 mVs⁻¹. The sixth scan is presented.</i>	93
Figure 3.8: <i>Plot of electrochemical area vs. deposition time for Au nanowires.</i> ...	96
Figure 3.9: <i>Plot of surface roughness vs. deposition time for Au nanowires.</i>	97
Figure 3.10: <i>Cyclic voltammogram demonstrating capacitance of a carbon electrode modified with gold nanowires grown for 10 minutes. The electrolyte was 0.1 M LiClO₄ in ACN. The potential was swept from 0 to 0.6V with a scan rate of 100mVs⁻¹. The reference electrode was Ag/AgCl in 3 M KCl. The sixth scan is presented.</i>	99
Figure 3.11: <i>Plot of capacitance values vs. deposition time for gold nanowires.</i>	101
Figure 3.12: <i>Integrated current-time transient for twenty minute deposition of gold nanotubes through the pores of a polycarbonate membrane. The applied potential was -0.273 V vs. Ag/AgCl in 3 M KCl.. The charge passed was 7.5 C.</i>	104
Figure 3.13: <i>Current-time transient for growth of gold nanotubes through a porous polycarbonate membrane mounted on FDTO. The potential applied was -0.273 V vs. Ag/AgCl in 3 M KCl for 2400 seconds.</i>	109
Figure 3.14: <i>SEM images of Au nanotubes after dissolution of polycarbonate membrane, sonication to remove sputtered gold layer and suspension dropcast for analysis. Deposition times are: (A) 10 min, (B) 20 min, (C) 30 min, (D) 40 min, (E) 50 min, (F) 60 min, (G) 12 hours. Accelerating voltages are 5 – 20 kV.</i>	112
Figure 3.15: <i>Cyclic voltammogram of a 12 hr Au nanotube modified carbon electrode in 0.1 M H₂SO₄ with a surface roughness factor of 2.60 (solid line) vs. a</i>	

*cyclic voltammogram of a bare glassy carbon electrode in 0.1M H₂SO₄ (dashed line). The counter electrode was a platinum wire and the reference electrode was Ag/AgCl in 3 M KCl. The scan rate is 100 mVs⁻¹. The sixth scan is presented.*115

*Figure 3.16: Cyclic voltammogram demonstrating capacitance of a glassy carbon electrode modified with nanotubes deposited for 12 hours. The electrolyte was 0.1M LiClO₄ in ACN. The potential was swept from 0 to 0.6V vs. Ag/AgCl in 3 M KCl with a scan rate of 100mVs⁻¹. The sixth scan is presented.*117

*Figure 3.17: Plot of capacitance vs. deposition time for gold nanotubes.*119

*Figure 3.18: Integrated current-time transient for ten minute deposition of gold nanotubes through the pores of a polycarbonate membrane. The applied potential was -0.273 V vs. Ag/AgCl in 3 M KCl. The charge passed was 0.036 C.*122

*Figure 4.1: SEM images of a commercial PC membrane. A 20 nm thick gold layer has been sputtered on the membrane surface and the membrane has been mounted on a carbon tab for SEM analysis. Accelerating voltage is 20 kV.*136

*Figure 4.2: Image of membrane following sputter coating with a ~300 nm thick layer of gold before electrodeposition. Membrane was sputtered for 18 mins at a sputtering voltage of 2 kV and a plasma current of 20 mA. (Membrane is mounted on an aluminium stub and adhered with a carbon tab for sputtering).*137

*Figure 4.3: Potential – time transient showing growth of copper nanotubes through the pores of a polycarbonate membrane mounted on FDTO glass. A fixed current of +0.02 A vs. Ag/AgCl in 3 M KCl was applied for 180 seconds.*139

*Figure 4.4: SEM analysis of deposited nanostructures following deposition of copper for 3minutes; the polycarbonate membrane was dissolved in dichloromethane. This solution was not sonicated, but centrifuged for 60 seconds before 20μL was dropcast onto carbon tab for analysis.*142

*Figure 4.5: SEM analysis of 20 μL drop cast Cu nanotubes placed on carbon tab for analysis (after dissolution of the membrane in dichloromethane, and sonication to remove PC membrane and sputtered gold layer).*143

Figure 4.6: Electrochemical reduction current as a function of time t for the potentiostatic deposition of Ni and Cu in pores of polycarbonate membrane. Pore

size: 200nm; deposition solution: $0.60 \text{ mol L}^{-1} \text{ CuSO}_4$, $5 \times 10^{-3} \text{ mol L}^{-1} \text{ H}_2\text{SO}_4$; deposition method: potentiostatic, potential not quoted. The schematics display three different stages of growth process: Stage I: metal wires grow in the pores; Stage II: the pores are completely filled; Stage III: growth commences over the whole membrane surface; Stage IV: an electrodeposited film of metal outside the membrane surface is further developed. Figure reproduced from M. Motoyama, Y. Fukunaka, T. Sakka and Y. H. Ogata, <i>Electrochim. Acta</i> , 2007, 53 , 205-212]	146
Figure 4.7: Current-time transient for growth of gold nanowires through a porous polycarbonate membrane mounted on FDTO following previous deposition of copper in the same membrane. The potential applied was -0.273 V vs. Ag/AgCl in 3 M KCl for 180 seconds.	147
Figure 4.8: The integrated curve of the current vs. time transient to provide information on the charge passed during Au deposition. The charge passed was $9.985 \times 10^{-1} \text{ C}$.	150
Figure 4.9: SEM image of Au:Cu nanowires dropcast from suspension onto a carbon tab for analysis. (After dissolution of the membrane in dichloromethane, and sonication to remove PC membrane and sputtered gold layer). Accelerating voltage is 5 kV.	152
Figure 4.10: SEM images of Cu:Au nanowires from suspension, dropcast onto a carbon tab. (Following dissolution of the membrane in dichloromethane, and sonication to remove PC membrane and sputtered gold layer). The accelerating voltage was 5kV.	153
Figure 4.11: High resolution images of hollow copper nanotubes following release from the polycarbonate membrane, suspension in dichloromethane and dropcasting onto planar gold slides. Inner diameter was shown to be $58 \text{ nm} \pm 4.5$ nm. Accelerating voltage was 5 kV. (Imaged by Dr Elaine Spain)	155
Figure 4.12: High resolution image of gold:copper core:shell nanotubes following release from membrane, suspension and dropcasting. Accelerating voltage was 10 kV. (Imaged by Dr Elaine Spain)	156

Figure 4.13: <i>EDX spectrum of hollow Cu nanotubes following release from the polycarbonate membrane, suspension in dichloromethane, and dropcasting onto carbon tabs for analysis. The spot size used was 100 nm. (Spectrum acquired by Dr Elaine Spain)</i>	157
Figure 4.14: <i>EDX Spectrum of Au:Cu nanowires following release from the polycarbonate membrane, suspension in dichloromethane, and dropcasting onto carbon tabs for analysis. The spectrum was acquired from the length of the nanowire. The spot size used was 300 nm.(Spectrum acquired by Dr Elaine Spain)</i>	158
Figure 4.15: <i>Cyclic voltammogram of a 1 cm² FDTO electrode modified with a PC template decorated with a conductive 300 nm Au back layer (dashed line),after electrodeposition of the copper (dotted line), and after deposition of the gold (solid line). The supporting electrolyte is 0.1 M H₂SO₄ and the scan rate is 100 mV s⁻¹. The reference electrode is Ag/AgCl in 3 M KCl. The sixth scan is presented.</i>	160
Figure 4.16: <i>Au electrode modified with hollow Cu nanotubes after removal of the polycarbonate membrane and suspension in dichloromethane. The nanowires are then dropcast onto the bare 2 mm diameter electrode surface and fixed with 2.5 % glutaraldehyde. The supporting electrolyte is 0.1 M H₂SO₄ and the scan rate is 100 mV s⁻¹. The reference electrode is Ag/AgCl in 3 M KCl. The sixth scan is presented.</i>	161
Figure 4.17: <i>Au electrode modified with Au:Cu core:shell nanowires after removal of the polycarbonate membrane and suspension in dichloromethane. The nanowires are then dropcast onto the bare 2 mm diameter electrode surface and fixed with 2.5 % glutaraldehyde. The supporting electrolyte is 0.1 M H₂SO₄ and the scan rate is 100 mV s⁻¹. The reference electrode is Ag/AgCl in 3 M KCl. The sixth scan is presented.</i>	162
Figure 4.18: <i>Raman spectra of the copper nanotube array (blue) and the Cu:Au core:shell nanowire array (black). The excitation wavelength was 488 nm. The nanowires were immersed in a 1μM solution of [Ru(bpy)₂(Qbpy)]²⁺ dye dissolved</i>	

in 40:60 ethanol and DI H₂O for 2 days and dropcast onto planar ITO glass for Raman analysis. 168

Figure 5.1: Current-time transient showing response of solid Au nanowires to addition of 200 μ M of 30% wt. Hydrogen Peroxide. The supporting electrolyte was 0.01 M H₂SO₄, and the applied potential was -0.1 V. vs. Ag/AgCl in 3 M KCl. The target DNA concentration was 10 aM. 183

Figure 5.2: Calibration curve for the electrochemical detection of target DNA range 1 μ M to 1 aM on a 2 mm diameter bare electrode following hybridisation with probe DNA that is labelled with solid gold nanowires. The supporting electrolyte is 0.01M H₂SO₄. The detection potential is -0.1 V vs. Ag/AgCl in 3 M KCl. The concentration of H₂O₂ added is 200 μ M. Where error bars are not visible, they are smaller than or the same size as the size of the symbol. In this experiment, n = 3 different batches of gold nanowires. 186

Figure 5.3: Calibration curve for the electrochemical detection of target DNA range 1 μ M to 1 aM on a 2 mm diameter bare electrode following hybridisation with probe DNA that is labelled with hollow gold nanotubes. The supporting electrolyte is 0.01M H₂SO₄. The detection potential is -0.1 V vs. Ag/AgCl in 3 M KCl. The concentration of H₂O₂ added is 200 μ M. Where error bars are not visible, they are smaller than, or the same size as the size of the symbol. In this experiment, n =3 different batches of gold nanotubes. 189

Figure 5.4: Calibration plots for the electrochemical detection of Staph. Aureus mastitis DNA on a 2 mm radius electrode modified with capture strand DNA following hybridization with the target DNA and gold nanowires regioselectively modified with probe strand DNA (◆) and uniformly decorated nanotubes (■). A control experiment showing the response of the electrode where the probe strand is not labelled is also shown (▲). The supporting electrolyte is 0.01M H₂SO₄. The detection potential is -0.1 V vs. Ag/AgCl in 3 M KCl. The concentration of peroxide added was 200 μ M. Where error bars are not visible, they are smaller than, or comparable to, the size of the symbols. 194

Figure 5.5: Calibration plots for the electrochemical detection of Staph. Aureus mastitis DNA on a 2 mm radius electrode modified with capture strand DNA

following hybridization with the target DNA and gold nanowires regioselectively modified with probe strand DNA for each of three individual batches of nanowires. The concentration of H_2O_2 added was $200\ \mu M$. The calibration curves are linear for $-15 < \log [DNA] < -9$ with acceptable correlation coefficients, $R^2=0.9973$, 0.9947 and 0.9917 . The concentration of hydrogen peroxide is $200\ \mu M$ 196

Figure 5.6: Calibration plots for the electrochemical detection of *Staph. Aureus mastitis* DNA on a 2 mm radius electrode modified with capture strand DNA following hybridization with the target DNA that contains a 1 base mismatch, and gold nanowires regioselectively modified with probe strand DNA. The supporting electrolyte is $0.01M\ H_2SO_4$. The detection potential is $-0.1\ V$ vs. $Ag/AgCl$ in $3\ M\ KCl$. The concentration of peroxide added was $200\ \mu M$. $n = 1$ for this experiment. 198

Figure 5.7: Cyclic voltammogram of a 2 mm diameter gold disc electrode after modification with capture strand DNA and hybridization with the target and core-shell nanowires labelled probe sequence where the target strand concentration is $100\ \mu M$. the supporting electrolyte was $0.01\ M\ H_2SO_4$. The scan rate is $100mVs^{-1}$ 208

Figure 5.8: SEM image of nanowires bound to the electrode surface via the DNA hybridisation. This image was captured before the reduction of thiol bonds. The target DNA concentration is $10nM$ and the accelerating voltage is $10kV$ 209

Figure 5.9: Cyclic voltammogram of a 2 mm diameter gold disc after the thiol bonds have been reduced from the nanowires and electrode. The supporting electrolyte is $0.01\ M\ H_2SO_4$. The scan rate is $100mVs^{-1}$. The reference electrode was $Ag/AgCl$ in $3\ M\ KCl$ 211

Figure 5.10: SEM images of DNA modified electrode surface following reduction of thiol bonds between nanowire and probe strand DNA. The accelerating voltage was $10kV$ 212

Figure 5.11: Calibration curve for the electrochemical detection of *Staph. Aureus mastitis* DNA on a 2 mm diameter bare electrode following hybridisation with probe DNA that is labelled with core:shell nanowires. ΔQ represents the

difference in charge before and after the reduction of thiol bonds. Where error bars are not visible, they are smaller than, or comparable to, the size of the symbols. In this case, n=3 different batches of nanowires. The supporting electrolyte is 0.01 M H₂SO₄ and the scan rate is 100 mVs⁻¹.....216

Figure 5.12: Cyclic Voltammogram of bare gold electrode modified with a monolayer of capture strand DNA and nanotube-labelled probe DNA. The supporting electrolyte is 0.01 M H₂SO₄ and the scan rate is 100mVs⁻¹220

Figure 5.13: Calibration curve for the electrochemical detection of target DNA containing a 1 base mismatch on a 2 mm diameter bare electrode following hybridisation with probe DNA that is labelled with core:shell nanotubes. The supporting electrolyte is 0.01M H₂SO₄.223

Figure 5.14: Calibration curve for the electrochemical detection of target DNA containing 3 base mismatch on a 2 mm diameter bare electrode following hybridisation with probe DNA that is labelled with core:shell nanotubes. The supporting electrolyte is 0.01M H₂SO₄.226

Figure 5.15: Electrochemical detection of sequence-specific Staphylococcus Aureus pathogen DNA concentration; (♦) represents a fully complementary target DNA sequence; (■) represents target DNA containing a single base mismatch; (▲) represents target DNA containing 3 base mismatches. The Y axis is the difference in charge before and after reduction of thiol bonds. Where error bars are not visible, they are smaller than, or comparable to, the size of the symbols. In this experiment, n = 3 for different batches of nanowires.228

Figure 5.16: SEM image of probe DNA labelled nanowires confined to the surface of a gold electrode functionalised with capture and 1nM target DNA containing a 1 base mismatch via DNA hybridisation. Accelerating voltage is 10kV.231

Figure 5.17: SEM images of probe-labelled nanowires confined to electrode surface of a gold electrode functionalised with capture DNA and 1nM target DNA containing a 1 base mismatch via DNA hybridisation following copper shell oxidation at +0.3 V vs. Ag/AgCl in 3 M KCl for ten minutes. The accelerating voltage is 10kV.232

Figure 5.18: <i>Current-time transient for selective oxidation of copper shell of core:shell nanowire at a fixed potential of +0.3 V vs. Ag/AgCl in 3 M KCl for 5 hours in 0.1M H₂SO₄. Inset: Charge vs. Time transient following selective oxidation of copper shell at fixed potential of 0.3 V vs. Ag/AgCl in 3 M KCl for 5 hours.....</i>	233
Figure 5.19: <i>SEM images of electrode surface following oxidation of copper shell from nanowire surface for five hours at +0.3V. The accelerating voltage is 10kV.</i>	234

List of Abbreviations

Acronyms

AAO - Anodic Alumina Oxide

Ag/AgCl - Silver/Silver Chloride

Au - Gold

AuNT - Gold nanotube

AuNW - Gold nanowire

Bpy – 2,2`bipyridiyl

CCD - Charged couple detector

Co - Cobalt

CoSO₄ - Cobalt sulphate

Cu - Copper

Cu₂O - Copper (I) oxide

CuCl₂ - Copper chloride

CuO - Copper (II) oxide

CuSO₄ - Copper sulphate

CV - Cyclic Voltammetry

DCM - Dichloromethane

DI - Deionised water

DNA - Deoxyribonucleic acid, either a single strand or double strand

ds - Double stranded

EDX - Energy Dispersive X-ray Spectroscopy

FDTO - Fluorine doped tin oxide

Fe - Iron

Fe(CN)₆³⁻ - Hexacyanoferrate

FeSEM - Field-Emission Scanning Electron Microscopy

GC - Glassy carbon

GOx - Glucose oxidase

GP - General Practitioner

H₂O₂ - Hydrogen Peroxide

H₂SO₄ - Sulphuric Acid

H₃BO₃ - Boric Acid

HAuCl_4 - Tetrachloroaurate (III)
 HCl - Hydrochloric acid
 ICP-MS - Inductively coupled plasma - mass spectrometry
 KCl - Potassium chloride
 KOH - Potassium hydroxide
 LiClO_4 - Lithium perchlorate
 LOD - Limit of Detection
 LOQ - Limit of Quantitation
 N_2 - Nitrogen
 NA - Nucleic acid
 NaCl - Sodium Chloride
 NASBA - Nucleic Acid Sequence Based Amplification
 Ni - Nickel
 NiCl_2 - Nickel chloride
 NiSO_4 - Nickel sulphate
 Ox - Oxidised species
 PBS - Phosphate buffered saline
 PC - Polycarbonate membrane
 PCR - Polymerase Chain Reaction
 PVP – polyvinylpyrrolidone
 Qbpy – 2,2':4,4':4''-quaterpyridyl
 Red - reduced species
 Redox - Reduction-oxidation reaction
 RF - Roughness factor
 RNA - ribonucleic acid
 RS - Raman spectroscopy
 RSD - Residual Standard Deviation
 Ru - Ruthenium
 $\text{Ru}(\text{NH}_3)_6^{3+}$ - Hexaamineruthenium
S. aureus - Staphylococcus aureus
 S/N - signal to noise ratio
 SCE - Saturated Calomel electrode

SE - Surface enhancement
SEM - Scanning Electron Microscopy
SERS - Surface enhanced Raman Spectroscopy
ss - single strand
TEM - Transmission electron microscopy
TiO₂ - Titanium dioxide
UV - Ultra violet

Symbols

μm - micrometre
μM - micromoles per litre
A - area of electrode - cm²
AG - geometric area
aM - attomoles per litre
A_p - area under the peak - cm²
C - Capacitance - F
C_{dl} - double layer capacitance - F
cm - centimetre
D_{ct} - Diffusion coefficient - cm² s⁻¹
E - electrochemical potential - V
e⁻ - electron
E⁰ - standard electrochemical potential - V
E_{1/2} - Half wave potential - V
F - Faraday Constant - C
fM - femtomoles per litre
G - gauss
I - Current - A
j - current density - Acm⁻²
kV - accelerating voltage of secondary electrons kilo volts
M - represents a metal
mA - milliampere

mL - millilitre
mM - millimoles per litre
M_n - number average molar mass
M_n⁺ - metallic ion with positive charge of n
M_w - molecular weight - g mol⁻¹
n - No. of electrons exchanged
nm - nanometre
nM - nanomoles per litre
Ox - oxidised species
pM - picomoles per litre
Q - Charge passed in electrochemical experiment - C
R - universal gas constant - J K⁻¹ mol⁻¹
Red - Reduced species
T - Temperature - °C
t - time - s
V - Volt
ΔG⁰ - Gibbs free energy - eV
ΔH - Line width value - G
μL - microlitre
μM - micromoles per litre
v - scan rate in a cyclic voltammetry experiment - mVs⁻¹

Abstract

Andrea McCooey

High Sensitivity Nucleic Acid detection using Metal Nanowires and Nanotubes

DNA and RNA can be classed as biomarkers of disease, i.e. proteins, antibodies, nucleic acids and cells that are found in abnormal amounts in body fluids or tissue when disease is present. As the number of deaths attributed to diseases such as cancer increase year on year, a strong emphasis is now being placed on the development of point of care devices which test for levels of these biomarkers in blood, serum, saliva, urine or other sample matrices.

An electrochemical biosensor has been developed which aims to amplify the signal associated with a single nucleic acid binding event, rather than amplifying the target nucleic acid, as per PCR or NASBA. This sensor involves a three step procedure, consisting of the immobilisation of a capture strand of single strand DNA to a gold electrode, it's hybridisation with a complementary target, followed by target hybridisation to a complementary probe strand which is labelled with a nanowire.

Nanowires have a number of unique physical and electronic properties that are different from those of spherical nanoparticles, which makes them ideal for use in an electrochemical biosensor. The advantage of nanowires and nanotubes is due to their increased surface area to volume ratio, which changes or enhances the properties of the material they are made of, but also nanotubes and rods can be further functionalised with nanoparticles or biomolecules such as proteins, enzymes or nucleic acids, which can create multi-functional structures.

A template-based electrodeposition process has been employed in order to deposit ordered arrays of uniformly-sized metal nanowires. The electrochemical and spectroscopic properties of these nanowires were investigated with respect to electrodeposition time. Hollow nanotubes were also electrochemically deposited within the walls of polycarbonate membranes. Nanotubes offer the advantage of increased surface area along the inside wall as well as the outside wall, which can enhance the signal associated with the binding of target DNA. The inside walls of nanotubes can also be functionalised with nanoparticles or biomolecules which can add a multi-functional dimension to these structures. The electrochemical and

spectroscopic properties of these nanotubes were also investigated and compared to those of the solid nanowires.

Gold nanowires were electrodeposited using the pores within a polycarbonate membrane as a template. Gold nanostructures are well known to catalyse the reduction of hydrogen peroxide. The catalytic activity of gold nanowires and nanotubes bound through DNA hybridization was assessed by monitoring the difference in current associated with the reduction of hydrogen peroxide in a solution of 0.01M H₂SO₄ before and after peroxide addition. Single stranded capture DNA was bound to the nanowires and an underlying gold electrode and allowed to hybridise with a complementary target strand that is uniquely associated with the pathogen *Staphylococcus Aureus*, (*S. aureus*), which causes mastitis. The modified electrode allows low potential detection of hydrogen peroxide with high sensitivity and fast response time. Semi-log plots of the pathogen DNA concentration vs. change in faradaic current were linear from 1 fM to 10 μ M. The hollow nanowires also produced a response that was linear from 1 fM to 10 μ M, but with a dramatically decreased sensitivity when compared with the solid nanowires (10.3 μ A dec⁻¹ vs. 15.5 μ A dec⁻¹).

Gold-Copper core:shell nanowires have been electrodeposited within the pores of a track etched polycarbonate membrane filter. The sacrificial “stripping” of the outer metal shell of the nanowire has been identified as an alternative detection strategy for nucleic acid detection, which is important for application in a multiplexed assay. Use of this method could allow for several types of target DNA to be detected in a single assay just by manipulating the properties of different metals. Core: shell nanowires functionalised with probe strand DNA that is complementary to that of the pathogen *S. Aureus* were immobilised onto an electrode surface via a DNA sandwich assay. The charge associated with the reductive desorption of the core-shell nanowires were linearly dependant on the log of the target DNA concentration from 1nM to 100 μ M.

Publications and Presentations

E. Spain, A. McCooey, C. Dolan, H. Bagshaw, N. Leddy, T. E. Keyes and R. J. Forster, *Analyst*, 2014, **139**, 5504-5508

E. Spain, A. McCooey, K. Joyce, T. E. Keyes and R. J. Forster, *Sensors and Actuators B-Chemical*, 2015, **215**, 159-165

Posters:

A. McCooey, E. Spain, T.E. Keyes, and R.J. Forster, “Synthesis of Au:Cu core:shell nanowires and their application in DNA detection”, Electrochem 2013, Southampton, September 2013.

A. McCooey, E. Spain, T.E. Keyes, and R.J. Forster, “High Sensitivity miRNA detection using uniformly decorated electrocatalytic Platinum nanoparticles”, Extracellular Biomarkers Summit, Cambridge, MA, March 2015.



1. SURVEY OF LITERATURE

1.1 Introduction

Nucleic acid sequences unique to every living organism and every bacterium, virus, or pathogen provide practical targets for the identification and diagnosis of various diseases. With the advent of rapid sequencing capabilities, sequence information is now available for many diseases. To more effectively combat these diseases in the medical arena, early and accurate detection of DNA markers is crucial.

In this area, multidisciplinary teams of researchers have been evaluating the prospect of using assays based upon nanomaterials to compete effectively with the polymerase chain reaction (PCR). PCR is a technology that allows duplication of portions of prospective targets, and represents the gold standard in terms of sensitivity,¹ but has significant drawbacks including complexity, sensitivity to contamination, cost, and lack of portability and major challenges with respect to multiplexing (detecting multiple targets in a single assay).²

A chemical sensor is a device that can be used to measure an analyte in a sample matrix; ideally it should be capable of responding continuously and reversibly and doesn't damage the sample analyte.³ A biosensor is a sensor device that can detect a biological event concentration of target DNA, or any other biological parameter.⁴ The minimum elements that a biosensor needs are^{5,6}

- A molecular recognition layer, that allows for specific biological interactions to take place, such as nucleic acid, enzymes, tissue, microorganisms, etc.
- A transducer that can be coupled to a readout device to convert the recognition to a measurable signal.
- A detector that can convert the measurable signal into something that can be understood, such as optical, electrochemical, magnetic, etc.

The definition for an electrochemical biosensor, as defined by the International Union of Pure and Applied Chemistry (IUPAC), is as follows⁷:

“An electrochemical biosensor is a self-contained integrated device, which is capable of providing specific quantitative or semi-quantitative analytical information using a biological recognition element (biochemical receptor) which is retained in direct spatial contact with an electrochemical transduction element.”

Therefore, the characteristics of a successful and useful electrochemical biosensor are^{8,9}

- Extremely specific to a certain recognition event, depending on the type of sensor required
- Portable, for point of care diagnostics
- Have self-contained instrumentation, with easily controlled reaction conditions and minimal need for sample preparation, for possible use outside of laboratory conditions
- Be accurate and simple to use, to have the capability for use by semi-skilled operators
- Rapid analysis and output of results
- Should be independent of physical parameters and surroundings, such as pH and temperature
- The probe DNA strands need to be functional after attachment to the electrochemical surface

There are two transducer methods that are most common for use in electrochemical biosensors; amperometric and potentiometric.¹⁰ In potentiometric biosensors, the biorecognition process is converted to a potential signal by using ion selective electrodes. In amperometric biosensors, a constant potential is applied and the current response that is in association with the oxidation or reduction of the species is monitored. Other electrochemical methods that can be used include impedance sensors, which measure the response of an electrochemical system to an oscillating potential, and conductometric sensors, which analyse the change in electrical properties between the two electrodes.¹¹ Amperometric detection would be the most attractive in most cases, due to it being more sensitive and having a wide range.¹² A nucleic acid (NA) biosensor contains a NA biorecognition layer immobilised over the signal transducer. This recognition layer would contain a known sequence of bases, as the sensing element of the sensor. The purpose of this recognition layer is to specifically detect and hybridise with the complementary strands of DNA or RNA, which is the target of the specific biosensor. The transducer determines whether or not hybridisation has occurred and produces an electrochemical signal

which is converted by the detector to a result that can be easily analysed by the user.¹³

DNA microarrays, also known as gene chips, are another form of DNA hybridisation detection that can be used¹⁴. They are similar to biosensors in that they have a specific oligonucleotide sequence immobilised on their surface; however DNA microarrays allow multiple parallel detections and analysis of gene patterns in thousands of gene expressions in a single experiment.^{15,16} The detection of DNA on microarrays involves binding the probe to the target DNA sequence and detecting the generated signal, using methods such as fluorescence, chemiluminescence, colorimetric, etc. However, these methods can take up to 20 hours to generate a result.¹⁷

Some DNA biosensors are known to give results within an hour, using optical biosensor techniques as an example.^{18,19} Despite this, electrochemical DNA biosensors are regarded as being more advantageous and of better use than optical biosensors, due to their increasing miniaturisation, increased portability, and also their compatibility with advanced microfabrication technologies.²⁰ They are also quick, low cost and they are extremely sensitive, with a very low limit of detection that doesn't need amplification from enzymes or other markers.²¹ Sensitivity is the main challenge in creating an electrochemical DNA biosensor, as the target DNA of the analyte may be present in such a low concentration, especially before symptoms of the disease manifest. Methods for improving the sensitivity of these electrochemical DNA biosensor assays include incorporating nanomaterials into the detection method,²² such as nanowires, nanoparticles, or quantum dots.²³

The size of a nanomaterial can be an advantage over a bulk structure, simply because a target binding event involving the nanomaterial can have a significant effect on its physical and chemical properties,²⁴ thereby providing a mode of signal transduction not necessarily available with a bulk structure made of the same material. Sizes, shapes, and compositions of metal nanoparticles can be varied to produce materials with distinct properties, which is important for multiplexed analyte detection.

However, new methods for the synthesis and characterisation of nanomaterials have evolved to the point that deliberate variation of their size, shape, and

composition is possible, allowing control of their electrochemical and optical properties. The ability to carefully tailor the physical properties of nanomaterials is essential for their application in bio-detection.²⁵ Tools and techniques for surface modification and patterning have advanced to a point that now allows generation of nanoscale arrays of bio-macromolecules and small molecules on surfaces. These capabilities allow materials that can potentially be implemented into new assays having improved modes of signal transduction that can compete favourably with PCR to be designed.²⁶

Nanostructures are structures which have at least one dimension of 10-1000Å, a size that is small by engineering standards, common by biological standards, and large to chemists.

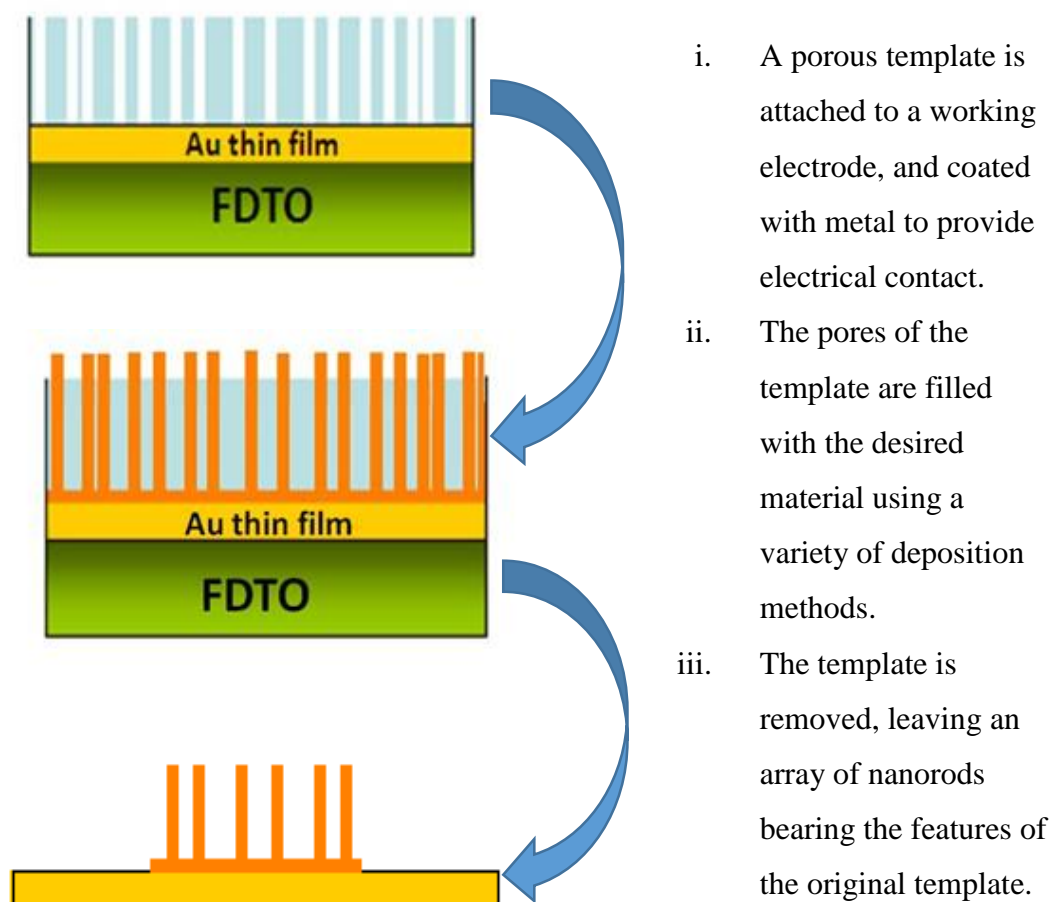
The large interest in nanostructures results from their numerous applications in the fields of energy storage, environmental and biomedical technologies, electronics, optics, magnetism, and electrochemistry due to their unique properties determined primarily by their size, composition and structure.²⁷

Of particular significance is the size dependence of many properties in nanomaterials, for example, an enhancement in the strength and hardness of solids, the possibility of modifying their electrical properties by controlling the arrangement within the constituent nanoclusters and their assembly, the control of chemical reactivity by the attachment of functional side groups, the control of optical properties by variation of the size and microstructure of the nanoclusters; the possibility of creating nanostructures of metastable phases with non-conventional properties, including superconductivity and magnetism.²⁸

Many methods for preparing nanomaterials have been developed, ranging from milling techniques to chemical and lithographic methods.²⁹ However, there is a weakness associated with these structures; it is quite difficult to control the final morphologies of these nanostructures.^{30,31}

A method termed “template-synthesis” entails the preparation of a variety of micro and nanomaterials of a desired morphology and, therefore, provides a route for enhancing nanostructure control. A template can be defined as anything that determines or serves as a pattern, i.e., a structure within which forms a network

such that the removal of the template creates a filled cavity, with features related to those of the original template.³²



Scheme 1: Schematic representation of the templated synthesis of nanowires.

Various porous templates have been employed to synthesise nanostructures within pores.^{55,56, 57, 58, 66} If the template used has cylindrical pores, then nanocylinders will be formed within the voids of the template material. Depending on the deposition procedure, the nanocylinders may be solid (nanowires/nanorods) or hollow (nanotubules).²⁷ These nanostructures can then remain inside the template, be freed from the pores of the template and collected as an ensemble of free nanostructures, or they can protrude from the surface of the template.

With the template approach, one is able to prepare mono-disperse rods and tubules of controlled diameter. This method has been used to synthesise both nanorods and nanofibrils composed of conductive polymers, metals, semiconductors, carbon and other materials.^{59, 66, 81}

In this review, various nanoporous structures used as templates for the synthesis of nanostructures, and the various methods employed for synthesis are described, as well as some of the recent applications of nanowires in the field of nucleic acid detection.

1.2 Template materials

Template synthesis is an elegant chemical approach for the synthesis of nanostructures, in particular for different kinds of nanowires. It can be considered as an alternative to conventional lithography methods. Arrays of nanowires are obtained by filling a porous template that contains a large number of straight cylindrical holes with a narrow size distribution. Template based synthesis is most commonly and widely used to prepare free standing, non-orientated and orientated nanowires, nanorods or nanotubes.³³ Many of the studies carried out to date have utilised one of two types of nanoporous material, “track-etch” polymeric membranes and porous alumina or silica membranes.^{34, 40} However, template-based synthesis suffers from the polycrystalline nature of the resultant nanowires and nanorods³³, in addition to the difficulties to find appropriate templates with pore channels of desired diameter, length and surface chemistry, and to remove the template completely without compromising the integrity of grown nanowires or nanorods.

The most commonly used and widely commercially available templates are anodised alumina oxide (AAO) membranes, or radiation track-etched polycarbonate (PC) membranes.^{34, 40} The commonly used alumina membranes with uniform and parallel pores are made by anodic oxidation of aluminium sheet in solutions of sulphuric, oxalic or phosphoric acids.^{34, 35} Pore densities as high as 10^{11} pores/cm² can be achieved.³⁶ Pore sizes ranging from 10 nm to 100 μ m can be made.^{36, 37} Membrane thickness can range from 10-100 μ m.^{38, 39, 36}

Polycarbonate membranes are made by bombarding a nanoporous polycarbonate sheet, typically 6 to 20 μ m in thickness, with nuclear fission fragments to create damage tracks, and then chemically etching these tracks into pores.⁴⁰ In these radiation track etched membranes, the pores are uniformly sized, and may be as small as 10 nm. These pores are evenly distributed, and the pore densities may be as high as 10^9 pores/cm². Track etch membranes are commercially available (Nuclepore,⁴¹ Millipore,⁴² Poretics,⁴³ Cyclopore,⁴⁴ and Osmonics⁴⁵) filtration

membranes and are usually prepared from materials such as polycarbonate or polyester.

Both templates are convenient to use with a variety of deposition approaches, but each type of template have their disadvantages. The advantage of using PC as the template is its easy handling and removal by means of pyrolysis at elevated temperatures, or dissolution in organic solvents such as dichloromethane³³; but the flexibility of PC makes it more prone to distortion during heating (e.g. during chemical vapour deposition), and the removal of the template could occur before complete densification of the nanostructures, leading to broken or deformed nanorods or nanotubes.

The advantage of using AAO as the template is its rigidity and resistance to high temperatures, which would allow the nanostructures to form completely before template removal, however AAO is difficult to remove completely after nanorod growth.

1.2.1 Other materials

Various other synthetic and natural nanoporous materials have been utilised in template synthesis. Other templates such as nanochannel arrays on glass,⁴⁶ radiation track-etched mica,⁴⁷ mesoporous materials,⁴⁸ porous silicon,⁴⁹ and carbon nanotubes^{50, 51} have also been used to prepare arrays of nanostructures.

Braun et al⁵² developed a two-step procedure that allowed the application of DNA as a template for the vectorial growth of 12 μm long, 100 nm wide conductive silver nanowires. DNA is particularly well suited for application to template synthesis of synthetic nanostructures as it is structurally regular, is able to reversibly assemble through hydrogen bonding, and it is relatively easy to obtain materials of precise length within the nanometre regime.

1.3 Template synthetic techniques

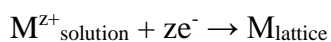
Nearly any solid matter can in principle be synthesised within nanoporous templates ²⁷, provided a suitable chemical pathway can be developed. There are some concerns that need to be considered, for example;

1. Does the deposited material “wet” the pore;
2. How to avoid blocking the pore (which will hinder the growth of the nanostructure);
3. Is the template stable with respect to the reaction conditions.

1.3.1 Electrochemical deposition

Electrochemical deposition of metals and alloys involves the reduction of metal ions from aqueous, organic and fused-salt electrolytes.

The reduction of metal ions M^{z+} in an aqueous solution is represented by



This can be accomplished via two different processes:

1. an electrodeposition process in which z electrons(e) are provided by an external power supply and
2. an electroless deposition process in which a reducing agent in the solution is the electron source.

In either case, the interest is in an “electrode” which is in contact with an aqueous ionic solution. ⁵³

Electrodeposition involves oriented diffusion of charged reactive species through a solution and reduction of the charged growth species at the deposition surface (which also serves as an electrode).⁵⁴

Electrodeposition of materials within the pores of a non-metallic material is preceded by coating one face of the template with a metal film, which is used as a

cathode for electroplating. This can be achieved by methods such as electroplating, electron beam evaporation, or sputtering.^{37, 38, 39}

The volume of the pore is continuously filled up beginning from the pore bottom. The length of the nanostructure can then be controlled by varying the amount of material deposited.^{39,27} When deposition is confined inside the pores of the template membranes nanowires or nanorods are produced. However, when the deposition occurs along the wall surface of the pore channels, nanotubes form.

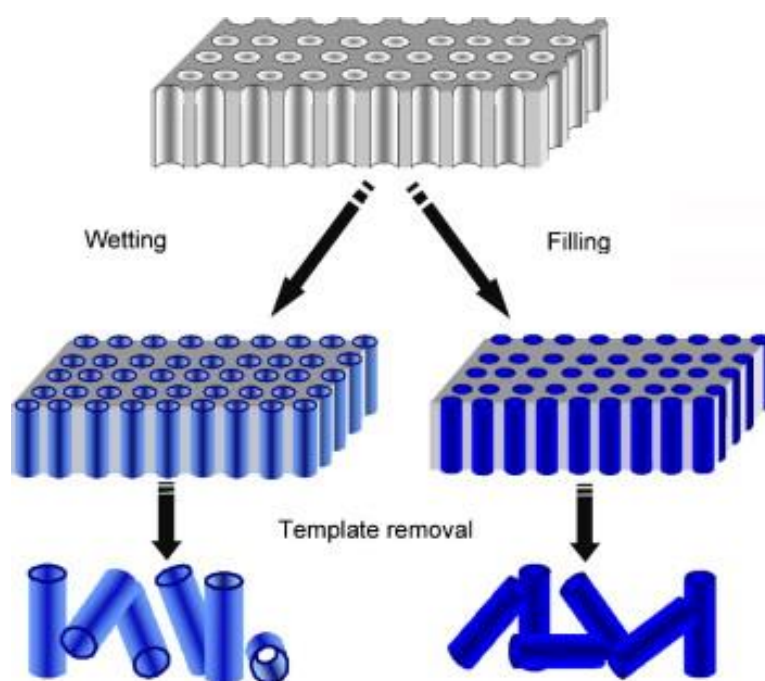


Figure 1.1: Schematic diagram of nanostructures formed within a membrane template; and the structures after removal of the template [reproduced from S. Barth, F. Hernandez-Ramirez, J. D. Holmes and A. Romano-Rodriguez, *Progress in Materials Science*, 2010, **55**, 563-627]

In general, electrochemical deposition is only applicable to electrical conductive materials such as metals, alloys, semiconductors and electrically conductive polymers and oxides.

Both metal and conductive polymer nanorods/tubes can be synthesised using this method.^{55, 56, 57, 58}

1.3.2 Electroless deposition

Electroless deposition is the process of depositing a coating with the aid of a chemical reducing agent in solution, and without the application of external electrical power. Metal deposition rates in electroless deposition are typically lower than that of electrochemical deposition.⁵⁴ In contrast to electrochemical deposition, the surface that is to be coated does not need to be electrochemically conductive.

In the case of templates with pores, the material deposition in the pores starts at the pore wall. The pore walls of the template are generally coated in a conducting substance, and the deposition material preferentially nucleates on the walls of the pores. Therefore, in general, electrochemical deposition results in the formation of “solid” nanorods or nanowires of conductive materials, whereas electroless deposition often grows hollow “fibrils” or tubules. This is because during electroless deposition, the growth of the metal layer starts from the sensitised/activated sites located on the pore walls and progresses from the pore walls to the centre of the pore.

In electrochemical deposition, the length of the nanostructures formed can be controlled by the deposition time; in contrast to electroless deposition, where the length of the nanotubules is solely dependent on the length of the deposition channels or pores. Variation of deposition time would result in different wall thickness in the nanotubes. An increase in deposition time leads to a thick wall, but sometimes a hollow tubule morphology remains even after a prolonged deposition.

Electrochemical deposition was used in this work so as to control the length of the nanowires/nanotubes formed.

1.4 Synthesis of nanomaterials

Nanostructures can be composed of many different types of materials, such as metals, carbon, semiconductors, and polymers.

1.4.1 Gold Nanowires

Schönenberger et al.⁵⁹ used polyvinylpyrrolidone (PVP) coated polycarbonate membranes to synthesise nanowires of different metals (Ni, Co, Cu, and Au) in membranes of different pore diameter. Membranes were used with pore diameters of $d_N = 10, 30, 50, 80,$ and 200 nm, as specified by the supplier. These diameters were quoted as per the manufacturers specifications, and there was no standard deviation data available. The thickness of the membranes used was ~ 6 μm . The following aqueous electrolytes were used: Ni solution, 515 g/L $\text{Ni}(\text{H}_2\text{NSO}_3)_2 \cdot 4\text{H}_2\text{O} + 20$ g/L $\text{NiCl}_2 \cdot 6\text{H}_2\text{O} + 20$ g/L H_3BO_3 ; Co solution, 400 g/L $\text{CoSO}_4 \cdot 7\text{H}_2\text{O} + 40$ g/L H_3BO_3 ; Au solution, 0.32 M gold(I) cyanide + 0.26 M citric acid and 0.65 M KOH ($\text{pH} = 5-6$); Cu solution, 125 g/L $\text{CuSO}_4 \cdot 5\text{H}_2\text{O} + \text{H}_2\text{SO}_4$ ($\text{pH} = 1$). Typical deposition voltages are $-1.2, -1.1, -1.0,$ and -0.2 , and V_{SCE} for Ni, Co, Au, and Cu respectively.

An array of Ni nanowires was successfully synthesised in the membranes whose pores measured $78\text{nm} \pm 18\text{nm}$, (see Figure 1.2). The polycarbonate membrane was dissolved off in dichloromethane and the resulting array was imaged under SEM.

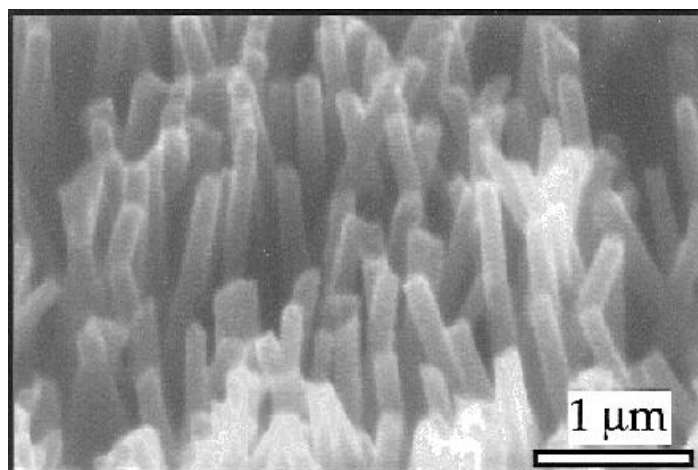


Figure 1.2: SEM image of the Ni nanowires obtained after the dissolution of the polycarbonate membrane. Electrodeposition has been stopped before the transition to bulk growth can occur. [Adapted from C. Schönenberger, B. vanderZande, L. Fokkink, M. Henny, C. Schmid, M. Kruger, A. Bachtold, R. Huber, H. Birk and U. Staufer, *J Phys Chem B*, 1997, **101**, 5497-5505]

As can be seen in the above image, an array of nano-sized cylindrical rods has been synthesised. The array has retained its structural integrity even after dissolution of the membrane template, implying that the rods are anchored by the metallic layer which was evaporated onto the membrane prior to electrochemical deposition. This metallic layer served as a back electrode in the deposition process. The wires in the image above are not orientated uniformly. This is due to a property intrinsic to commercial screen membranes. The pores in these membranes are not aligned parallel but have a considerable angular distribution, in the case of the membranes used in this experiment, of $\pm 34^\circ$.

Even if electrochemical deposition proceeds at an exactly constant rate, complete pore filling may not occur in all pores at an equal rate. If some of the pores are initially poorly wetted, the number of pores in which electrodeposition occurs can increase with time. This results in inhomogeneous growth, which results in wires which are not of equal length. Inhomogeneous growth can be observed in the current-time transient, characterised by a broadening of the “sharp” current increase as the growth transitions to the bulk.

At sufficiently long deposition times, the deposition of the metal changes from growth in the pores to growth on the whole surface of the membrane. This growth change can be seen in Figure 1.3 below. In Figure 1.3a, the deposition has been stopped at the point of transition from growth in the pores to “bulk growth” and some of the wires can be seen to have small hemispherical caps forming on the top of them. In Figure 1.3b, the deposition has been stopped long after the point of transition, and now all of the wires have hemispherical caps, which have grown together into a metallic deposit that covers the entire membrane surface.

The authors claim that the growth in pores proceeds until $\sim 100 - 200$ seconds, after which the transition to bulk growth occurs.

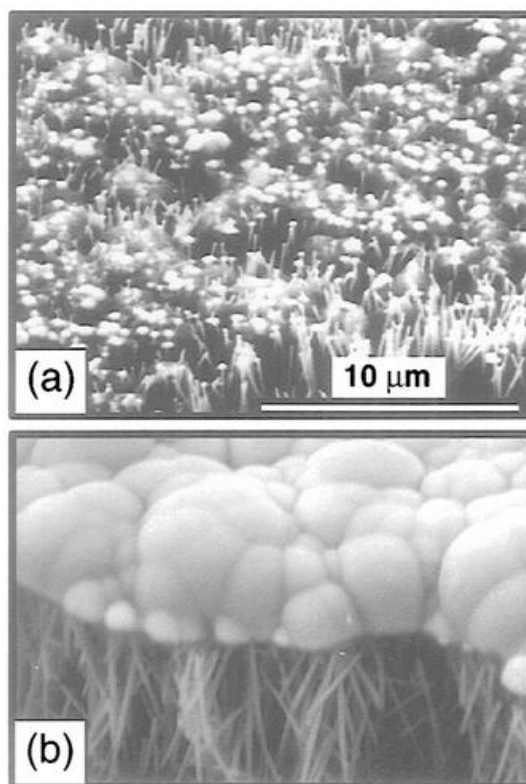


Figure 1.3: SEM images of Ni deposited in 80nm porous membranes obtained after dissolution of the membrane. Electrodeposition has been stopped at the transition to bulk growth and long afterwards for (a) and (b) respectively. [Reproduced from C. Schönenberger, B. vanderZande, L. Fokkink, M. Henny, C. Schmid, M. Kruger, A. Bachtold, R. Huber, H. Birk and U. Staufer, *J Phys Chem B*, 1997, **101**, 5497-5505]

Lu et al.⁶⁰ have deposited gold nanowires in the pores of polycarbonate membranes. The polycarbonate membranes had a pore size of 200 nm, and prior to electrodeposition, were sputtered with a 30 nm thick layer of gold. The nanowires were electrodeposited at a constant potential of 0.18 V vs. SCE from a 0.5M HAuCl₄ solution for 15 minutes.

SEM and TEM micrographs, Figure 1.4, show that the gold nanowires grew well within the pores of the template and display a highly regular and uniform pattern with an average diameter of ~250 nm, which is ~ 25% larger than the dimension of the nanopore in the template, and the length of the nanowire is ~ 10 μm.

The TEM image shows a single gold nanowire dispersed in chitosan solution following dissolution of the membrane in dichloromethane. The wires were dispersed in chitosan solution following dissolution of the membrane in order to immobilise them onto a glassy carbon electrode surface. A straight nanowire can be seen with a diameter of 250 nm, which agrees with the SEM characterisation.

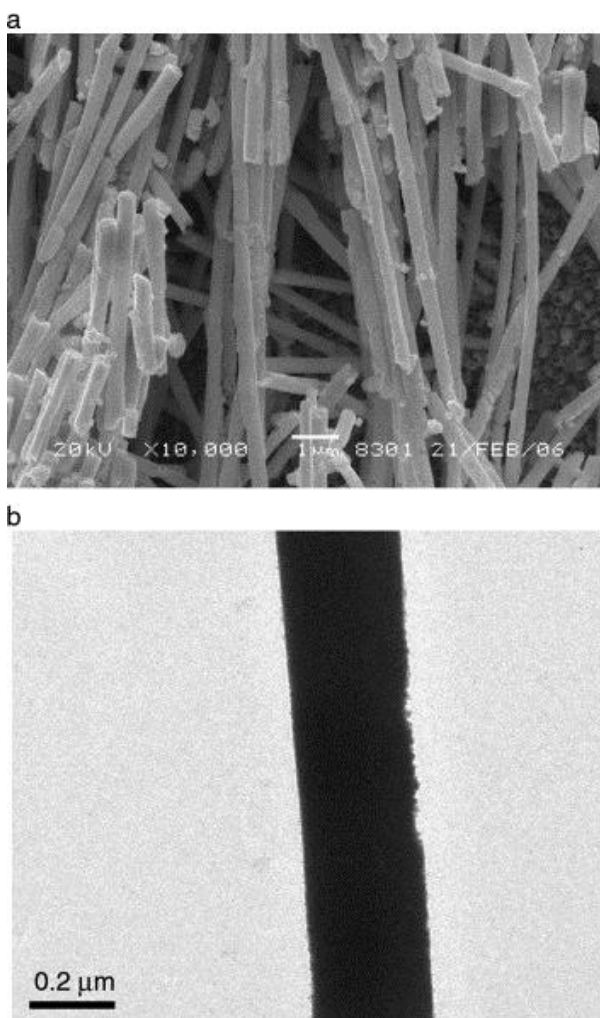


Figure 1.4: (a) SEM micrograph of the gold nanowires following dissolution of the polycarbonate membrane in dichloromethane for 2h. (b) TEM image of a single nanowire dispersed in chitosan solution. [Reproduced from Y. Lu, M. Yang, F. Qu, G. Shen and R. Yu, *Bioelectrochemistry*, 2007, **71**, 211-216]

Karim et al.⁶¹ have also synthesised gold nanowires within the pores of polycarbonate membranes. Membranes 30 μm thick with varying diameters were used as templates, and the wires were deposited from a commercial gold bath of potassium dicyanoaurate (I) containing 10 g/l of gold at 65°C. Four deposition potentials were used: 1.1 V, 1.2 V, 1.3 V, and 1.4 V using a two electrode cell set up, an Au rod acted as anode, and the Cu coated polycarbonate membrane acted as cathode.

SEM micrographs confirm the shape of the nanowires.

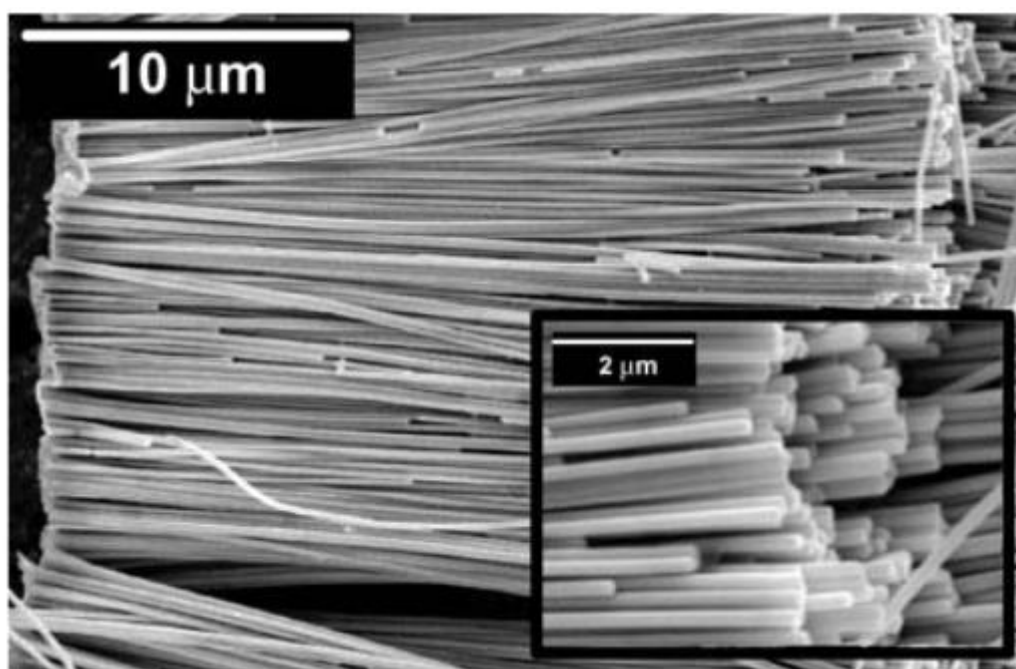


Figure 1.5: SEM micrograph of 160 nm diameter AuNWs. Inset: end sections of wires. [Adapted from S. Karim, M. E. Toimil-Molaes, F. Maurer, G. Mieke, W. Ensinger, J. Liu, T. W. Cornelius and R. Neumann, *Applied Physics A-Materials Science & Processing*, 2006, **84**, 403-407]

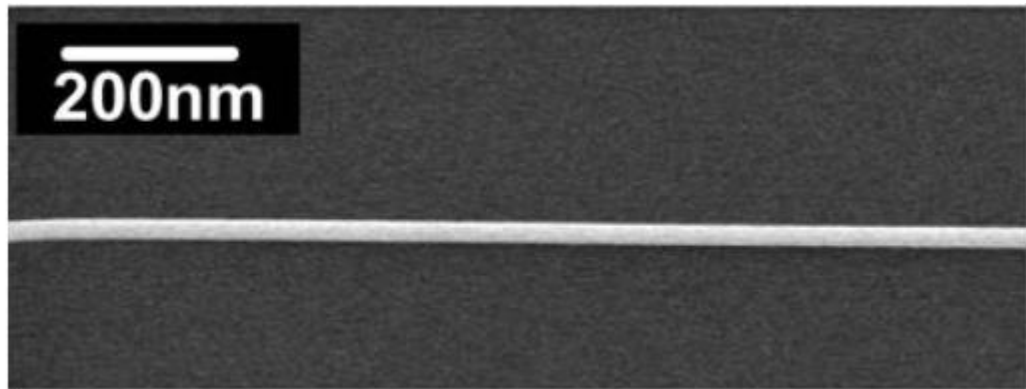


Figure 1.6: HRSEM of a 25 nm nanowire. [Adapted from S. Karim, M. E. Toimil-Molares, F. Maurer, G. Miehe, W. Ensinger, J. Liu, T. W. Cornelius and R. Neumann, *Applied Physics A-Materials Science & Processing*, 2006, 84, 403-407]

Independent of diameter, the nanowires possess homogenous contours and are cylindrical in shape. The inset of Figure 1.5 shows a magnified image of end sections of wires in Figure 1.5 revealing that the wires are cylindrical with uniform cross-section over the whole length.

Since the deposited material acquires exactly the same shape as the pore, the characteristics of membranes employed are extremely important for the fabrication of nanowires. The shape of the pores in commercially available membranes is, in general, not cylindrical with a constant cross-section but is rather toothpick- or cigar-like.⁶² Resultantly, the wires prepared using the commercial membranes are reported to be up to a factor 2.5 wider in the middle than at the end.⁵⁹ Measurements by SEM and TEM of wires prepared by this group did not reveal any diameter variation beyond 10% along the whole length. The authors state that they added an irradiation with UV light step in the formation of their polycarbonate membrane, which the authors propose is the reason there is low variation in pore diameter throughout the membrane length. Templates fabricated without UV sensitization were found to contain pores with rather large diameter variation. In addition, no surfactants were added to the etching solution, which are also known to

considerably influence the pore shape.⁶³ The surfactant is adsorbed onto the film surface, and at the entrances of etched tracks of heavy ions, surfactant molecules tend to decrease the etching rate, thus leading to formation of “spindle-shaped” pores.

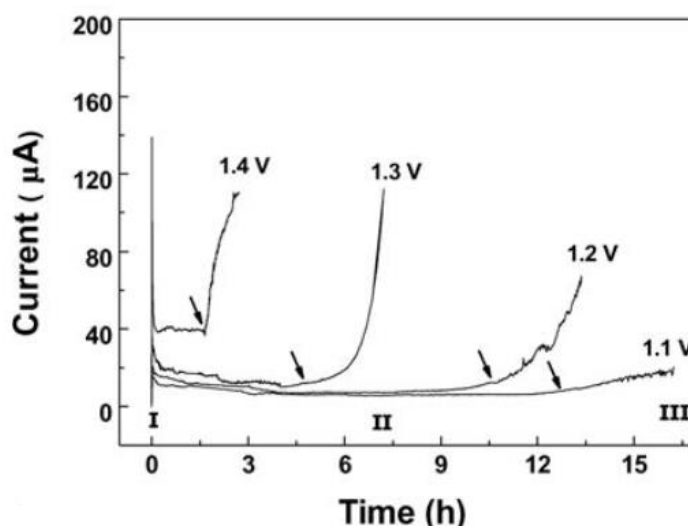


Figure 1.7: Current–time transients for Au electrodeposition in membranes with 70 nm diameter pores for different potentiostatic voltages at 65°C. Arrows indicate the end of zone II, i.e., the point at which the current starts to increase [reproduced from S. Karim, M. E. Toimil-Molares, F. Maurer, G. Mieke, W. Ensinger, J. Liu, T. W. Cornelius and R. Neumann, *Applied Physics A-Materials Science & Processing*, 2006, **84**, 403-407]

Figure 1.7 displays the current-vs.-time transients recorded during electrodeposition of Au nanowires of 70 nm diameter at different voltages and 65°C. The shape of the curves is in agreement with the behaviour described previously for copper deposition in template.⁶⁴ After immersion of the sample in the electrolyte, no external voltage is applied until the open-circuit voltage between cathode and anode stabilises. When a potential is applied, the current exhibits a sharp increase (I) that is attributed to the charge of the electrical double layer. The reduction of ions directly located at the cathode surface generates a concentration gradient, and causes a flux of ions towards the cathode. In this process, the decrease

of current indicates the formation of the diffusion layer. During the growth of the metal in the pores, the current remains nearly constant (II) until the wires reach the polymer surface. When this happens, caps start to grow on top of the wires, and due to the increased surface area, the current increases (III). The increase of the current indicated the point at which the growth transitions to the bulk and begins to form a layer over the top of the template.

1.4.2 Copper nanowires

Irshad et al.⁶⁵ have synthesised copper nanowires within the pores of anodic alumina templates. The electrolyte used was $\text{CuCl}_2 \cdot 6\text{H}_2\text{O}$ buffered with H_3BO_3 and acidified with dilute H_2SO_4 . The nanowires were electrodeposited using a constant applied potential of -1.8 V, using a two electrode set up in which a Cu rod acted as anode, and the gold sputtered anodic alumina template acted as cathode. The deposition was performed for approximately 6000 s.

SEM images confirmed that the wires formed were aligned parallel to each other and had lengths ranging from 20-25 μm . TEM images show that the minimum diameter of the nanowires was approximately 15 nm, which is the smallest template diameter measured by the authors before deposition.

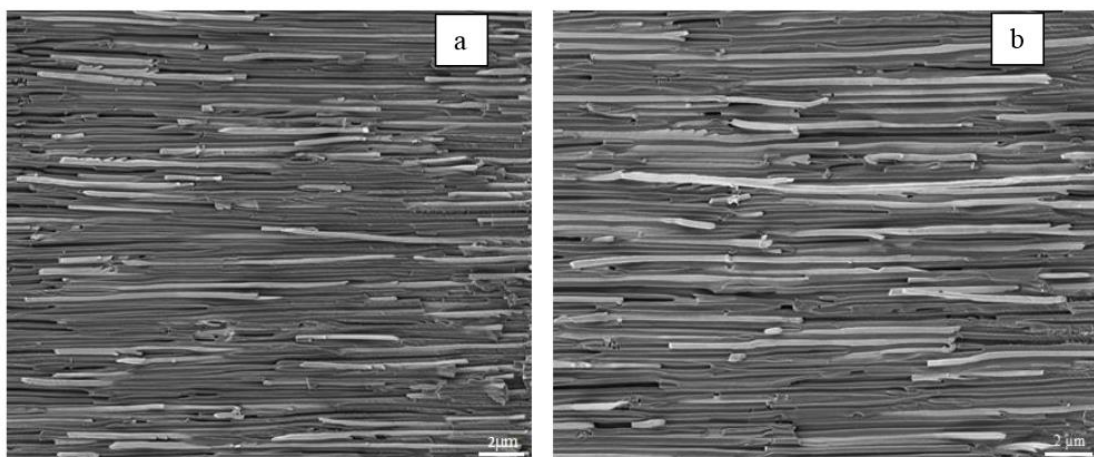


Figure 1.8: Cross sectional view of electrodeposited CuNWs. [Reproduced from M. I. Irshad, F. Ahmad, N. M. Mohamed and M. Z. Abdullah, *International Journal of Electrochemical Science*, 2014, **9**, 2548-2555]

The current density profile is shown in Figure 1.9. In order to understand the growth mechanism of the copper nanowires, the current density profile is divided into three parts, as indicated by the arrows. In the beginning, the current density decreases, showing that all the pores are empty before deposition. After approximately 12 minutes, as in the second region of the curve, the pore-filling factor increases leading to an increase in the current density. In the third region, after approximately 50 minutes, the current density becomes almost constant, indicating that the growth of the nanowire has transitioned to bulk growth that proceeds onto the whole template surface.

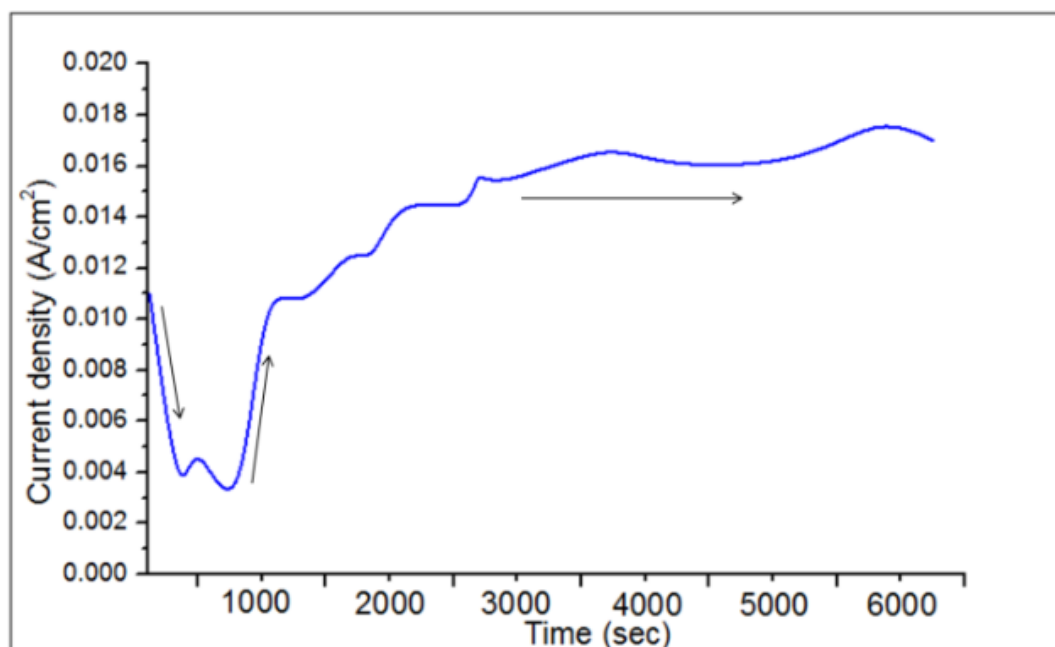


Figure 1.9: Current density profile of Cu nanowire deposition. The three stages of growth are indicated by the arrows: Stage 1: decrease in current density showing pores are empty before deposition, Stage 2: density increases as nanowires begin to grow, and Stage 3: current density becomes constant as growth transitions to a bulk film. [Reproduced from M. I. Irshad, F. Ahmad, N. M. Mohamed and M. Z. Abdullah, *International Journal of Electrochemical Science*, 2014, **9**, 2548-2555]

Inguanta et al.⁶⁶ synthesised copper nanowires in anodic alumina templates. The electrodeposition solution was prepared dissolving 0.2 M of $\text{CuSO}_4 \cdot 5\text{H}_2\text{O}$ and

0.1 M of H_3BO_3 in distilled water; pH of the solution was adjusted to 3 by adding H_2SO_4 . Electrodeposition potentials were -0.3 , -0.45 and -0.6 V vs. SCE. The deposition time used was 3 hours. This time was enough to completely fill the membrane pores, as well as create a continuous Cu overlayer on the top of the membrane. The authors chose different deposition potentials in order to determine whether deposition potentials (both in the region where hydrogen evolution reaction is allowed or not) had any effect on the growth and structure of nanowires formed. In all cases, pure polycrystalline Cu nanowires were fabricated into template pores, having lengths increasing with the total deposition time. Continuous electrodeposition resulted in higher growth rates and less uniform lengths of nanowires.

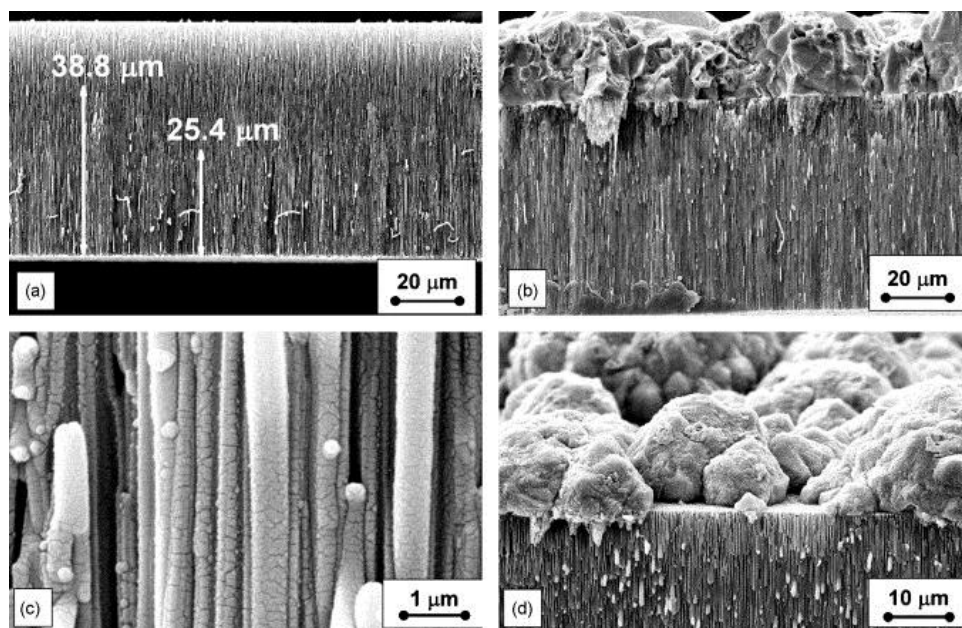


Figure 1.10: Cross-section views of anodic alumina membranes filled with Cu nanowires obtained by continuous deposition. ((a) and (b)) -0.3 V(SCE) after (a) 1 h and (b) 3 h. ((c) and (d)) -0.6 V(SCE) after 1 h of electrodeposition in central part of the cross-section (c) and in proximity of the template surface (d) [Reproduced from R. Inguanta, S. Piazza and C. Sunseri, *Appl. Surf. Sci.*, 2009, **255**, 8816-8823]

Fang et al.⁶⁷ have synthesised copper nanowires inside the pores of TiO₂ films. Anodic Titania templates with pore size of 120 nm were used as template, and the nanowires were electrodeposited from 0.5 M CuSO₄ solution by constant current of -1 mA. SEM images of the solid nanowires formed are shown in

Figure 1.11.

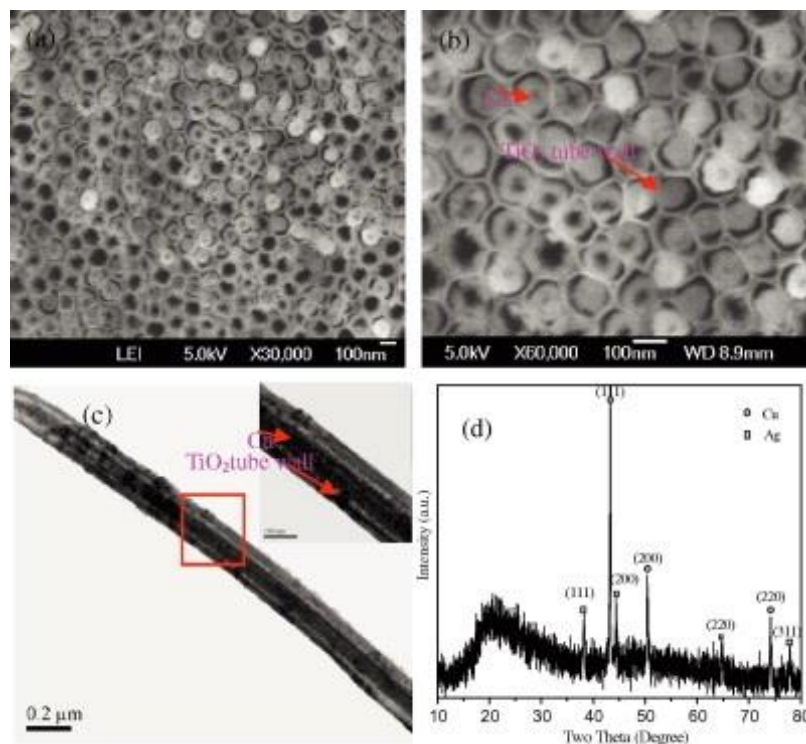


Figure 1.11: Images of TiO₂ templates after filling with Cu: SEM images of top view (a,b), TEM image of cross section (c), and XRD spectrum (d). [Adapted from D. Fang, K. Huang, S. Liu and D. Qin, *Electrochemistry Communications*, 2009, **11**, 901-904]

Based on the SEM and TEM results, the authors suppose that the Cu electroplating inside the TiO₂ membrane proceeds in two ways. The titania template has excellent adsorption ability, so this favours Cu deposition on the pore wall.⁶⁸ In addition, due to the presence of the Ag on the bottom surface, metal plating starts to generate a tube like structure early in the deposition process. As the deposition proceeds, however, the Cu is slowly electroplated, and preferentially deposits on the

electrode surface to smooth the initial tube-like structure, which produces completely packed nanowires growing in the channel direction.⁶⁹

This proposed mechanism is shown in Figure 1.12.

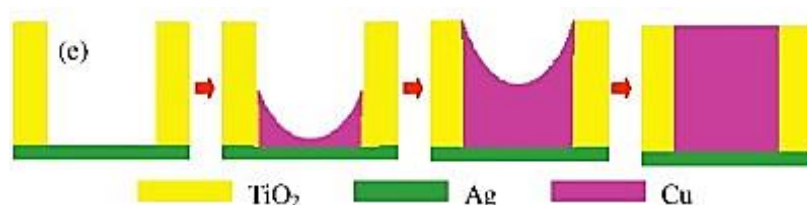


Figure 1.12: The schematic illustration of formation process of Cu nanowires inside the porous anodic titania template. [Adapted from D. Fang, K. Huang, S. Liu and D. Qin, *Electrochemistry Communications*, 2009, **11**, 901-904]

1.4.3 Potentiostatic deposition vs. galvanostatic deposition

Potentiostatic deposition relies on the position of the reference electrode relative to the growth surface. Any voltage drop between the reference and the working electrodes acts as an error, and, in case of nanowire deposition, this will decrease the magnitude of the overpotential at the bottom of the pores. Since the distance from the pore mouth to the bottom of the electrode is decreasing as the nanowires are deposited, the Ohmic error is constantly decreasing, making the deposition potential at the surface closer and closer to the potential set by the potentiostat. Galvanostatic deposition would seem to solve this problem, since the applied voltage between working and counter electrodes would reduce slightly as the nanowires grew, requiring less voltage to pass the same current density into the pores. However, several difficulties have been observed when applying the technique to nanowires, especially in processes with low cathodic current efficiency.⁷² Low current efficiency plating reactions produce hydrogen gas in the pores which sometimes produces bubbles which can lead to the pores becoming blocked.⁷⁰ Even if the pore does not become fully blocked, the presence of these hydrogen bubbles block a certain portion of the pore, leading to deposition of the

metal around this blockage. In these cases, hollow nanotubes are normally formed, rather than solid nanowires.^{71, 72} As a greater portion of the pores become blocked, the reduced electrode surface area results in a greater current density everywhere else. This increased current density in the unblocked pores leads to more rapid deposition, an altered alloy composition, and a very low fill-factor.⁷⁰

These observations would suggest that galvanostatic deposition is more suited to hollow tube formation, and potentiostatic deposition for solid nanowire fabrication.

1.5 Core shell nanowires

Davis and Podlaha⁷² have synthesised Cu nanotubes, and CoNiCu nanotubes with a CuSO₄ filling, from a CoNiCu electrolyte, within the pores of a polycarbonate membrane. The membrane was 10 μm thick, and the pore diameter was 800 nm. The membrane was sputtered with Au prior to deposition of the tubes in order to provide electrical contact. The sputtering times varied from 10 minutes to 50 minutes. Longer sputtering times resulted in thinner tube walls, and longer tubes formed. The tubes were formed from a low efficiency CoNiCu electrolyte composed of 50 mM CoSO₄, 57 mM NiSO₄, and 1 mM CuSO₄. The alloy deposition was carried out at a potential of -1 V vs. SCE. The CuSO₄ filling was deposited at a potential of -0.325 V vs. SCE, which formed solid nanowires inside the preformed tubes.

Hollow Cu tubes were formed by deposition from the alloy solution at a potential of -0.325 V vs. SCE for 14 hours. The membrane was sputtered for 50 minutes. The electrodeposition time was increased from 1 hour to compensate for the lower current density.

SEM images of the deposited wires confirm their tube structure, and EDX spectroscopy confirms their Cu composition.

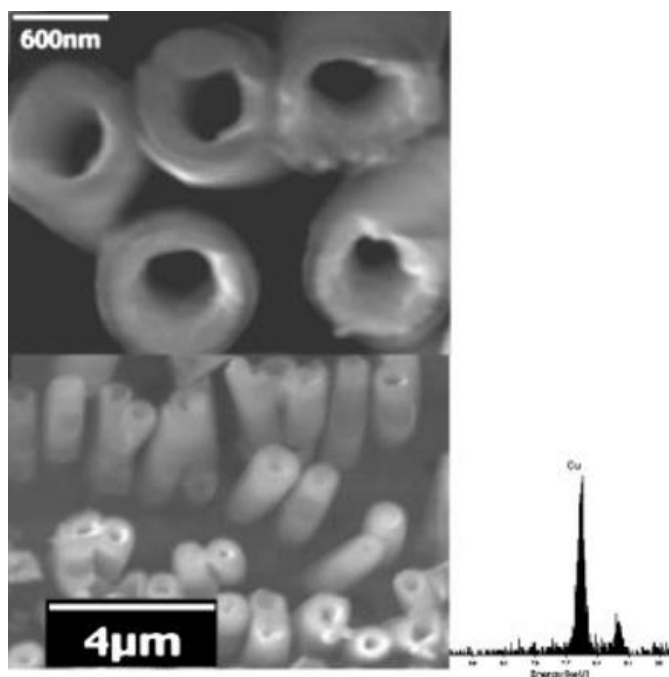


Figure 1.13 SEM of Cu nanotubes plated from the CoNiCu bath at -0.325 V. Cu EDX spectrum shown on lower right. [Reproduced from D. M. Davis and E. J. Podlaha, *Electrochemical and Solid State Letters*, 2005, **8**, D1-D4]

The nanotubes were shown to be $\sim 5 \mu\text{m}$ long, and the wall thickness averaged $218 \text{ nm} \pm 54 \text{ nm}$. The EDX spectrum showed that pure Cu was deposited.

Despite the very long sputtering times, SEM images confirm that the pores of the membrane were not sealed before deposition. The preferential plating along the inner wall is then attributed to the small amount of Au sputtered along the edges of the pores, but this does not explain why the tubes do not deposit axially to form nanowires, especially at long deposition times. Due to the low current efficiency of the CoNiCu electrolyte, the authors proposed that gas evolution during deposition was responsible for the tube formation. This was confirmed by the use of a high efficiency CuSO_4 electrolyte at less negative deposition potential and low sputter time (10 min). This formed solid gold nanowires instead of hollow tubes.

Thus, gas evolution plays a significant role in the formation of nanotubes. When there is no gas generation, such as in a concentrated electrolyte, solid nanowires are formed instead of hollow tubes. A suggested mechanism for this is that for

horizontally positioned membranes, the generated hydrogen gas finds a path from the growing electrode surface through the pore centre to the pore mouth, and subsequently blocks the deposition in its path, and shields the centre of the nanopore.

Following this, the authors formed core:shell nanowires. CoNiCu tubes were first deposited at -1 V vs. SCE for 60 min on a membrane sputtered for 20 min. after making the CoNiCu tubes, the centre area was filled by electrodepositing Cu from the concentrated Cu electrolyte at -0.325 V vs. SCE. SEM images confirmed that the wires were indeed solid following Cu deposition, and EDX indicates a slightly larger Cu peak compared to EDX of CoNiCu tubes formed earlier Figure 1.14. XRF was also performed and confirmed increased Cu content in the core shell nanowire.

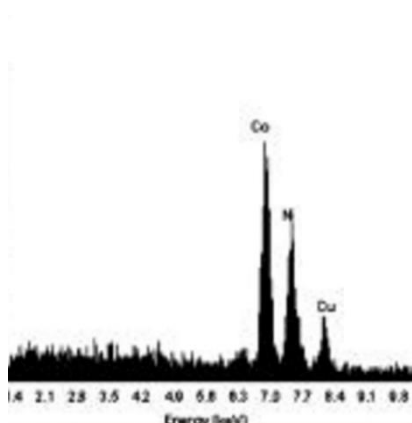


Figure 1.14: *EDX spectrum of CoNiCu nanotubes deposited for 60 min at -1 V from CoNiCu electrolyte. [Adapted from D. M. Davis and E. J. Podlaha, *Electrochemical and Solid State Letters*, 2005, **8**, D1-D4]*

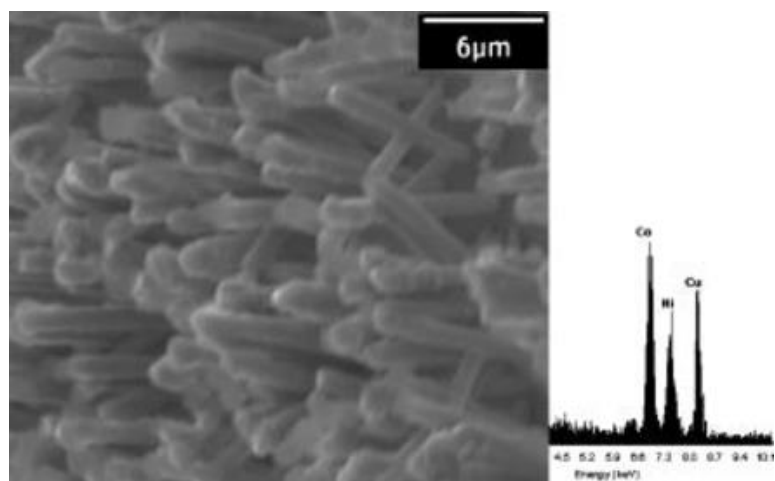


Figure 1.15: SEM of core:shell wires obtained by filling CoNiCu tubes with Cu from a concentrated Cu electrolyte. EDS spectrum is shown on the right. [Reproduced from D. M. Davis and E. J. Podlaha, *Electrochemical and Solid State Letters*, 2005, **8**, D1-D4]

1.6 Summary

Nanowires can be deposited in the pores of templates via electrodeposition or electroless deposition. A wide range of potentials can be applied in order to form solid metal nanowires. Minimising side reactions such as gas evolution will ensure that solid nanowires are created, as will ensuring that the electrodeposition solution used is highly efficient. Polycarbonate membranes must be sputtered or plated with a layer of metal prior to electrodeposition to provide electrical contact, and there are several methods of attaching the membrane to the working electrode, e.g. Nafion interlayer, adhesive tape or sticker, polyelectrolytic glue, or melamine foam.

Core shell nanowires can be formed by filling the centre of pre deposited nanotubes. The formation of nanotubes can be controlled by the use of a low-efficiency electrolyte, a low over-potential which causes side reactions such as gas evolution, or not sealing the pores of the template with the sputtering metal, so that the metal preferentially deposits on the walls of the pore, where the sputtered metal has deposited.

The centre of these preformed tubes can then be filled with a different metal either by using a highly concentrated electrolyte solution, or depositing at a less negative potential.

1.7 Applications

The emergence of nanomaterials over the last decade as versatile and functionalisable platforms has spurred an era of great advances in the biosensing field, particularly in the area of nucleic acid detection.^{73,74,75} Taking electrode platforms from the micro- to the nanoscale has practical implications that may allow wider implementations of electrochemical nucleic acid biosensors as clinical tools.

There are several challenges inherent with working with nanomaterials that must be considered when developing a biosensor. For example, issues with sensor homogeneity and reproducible fabrication of the electrodes can be a challenge at the nanoscale.

A range of nanomaterials have been used in nucleic acids biosensors, including metal and metal-semiconductor nanoparticles, magnetic nanoparticles, quantum dots, nanowires and carbon nanotubes.^{76,77,78,79} They may be used in electrochemical DNA sensors either as the electrode, as reporter groups to signal hybridisation and initiate a transduction event, or (in the case of magnetic nanoparticles), either for separation and sample preparation prior to analysis or for signal amplification. Nanoparticles as labels for electrochemical biosensing provide benefits such as stability, flexibility, sensitivity, high reaction rates, low cost, and applicability to multiplexed assays.⁸⁰

The detection strategies used for nanomaterial-based nucleic acid sensors are varied, but include direct electrical readout of conductance or resistance, and electrochemical techniques.

1.7.1 Gold Nanowires

Ramulu et al.⁸¹ have synthesised gold nanowires in the pores of a polycarbonate membrane via a two-step electrochemical deposition technique. These nanowires were then functionalised with DNA and their nucleic acid sensing capabilities were then studied via cyclic voltammetry and electrochemical impedance spectroscopy.

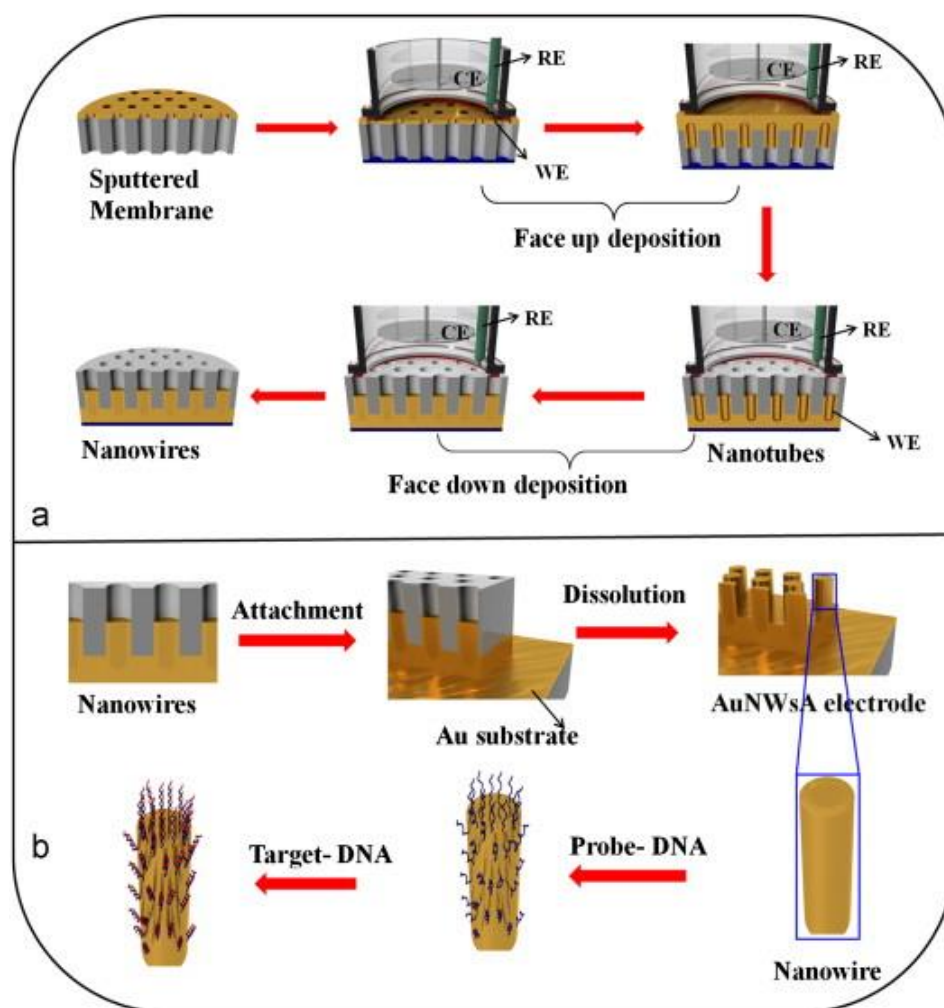


Figure 1.16: Schematic illustration of (a) Synthesis of AuNWs and (b) fabrication of the DNA biosensor electrodes. (WE-working electrode, RE-reference electrode, CE-counter electrode) [Reproduced from T. S. Ramulu, R. Venu, B. Sinha, B. Lim, S. J. Jeon, S. S. Yoon and C. G. Kim, *Biosens. Bioelectron.*, 2013, 40, 258-264]

After deposition of the nanowires, the wires are attached to a gold-coated glass substrate using a chitosan solution, and the polycarbonate membrane is removed by dissolution in dichloromethane. This method gives rise to a modified electrode surface with aligned unidirectional wires on the surface. The wires have an average length of 1.5 μm and diameter of 200 nm (as per the pore size of the membrane).

The wires were then functionalised with thiolated probe DNA at a concentration of $1.3 \times 10^{-5} \text{ M}$ for 12 hours. Hybridisation to the probe DNA immobilised electrode was accomplished by incubating it with different concentrations of target DNA for 1 h at 37 °C. The nanowire-modified electrode was then characterised using cyclic voltammetry. The cyclic voltammograms obtained at a scan rate of 20 mVs^{-1} for Au electrode with bare wires attached (i), thiolated probe DNA immobilised on Au/NWs electrode (ii), AuNW/thiolated probe-DNA) and hybridised complimentary DNA (iii), AuNW/thiolated probe-DNA/complementary target-DNA) electrodes are shown in Figure 1.17. The Au/NW electrode produces a well-defined cathodic peak and anodic peak at in the potential range of 0.6 to -0.4 V with an I_a of 0.9 mA (curve i). The immobilisation of thiolated probe DNA on the AuNW electrode surface results in a decrease in the peak current (0.622 mA), indicating that the probe DNA was successfully immobilized on the AuNW electrode surfaces (curve ii). A further decrease in the peak current (0.502 mA) was observed when the complementary DNA was hybridised with the probe DNA (curve iii).

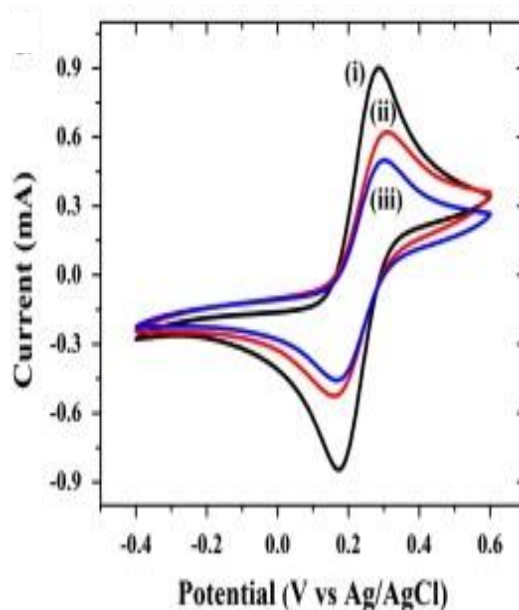


Figure 1.17: Cyclic voltammograms of AuNW (i), AuNW/thiolated probe-DNA (ii) AuNW/thiolated probe-DNA/complementary target-DNA (iii) electrodes in 0.05 M PBS (pH 7.4, 0.15 M NaCl) containing 5 mM $[\text{Fe}(\text{CN})_6]^{3-/4-}$ [Reproduced from T. S. Ramulu, R. Venu, B. Sinha, B. Lim, S. J. Jeon, S. S. Yoon and C. G. Kim, *Biosens. Bioelectron.*, 2013, 40, 258-264].

The authors also performed two selectivity assays using a non-complementary target strand of DNA and a complementary strand containing a one-base mismatch, as well as incubating with varying concentrations of probe DNA from 1.35×10^{-5} M to 1.35×10^{-9} M. The change in current was plotted vs. log of [DNA], and the response of the array was linear across all target concentrations used (Figure 1.18). The authors have not reported standard deviations in their results, suggesting that the results shown are from one experiment only, therefore no comment can be made on the repeatability and reproducibility of this assay.

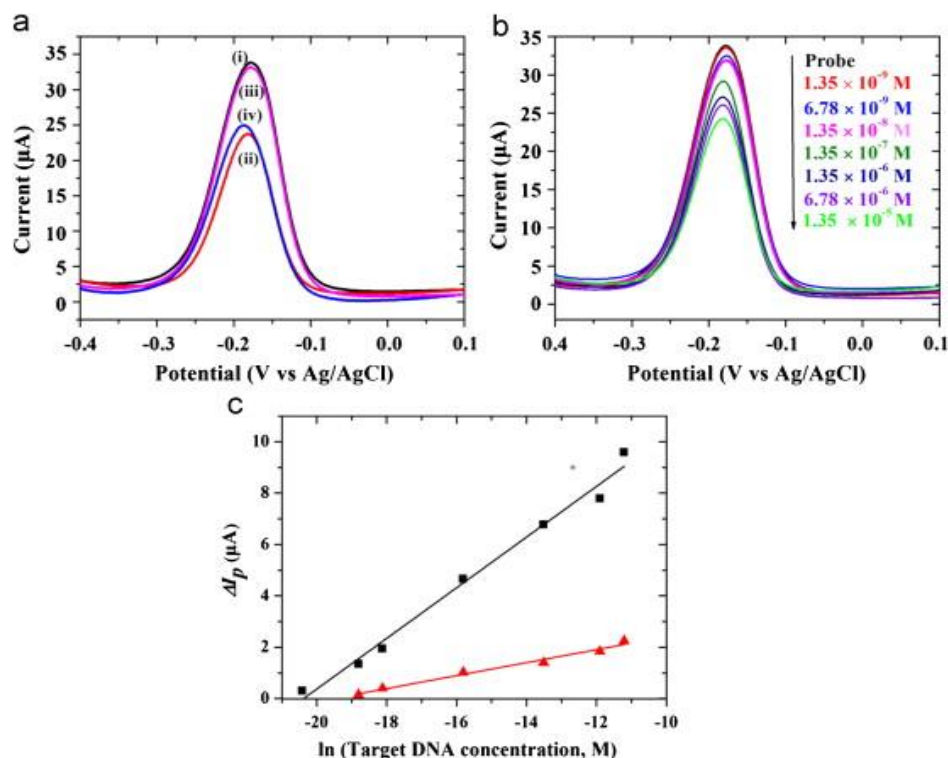


Figure 1.18: (a) Differential pulse voltammograms of (i) AuNWsA/t-DNA (ii) AuNWsA/t-DNA/c-DNA (iii) AuNWsA/t-DNA/nc-DNA(iv) AuNWsA/t-DNA/m-DNA electrodes; (b) DPV measurements of AuNWsA/t-DNA electrode after hybridization with different concentrations of complimentary sequence in 0.05 M PBS (pH 7.4, 0.15 M NaCl) containing 20 μM methylene blue and (c) ΔI_p as a function of $\ln(\text{target DNA concentration})$ of (i) bare Au electrode (ii) and AuNWsA electrode. [Reproduced from T. S. Ramulu, R. Venu, B. Sinha, B. Lim, S. J. Jeon, S. S. Yoon and C. G. Kim, *Biosens. Bioelectron.*, 2013, 40, 258-264]

The LOD of the modified electrode is $6.78 \times 10^{-9} M$, which is two times lower than the detection limit of the unmodified Au electrode. The concentration of free, circulating DNA in blood in healthy individuals is reported to vary between 10-1500 ng/mL⁸²; but it has been shown to increase slightly in patients with diseases such as malignant tumours.⁸³ This corresponds to a femtomolar ($10^{-15} M$) concentration of free circulating DNA per mL of blood. This sensor's LOD is not sensitive enough to detect these levels of free DNA in a small volume of sample, which would render it difficult to adapt to a point-of-care system.

Gasparac et al.⁸⁴ have utilised the electrocatalytic capability of gold nanowires in order to detect DNA associated with *Helicobacter pylori*, a pathogen implicated in gastric ulcers and cancer.⁸⁵ Their gold nanowires were prepared using an electroless plating procedure within the pores of polycarbonate track-etch membranes. Oxygen plasma was then used to remove a thin layer of the polycarbonate, exposing ~200 nm of the deposited nanowires. These exposed nanowires mounted in the PC membrane were then used to prepare a three-dimensional gold nanoelectrode ensemble (NEE).

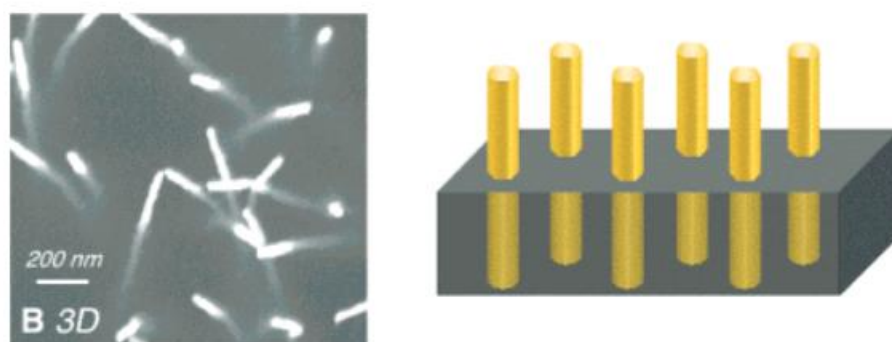


Figure 1.19: *Scanning electron micrograph and schematic illustration of 3D nanoelectrode ensemble. [Reproduced from Gasparac, R.; Taft, B. J.; Lapierre-Devlin, M. A.; Lazareck, A. D.; Xu, J. M.; Kelley, S. O. *J. Am. Chem. Soc.* **2004**, 126, 12270-12271]*

The gold nanowires were functionalised with thiolated probe DNA, which was complementary to the pathogen *H. pylori*. The label-free system reports on the binding of the target DNA to an immobilised probe oligonucleotide using a catalytic reaction between two transition-metal ions, $[\text{Ru}(\text{NH}_3)_6]^{3+}$ and $[\text{Fe}(\text{CN})_6]^{3-}$. The Ru(III) electron acceptor is reduced at the electrode surface, and re-oxidised by excess Fe(III), making the electrochemical process catalytic. The increased concentration of anionic phosphates at the electrode surface that accompanies DNA hybridisation increases the local concentration of $[\text{Ru}(\text{NH}_3)_6]^{3+}$, and therefore produces large changes in the electrocatalytic signal.

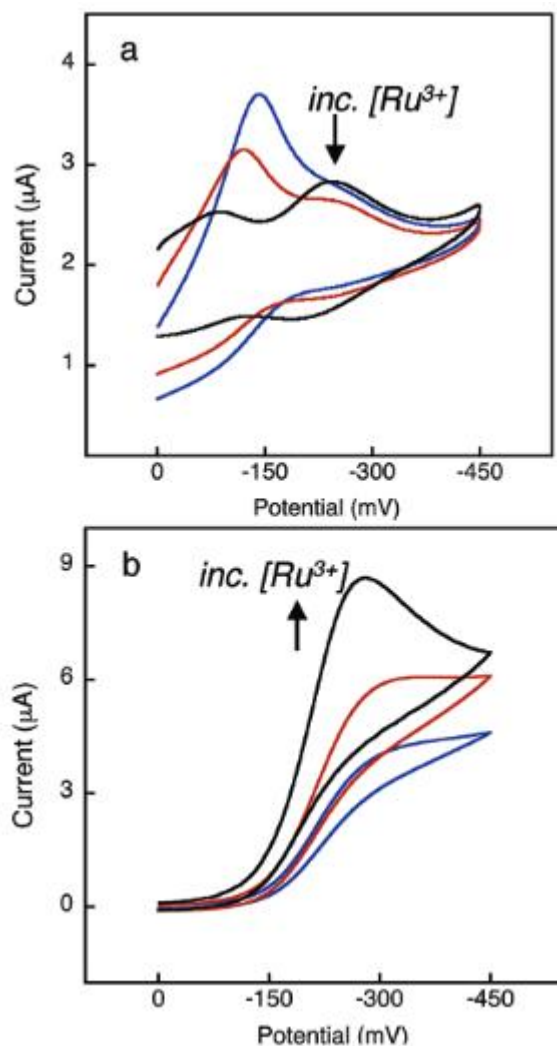


Figure 1.20: Representative cyclic voltammograms for 18-mer duplex DNA modified macroelectrode (a), and NEE (b) collected in solutions containing 2 mM $[Fe(CN)_6]^{3-}$ and 10 (blue), 20 (red), and 80 μM (black) $[Ru(NH_3)_6]^{3+}$ [Reproduced from M. A. Lapierre-Devlin, C. L. Asher, B. J. Taft, R. Gasparac, M. A. Roberts and S. O. Kelley, *Nano Letters*, 2005, **5**, 1051-1055]

The dependence of the electrocatalytic currents on the concentration of $[Ru(NH_3)_6]^{3+}$ at NEEs is markedly different than at macroelectrodes. At the macroelectrode, the addition of Ru^{3+} strongly attenuated the efficiency of the electrocatalysis. As $[Ru(NH_3)_6]^{3+}$ is titrated into the immobilised DNA monolayer, the catalytic wave disappears while the direct $Ru(III)$ reduction becomes more

pronounced (Figure 1.20a). However, at NEEs, electrocatalytic currents increase with $[\text{Ru}(\text{NH}_3)_6]^{3+}$ (Figure 1.20b).

The electrocatalytic signals generated after the hybridisation of the target DNA exhibit a large increase when compared to results obtained by the same group when using Au macroelectrodes.⁸⁶ These results strongly support the notion that the three-dimensional architectures of nanowires facilitate the electrocatalytic reaction because of enhanced diffusion occurring around these structures.

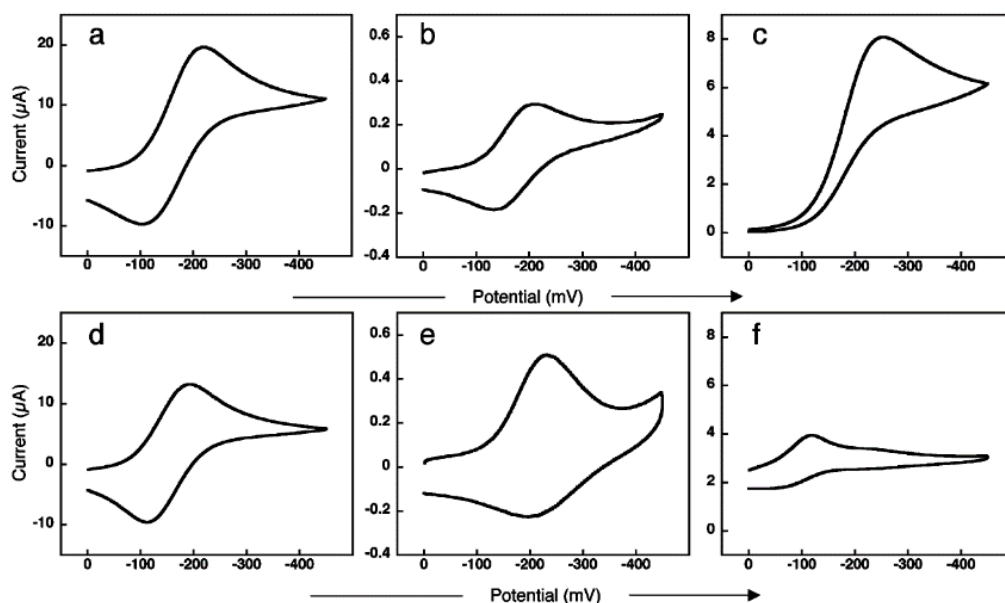


Figure 1.21: Representative cyclic voltammograms of (a) 3 mM $[\text{Ru}(\text{NH}_3)_6]^{3+}$ at a bare NEE, (b) 27 μM $[\text{Ru}(\text{NH}_3)_6]^{3+}$ at a NEE modified with 30-mer duplex DNA, (c) 27 μM $[\text{Ru}(\text{NH}_3)_6]^{3+}$ and 2 mM $[\text{Fe}(\text{CN})_6]^{3-}$ at a NEE modified with 30-mer duplex DNA, (d) 3 mM $[\text{Ru}(\text{NH}_3)_6]^{3+}$ at a bare Au macroelectrode, (e) 27 μM $[\text{Ru}(\text{NH}_3)_6]^{3+}$ at a macroelectrode modified with 30-mer duplex DNA, (f) 27 μM $[\text{Ru}(\text{NH}_3)_6]^{3+}$ and 2 mM $[\text{Fe}(\text{CN})_6]^{3-}$ at a macroelectrode modified with 30-mer duplex DNA [Reproduced from M. A. Lapierre-Devlin, C. L. Asher, B. J. Taft, R. Gasparac, M. A. Roberts and S. O. Kelley, *Nano Letters*, 2005, **5**, 1051-1055]

The 3D NEEs were used to establish the sensitivity of the electrocatalytic DNA assay performed on the nanoscale architecture. When a probe-modified 3D NEE

electrode was titrated with a target DNA strand, solutions containing picomolar concentrations of the analyte produced detectable changes in the electrochemical signal. The authors state that as the exposed geometric area of their NEE electrode is 0.07 cm^2 , zeptomole detection limits could easily be detected with just a slight modification of the aperture used in the electrochemical analysis.

Lu et al.⁶⁰ have synthesised gold nanowires and functionalised them with enzymes for utilisation in a hydrogen peroxide biosensor. The synthesis of these nanowires is described previously in synthesis of nanomaterials section.

The gold nanowires were functionalised with glucose oxidase by dispersing them in a 10 mg/mL solution overnight at 4 °C. The functionalised wires were then dispersed in 0.5 wt.% chitosan solution in acetic acid, and sonicated for 15 minutes. 10 μL of this mixture was then coated onto the surface of a polished glassy carbon electrode in order to form the Au NW modified electrode used in the hydrogen peroxide sensor.

The response of the glucose oxidase modified nanowires to hydrogen peroxide was compared to unmodified wires (both cast on bare glassy carbon electrodes).

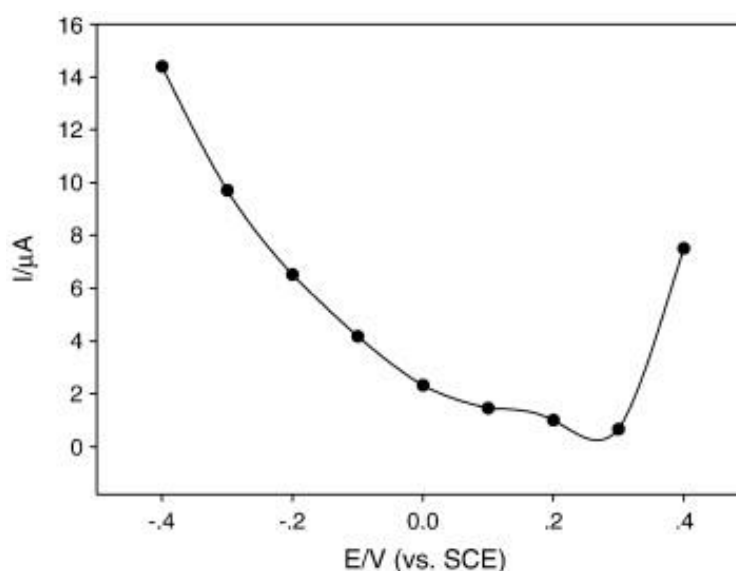


Figure 1.22: Effect of potential on the response of the gold nanowire modified electrode towards 1 mM hydrogen peroxide in 0.06 M PBS. [Reproduced from Y. Lu, M. Yang, F. Qu, G. Shen and R. Yu, *Bioelectrochemistry*, 2007, **71**, 211-216]

Figure 1.22 shows the effect of applied potential on the gold nanowire modified electrode response toward hydrogen peroxide in 0.06 M phosphate buffer. The range of potential was controlled from -0.4 to 0.4 V vs. SCE. As can be seen, during the potential range studied, high response current was observed and the potential of 0.3 V vs. SCE is a turning point. In this study, the potential of -0.2 V vs. SCE was selected. At such a low applied potential, the background current decreased, the responses of common interference species can be minimised, and the oxygen reduction current can be limited.

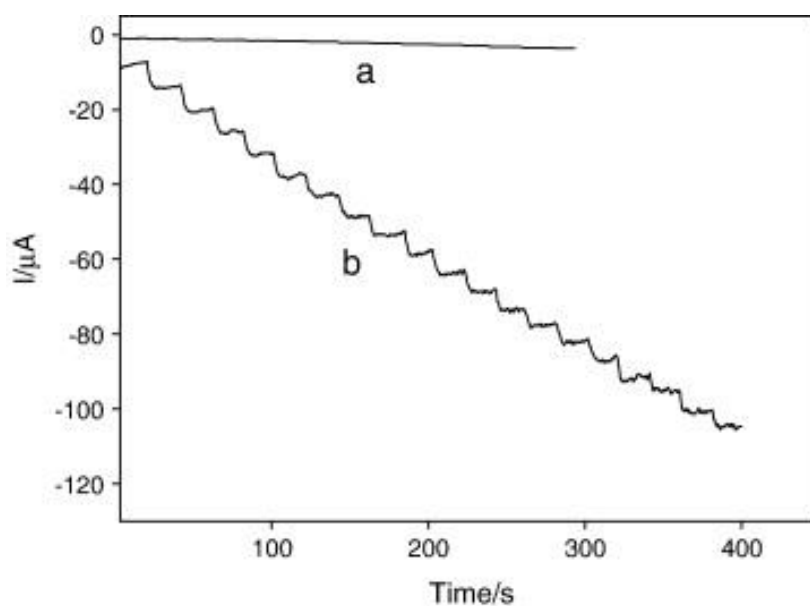


Figure 1.23: Current-time transient obtained at the conventional gold electrode (a) and the gold nanowire modified electrode (b) upon increasing the concentration of hydrogen peroxide in steps of 1 mM at -0.2 V vs. SCE in 0.06 M PBS. [Reproduced from Y. Lu, M. Yang, F. Qu, G. Shen and R. Yu, *Bioelectrochemistry*, 2007, 71, 211-216]

Figure 1.23 displays the typical current–time curve at the conventional gold electrode (a) and the Au nanowire modified electrode (b) to H_2O_2 . The process of detection was carried out at -0.2 V vs. SCE under air-saturated condition and 1 mM H_2O_2 were successively added into the phosphate buffer. As shown in Figure 1.23, the modified electrode responds rapidly to the changes in the level of hydrogen peroxide, producing steady signals within 5 s. The sensitivity of the gold

nanowire modified electrode is about 30 times higher than conventional gold electrode. The excellent electrochemical response observed is due not only to the higher effective surface area of the gold nanowire modified electrode, but also the properties of Au nanowires themselves, including excellent catalytic activities, unique electrical properties and high conductivity.

The amperometric responses of the glucose oxidase (GOx) modified biosensor for successive addition of 0.5 mM glucose at -0.2 V vs. SCE are presented in Figure 1.24, and inset is the calibration curve. One can see that the biosensor was sensitive toward glucose and a steady-state current signal was generated within 8 s. The sensitive response means that large amount of enzymes are adsorbed onto the nanowire surface. Meanwhile, as can be seen from the calibration curve, the glucose biosensor exhibits the linear range of 0.01 mM up to 20 mM with a correlation coefficient of 0.997 and based on $S/N = 3$, a detection limit of 5×10^{-6} M was obtained. The lower detection limit of the linear calibration range of the gold nanowire modified electrode toward glucose is 1.0×10^{-5} M.

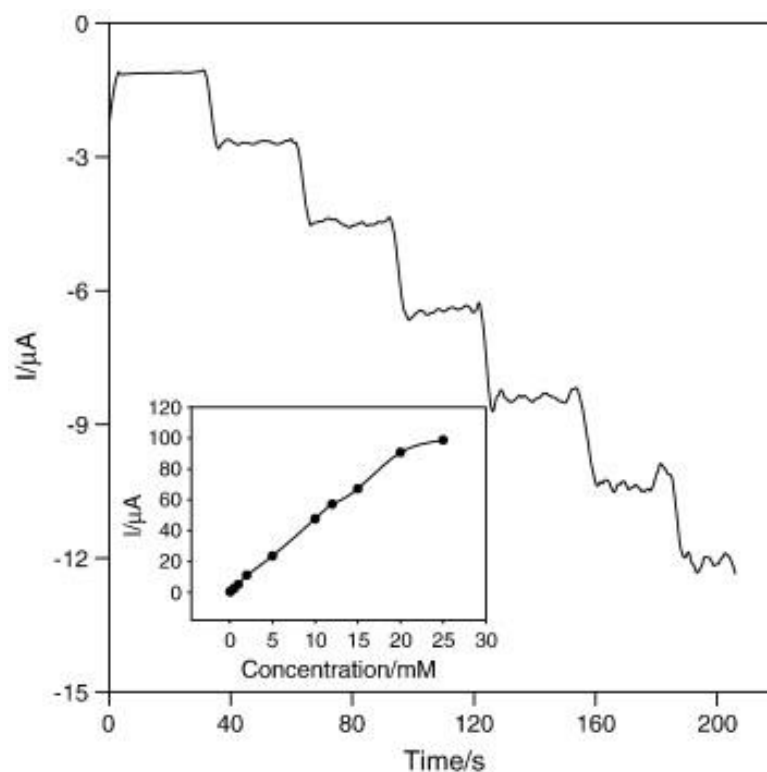


Figure 1.24: Current time transient of GOx modified biosensor for the successive addition of 0.5 mM glucose at -0.2 V vs. SCE. Inset: Calibration curve of current response over range of glucose concentrations. [Reproduced from Y. Lu, M. Yang, F. Qu, G. Shen and R. Yu, *Bioelectrochemistry*, 2007, **71**, 211-216]

The interference-free determination of glucose was demonstrated by an independent recovery test. The recovery test was carried out in 10 mL phosphate buffer containing real physiological samples (0.5 mL serum). By using standard addition method, standard glucose solutions were added to the assay solution. Five assays were performed with the recoveries in the range of 97.6–104%, which illustrated the reliability of the results of the biosensor. The RSD were obtained from three determination and the low values mean that the GOx is stable when absorbed onto the electrode surface and can be used for practical applications.

1.7.2 Core:Shell Nanowires

The electrochemical reduction of H_2O_2 at the surface of bimetallic Ag:Cu core:shell nanowires has been investigated.⁸⁷ The core:shell nanowires were seeded onto the surface of a glassy carbon disk electrode that had been treated with 0.5% Nafion.

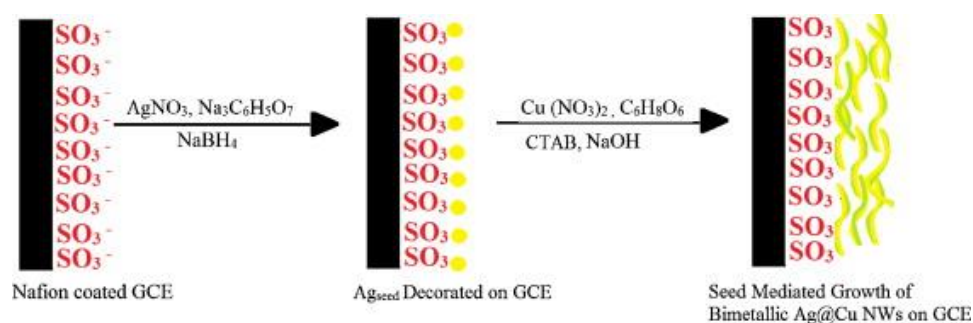


Figure 1.25: Schematic representation of formation of bimetallic Ag:Cu core:shell nanowire modified glassy carbon electrode [Reproduced from J. S. Easow and T. Selvaraju, *Electrochim. Acta*, 2013, **112**, 648-654]

The nanowires formed were characterised using SEM.

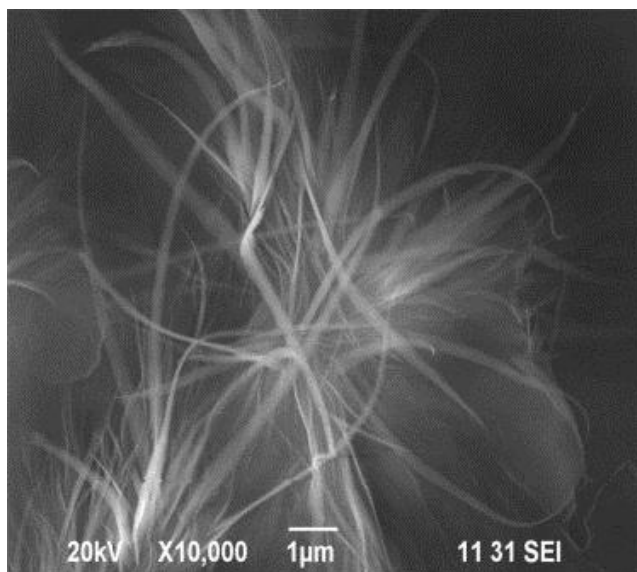


Figure 1.26: SEM image of Ag:Cu bimetallic nanowires grown on glass substrates for SEM analysis. [Reproduced from J. S. Easow and T. Selvaraju, *Electrochim. Acta*, 2013, **112**, 648-654]

Voltammetric characterisation of the core:shell nanowires was performed in PBS in the presence of 0.2 mM H_2O_2 , and compared with the response of a bare glassy carbon (GC) electrode, and a glassy carbon electrode modified with 0.5% Nafion and Ag seeds (GC/Nf/Ag_{seed}). The voltammograms are shown in Figure 1.27.

No observable reduction peak current was recorded for the GC/Nf/Ag_{seed} electrode, and a slight peak was observed for the bare GC electrode in the potential window $0 \rightarrow -0.6$ V vs. Ag/AgCl (Figure 1.27a and Figure 1.27b). An enhanced reduction peak at -0.438 V vs. Ag/AgCl was recorded for the core:shell nanowire modified electrode (Figure 1.27c).

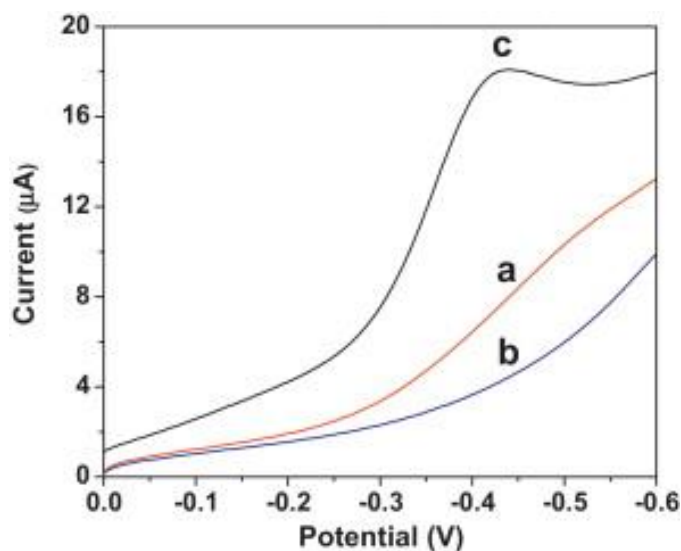


Figure 1.27: Cyclic voltammetric response of (a) bare GC, (b) GC/Nf/Ag_{seed}, and (c) bimetallic GC/Nf/Ag:CuNW electrodes in the presence of 0.2 mM H₂O₂. The supporting electrolyte was 0.01 M PBS (pH 7.2). [Reproduced from J. S. Easow and T. Selvaraju, *Electrochim. Acta*, 2013, **112**, 648-654]

These bimetallic core:shell NW modified GC electrodes were then used to construct an amperometric sensor for H₂O₂ reduction. Figure 1.28 shows the amperometric current vs. time response of the modified electrode to different concentrations of H₂O₂ in PBS. The concentration of H₂O₂ is varied from 1 mM to 10 mM and injected every 40 seconds. Figure 1.28 inset shows a linear calibration based on the steady state H₂O₂ electrocatalytic reduction current observed at the core:shell nanowire modified electrode. The LOD of this assay was 3 μM H₂O₂ with a S/N ratio of 3.

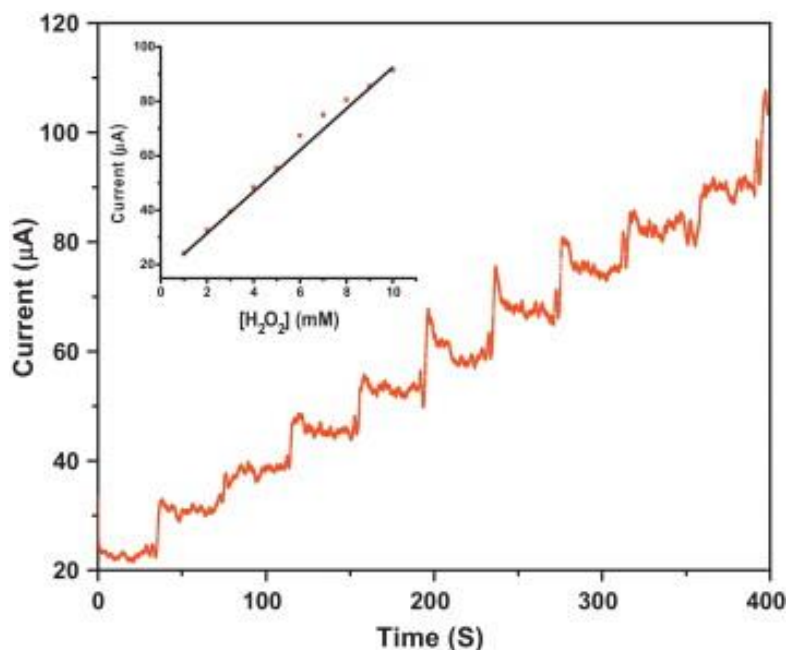


Figure 1.28: Chronoamperometric response of bimetallic GC/Nf/Ag:Cu NWs electrode toward different concentrations of H_2O_2 in PBS (pH 7.2). The electrode potential is fixed at -0.6 V vs. Ag/AgCl. Inset: Current correlation vs. H_2O_2 concentration. [Reproduced from J. S. Easow and T. Selvaraju, *Electrochim. Acta*, 2013, **112**, 648-654]

While a linear correlation is observed for H_2O_2 concentration, no correlation coefficient is reported in the article, therefore the sensitivity of this assay is unknown.

The use of bimetallic core:shell nanowires for detection of biomolecules could lend itself to multiplex devices, as each metal will be electrochemically active at different potentials. Modifying these nanowires with biomolecules such as nucleic acids specific to different diseases, or with antibodies that capture different types of bacteria, could allow two or more diseases to be detected with a single test.

Developing a multiplexed assay has significant impacts for point of care diagnostic devices, which many see as the future of medicine. These devices should be easy to use and require low sample volumes with little-to-no sample preparation, allowing them to be used by a GP or patient without need for specialised training or extra equipment.

1.7.3 Summary

Table 1.1: *Summary of applications of nanowires in different biosensors*

Author	Metal Used	Rod Architecture	Sensor type	LOD
Ramulu	Gold	Nanowire	Electrochemical DNA biosensor	6.78 nM
Gasparac	Gold	Nanowire	Electrochemical DNA biosensor	pM
Lu	Gold	Nanowire	Electrochemical H ₂ O ₂ biosensor	5 μ M
Easow	Silver: Copper	Core:shell nanowire	Electrochemical H ₂ O ₂ biosensor	3 μ M

Most of the previously reported systems do not have an LOD low enough to detect the concentration of target DNA in the early stages of disease, before symptoms have manifested.

The aim of this work is to increase the sensitivity of the assay by utilising the larger nanowire or nanotube surface area, resulting in a large amplification of the signal generated by target binding, especially when compared to a nanoparticle. The advantage of this system over current available systems is that without the need for target amplification, the assay time reduces significantly, as PCR cycles can take up to 30 hours to complete.

1.8 Conclusion

Template-based synthesis has been shown to be an effective technique for synthesising nanostructures whose morphologies and dimensions can be controlled. These nanostructures have applications in a large range of fields of study, including energy storage, biosensors, and optics.

Templates such as polycarbonate membrane are readily available at low cost, and they provide nanowires/tubules/rods with uniform diameter which are easily harvested from the membrane due to its ability to readily dissolve in organic solvents. These membranes are available with a large range of pore sizes, which means that wires/tubes/rods with different diameters can be synthesised.

Electrodeposition of a metal into the pores of these templates allows for synthesis of nanorods/nanotubes whose length can be controlled by controlling the deposition time. The structure formed may be hollow or solid depending on the parameters used.

The advantage of nanowires and nanotubes is due to their increased surface area to volume ratio, which changes or enhances the properties of the material they are made of, but also nanotubes and rods can be further functionalised with nanoparticles or biomolecules such as proteins, enzymes or nucleic acids, which can create multi-functional structures. These functionalised rods or tubules can then be utilised in biosensors e.g. electrocatalytic activity of metal nanoparticles decorated on tubule surface, nucleic acid detection, environmental sensors, or fuel cells.

This survey also presents an overview of the electrodeposition of metals in templates and their applications in environmental sensors and biosensors.

The focus of this work is on the catalytic ability of the metals at the nanoscale, and on the utilisation of the enhanced signals attributed to catalytic activity at nanowire surfaces in order to improve the sensitivity of nucleic acid biosensors. The literature reviewed has shown that gold nanowires are useful catalysts of hydrogen peroxide, and hexaamineruthenium/ ferrocyanide. The catalytic activity of the nanowires is greatly increased compared to bulk gold electrodes, which has positive

implications for the improvement of the sensitivity and limits of detection of biosensors. The literature has also shown that gold nanowires exhibit good biocompatibility, and this allows them to be functionalised with enzymes, nucleic acids and other biomolecules. Copper is also shown to have excellent catalytic sensitivity towards hydrogen peroxide.

The use of two different metals in a core:shell structure was anticipated to yield a second detection strategy that could be combined with electrocatalysis, in order to produce an assay that was capable of detecting two separate nucleic acid sequences. The use of two metals in a single nanowire structure also has the potential to detect more than one biomolecule simultaneously just by changing the potential at which their response to an electrocatalytic reagent is recorded.

The aim of this work is to develop an ultrasensitive, multiplexed approach to directly detect low concentrations of disease biomarkers, such as upregulated proteins, antibodies and nucleic acids in blood and tissue. Functionalised electrocatalytic metal nanowires could significantly amplify ($\sim 10^9$) the signal generated by biomarker capture. Multiplexing will allow a small panel of biomarkers to be detected thus improving early diagnosis as well as the monitoring of treatment efficacy and disease recurrence. This approach will negate the need for target amplification, and will significantly decrease the time from blood sample taken to diagnosis. The high sensitivity of this method will also aid early diagnosis and hopefully lead to faster treatment and improved prognosis.

1.1 References

- ¹ R. Saiki, S. Scharf, F. Faloona, K. Mullis, G. Horn, H. Erlich and N. Arnheim, *Science*, 1985, **230**, 1350-1354.
- ² B. W. Kirk, M. Feinsod, R. Favis, R. M. Kliman and F. Barany, *Nucleic Acids Research*, 2002, **30**, 3295-3311.
- ³ J. Wang, *Analytical Electrochemistry*, Wiley, New York, 2001.
- ⁴ J. R. Chen, Y. Q. Miao, N. Y. He, X. H. Wu and S. J. Li, *Biotechnol. Adv.*, 2004, **22**, 505-518
- ⁵ J. Wang, R. Krause, K. Block, M. Musameh, A. Mulchandani, P. Mulchandani, W. Chen and M. J. Schoning, *Anal. Chim. Acta*, 2002, **469**, 197-203.
- ⁶ T. G. Drummond, M. G. Hill and J. K. Barton, *Nat. Biotechnol.*, 2003, **21**, 1192-1199.
- ⁷ D. R. Thevenot, K. Toth, R. A. Durst and G. S. Wilson, *Pure and Applied Chemistry*, 1999, **71**, 2333-2348.
- ⁸ K. J. Odenthal and J. J. Gooding, *Analyst*, 2007, **132**, 603-610.
- ⁹ M. Pohanka and P. Skladai, *Journal of Applied Biomedicine*, 2008, **6**, 57-64.
- ¹⁰ J. Wang, *Biosens. Bioelectron.*, 2006, **21**, 1887-1892.
- ¹¹ D. Wei, M. J. A. Bailey, P. Andrew and T. Ryhaenen, *Lab on a Chip*, 2009, **9**, 2123-2131
- ¹² J. Wang, *J. Pharm. Biomed. Anal.*, 1999, **19**, 47-53
- ¹³ J. J. Gooding, *Electroanalysis*, 2002, **14**, 1149-1156.
- ¹⁴ A. Sassolas, B. D. Leca-Bouvier and L. J. Blum, *Chem. Rev.*, 2008, **108**, 109-139.
- ¹⁵ D. D. Shoemaker and P. S. Linsley, *Curr. Opin. Microbiol.*, 2002, **5**, 334-337.
- ¹⁶ C. C. Xiang and Y. D. Chen, *Biotechnol. Adv.*, 2000, **18**, 35-46.

- ¹⁷ J. H. Zhai, H. Cui and R. F. Yang, *Biotechnol. Adv.*, 1997, **15**, 43-58.
- ¹⁸ P. A. E. Piunno, U. J. Krull, R. H. E. Hudson, M. J. Damha and H. Cohen, *Anal. Chem.*, 1995, **67**, 2635-2643.
- ¹⁹ H. J. Watts, D. Yeung and H. Parkes, *Anal. Chem.*, 1995, **67**, 4283-4289.
- ²⁰ J. Wang, *Nucleic Acids Res.*, 2000, **28**, 3011-3016.
- ²¹ S. R. Mickelsen, *Electroanalysis*, 1996, **8**, 15-19.
- ²² J. Wang, *Analyst*, 2005, **130**, 421-426.
- ²³ J. E. N. Dolatabadi, O. Mashinchian, B. Ayoubi, A. A. Jamali, A. Mobed, D. Losic, Y. Omid and M. de la Guardia, *TrAC Trends in Analytical Chemistry*, 2011, **30**, 459-472.
- ²⁴ J. Wang and X. Qu, *Nanoscale*, 2013, **5**, 3589-3600.
- ²⁵ P. Alivisatos, *Nat Biotech*, 2004, **22**, 47-52.
- ²⁶ N. L. Rosi and C. A. Mirkin, *Chem. Rev.*, 2005, **105**, 1547-1562.
- ²⁷ A. Huczko, *Applied Physics A-Materials Science & Processing*, 2000, **70**, 365-376.
- ²⁸ M. S. Dresselhaus, *Materials Science and Engineering B-Solid State Materials for Advanced Technology*, 1993, **19**, 192-197.
- ²⁹ G.C. Hadjipanayis (Editor), Richard W. Siegel (Editor), ***Nanophase Materials: Synthesis - Properties - Applications (NATO Science Series E: Applied Sciences, Volume 260)***, Kluwer Academic, 1994. p.260.
- ³⁰ M. Moskovits, *Rev. Mod. Phys.*, 1985, **57**, 783-826.
- ³¹ S. Kivelson and A. J. Heeger, *Synth. Met.*, 1988, **22**, 371-384.
- ³² Template | Define Template at Dictionary.com
- ³³ G. Cao and D. Liu, *Adv. Colloid Interface Sci.*, 2008, **136**, 45-64.
- ³⁴ R. Furneaux, W. Rigby and A. Davidson, *Nature*, 1989, **337**, 147-149.

- ³⁵ J. O'M. Bockris, R. E. White, and B. E. Conway, *Modern aspects of electrochemistry*, Pergamon Press, New York, 1982.
- ³⁶ D. Almawlawi, N. Coombs and M. Moskovits, *J. Appl. Phys.*, 1991, **70**, 4421-4425.
- ³⁷ C. Foss, M. Tierney and C. Martin, *J. Phys. Chem.*, 1992, **96**, 9001-9007.
- ³⁸ C. R. Martin, *Chem. Mater.*, 1996, **8**, 1739-1746.
- ³⁹ J. Hulteen C. and C. R. Martin, *J. Mater. Chem.*, 1997, **7**, 1075-1087.
- ⁴⁰ R. L. Fleischer, P. B. Price and R. H. Walker, *Nuclear tracks in solids: principles and applications*, University of California Press, Berkeley, 1975.
- ⁴¹ Nuclepore Track-Etched Membranes. <http://www.whatman.com/>
- ⁴² Isopore™ Membrane Filters – Millipore www.millipore.com
- ⁴³ Sphaero Q <http://www.sphaero-q.com/>
- ⁴⁴ Cyclopore Polycarbonate and Polyester Membranes <http://www.whatman.com/>
- ⁴⁵ Osmonics Sdn Bhd <http://osmonics.com>.
- ⁴⁶ R. J. Tonucci, B. L. Justus, A. J. Campillo and C. E. Ford, *Science*, 1992, **258**, 783-785.
- ⁴⁷ G. Possin, *Rev Sci Instrum*, 1970, **41**, 772-774.
- ⁴⁸ C. G. Wu and T. Bein, *Science*, 1994, **264**, 1757-1759.
- ⁴⁹ S. S. Fan, M. G. Chapline, N. R. Franklin, T. W. Tombler, A. M. Cassell and H. J. Dai, *Science*, 1999, **283**, 512-514.
- ⁵⁰ C. Guerret-Piecourt, Y. Lebouar, A. Loiseau and H. Pascard, *Nature*, 1994, **372**, 761-765.
- ⁵¹ P. M. Ajayan, O. Stephan, P. Redlich and C. Colliex, *Nature*, 1995, **375**, 564-567.

- ⁵² E. Braun, Y. Eichen, U. Sivan and G. Ben-Yoseph, *Nature*, 1998, **391**, 775-778.
- ⁵³ M. Paunovic and M. Schlesinger, *Fundamentals of electrochemical deposition*, Wiley, New York, 1998.
- ⁵⁴ Mohler JB, *Electroplating for the Metallurgist, Engineer and Chemist*, John Wiley & Sons, New York, 1951.
- ⁵⁵ H. Kaur, S. Singh, J. Kaur and R. Kumar, *Polym. Plast. Technol. Eng.*, 2012, **51**, 1193-1197.
- ⁵⁶ A. Keilbach, J. Moses, R. Koehn, M. Doeblinger and T. Bein, *Chemistry of Materials*, 2010, **22**, 5430-5436.
- ⁵⁷ S. Kumar, D. Saini, G. S. Lotey and N. K. Verma, *Superlattices and Microstructures*, 2011, **50**, 698-702.
- ⁵⁸ Z. Liu, Y. Wang, Y. Liao and G. J. Cheng, *Nanotechnology*, 2012, **23**, 125602.
- ⁵⁹ C. Schonenberger, B. vanderZande, L. Fokkink, M. Henny, C. Schmid, M. Kruger, A. Bachtold, R. Huber, H. Birk and U. Staufer, *J Phys Chem B*, 1997, **101**, 5497-5505.
- ⁶⁰ Y. Lu, M. Yang, F. Qu, G. Shen and R. Yu, *Bioelectrochemistry*, 2007, **71**, 211-216.
- ⁶¹ S. Karim, M. E. Toimil-Molares, F. Maurer, G. Mieke, W. Ensinger, J. Liu, T. W. Cornelius and R. Neumann, *Applied Physics A-Materials Science & Processing*, 2006, **84**, 403-407.
- ⁶² E. Ferain and R. Legras, *Nuclear Instruments & Methods in Physics Research Section B-Beam Interactions with Materials and Atoms*, 2001, **174**, 116-122.
- ⁶³ P. Y. Apel, I. V. Blonskaya, O. L. Orelovich, S. N. Akimenko, B. Sartowska and S. N. Dmitriev, *Colloid Journal*, 2004, **66**, 649-656.

- ⁶⁴ M. E. Toimil-Molares, V. Buschmann, D. Dobrev, R. Neumann, R. Scholz, I. U. Schuchert and J. Vetter, *Adv Mater*, 2001, **13**, 62-65.
- ⁶⁵ M. I. Irshad, F. Ahmad, N. M. Mohamed and M. Z. Abdullah, *International Journal of Electrochemical Science*, 2014, **9**, 2548-2555.
- ⁶⁶ R. Inguanta, S. Piazza and C. Sunseri, *Appl. Surf. Sci.*, 2009, **255**, 8816-8823.
- ⁶⁷ D. Fang, K. Huang, S. Liu and D. Qin, *Electrochemistry Communications*, 2009, **11**, 901-904.
- ⁶⁸ F. Tao, M. Guan, Y. Jiang, J. Zhu, Z. Xu and Z. Xue, *Adv Mater*, 2006, **18**, 2161-2164.
- ⁶⁹ W. Yoo and J. Lee, *Adv Mater*, 2004, **16**, 1097-1101.
- ⁷⁰ Patrick David McGary, PhD Thesis, University of Minnesota, 2008.
- ⁷¹ Y. Fukunaka, M. Motoyama, Y. Konishi and R. Ishii, *Electrochemical and Solid State Letters*, 2006, **9**, C62-C64.
- ⁷² D. M. Davis and E. J. Podlaha, *Electrochemical and Solid State Letters*, 2005, **8**, D1-D4.
- ⁷³ H. Cai, C. Xu, P. He and Y. Fang, *J Electroanal Chem*, 2001, **510**, 78-85.
- ⁷⁴ M. Wang, C. Sun, L. Wang, X. Ji, Y. Bai, T. Li and J. Li, *J. Pharm. Biomed. Anal.*, 2003, **33**, 1117-1125.
- ⁷⁵ H. Cai, Y. Wang, P. He and Y. Fang, *Anal. Chim. Acta*, 2002, **469**, 165-172.
- ⁷⁶ A. Merkoci, *Febs Journal*, 2007, **274**, 310-316.
- ⁷⁷ J. Wang, *Analyst*, 2005, **130**, 421-426.
- ⁷⁸ J. Wang, *Small*, 2005, **1**, 1036-1043.
- ⁷⁹ A. Merkoçi, M. Aldavert, S. Marín and S. Alegret, *TrAC Trends in Analytical Chemistry*, 2005, **24**, 341-349.
- ⁸⁰ E. Bakker and Y. Qin, *Anal. Chem.*, 2006, **78**, 3965-3983.

- ⁸¹ T. S. Ramulu, R. Venu, B. Sinha, B. Lim, S. J. Jeon, S. S. Yoon and C. G. Kim, *Biosens. Bioelectron.*, 2013, **40**, 258-264.
- ⁸² Y. I. Elshimali, H. Khaddour, M. Sarkissyan, Y. Wu and J. V. Vadgama, *International Journal of Molecular Sciences*, 2013, **14**, 18925-18958.
- ⁸³ A. V. Cherepanova, S. N. Tamkovich, O. E. Bryzgunova, V. V. Vlassov and P. P. Laktionov, *Ann. N. Y. Acad. Sci.*, 2008, **1137**, 218-221.
- ⁸⁴ Gasparac, R.; Taft, B. J.; Lapierre-Devlin, M. A.; Lazareck, A. D.; Xu, J. M.; Kelley, S. O. *J. Am. Chem. Soc.* **2004**, *126*, 12270-12271.
- ⁸⁵ M. J. Blaser, *Journal of Infectious Diseases*, 1990, **161**, 626-633.
- ⁸⁶ M. A. Lapierre-Devlin, C. L. Asher, B. J. Taft, R. Gasparac, M. A. Roberts and S. O. Kelley, *Nano Letters*, 2005, **5**, 1051-1055.
- ⁸⁷ J. S. Easow and T. Selvaraju, *Electrochim. Acta*, 2013, **112**, 648-654.



2. EXPERIMENTAL PROCEDURES

2.1 Materials

Hydrogen tetrachloroaurate (III) (HAuCl_4 , $\geq 99.99\%$), sulphuric acid (H_2SO_4 , 99.99%), dichloromethane ($\text{CH}_2\text{Cl}_2 \geq 99.9\%$), copper sulphate ($\text{CuSO}_4 \geq 99.9\%$), Phosphate Buffered Saline (PBS), Fluorine Doped Tin Oxide (FDTO) glass slides were obtained from Sigma-Aldrich, and all the solutions were prepared with Milli-Q 18-m Ω water (Millipore purification system). FDTO glass slides were also obtained from Solaronix, Aubonne VD, Switzerland. Isopore™ Polycarbonate (PC) Membrane Filters were obtained from Millipore (25 μm thick with pore diameters of approximately 70 ± 20 nm). The oligonucleotides were purchased from Eurogentec©™ and their purity was $>98\%$. The base sequences are as follows:

Capture: 5`- CGG-CAG-TGT-TTA-TCA -3` – SH

Target: 5`-TGA-TAA-ACA-CTG-CCG-TTT-GAA-GTC-TGT-TTA-GAA-GAA-ACT-TA-3`

Probe: SH-5`- TA-AGT-TTC-TTC-TAA-ACA-GAC- -3`

1 Base-Mismatch: 5`-TGC-TAA-ACA-CTG-CCG-TTT-GAA-GTC-TGT-TTA-AAA-GAA-ACT-TA-3`

3 Base-Mismatch: 5`-TGC-TAA-ACA-CTG-CCG-CTT-GAA-GTC-TGT-TTA-GAT-GAA- ATA-TA-3`

A 30mM gold deposition solution was prepared using tetrachloroaurate in 0.1 M KCl. These solutions were then stored in the dark and wrapped in tin foil when not in use. The gold solutions were deoxygenated using nitrogen gas prior to electrochemical deposition. A 0.2 M copper deposition solution was made up using copper sulphate and 0.1 M aqueous H_2SO_4 (adjusted to pH 3 by HCl) in deionised water. The copper solutions were deoxygenated using nitrogen gas prior to use for electrochemical deposition.

FDTO glass slides were used as working electrodes for nanotube and nanowire deposition. Before use the slides were washed in acetone and deionised water, before drying with a heat gun until completely dry.

The membranes used had a pore diameter of ~100 nm and a pore thickness of ~25 μm . A ~300 nm thick gold layer serving as a back electrode was sputter coated onto one side of the membranes. After sputtering, the membranes are fixed with the gold layer facing down on to the conducting side of the FDTO glass slide using an adhesive sticker. The sticker leaves the central part of the membrane open over a diameter of ~6 mm, which is the part that was exposed to the electrolyte solution. In the case of nanotube deposition, the sputtered layer was removed from the membrane surface, leaving small annular deposits of Au inside the pore walls only. The membrane is placed with the stripped side facing the FDTO surface for electrodeposition. The diameter of the stripped membrane exposed to the electrolyte solution is the same as for the non-stripped membranes.

Following electrodeposition of the metal, the membrane is physically removed from the surface of the FDTO electrode, and dissolved in dichloromethane, centrifuged and rinsed several times in dichloromethane before a final suspension in water. In the case of the non-stripped membranes, the membrane is sonicated for ~30 seconds following initial dissolution step in order to break up the pieces of sputtered gold and free nanowires into solution.

2.2 Electrochemistry

For voltammetric characterisation of the nanostructures, a three-electrode electrochemical cell was used at a temperature of $22\pm 2^{\circ}\text{C}$. The working electrode was a 2 mm diameter planar gold disc. It was polished with a nylon cloth with 1 μm diamond polish, and 0.3 μm and 0.05 μm alumina polish, and thoroughly rinsed with Milli-Q water and ethanol before sonication in Milli-Q water for 5 minutes. Voltammetry in aqueous 0.1 M H_2SO_4 was used to determine the surface roughness factor by scanning the electrode between 0.000 and +1.500 V at a scan rate of 100 mV s^{-1} . The counter electrode was a large area coiled platinum wire and a silver/silver chloride (Ag/AgCl in 3 M KCl) acted as reference.

Cyclic voltammetric and amperometric measurements were carried out using a CHI 760d and CHI 760b electrochemical workstation.

2.3 Sample preparation

Isopore membranes were sputter coated using a Polaron SC7640 'Cool' Sputter Coater at a voltage of 2 kV and current of 20 mA for ~20 minutes. The sputtered layer was ~300 nm thick.

2.4 Spectroscopic Techniques

2.4.1 Raman Spectroscopy

Raman spectroscopy was carried out on a Horiba Jobin Yvon HR800UV microscope connected to a CCD detector. The laser beam (He-Ne laser) utilising a 488 nm excitation line was focused through a 100x objective lens. The acquisition time was 10 seconds. Baseline correction and smoothing was incorporated using Lab Spec software.

2.4.2 EDX Spectroscopy

EDX was used in this work to determine the presence of copper and gold in the core:shell nanotubes. The measurements were performed using an Oxford INCA microanalysis system using an X-Max detection system. The accelerating voltage was 10 – 20kV and the probe current was 35mA.

2.5 Microscopic Techniques

2.5.1 Scanning Electron Microscopy

Scanning electron microscopy (SEM) analysis was performed using a Hitachi S3400N microscope with an accelerating voltage of 5 - 20kV and a probe current of 25 - 35mA.

2.5.2 Field-Emission Scanning Electron Microscopy (FE-SEM)

FE-SEM was performed using a Carl Zeiss Supra Ultra plus microscope. The accelerating voltage was 5 – 20kV and the probe current was 35mA.

2.6 Inductively Coupled Plasma - Mass Spectrometry (ICP-MS)

The nanowires/nanotubes were analysed for gold content (Au197) using an Agilent 7700e ICP-MS equipped with a 3rd generation Octopole Reaction System (ORS) using Mass Hunter software, in no gas mode using external calibration.

2.7 Calculation of Electrochemical Area and Surface Roughness of a bare gold electrode

Voltammetry in acidic electrolyte (0.1 M H₂SO₄) was used to determine the microscopic area by cycling the electrode between 0 and 1.5 V, as shown in Figure 2.1. The gold oxide reduction peak (typically found at 0.8 V) was used to calculate the surface roughness factor (ratio of the microscopic to geometric areas) from the geometric area, 0.0314 cm².¹ The calculation of electrochemical area and surface roughness factor is given below in Equation 2.1 - 2.3, where A_G is the geometric area, EA is the electrochemical area, A_p (in Coulombs) is the area under the peak of interest, and R.F. is the roughness factor.

The determination was done by integration of the gold oxide reduction peak from the voltammetric curves obtained at 25°C between 0 V and 1.5 V (vs. Ag/AgCl/3 M KCl reference electrode), at a scan rate of 0.1 V s⁻¹ in 0.1 M sulphuric acid. Then, electrochemical area (EA) is the ratio between the charge of the gold oxide reduction presented on the studied electrode surface ($Q_{\text{Au}/\alpha \text{ oxide}}$) and Q_{Std} .

$$A_G = \pi r^2$$

Equation 2.1

$$EA = \frac{A_p}{390 \mu\text{C cm}^{-2}}$$

Equation 2.2

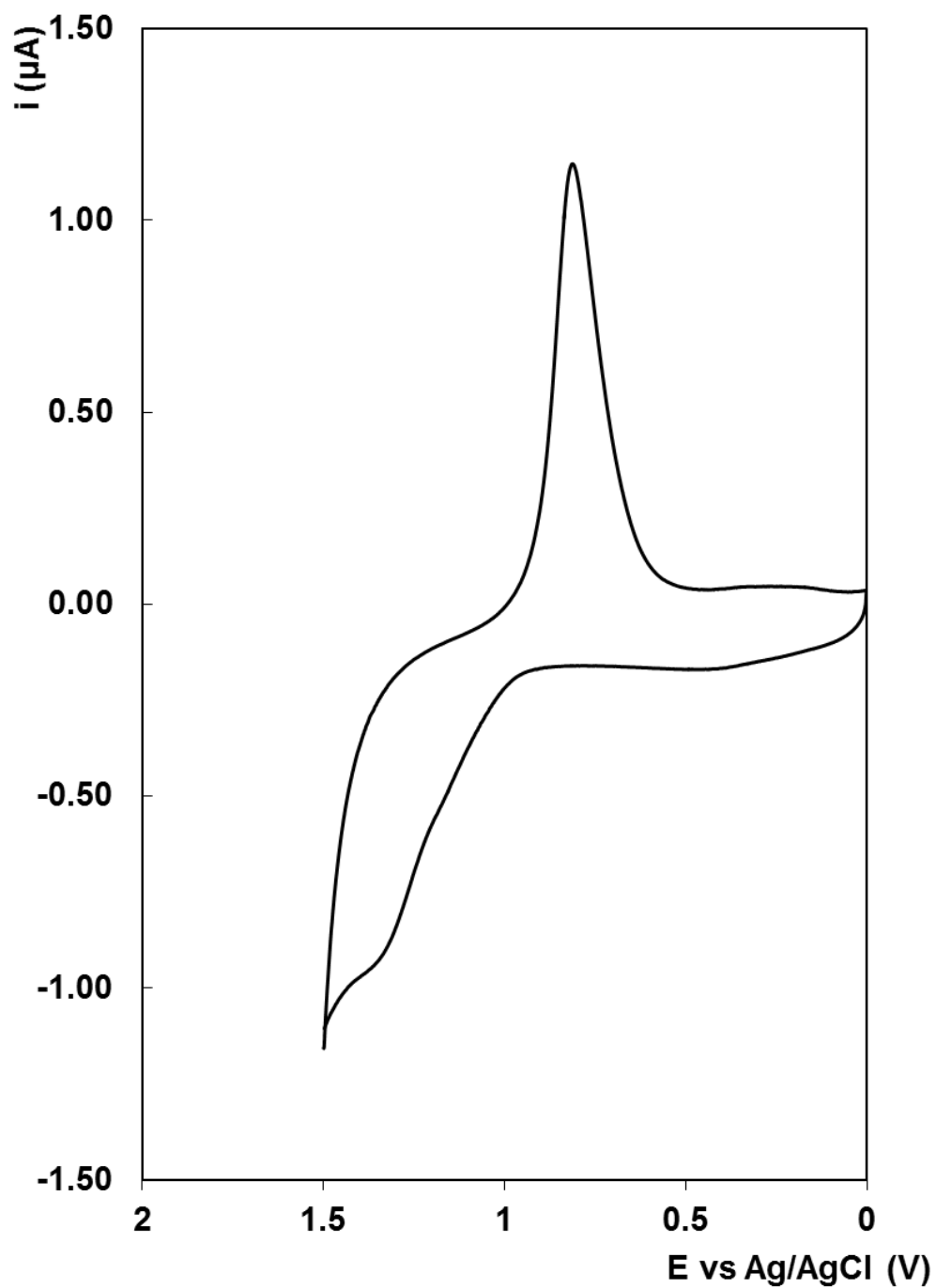


Figure 2.1: Cyclic voltammogram of a 2 mm diameter gold electrode in 0.1 M H_2SO_4 with a surface roughness factor of 1.5. The counter electrode was a platinum wire and the reference electrode was Ag/AgCl in 3M KCl. The scan rate is 100 mVs^{-1} . The sixth scan is presented.

Usually, calculations of EA are expressed as a roughness factor, which EA is expressed per unit of geometric surface area.²

$$R.F. = \frac{EA}{A_G} \quad \text{Equation 2.3}$$

Where A_G is the geometric area of the working electrode.

2.8 Capacitance of gold electrodes

The double layer capacitance of bare gold electrodes and AuNW-modified electrodes was determined using cyclic voltammetry as illustrated in Figure 2.2.

The current associated with the double layer charging is given by:

$$\Delta i = 2C_{dl}AV \quad \text{Equation 2.4}$$

Where Δi is the change in current, A is the microscopic area, and v is the scan rate in Vs^{-1}

A satisfactory value for capacitance for a clean gold electrode in 0.1 M aqueous electrolyte is between 10 and 40 μFcm^{-2} .³

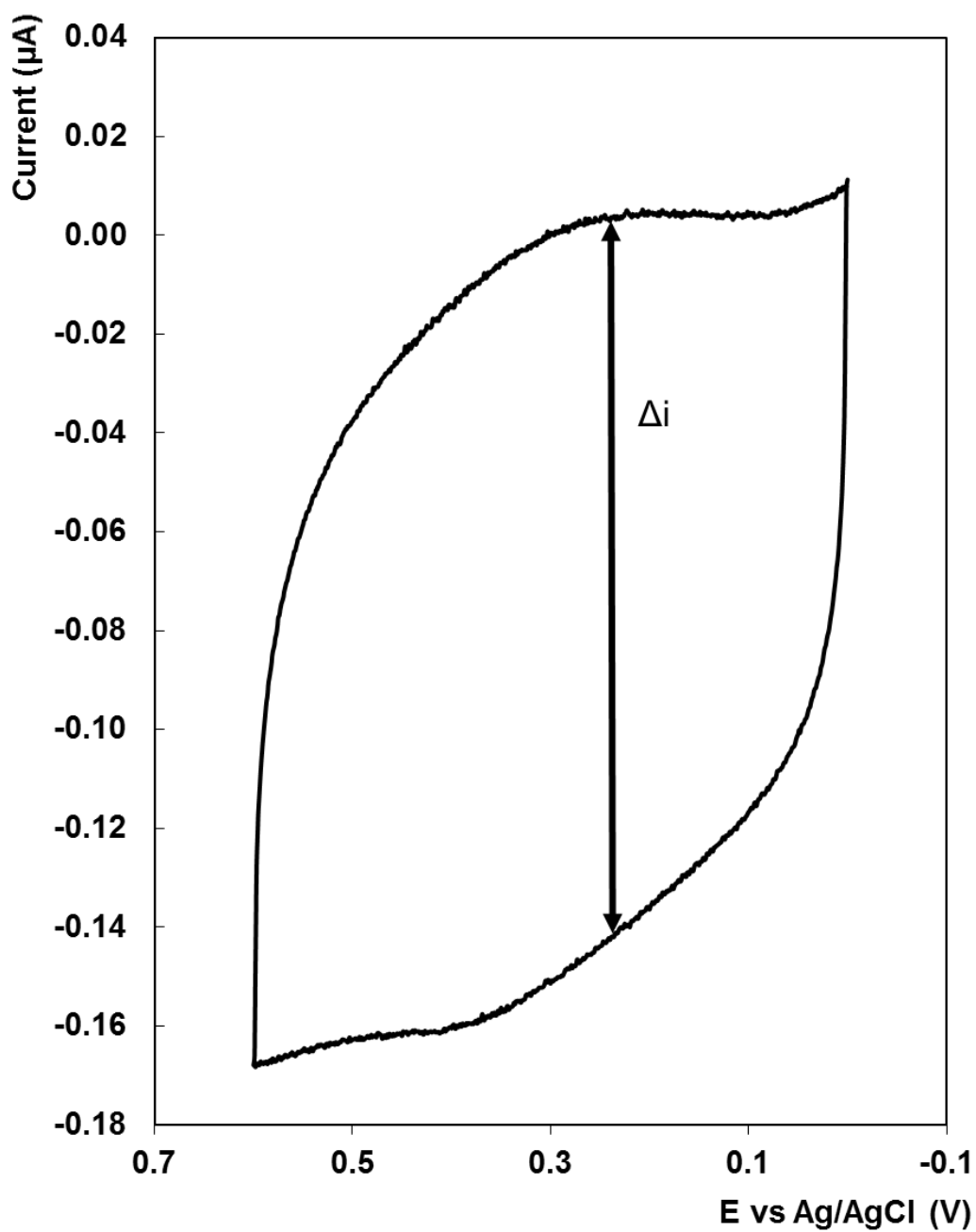


Figure 2.2: Cyclic voltammogram demonstrating capacitance of a bare gold electrode in 0.1M LiClO_4 in ACN. The potential was swept from 0 to 0.6V with a scan rate of 100mVs^{-1} . The reference electrode was Ag/AgCl in 3 M KCl. The sixth scan is presented.

2.9 Experimental Procedures

2.9.1 Synthesis of gold nanowires and nanotubes

Electrochemical deposition through this template was achieved using a commercially available HAuCl_4 gold salt solution at an applied potential of -0.273 V vs. Ag/AgCl in 3 M KCl to fabricate gold nanowires and nanotubes within the nanopores.

2.9.2 DNA modification of the gold nanowires/nanotubes

The exposed top surface of the AuNWs/AuNTs were functionalised with probe oligo (5' thiolate) by immersing the AuNW/NT functionalised PC membrane in a $1\ \mu\text{M}$ solution of the thiolated probe DNA strand dissolved in 1 M Denhardt's buffer for 3 hours. Denhardt's buffer consists of 1% Bovine Serum Albumin (BSA), 1 % Ficoll, and 1 % Polyvinylpyrrolidone (PVP) in water. The buffer has a pH of 7. The template containing the nanowires was then washed with deionised water for 15 s to remove loosely bound oligo. Subsequently, the membranes were then placed in dichloromethane (DCM) for 1 hour to dissolve the PC template. The membranes were then sonicated for 45 min to break the separate the nanowires from the underlying gold layer. This was followed by several washings of DCM and DI water to remove any residual polycarbonate membrane. The suspension of the released DNA modified AuNWs was stored in DI water until further use. The nanowires were decorated with probe strand DNA at their top ends only.

The gold nanotubes were functionalised in the same way as the nanowires. Due to the fact that the nanotubes have a hollow centre, some of the probe strand of DNA may diffuse into this centre and bind to the inner walls of the nanotubes.

2.9.3 DNA Hybridisation

Step 1: Monolayer of Capture Strand DNA. Capture strand DNA was immobilised on a freshly polished and electrochemically cleaned gold disk electrode by immersing it in a 10 μM solution of the capture strand DNA dissolved in 1 M Denhardt's Buffer. After 5 hours, the electrode was rinsed with deionised water for 15 s to remove loosely bound oligo.

Step 2: Hybridisation of target oligo to the capture surface. Hybridisation of the target at concentrations between 1 μM and 1 aM to the immobilised capture strand was performed at 37°C in 1 M Denhardt's Buffer for 90 min. Following hybridisation, the modified electrode was rinsed thoroughly with buffer.

Step 3: Probe Hybridisation. The AuNW labelled probe DNA was then hybridised to the complementary section of the target not used for binding to the capture strand for 3 hours at 37 °C in 1 M Denhardt's Buffer. Finally, before quantitation, it was thoroughly washed with deionised water.

2.9.4 Electrochemical detection of ss-DNA coding for *S. aureus* target by solid gold nanowires and hollow gold nanotubes

Following assembly of the capture-target-nanowire labelled probe DNA sequence, the modified electrode was placed in an aqueous solution of 0.01 M H_2SO_4 and the current measured at -0.1 V vs. Ag/AgCl in 3 M KCl after equilibration for 10 minutes (background current). Then, sufficient hydrogen peroxide was added to give a final concentration of 200 μM and the reduction current associated with peroxide reduction at the bound AuNWs measured at -0.1 V vs. Ag/AgCl in 3 M KCl after 10 minutes. The analytical response is taken as the difference in current, Δi , measured before and after peroxide addition.

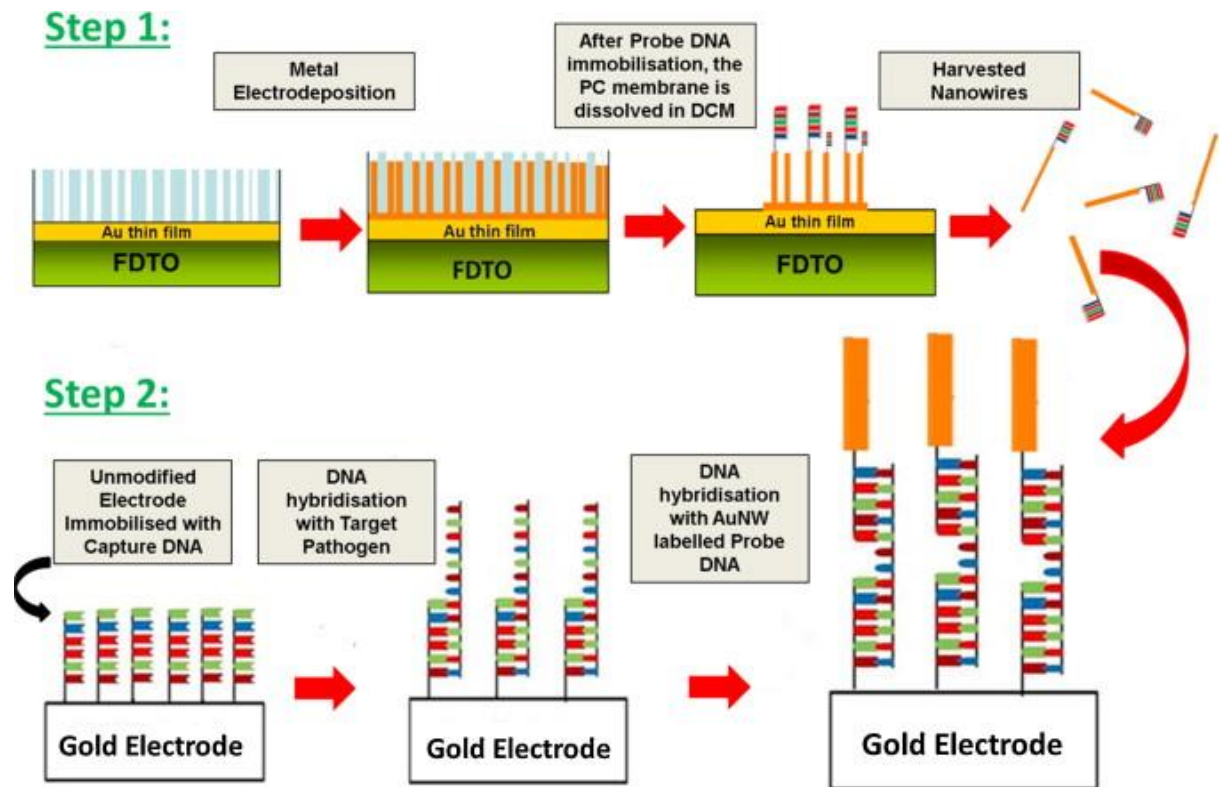


Figure 2.3: Schematic representation of the synthesis of gold nanowires/nanotubes within the pores of a polycarbonate membrane, and their subsequent incorporation into a DNA biosensor. **Step 1:** Metal deposition through the pores of a metal sputtered polycarbonate membrane results in nanowires or nanotubes of gold. These nanostructures are then functionalised with probe strand DNA that is complementary to a section of the target of interest, *S. aureus mastitis*. Following functionalisation, the membrane is removed and the wires are suspended in solution, creating a solution of free wires that are functionalised on one end with probe DNA. **Step 2:** Separately, on a gold disk electrode, thiol modified capture DNA is functionalised to the electrode surface. This capture DNA strand is complementary to a section of the target of interest. Following complete coverage of the electrode with a monolayer of capture DNA, the electrode is immersed in a solution of the target DNA, where it hybridises with the capture strand. The electrode is then immersed in the previously labelled gold nanowire solution, and the section of the target that is not already bound to capture DNA will bind to the probe DNA present on the nanowire surface. This electrode is now fully hybridised, and the target DNA can be detected due to the presence of the gold nanowires.

2.9.5 Regeneration of gold electrodes following modification with DNA monolayer and nanowire-labelled probe DNA

Initially, the surface of the gold disk electrode was cycled in an electrolyte of 0.1 M KOH solution which had been deoxygenated by purging with nitrogen for 15 minutes. A potential range of -400 mV to -1200 mV vs. Ag/AgCl was applied at a scan rate of 100mV/s to electrochemically clean the surface of the electrode. This was done in order to remove the thiolated DNA monolayer present on the Au electrode surface.⁴ The electrode was then polished as described in Section 2.2 previously, and the electrochemical area determined in acidic solution prior to reuse.

2.9.6 Optimal conditions used to synthesise core:shell nanowires

Hollow Cu nanotubes were fabricated in a method similar to that described by Kumar and co-workers.⁵ Gold (300 nm) coated polycarbonate templates were fixed with the gold side facing down onto a conducting substrate (FDTO glass) using a double-sided adhesive carbon sticker. Electrochemical deposition of copper through this template was achieved using a commercially available (obtained from Sigma Aldrich) copper sulphate salt solution (0.2 M in 0.1 M aqueous H₂SO₄ (adjusted to pH 3 by HCl)) at an applied current of 0.02 A for 3 min. Electrochemical deposition of gold was achieved using 30 mM HAuCl₄ gold salt solution at a potential of -0.273 V vs Ag/AgCl in 3 M KCl for 3 min. The membranes were then placed in an aqueous solution of DCM for 1 hour to dissolve the polycarbonate membrane and free the nanowires into solution. The membranes were then sonicated for 45 min to separate the adhesion between the electrode and metallic layer of gold. This was followed by several washings of DCM and DI water to remove and residual polycarbonate membrane.

2.9.7 Functionalisation of hollow nanotubes and core:shell nanowires with $[(Ru(bpy)_2(Qbpy))]^{2+} (ClO_4)_2$

$[Ru(bpy)_2(Qbpy)]^{2+}$ (where bpy is 2,2'-bipyridyl, and Qbpy is 2,2':4,4'':4''':4''''-quaterpyridyl), dye was obtained from Dr Ciarán Dolan, School of Chemical Sciences, Dublin City University.

114 mg (0.12 mM) of dye was obtained and dissolved in 10 cm³ of ethanol and deionised water. This gives a 1.2 mM solution of dye. 20 μL of this solution was then removed and diluted in 25 cm³ of ethanol and DI water to give a 1 μM solution of dye. The wires were suspended in 200 μL of the 1 μM solution of dye for 24 hours in order to functionalise their surface with the dye.

The purpose of this experiment was to determine whether the gold cores of the core:shell nanowires would provide a significant Raman enhancement of the dye modes compared to the hollow copper nanotubes.

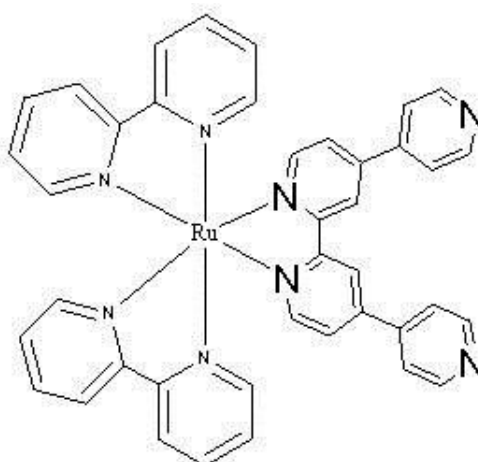


Figure 2.4: Structure of $[(Ru(bpy)_2(Qbpy))]^{2+}$ dye.

Pyridine molecules contain a delocalised π -electron system and a lone pair located on the nitrogen atom, both of which participate in bonding.⁶ There is also a possible overlap of π -orbitals and non-bonding orbitals of a nitrogen atom of the pyridine molecule and the d-band of the metal.⁷ Because of this, the dye will bind more strongly to the gold in the core:shell nanowires than the copper in the hollow nanotubes. The presence of the gold may also provide a surface enhancement effect.

2.9.8 Electrochemical detection of ss-DNA coding for *S. aureus* target by gold:copper core:shell nanowires

Detection of the DNA hybridisation event was carried out using cyclic voltammetry. The nanotube/probe-functionalised electrodes were cycled in 0.01 M H₂SO₄ at potentials between -0.1 V and 0.6 V vs. Ag/AgCl in 3 M KCl. A copper oxidation peak was observed at +0.235 V and the area of this peak was calculated. The presence of copper is due to the presence of target DNA, and the magnitude of the area of the peak (charge passed, in Coulombs) ought to be proportional to the concentration of target DNA present on the electrode. The thiol bonds were reduced by application of a fixed potential for approximately ten minutes. The difference in the magnitude of the charge passed under the copper oxidation peak before and after thiol reduction was plotted.


2.10 Conclusion

In this chapter, the parameters for synthesis of the nanomaterials studied in this thesis are described. The conditions used for characterisation of these nanomaterials by various techniques are also outlined. Also described here are the preparation and cleaning processes for several substrates used in this thesis, including gold disc electrodes, polycarbonate membranes, and FDTD glass slides.

The specific details for the preparation of a mastitis DNA biosensor utilising these synthesised nanomaterials are also included.

2.11 References

- ¹ S. Trasatti and O. A. Petrii, *Pure Appl. Chem.*, 1991; 1991, **63**, 711-734.
- ² M. Dijkma, B. Kamp, J. C. Hoogvliet and W. P. van Bennekom, *Langmuir*, 2000, **16**, 3852-3857.
- ³ A. J. Bard and L. R. Faulkner, *Electrochemical methods: fundamentals and applications*, Wiley, New York, 1980.
- ⁴ R. T. Carvalhal, R. S. Freire and L. T. Kubota, *Electroanalysis*, 2005, **17**, 1251-1259.
- ⁵ S. Kumar, D. Zagorski, S. Kumar and S. Chakarvarti, *J. Mater. Sci.*, 2004, **39**, 6137-6139.
- ⁶ A. Wieckowski, *Interfacial Electrochemistry: Theory: Experiment, and Applications*, CRC Press, Florida, 1999, pp.339.
- ⁷ A. Wieckowski, *Interfacial Electrochemistry: Theory: Experiment, and Applications*, CRC Press, Florida, 1999, pp.432.



3. SYNTHESIS AND CHARACTERISATION OF GOLD NANOWIRES AND NANOTUBES

3.1 Introduction

The fabrication of one-dimensional materials¹ such as nanowires, nanorods and nanotubes have attracted much interest due to their potential applications in biosensors,^{2,3,4,5} catalysis,⁶ batteries^{7,8,9} and electronic nanodevices.^{10,11,12,13} Many methods for preparing nanomaterials have been developed, ranging from milling techniques to chemical and lithographic methods.¹⁴ However, there is a weakness associated with these structures; i.e., it is quite difficult to control the final morphologies, lengths, diameters etc., of these nanostructures.^{15,16} A method termed “template-synthesis,” pioneered by Martin and co-workers^{17,18} entails the preparation of a variety of micro and nanomaterials of a desired morphology and, therefore, provides a route for enhancing nanostructure control. The diameter of a nanowire is typically less than 200 nm and the ratio of the length to the diameter is greater than five.

Bean¹⁹ first demonstrated the art of filling the pores of a membrane with silver followed by Possin²⁰ who utilised electrodeposition technique in the fabrication of thin wires as small as 400 Å using mica with etched pores as templates for synthesis of such elements of the nanostructures. Williams and Giordano²¹ claimed to have reduced the size down to 80 Å after effecting some refinements to the technique. Penner and Martin²² reported on the generation and characterisation of ultra-microelectrodes with radii as small as 1000 Å.

Nanomaterials have unique electrochemical, optical, and mechanical properties, which gives rise to a diverse range of application domains.^{23,24} In particular, noble metal nanostructures such as gold have gained special interest because of its electrocatalytic conductivity, optical, and biocompatibility properties.^{25,26} In particular, when seeking to develop high sensitivity sensors, gold nanostructures can simultaneously increase the surface area for detection while acting as an efficient electrocatalyst, e.g. for hydrogen peroxide. Both of these features can dramatically increase the sensitivity compared to a planar gold electrode. In addition, bioreceptors, such as enzymes, antibodies, or nucleic acids can be adsorbed while retaining their biological functionality, and their electrochemical activity.²⁷ Moreover, nanostructures increase the rates of mass transport, giving a

higher current density, higher signal to noise ratios and steady-state voltammograms, even at relatively high measurement rates.²⁸ However, despite the attractive features, the production of well-defined, discrete nanowire structures with reproducible dimensions, and their subsequent facile integration into device platforms, remains challenging.

Metal electrodeposition within the pores of a template, such as porous silica, anodic alumina oxide or ion track-etched polymer membranes, represents a useful approach to producing wires with tightly defined outer diameters. Track-etched polycarbonate membranes are especially attractive since they are stable in numerous electrolytes including strong acidic and alkaline solutions, but can be easily dissolved in dichloromethane, which does not degrade many biomolecules.²⁹

The morphology of nanowires, including their geometry, size, and surface contour, is primarily determined by the shape of the template channels. The production of templates using heavy ion beams in combination with track etching enables several template parameters to be controlled, such as well-defined pore shape and geometry. The diameter is adjustable between a few nanometres up to micrometres, membrane thickness up to 100 μm , and aspect ratios up to 1000 can be achieved.³⁰

This chapter describes the fabrication of gold nanowires and nanotubes through the pores of a track-etched polycarbonate membrane via electrodeposition, and their characterisation by SEM, voltammetry, and ICP-MS.

Gold nanowires with a diameter of 118 ± 20 nm, and gold nanotubes of the same diameter with a wall thicknesses of 20 ± 10 nm, have been electrodeposited within the pores of a track etched polycarbonate membrane filter.

3.2 Results and Discussion

3.2.1 Substrate used for electrochemical deposition of nanowires and nanotubes

A commercially available polycarbonate membrane (shown in Figure 3.1) was used as a template for the deposition of the nanowires. Polycarbonate membranes were used as they are easily available, have high pore density, and are easy to remove after deposition of the nanostructure by dissolution in organic solvent such as dichloromethane, which causes minimal damage to the deposited nanowires.

The pore size is specified as 100 nm³¹, and SEM analysis showed the size of the pores to be 100 ± 20 nm. The pore-density according to manufacturer³¹ is 6×10^8 pores/cm². The surface of the membrane was sputtered with a layer of gold ~ 300 nm thick to create electrical contact with the working electrode during the electrodeposition process.

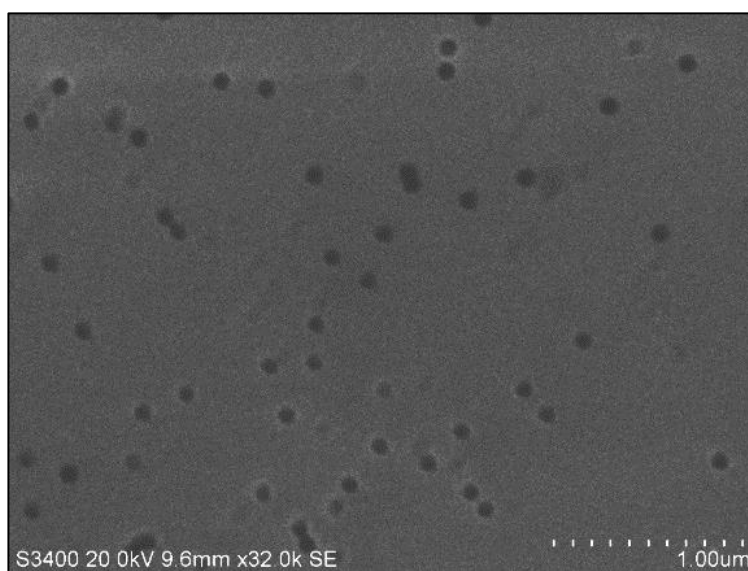


Figure 3.1: SEM image of a commercial PC membrane. A 20 nm thick gold layer has been sputtered on the membrane surface and the membrane has been mounted on a carbon tab for SEM analysis. Accelerating voltage was 20 kV.

3.2.2 Potentiostatic deposition of gold nanowires

Gold nanowires were deposited for: 10 - 50 minutes, and from 1 – 12 hours from a 30mM HAuCl_4 solution in 0.1 M KCl. The potential used was -0.273 V vs. Ag/AgCl in 3 M KCl.

The deposition times were varied in order to create nanowires with varying lengths, as the length of the nanowire is controlled by the deposition time in electrochemical deposition experiments.

Figure 3.2 shows the current-time transient for a 30 minute deposition of gold through the membrane template.

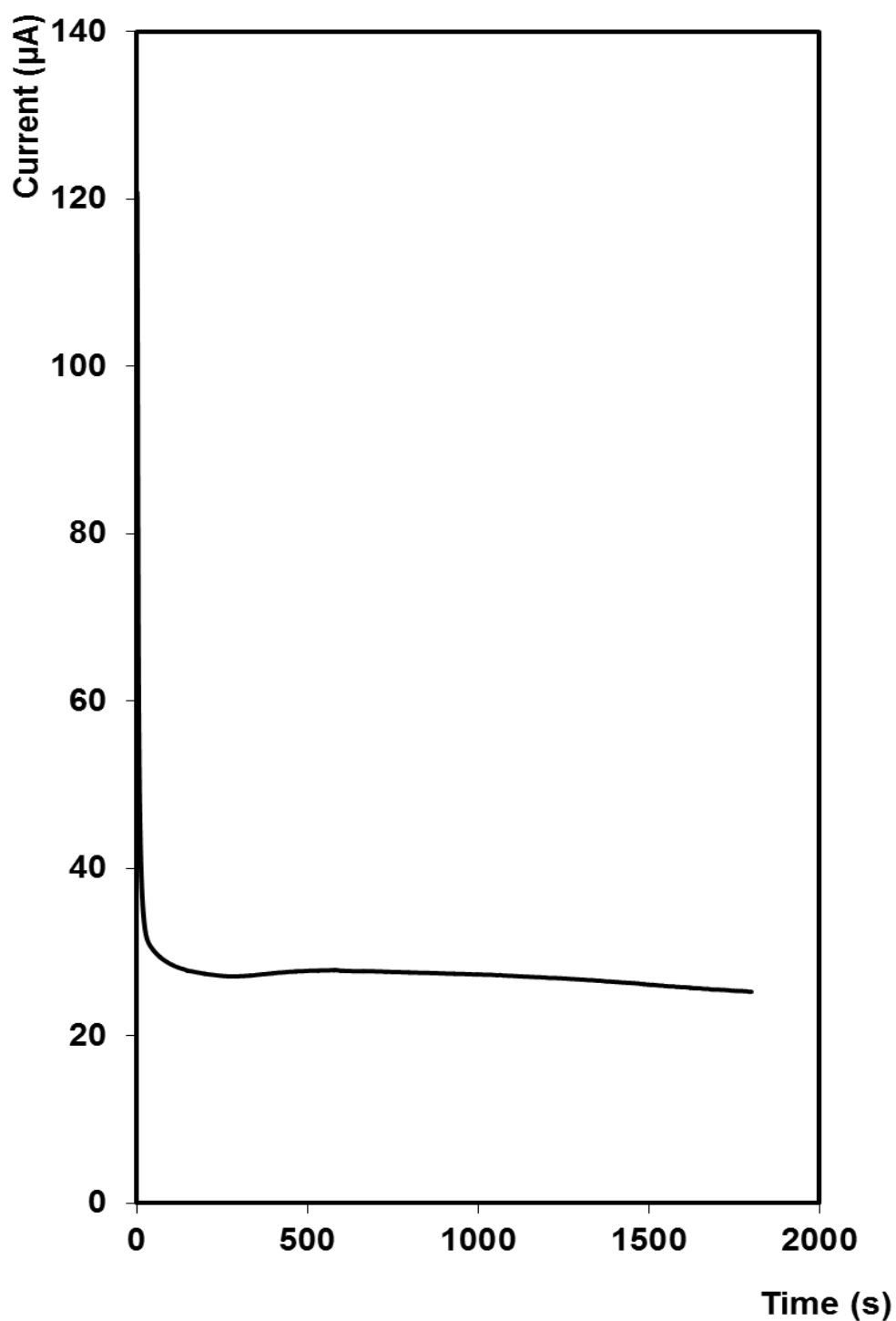


Figure 3.2: *Current-time transient for growth of gold nanowires through a porous polycarbonate membrane mounted on FDTO. The potential applied was -0.273 V vs. Ag/AgCl in 3 M KCl for 1800 seconds. The membrane had been sputter coated with a ~300 nm thick layer prior to electrodeposition.*

There are two regions observed in the transient shown in Figure 3.2. The first region is a current spike immediately at the beginning of the transient which quickly depletes once nucleation of the metal ions immediately at the electrode surface occurs. The second region is the decay of the current to slightly decreasing, which corresponds to the gold depositing into the pores.

The current response during pore filling is usually divided into four main regions. The first region involves the immediate nucleation of the material at the surface of the electrode, which results in a current spike in the current-time transient that quickly depletes once the diffusion layer is formed. The second region is noted as the growth of the material in the pores, and the current is close to stagnant or slightly decreasing due to the interplay between the imperfect conductivity of the membrane, and the diminishing diffusion length of the ions in the filling pores.³² The third region involves an increase in the current, which corresponds to the material growing out of the pores as hemispherical caps, resulting in a larger surface area for deposition. A fourth region consists of the overfilling of pores, and eventually results in a linear film growth with a steady-state current.³⁸

During pore filling, the current is described by two main types of diffusion, namely a time-dependent linear diffusion at short times and spherical nature of diffusion at longer times which gives rise to a steady-state limiting current.^{33,34}

As the potential is first applied current begins to flow as nucleation occurs. The current rapidly decreases due to depletion of Au^{3+} ions at the electrode surface within the pores of the membrane. This corresponds to the linear diffusion inside the pores indicating occurrence of the charge transfer reaction.³⁵ This will only occur at very short times (in the order of seconds) when the depletion layer is shorter than the pore diameter.

The metal deposits in the pores of the template, and the current remains steady as growth progresses through the pores. This represents the spherical diffusion, whereby the limiting current plateau is obtained.³⁵ Martin et al.³⁶ were able to divide the second region where the material is growing in the pores into three subdivisions, by plotting the current vs. $t^{-0.5}$, as shown in Figure 3.3 and represented by sections 3-5.

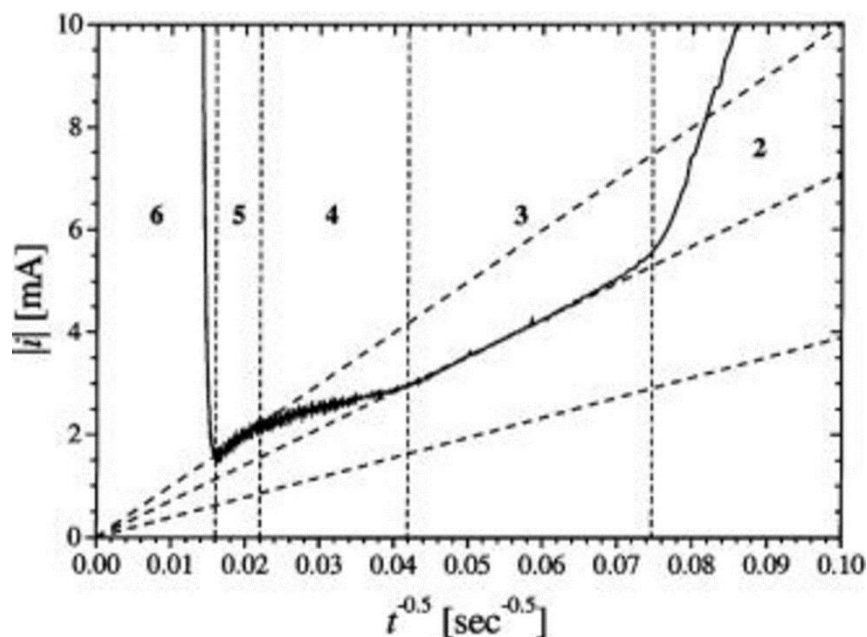


Figure 3.3: Current density vs. $t^{-0.5}$ for copper electrodeposition within the pores of a polycarbonate membrane. [Reproduced from I. U. Schuchert, M. E. Toimil-Molares, D. Dobrev, J. Vetter, R. Neumann and M. Martin, J. Electrochem. Soc., 2003, 150, C189-C194]

For relatively short times, (Figure 3.3, region 3), the thickness of the Nernst layer is small compared to the remaining empty pore length, and linear diffusion inside the pores is rate determining (Figure 3.4a). On a longer time scale, the depletion layer exceeds the pore length and a radial diffusion layer is established around each pore (Figure 3.4b). The ions diffuse rapidly toward the pore openings and proceed linearly inside the pores. In this case, the radial diffusion determines the overall process, as shown by the fit of Figure 3.3, region 4, having an intersection with the current axis. For long times, the radial diffusion fields begin to overlap with neighbouring fields, as shown in Figure 3.4c. The diffusion once again occurs linearly, but now towards the entire membrane surface, subsequently radially towards the pore openings, and linearly inside the pores. The overall process is determined by the first step, because the observed straight line (Figure 3.3, region 5) goes through the origin and has a larger slope than that of region 3, which corresponds to a larger surface area. Finally, the increase of current in region 6 indicated that metal caps start to overgrow the membrane surface.³⁶

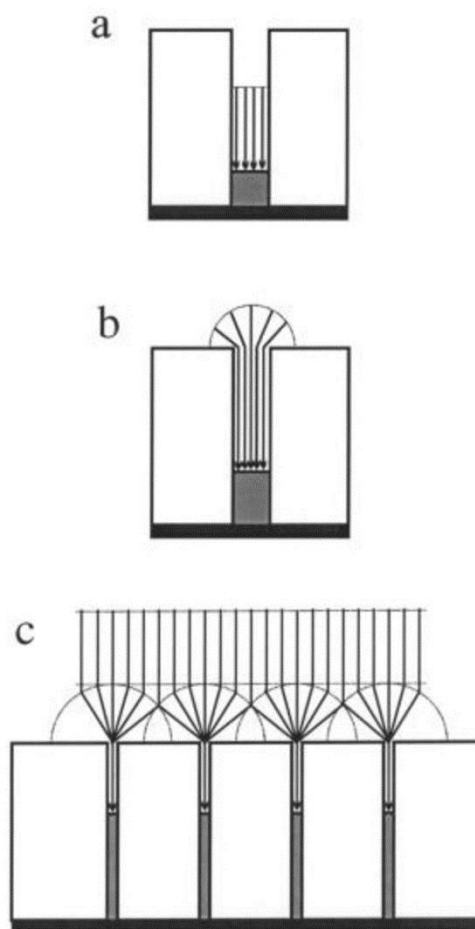


Figure 3.4: Diffusion processes during pore filling: (a) linear diffusion inside the pore, (b) radial diffusion toward the pore opening, and (c) linear diffusion toward the whole membrane surface. [Reproduced from I. U. Schuchert, M. E. Toimil-Molares, D. Dobrev, J. Vetter, R. Neumann and M. Martin, J. Electrochem. Soc., 2003, 150, C189-C194]

They associated these different regions with the differences of the geometries of the Nernst layer. This was explained by noting that there are essentially three different diffusion zones, as illustrated in Figure 3.4. There is the linear diffusion from the bulk of the electrolyte toward the pore, radial diffusion at the pore opening, and linear diffusion again in the pore toward the pore surface. At short times, the linear diffusion in the pore is the rate limiting fragment; however, as the Nernst layer becomes thicker than the pore length, the radial diffusion at the pore openings becomes the rate limiting fragment. At even longer times, the radial

diffusion layers at each pore opening begin to overlap, and the linear diffusion from the bulk of the solution towards the pores becomes the limiting fragment.

If the deposition time were increased, the current would remain constant until the pores are filled to the top, and a surface cap is formed which would increase the electroactive area giving a large current. Eventually, the radial diffusion layers at each of these caps would coalesce, linear diffusion would predominate and the current observed would be equal to that of a uniform accessible electrode.^{37,38}

As no increase in the current is observed in the transient in Figure 3.2, it can be concluded that the deposition of metal did not extend so as to cover the top of the membrane.

This characteristic increase in current did not occur for any of the deposition times investigated, which suggests that the nanowires deposited will be shorter in length than the maximum thickness of the membrane in all cases.

3.2.3 SEM images of nanowires after release from the membrane

The deposited nanowires were freed from the membrane by dissolution in dichloromethane, and after several washings with DCM and sonication to remove sputtered gold layer, were suspended in a solution of DI. The nanowires were dropcast onto carbon tabs for analysis under SEM, and their average lengths and diameters were measured, as shown in Figure 3.5.

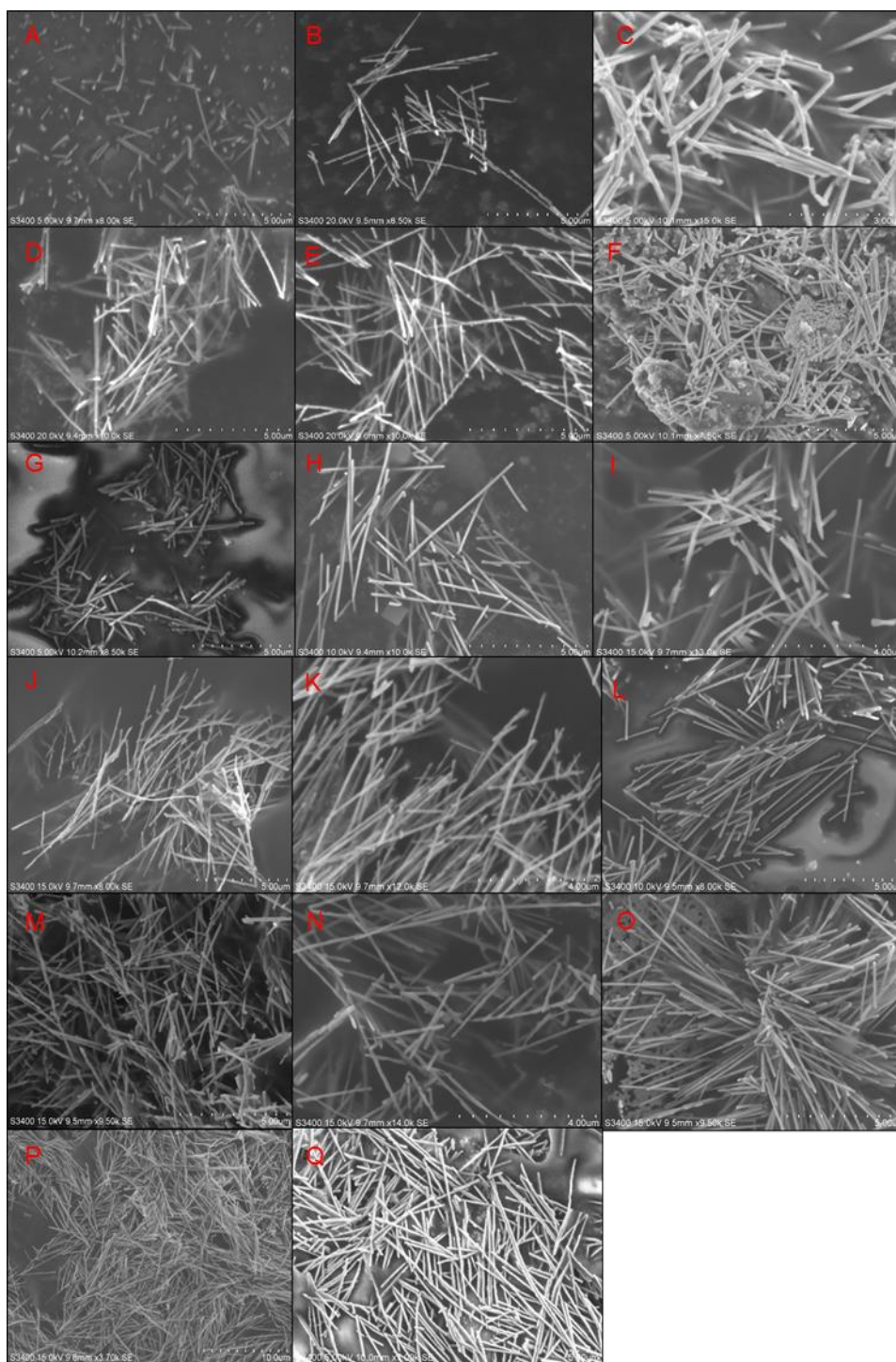


Figure 3.5: SEM images of Au nanowires after dissolution of polycarbonate membrane, sonication to remove sputtered gold layer and suspension dropcast for analysis. Deposition times are: (A) 10 min, (B) 20 min, (C) 30 min, (D) 40 min, (E) 50 min, (F) 60 min, (G) 2 hours, (H) 3 hours, (I) 4 hours, (J) 5 hours, (K) 6 hours, (L) 7 hours, (M) 8 hours, (N) 9 hours, (O) 10 hours, (P) 11 hours, and (Q) 12 hours. Accelerating voltages are 5 – 20 kV.

If the length of the nanowires can be controlled, this could be effectively utilised in a biosensor application; specifically, the relationship between surface area and volume, i.e. that a nanowire of gold would have a significantly larger surface area compared to a gold particle. For example, the surface area of a nanoparticle with a radius equal to that of the nanowires would be $\sim 3 \times 10^{-14} \text{ m}^2$, whereas the surface area of the shortest nanowire is $\sim 3 \times 10^{-13} \text{ m}^2$, and the largest nanowire has a surface area of $\sim 3 \times 10^{-12} \text{ m}^2$.

The use of nanostructures of gold would significantly decrease the cost involved in using bulk gold, with the advantages of sensitivity and rapidity of response. For example, approximately 1.48×10^{12} nanowires would be needed to provide the same area as a conventional gold electrode, (assuming that the wires are oriented standing up and in a closely packed layer). As shown in Section 3.2.6, the concentration of nanowires produced in a single membrane is $\sim 2 \times 10^{10}$. Based on the current cost of 25 g of $\text{HAuCl}_4 \cdot 3\text{H}_2\text{O}$ from Sigma Aldrich, each deposition costs $\sim \text{€}2.00$ per solution used.

Table 3.1: *Length of nanowires for each deposition time*

Deposition time (min)	Length of nanowire (μm)
10	0.95
20	1.83
30	2.49
40	2.78
50	3.63
60	3.82
120	4.11
180	4.24
240	4.31
300	4.42
360	4.56
420	5.08
480	5.63
540	5.83
600	6.95
660	7.01
720	9.61

As seen in Table 3.1, the length of the nanowires increases with increasing deposition time, which indicates that the size of the nanowires can be controlled somewhat by varying the deposition times. This is important since the electrocatalytic current observed depends directly on the area of the nanowire when they are used as a label in a bioassay.

Figure 3.6 shows a plot of average wire length vs. deposition time. The relationship is somewhat linear, with a correlation coefficient of 0.86. The standard deviations of the wire lengths are quite large, due to the nature of how the lengths are calculated, and due to the fact that different numbers of wires were measured for each sample. The %RSD for the nanowires measured is 32%, which is very high. Again, this is most likely because the numbers of wires measured was not the same for each deposition time. Additionally, factors such as wire breakage during centrifugation and sonication steps may be an issue, as well as breakage during pipetting, and inhomogeneous pore filling during growth stages.

A more accurate wire length may be obtained by TEM analysis of a cross section of the membrane after deposition of gold, before dissolution, centrifugation and sonication steps have been completed. This may also be useful in determining whether the growth proceeded in all pores equally, and whether pore widening effects are observed.

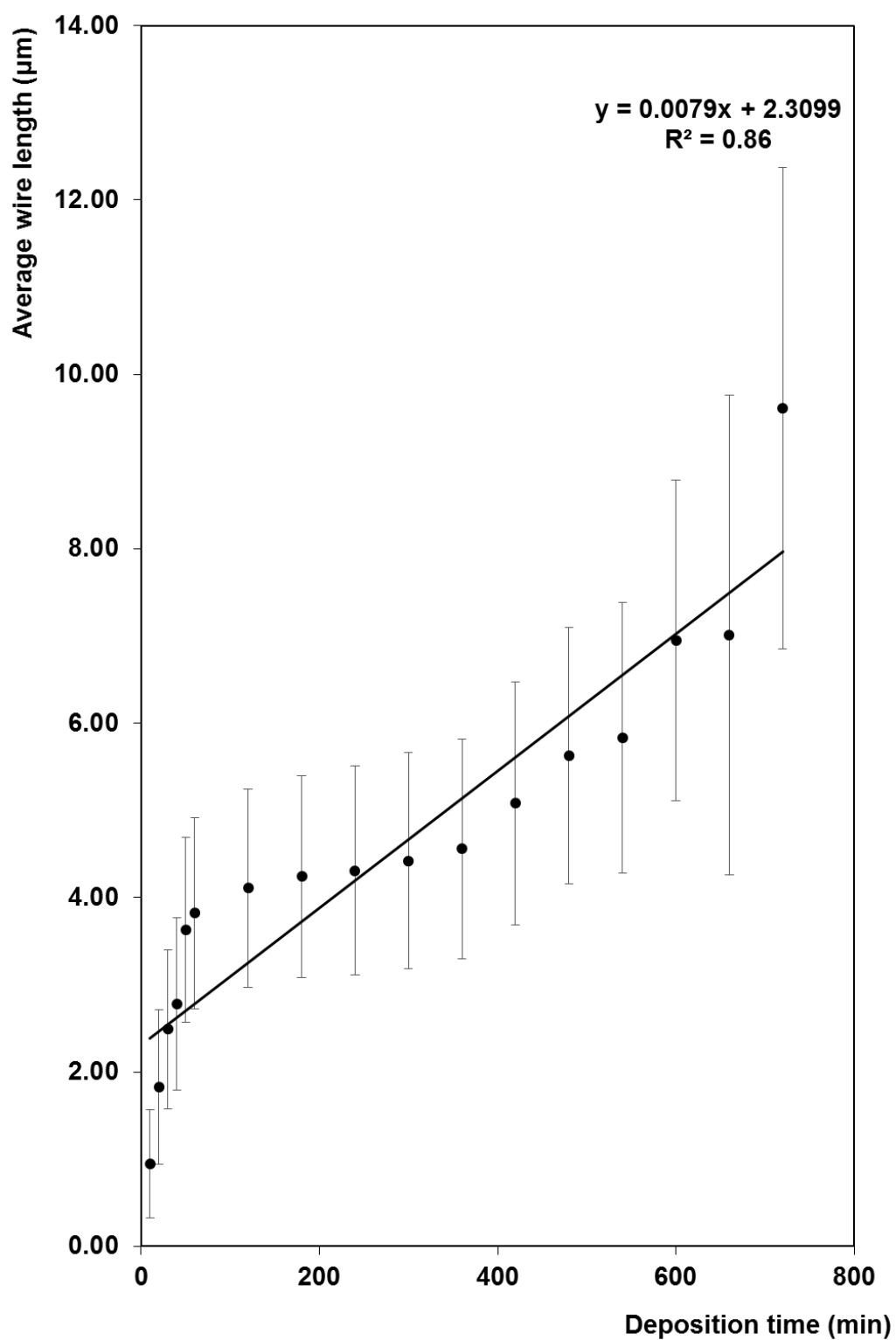


Figure 3.6: Plot of average wire length from SEM analysis vs. deposition time for solid gold nanowires.

According to the manufacturer's specifications, the thickness of the membrane used as template was 22 μm .³¹ A nanowire length of 9.61 μm for the longest deposition time suggests that the deposition does not fill the entire length of the membrane's pores. This is also seen from the current-time transient for 12 hour deposition, where the characteristic increase in current that represents the transition to bulk growth over the top of the membrane is not observed. Theoretically, the charge required to fill the entire length of the membrane using this solution is ~ 10.2 C. This value assumes 100% Faradaic efficiency, and assumes that the pore-density does not vary between membranes.

In reality, 100% Faradaic efficiency is unlikely, and the variation of pore-density between membranes is likely to be quite high. In addition, other factors such as pore "wetting", homogeneous nucleation of the gold, and homogeneous rate of deposition within the pores, are likely to affect the length of the nanowires formed.

It is also possible that at longer deposition times, the number of Au^{3+} ions becomes depleted throughout the entire solution, and that this occurs long before the deposited metal can reach the top of the pores.

3.2.4 Electrochemical characterisation of Au nanowire – modified carbon electrodes

In order to determine if the nanowires could be functionalised and used for DNA detection, they first had to be characterised using electrochemistry. This was done by drop casting the nanowires onto bare carbon electrodes, fixing with glutaraldehyde, and running cyclic voltammetry in acidic electrolyte. Glutaraldehyde is an organic compound with the formula $\text{CH}_2(\text{CH}_2\text{CHO})_2$. A pungent colourless oily liquid, glutaraldehyde is used as a fixative in many laboratories.

The potential was scanned between 0 V and 1.2 V vs Ag/AgCl in 3 M KCl. The resulting voltammograms were used to calculate the electrochemical area and the surface roughness of these modified electrodes, based on the area of the gold-oxide reduction peak.

3.2.4.1 Cyclic Voltammetry

Using cyclic voltammetry, the modified gold electrodes were characterised electrochemically. Using the A_p (the area under the peak), the electrochemical area and surface roughness of the modified carbon electrodes were calculated.

A sample voltammogram for a modified nanowire electrode is shown in Figure 3.7. In this case, the electrode has been modified with nanowires that were grown for 50 minutes.

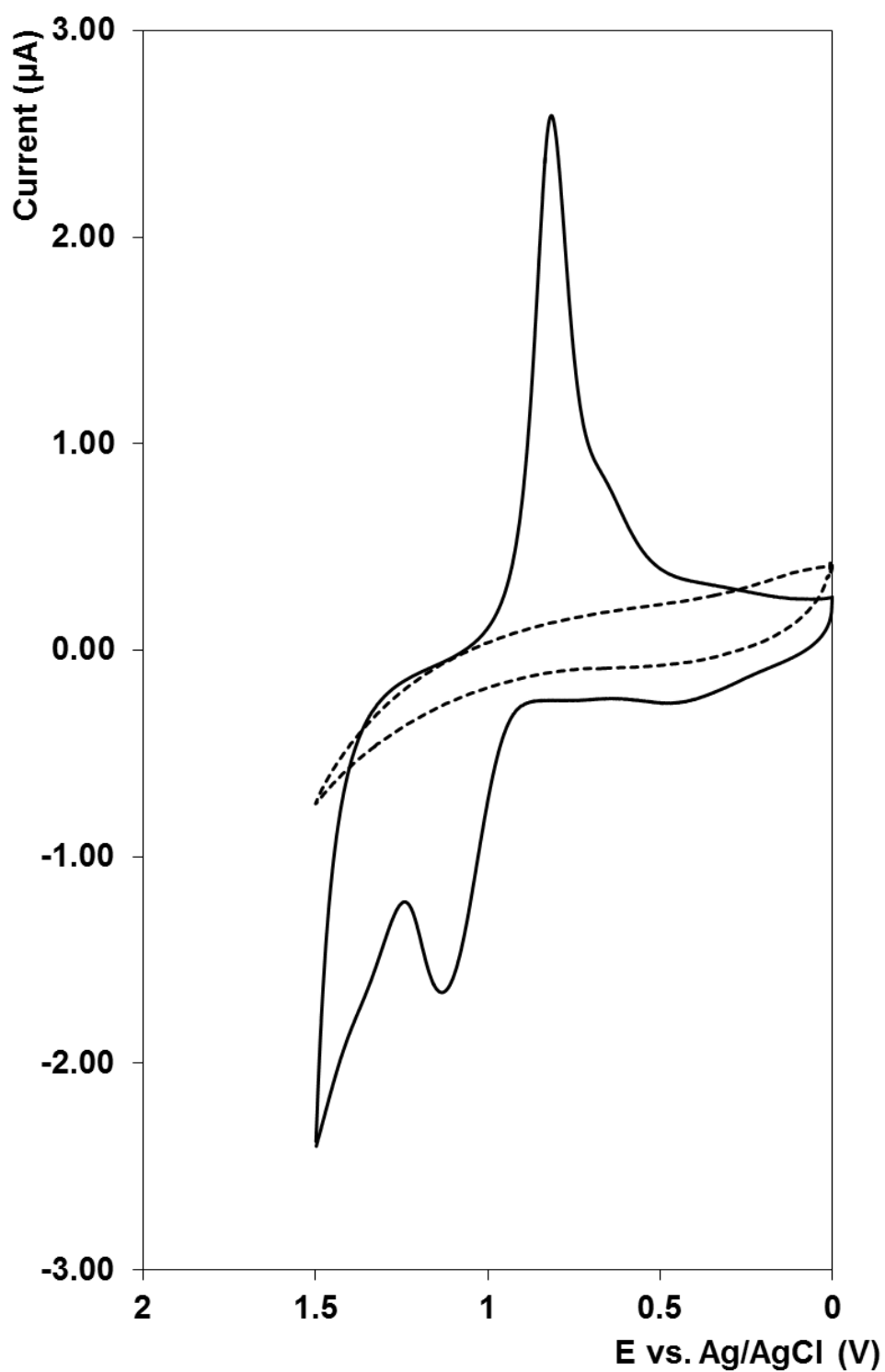


Figure 3.7: Cyclic voltammogram of a 50 min Au nanowire modified carbon electrode in 0.01 M H_2SO_4 with a surface roughness factor of 1.95 (solid line) vs. a cyclic voltammogram of a bare carbon electrode in 0.1M H_2SO_4 (dashed line). The reference electrode is Ag/AgCl in 3 M KCl. The scan rate is 100 mVs^{-1} . The sixth scan is presented.

The nanowire modified electrode exhibits a larger residual current than a bare gold electrode, with a large cathodic peak at ~ 0.83 V, and a wide anodic peak between ~ 1 and 1.5 V, characteristic of gold oxide formation and subsequent reduction.³⁹

The expected surface roughness value of a clean bare gold electrode is ~ 1.1 ⁴⁰. As can be seen in Table 3.2, the surface roughness values of the modified electrodes increases with increasing deposition time, i.e. the 12 hr nanowires have the highest surface roughness values, and the 10 minute nanowires have the lowest. This is due to the increasing surface area of nanowires that is exposed to the electrolyte as their lengths increase.

.

Table 3.2: *Electrochemical Area and Surface Roughness of nanowire modified carbon electrodes*

Deposition time (min)	Electrochemical Area (cm²)	Surface Roughness
10	3.87E-06	1.19
20	5.02E-06	1.30
30	1.12E-05	1.41
40	1.14E-05	1.46
50	1.47E-05	1.95
60	1.60E-05	2.02
120	1.61E-05	2.39
180	1.73E-05	2.44
240	1.80E-05	2.49
300	2.39E-05	2.57
360	2.48E-05	2.63
420	2.93E-05	2.74
480	2.99E-05	2.92
540	3.06E-05	3.02
600	3.15E-05	3.08
660	3.34E-05	3.11
720	3.87E-05	3.15

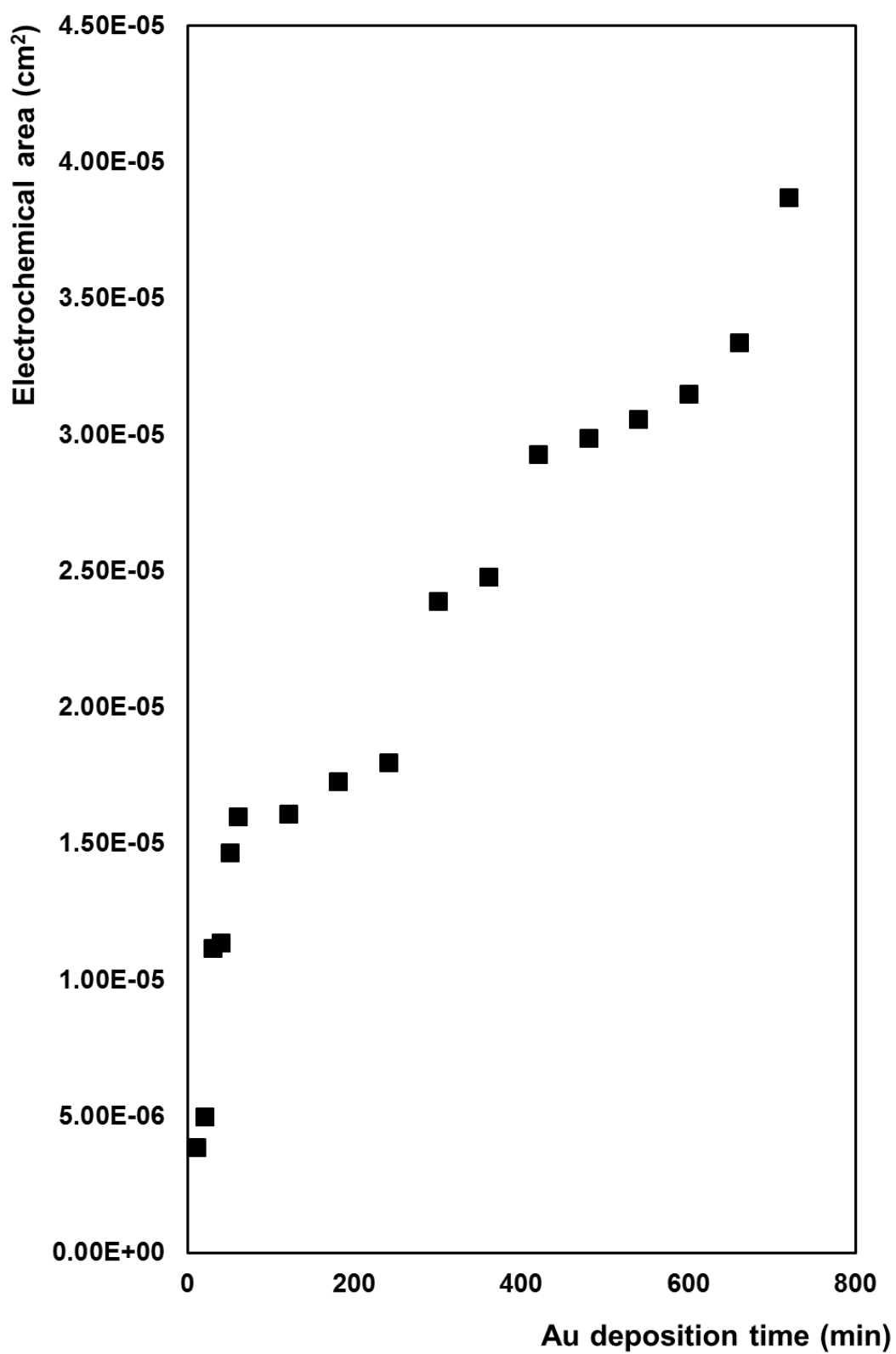


Figure 3.8: *Plot of electrochemical area vs. deposition time for Au nanowires.*

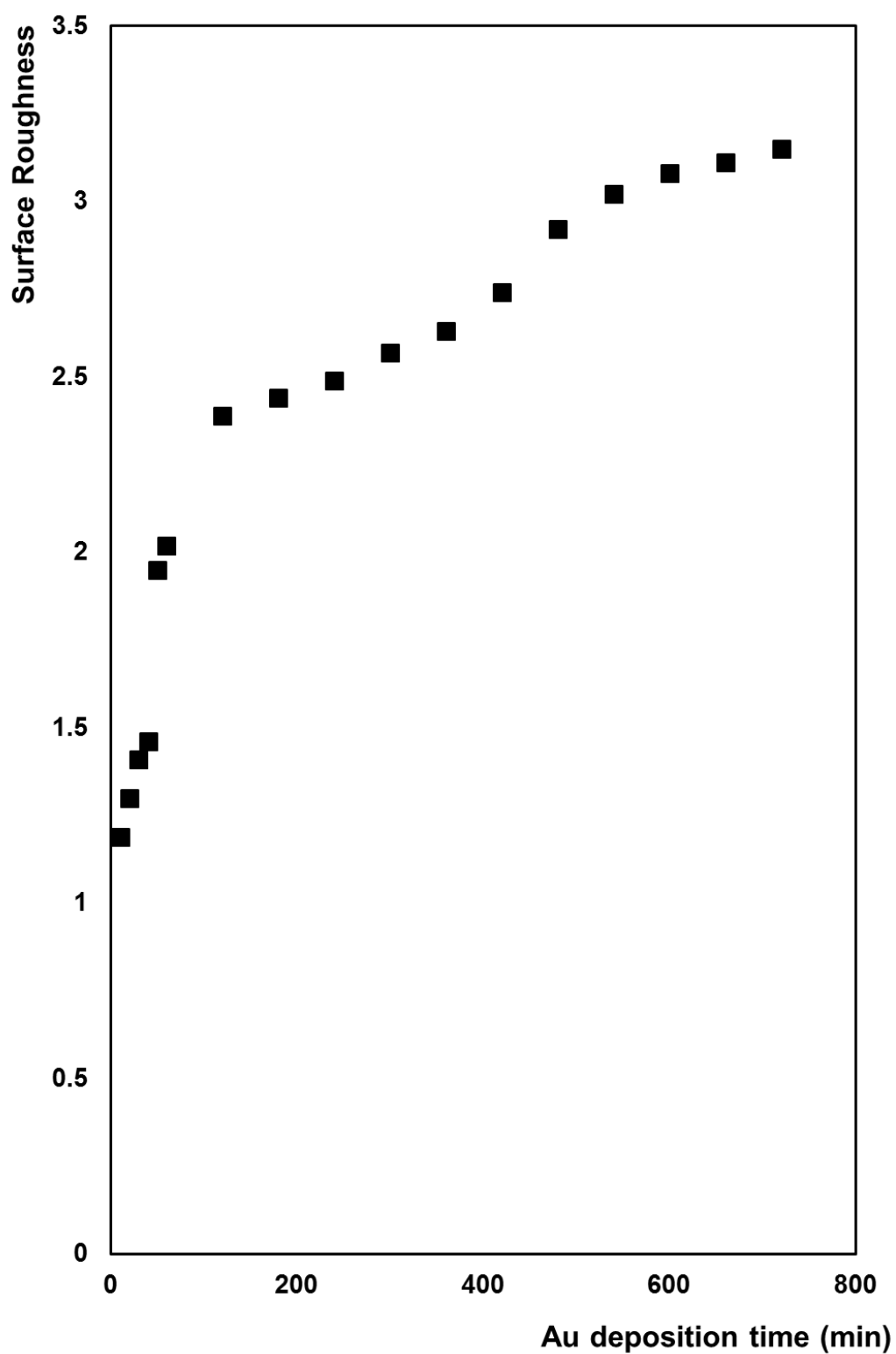


Figure 3.9: *Plot of surface roughness vs. deposition time for Au nanowires.*

Figure 3.8 and Figure 3.9 show that the increase of the electrochemical area and of the surface roughness is not proportional to the deposition time.

3.2.4.2 Capacitance

The current in an electrochemical cell includes non-faradaic sources. For example, if the charge on an electrode is zero and the potential is suddenly changed so that the electrode's surface acquires a positive charge; cations near the electrode's surface will respond to this positive charge by diffusing away from the electrode; anions, on the other hand, will diffuse toward the electrode. This diffusion of ions occurs until the electrode's positive surface charge and the negative charge of the solution near the electrode are equal. Because the movement of ions and the movement of electrons are indistinguishable, the result is a small, short-lived non-faradaic current that is known as the charging current (capacitance). Every time the electrode's potential is changed, transient charging current flows.⁴¹

The behaviour of the electrode-solution interface is analogous to that of a capacitor, and a model of the interfacial region somewhat resembling a capacitor can be given. At a given potential, there will exist a charge on the metal electrode, q^M and a charge in the solution, q^S . Whether the charge on the metal is negative or positive with respect to the solution depends on the potential across the interface and the composition of the solution. At all times however, $q^M = -q^S$. The charge on the metal q^M represents an excess or deficiency of electrons and resides in a very thin layer on the metal surface. The charge in solution q^S is made up of an excess of either cations or anions in the vicinity of the electrodes surface. At a given potential, the electrode-solution interface is characterised by a double layer capacitance, C_d typically in the range of 10-40 μFcm^{-2} for an electrode in contact with aqueous electrolyte.⁴²

The formula used to calculate the capacitance values is given in Chapter 2.

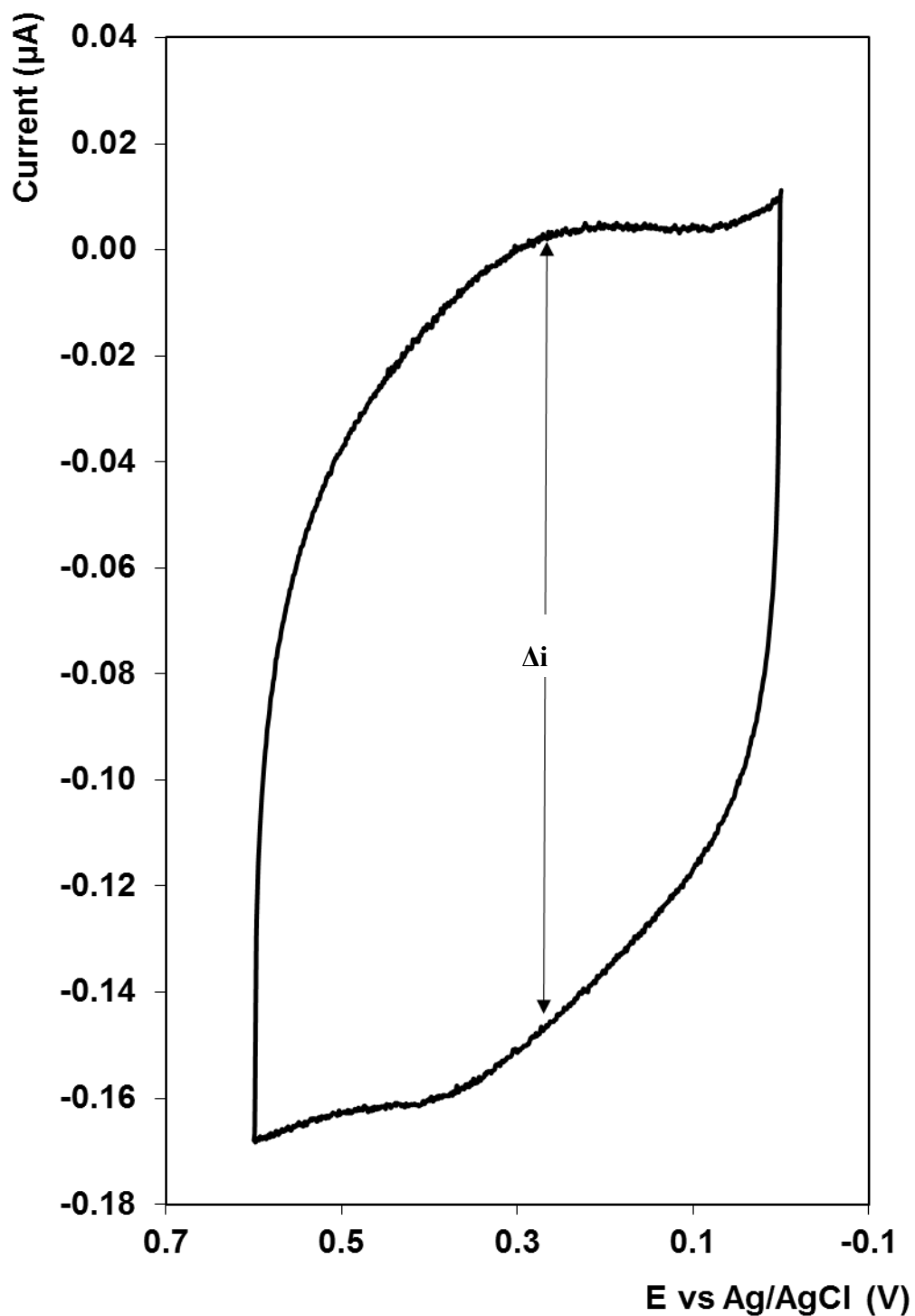


Figure 3.10: Cyclic voltammogram demonstrating capacitance of a carbon electrode modified with gold nanowires grown for 10 minutes. The electrolyte was 0.1 M LiClO₄ in ACN. The potential was swept from 0 to 0.6V with a scan rate of 100mVs⁻¹. The reference electrode was Ag/AgCl in 3 M KCl. The sixth scan is presented.

Table 3.3: *Capacitance measurements of nanowire modified electrodes*

Nanowire deposition time (min)	Capacitance (μFcm^{-2})
10	7.318
20	7.723
30	8.112
40	8.119
50	8.261
60	8.650
120	9.199
180	10.597
240	10.943
300	11.473
360	11.725
420	11.759
480	13.859
540	14.145
600	14.235
660	18.680
720	28.930

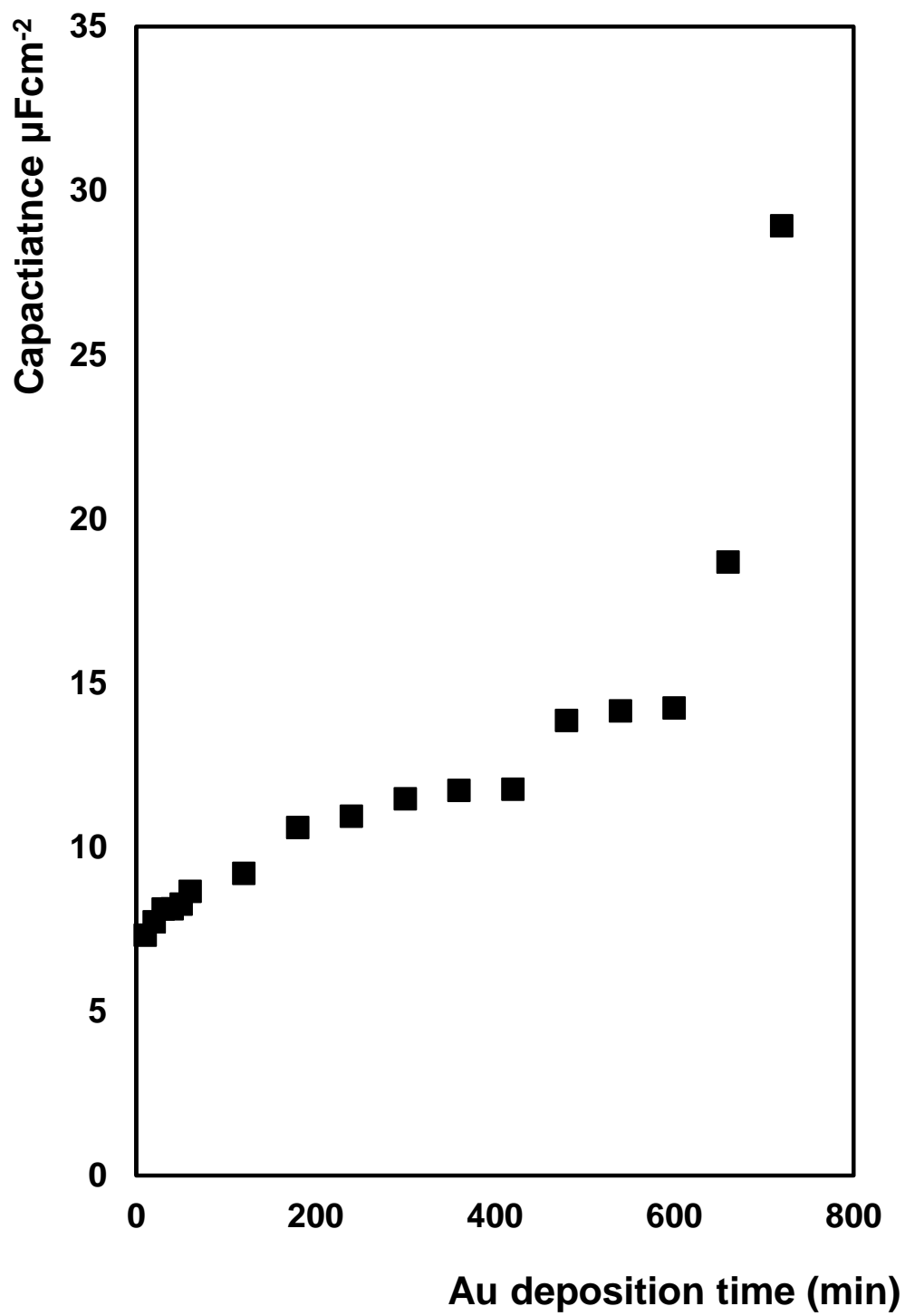


Figure 3.11: *Plot of capacitance values vs. deposition time for gold nanowires.*

As stated earlier, a satisfactory value for capacitance for clean gold electrodes is somewhere in the range of $10 - 40 \mu\text{Fcm}^{-2}$. As can be seen in Table 3.7 and Figure 3.11, the values for the capacitance of the nanowires fall within this range, generally on the lower end. The bare gold electrode used in the example in Section 2.8 had a capacitance value of $7.53 \mu\text{Fcm}^{-2}$. The capacitance values of the nanowires are almost all larger than this value, which indicates that the nanowire modified electrode induces more of a change in the charge in the electrolyte solution than the bare gold electrode. This also indicates that the gold nanowires have adhered to the electrode surface, and retain electrochemical ability even when confined to an electrode surface.

Figure 3.11 also shows that the capacitance of the nanowires does not increase linearly with increasing deposition times, suggesting that the increase in the capacitance value arises from the fact that there are more nanowires present, rather than the increased surface area of the nanowires.

3.2.5 Mass of gold deposited during deposition of nanowires

The mass of gold deposited during deposition can be calculated from Faraday's law:

$$mass = \frac{1}{F} \times \frac{Q.M}{n} \quad \text{Equation 3.1}$$

Where F is Faraday's constant (96485 Cmol^{-1}), Q is the charge passed (C), M is the molecular weight of the metal deposited, (gmol^{-1}), and n is the number of electrons transferred, (in this case, 2).

The charge passed during deposition can be calculated from the integral of the current-time transient.

A sample of an integrated current-time transient is shown in Figure 3.12. Table 3.4 shows the mass of gold deposited for all deposition times. As expected, the mass of gold deposited increases as the deposition time increases. This is also reflected in the increasing length of the nanowires as deposition time increases.

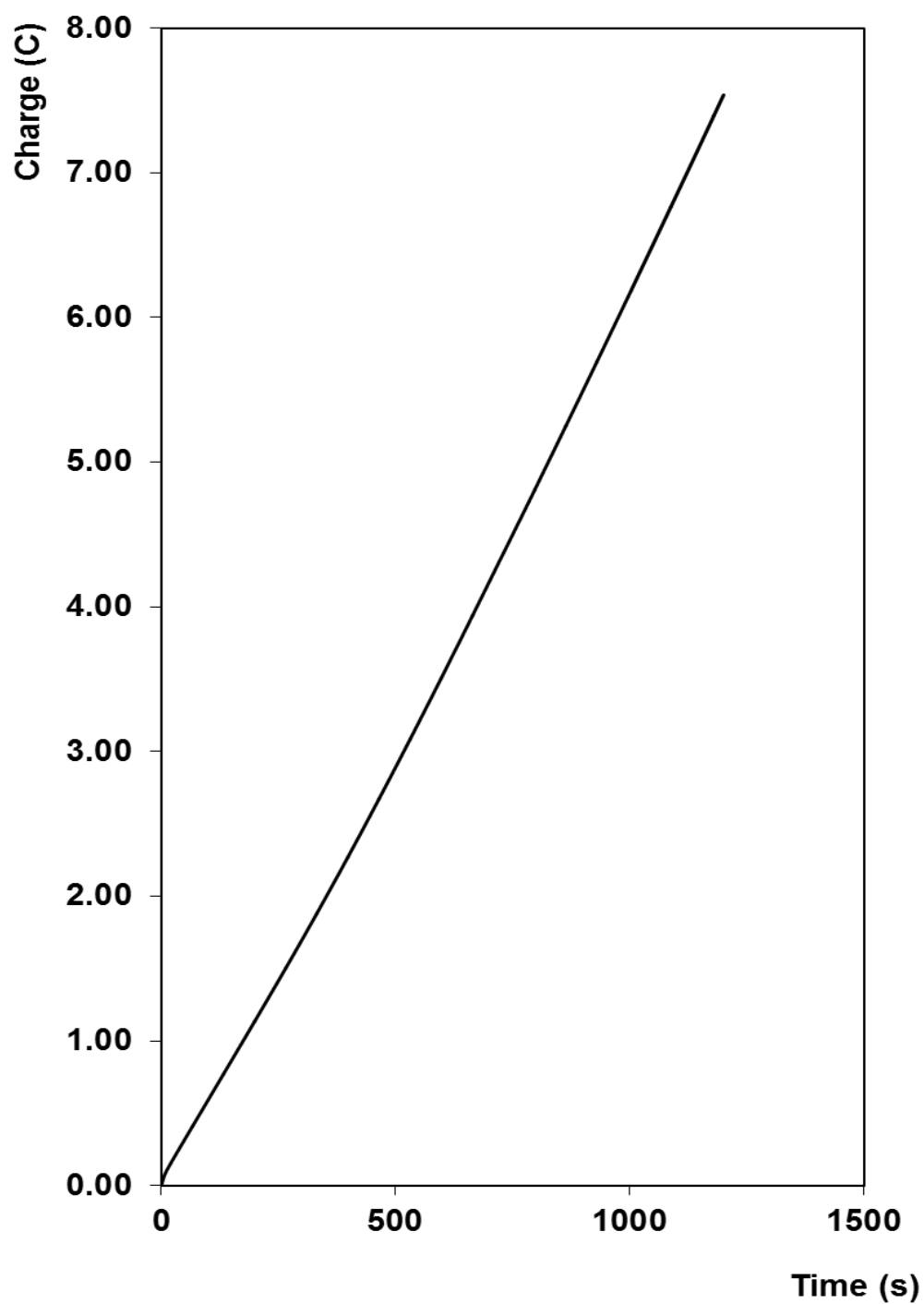


Figure 3.12: *Integrated current-time transient for twenty minute deposition of gold nanotubes through the pores of a polycarbonate membrane. The applied potential was -0.273 V vs. Ag/AgCl in 3 M KCl.. The charge passed was 7.5 C.*

Table 3.4: *Mass of gold deposited during nanowire growth*

Charge passed (C)	Deposition time (min)	Mass of gold deposited (g)
3	10	0.00306
7.5	20	0.00765
13	30	0.01327
15	40	0.01531
16.7	50	0.01704
18.3	60	0.01868
23.6	120	0.02409
32.1	180	0.03277
42.2	240	0.04308
45.3	300	0.04624
48.3	360	0.04930
52.4	420	0.05349
60.7	480	0.06196
78.1	540	0.07973
82.4	600	0.08412
84.5	660	0.08624
91.7	720	0.09361

As can be seen from the values above, the charge increases with increasing deposition time, indicating that the length of nanowire deposited increases also, as well as increasing mass of metal deposited. The maximum charge passed was during the 12 hour deposition, 91.7 C. this value corresponds to an expected wire length of $\sim 9.2 \mu\text{m}$. This is not significantly different to the average length of the deposited nanowires according to the SEM analysis carried out, which was calculated to be $9.61 \mu\text{m}$.

3.2.6 Concentration of Nanowires

Inductively Coupled Plasma – Mass Spectrometry (ICP-MS) was performed in order to determine a concentration of nanowires formed.

ICP-MS indicated that after depositing the nanowires for 12 hours, the 6 mm diameter disk contained 10.56 mg of gold (including the sputtered gold layer). Assuming that the nanowire length is $\sim 9\text{ }\mu\text{m}$, this corresponds to 2.37×10^{10} nanowires. This value was calculated after subtracting the contribution of the 300 nm sputtered gold which was calculated separately. The mass of the sputtered gold layer was calculated to be 0.54 μg in 50 mL of sample.

Pore density of the membranes used is $\sim 1.27 \times 10^{10}$ pores cm^{-2} . The calculated number of nanowires deposited is not significantly different to the pore density.

The ICP-MS analysis has confirmed that a large number of nanowires can be fabricated using this template technique.

3.2.7 Potentiostatic deposition of gold nanotubes

Gold nanotubes were deposited for 10 - 60 minutes, and for 12 hours. The electrolyte solution used was 30 mM HAuCl_4 in 0.1 M KCl. A fixed potential of -0.273 V vs. Ag/AgCl in 3 M KCl was applied for each deposition time.

Gold nanotubes were deposited for varying deposition times through the pores of a polycarbonate membrane. The gold sputtered layer was removed from the surface of the membrane using an adhesive tape. This process removes the gold from the planar surface but leaves a ring of gold within the pore which acts as a site for gold nucleation in the subsequent electrodeposition step. Electrochemical deposition was carried out using the same conditions as for the solid gold nanowires.

Figure 3.13 shows the current-time transient for a 40 minute deposition of gold through the gold ring modified membrane template.

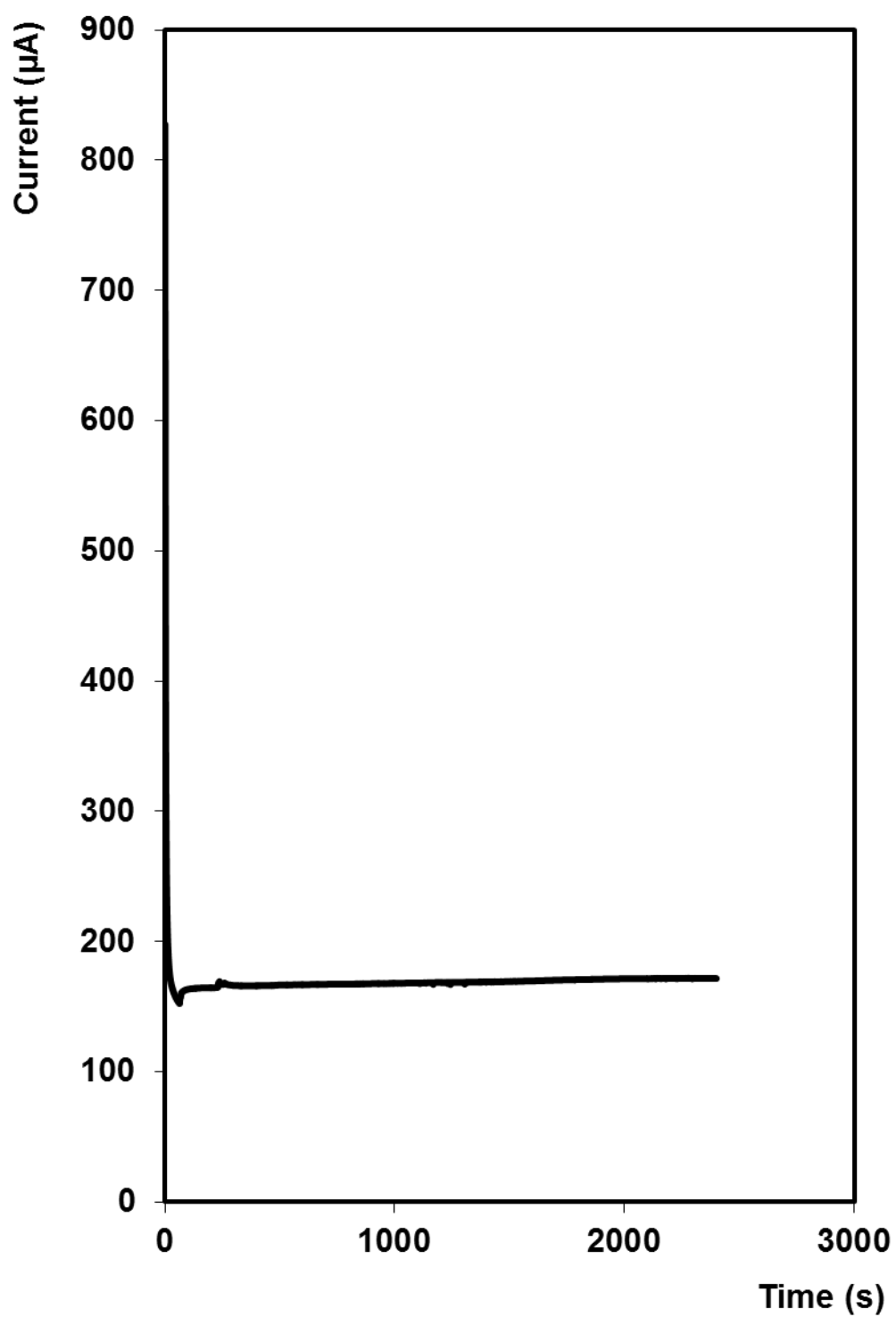


Figure 3.13: *Current-time transient for growth of gold nanotubes through a porous polycarbonate membrane mounted on FDTO. The potential applied was -0.273 V vs. Ag/AgCl in 3 M KCl for 2400 seconds.*

The current rapidly decreases due to depletion of ions immediately at the membrane surface. The current appears to decrease more rapidly in the deposition of nanotubes compared to nanowire deposition, Figure 3.2. This is because the available surface areas for the ion reduction reaction in the case of nanotubes is much smaller than those for nanowires, so the concentration of the electroactive species in the vicinity of electrode and at the mouth of nanotube arrays will be more rapidly depleted to zero.³⁵

Consequently, a higher concentration gradient between the pore mouth and the bulk solution results in a higher diffusion-controlled current for nanotubes.

Once again, the characteristic shape for deposition within the pores only is observed, i.e. the rapid increase in current that signals transition to bulk growth over the top of the membrane is not observed.

This suggests that the nanotubes formed will be shorter in length than the height of the pore ($\sim 22\mu\text{m}$).³¹

3.2.8 SEM images of nanotubes after release from the membrane

The deposited nanotubes were freed from the membrane by dissolution in dichloromethane, and suspended in a solution of DI, following several washings with DCM and sonication to remove sputtered gold layer. The nanotubes were dropcast onto carbon tabs for analysis under SEM, and their average lengths and diameters were studied.

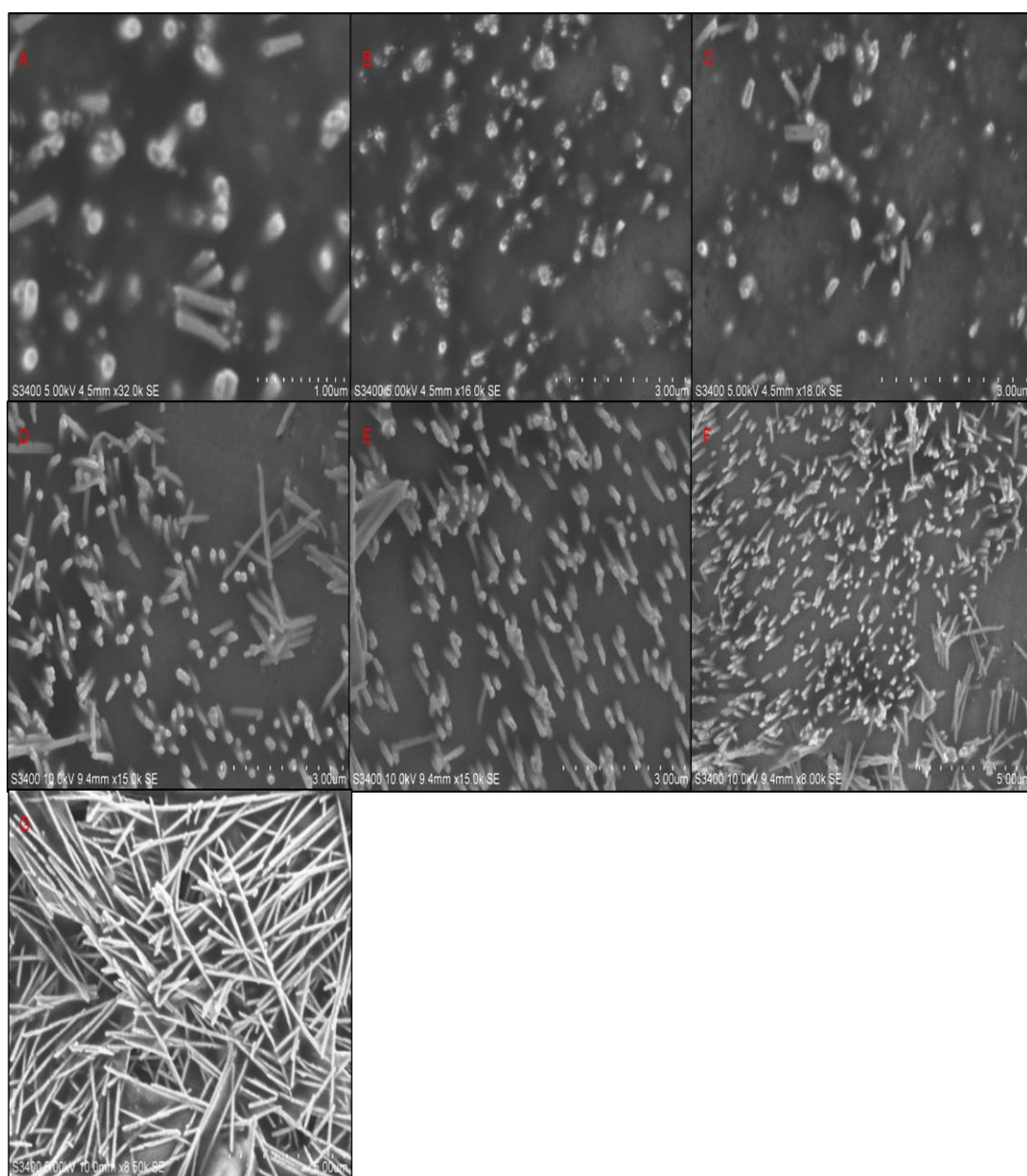


Figure 3.14: SEM images of Au nanotubes after dissolution of polycarbonate membrane, sonication to remove sputtered gold layer and suspension dropcast for analysis. Deposition times are: (A) 10 min, (B) 20 min, (C) 30 min, (D) 40 min, (E) 50 min, (F) 60 min, (G) 12 hours. Accelerating voltages are 5 – 20 kV.

Table 3.5: *Length of Au nanotube vs. deposition time*

Deposition time (min)	Length of nanotube (μm)
10	1.15
20	2.25
30	2.32
40	2.45
50	3.05
60	3.37
720	5.25

The lengths of the nanotubes increase with increasing deposition time, as is the case with the nanowires. The lengths of the nanotubes are somewhat shorter than the lengths of the nanowires, Table 3.1 and Figure 3.6.

This is unexpected, as one would assume that as the nanotubes deposit only on the walls of the pore, rather than filling from the bottom of the pore upwards, that their lengths would be greater than those of the solid nanowires.

3.2.9 Electrochemical characterisation of Au nanotube - modified carbon electrodes

The nanotubes were characterised in the same way as the gold nanowires.

The inner wall of the hollow nanotubes could create a higher electrochemical surface area than the solid nanowires, depending on the rate of diffusion of electrolyte inside the hollow tubes. Access to the interior would also be evident in the surface roughness and capacitance values.

3.2.9.1 Cyclic Voltammetry

The nanotubes were dropcast onto bare carbon electrodes, fixed with glutaraldehyde, and voltammetry in acidic electrolyte was performed. The electrochemical area and surface roughness values for the nanotubes adsorbed to an electrode surface were determined.

Table 3.6: *Electrochemical Area and Surface Roughness of nanotube modified carbon electrodes*

Deposition time (min)	Electrochemical Area (cm ²)	Surface Roughness
10	5.31E-06	0.43
20	1.33E-05	1.08
30	3.19E-05	2.60
40	3.40E-05	2.78
50	3.65E-05	2.98
60	4.02E-05	3.28
720	4.52E-05	3.69

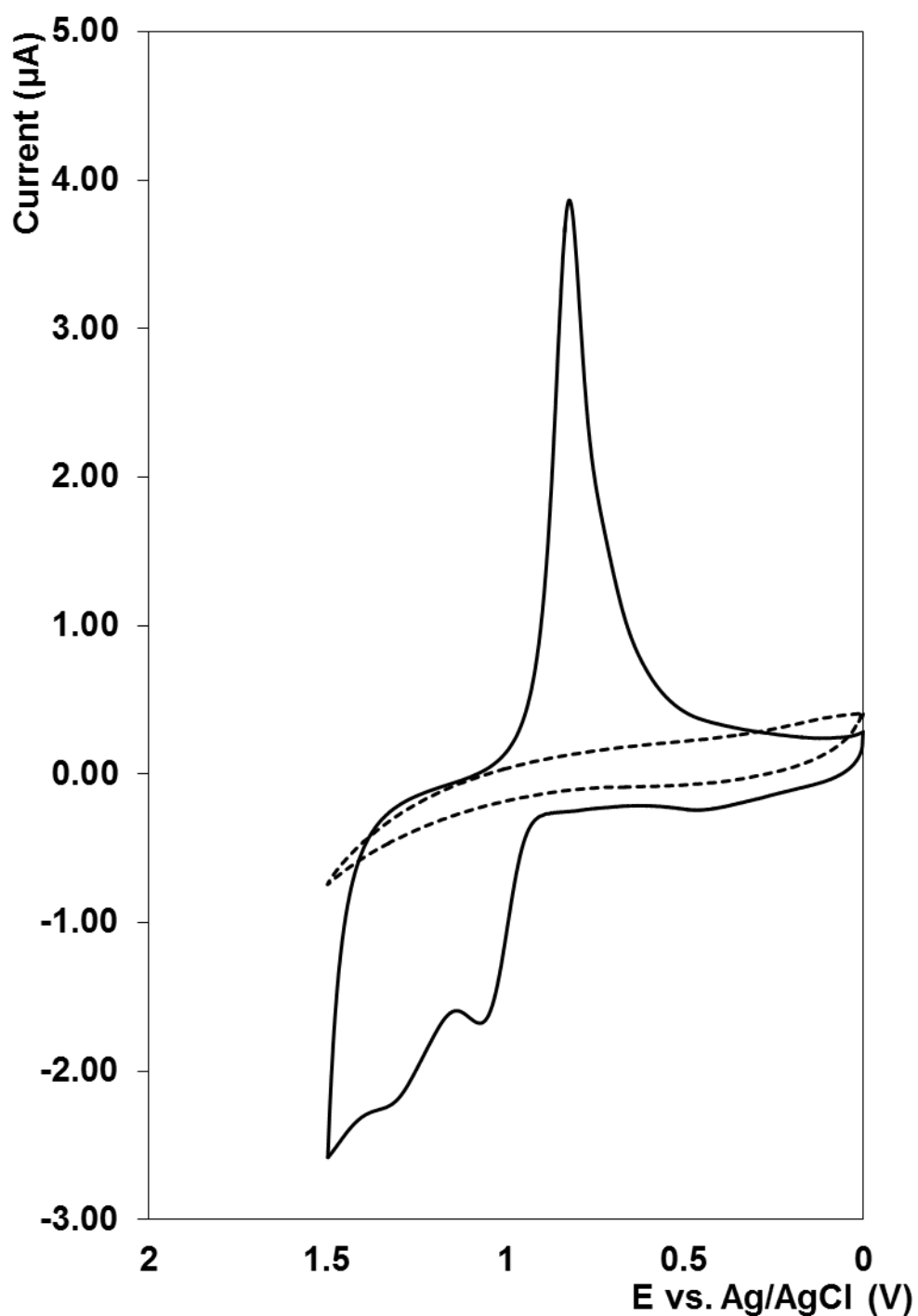


Figure 3.15: Cyclic voltammogram of a 12 hr Au nanotube modified carbon electrode in 0.1 M H_2SO_4 with a surface roughness factor of 2.60 (solid line) vs. a cyclic voltammogram of a bare glassy carbon electrode in 0.1M H_2SO_4 (dashed line). The counter electrode was a platinum wire and the reference electrode was Ag/AgCl in 3 M KCl. The scan rate is 100 mVs^{-1} . The sixth scan is presented.

The nanotube modified electrode shows characteristic gold oxide and reduction formation peaks at $\sim 1-1.5$ V and 0.86 V vs. Ag/AgCl in 3 M KCl respectively.³⁹ These redox peaks are not present in the voltammogram of the bare glassy carbon electrode, which confirms that the nanotubes have adsorbed onto the surface of the electrode.

The increased surface roughness of the nanotubes may be due to diffusion of the electrolyte inside the nanotubes, indicating that the inner wall of the tubes may be electrochemically active as well as the outer wall.

The full effect of this increased surface area would be maximised if the nanotubes were oriented in an ordered, upright, array on the surface of the electrode, and if the diffusion of the electrolyte inside the tube was quick.

3.2.9.2 Capacitance

The capacitance values for the nanotubes were determined by dropcasting the nanotubes onto the surface of a bare glassy carbon electrode, and fixing with glutaraldehyde. A voltammogram of an electrode modified with nanotubes grown for 12 hours is shown in Figure 3.16. The capacitance values for all the nanotubes are shown in Table 3.7.

The formula used to calculate the capacitance values is given in Chapter 2.

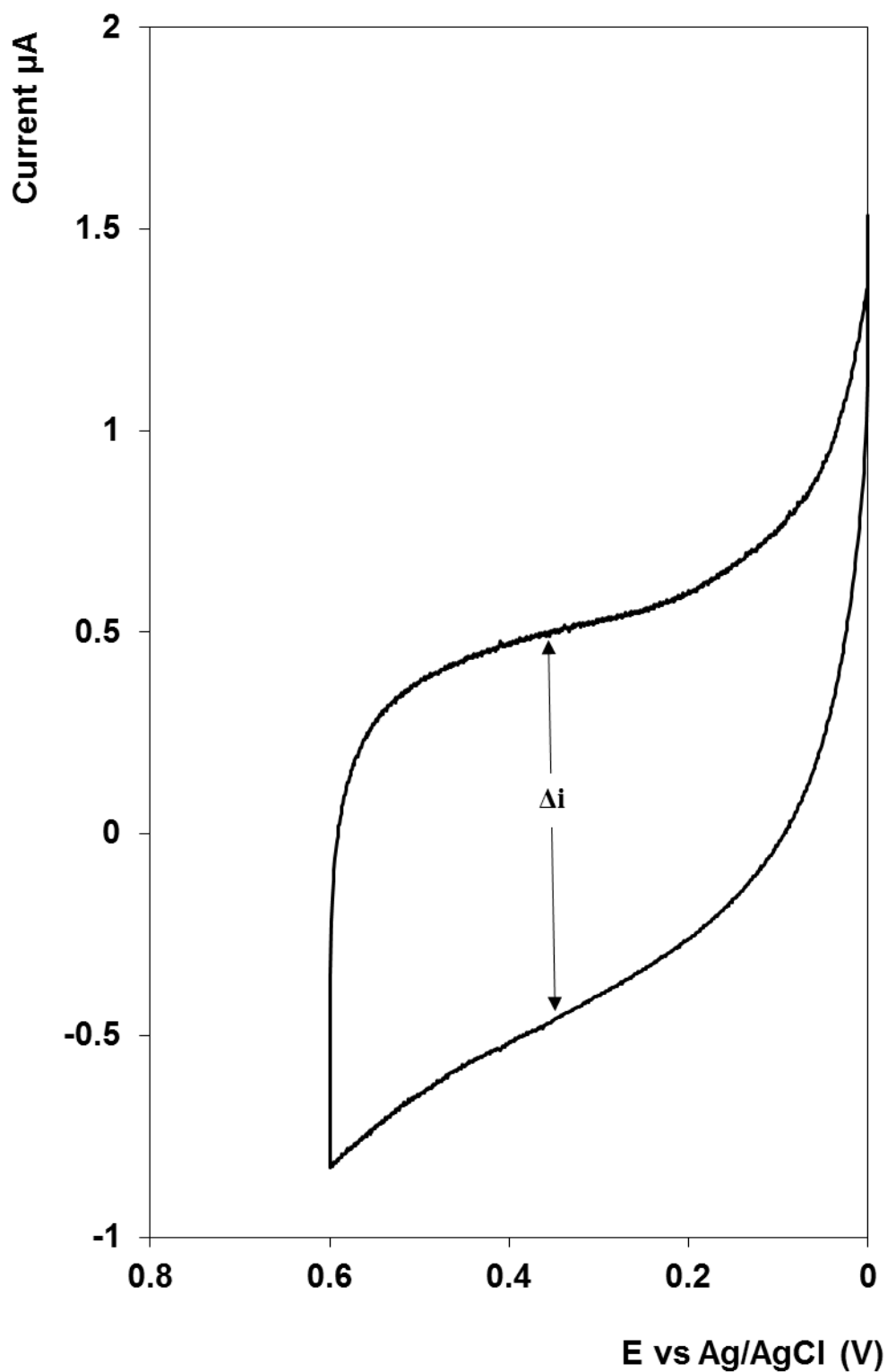


Figure 3.16: Cyclic voltammogram demonstrating capacitance of a glassy carbon electrode modified with nanotubes deposited for 12 hours. The electrolyte was 0.1M LiClO_4 in ACN. The potential was swept from 0 to 0.6V vs. Ag/AgCl in 3 M KCl with a scan rate of 100mVs^{-1} . The sixth scan is presented.

Table 3.7: *Capacitance measurements of nanotube modified electrodes*

Nanotube Deposition Time (min)	Capacitance μFcm^{-2}
10	10.4
20	11.8
30	12.8
40	14.9
50	15.7
60	20.9
720	39.6

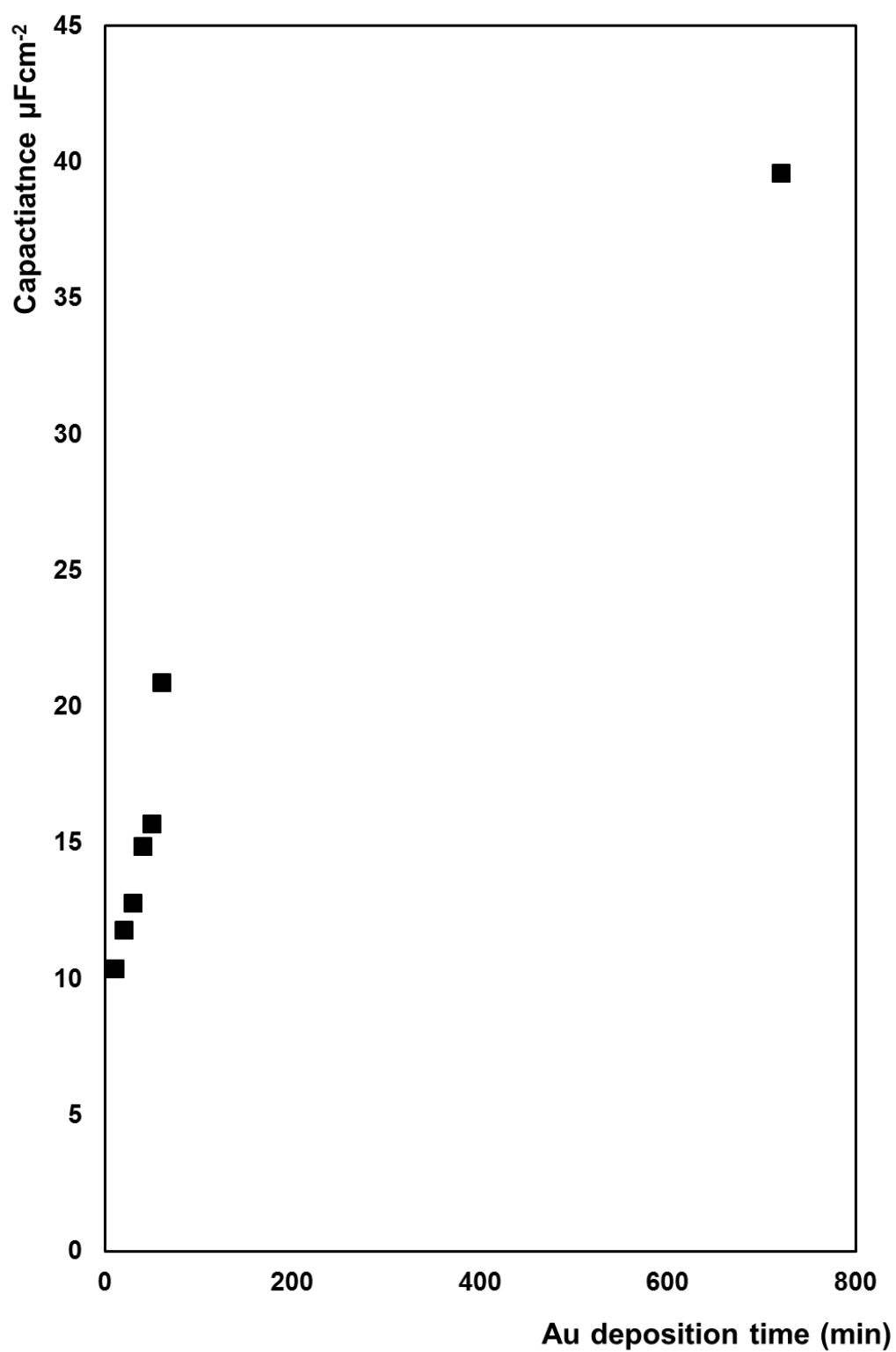


Figure 3.17: *Plot of capacitance vs. deposition time for gold nanotubes.*

As seen previously in section 3.2.4.2, the capacitance of the nanotubes increases with increasing deposition time, similar to the behaviour of the solid nanowires. In addition, Figure 3.17 shows that the increase of the capacitance of the nanotubes does not increase linearly with increasing deposition time.

This behaviour is expected of nanotubes and nanowires, due to the larger electrochemical area that is in contact with the electrolyte. This type of behaviour has been observed in gold nanowire arrays previously by Forrer et al.⁴³

These capacitance values are larger than those of the solid nanowires for the same deposition times. This may be due to the increased active surface area of the tubes, i.e. the inner walls may also be electrochemically active.

This may have positive implications for the use of nanotubes in an electrocatalytic detection assay, as utilising the inner walls of the tubes as well as the outer walls to produce a signal could dramatically amplify the measurable signal, without the need for target amplification, over the signal produced by solid nanowires.

3.2.10 Mass of gold deposited during deposition of nanotubes

The mass of gold deposited as nanotubes was calculated as described in section 3.2.5 previously. An integrated current-time transient for ten minute deposition time is shown in Figure 3.18.

The mass of gold deposited as nanotubes for each deposition time is listed in Table 3.8.

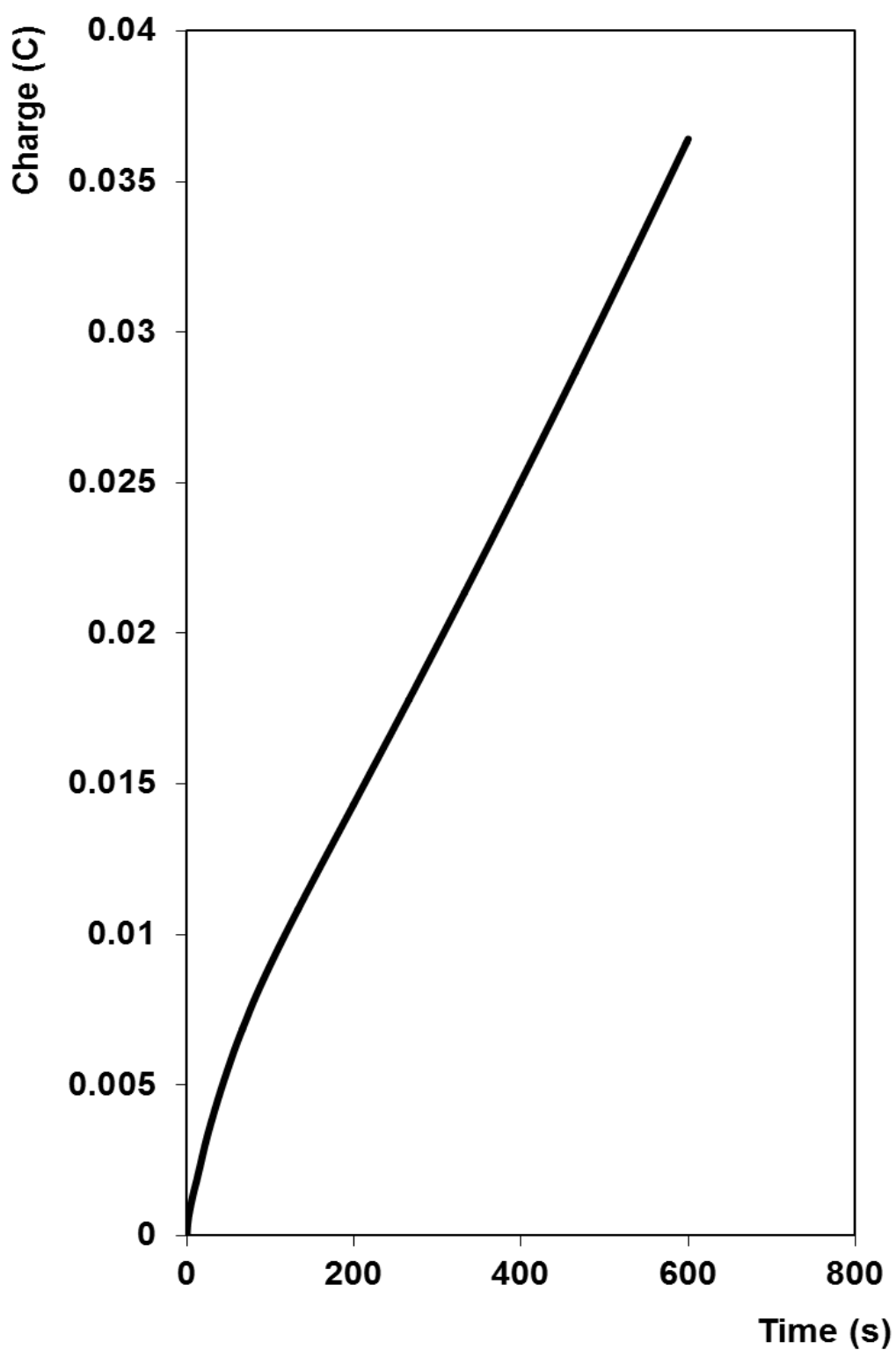


Figure 3.18: *Integrated current-time transient for ten minute deposition of gold nanotubes through the pores of a polycarbonate membrane. The applied potential was -0.273 V vs. Ag/AgCl in 3 M KCl. The charge passed was 0.036 C.*

Table 3.8: *Mass of gold deposited as nanotubes*

Charge passed (C)	Deposition time (min)	Mass of gold deposited (g)
0.036	10	0.00004
0.12	20	0.00012
1.7	30	0.00177
2.8	40	0.00286
16.7	50	0.01704
20.1	60	0.02041
50.7	720	0.05104

As would be expected, according to the charge passed during deposition, the mass of gold deposited as nanotubes is lower than that deposited as solid nanowires.

This also correlates with SEM analysis of the average lengths of the nanotubes, which are shorter than those of the solid nanowires, e.g. 5.25 μm length for a 12 hour nanotube compared to 9.61 μm for a 12 hour nanowire.

As stated previously, the method of determining the lengths of the nanowires may not be reliable, and a TEM analysis of a cross section of the membrane following deposition would likely give a more accurate representation of the average tube length, prior to any agitation steps that may cause structural damage.

The maximum charge passed was during the 12 hour deposition, 50.7 C. this value corresponds to an expected tube length of $\sim 5.1 \mu\text{m}$. This is not significantly different to the average length of the deposited nanotubes according to the SEM analysis carried out.

3.2.11 Concentration of Nanotubes

ICP-MS indicated that 1×10^{10} nanotubes are fabricated using this method, which is less than the number of solid nanowires deposited previously. The pore density of the membrane is 1.27×10^{10} . The concentration of nanotubes calculated using ICP-MS suggests that almost all of the pores in the membrane were filled with a nanotube. This is unlikely, and may support the suggestion that the tubes are breaking during membrane dissolution and centrifugation steps.

The reason for the lower number of nanotubes formed may be due to the fact that as there is less sputtered gold on the membrane, it is more difficult to deposit the gold homogenously into all of the pores in the membrane. This may result in less nanotubes being created compared to nanowires.

3.3 Summary

Table 3.9: *Summary of characterisation of gold nanowires for all deposition times*

Deposition time (min)	Length (μm)	Surface Roughness	Capacitance (μFcm^{-2})	Mass Au deposited (g)
10	0.95	1.19	7.318	0.00306
20	1.83	1.3	7.723	0.00765
30	2.49	1.41	8.112	0.01327
40	2.78	1.46	8.119	0.01531
50	3.63	1.95	8.261	0.01704
60	3.82	2.02	8.65	0.01868
120	4.11	2.39	9.199	0.02409
180	4.24	2.44	10.597	0.03277
240	4.31	2.49	10.943	0.04308
300	4.42	2.57	11.473	0.04624
360	4.56	2.63	11.725	0.0493
420	5.08	2.74	11.759	0.05349
480	5.63	2.92	13.859	0.06196
540	5.83	3.02	14.145	0.07973
600	6.95	3.08	14.235	0.08412
660	7.01	3.11	18.68	0.08624
720	9.61	3.15	28.93	0.09361

Table 3.10: *Summary of characterisation of gold nanotubes for all deposition times*

Deposition time (min)	Length (μm)	Surface Roughness	Capacitance (μFcm^{-2})	Mass Au deposited (g)
10	1.15	0.43	10.4	0.00004
20	2.25	1.08	11.8	0.00012
30	2.32	2.6	12.8	0.00177
40	2.45	2.78	14.9	0.00286
50	3.05	2.98	15.7	0.01704
60	3.37	3.28	20.9	0.02041
720	5.25	3.69	39.6	0.05104

Table 3.9 and Table 3.10 show the results of the different characterisations that have been carried out on both the solid gold nanowires and the gold nanotubes.

From these tables, it can be seen that the length, surface roughness, capacitance and mass of gold deposited increases with increasing deposition time for both nanowires and nanotubes. Overall, the lengths of the nanowires are larger than the lengths of the nanotubes for the same deposition time. This is expected from the charge passed during deposition, and from the calculation of the mass of gold deposited, which was also larger for the nanowires at the same deposition times.

The surface roughness for the nanotubes at short deposition times is lower than for the nanowires at these deposition times, but for longer times, such as 50 and 60 minutes, and 12 hours, the roughness of the nanotubes is larger than that of the nanowires. This may be due to the increased surface area of the nanotubes inner wall.

The capacitance of the nanotubes is also higher than the nanowires for all deposition times, again possibly due to the extra active surface area provided by the inner walls of the tubes.

If the inner wall of the tubes is indeed active, it may prove advantageous in an electrocatalysis type assay, for example, as the higher surface area will provide a higher current. These higher currents may enable very low concentrations of target molecules such as DNA to be detected without the need for amplification.

Both the gold nanowires and gold nanotubes were utilised in an electrocatalysis assay to detect ss-DNA associated with *S. aureus* mastitis, and these results are discussed in Chapter 5.

3.4 Conclusion

In conclusion, gold nanowires and nanotubes were created by electrodeposition within the pores of a track etched polycarbonate membrane.

The nanowires and nanotubes were deposited for varying deposition times, and characterised via SEM and cyclic voltammetry.

SEM analysis of the nanowires revealed that they were solid, and had varying lengths depending on the deposition times. The shortest nanowires fabricated were 0.95 μm , while the longest were 9.61 μm .

Following release from the template, the nanowires were characterised using voltammetry in acidic solution, showing a well resolved redox couple for gold oxide formation and reduction. Capacitance measurements revealed that the longer nanowires showed increasing absolute capacitance values, indicating that there is a larger area exposed to the electrolyte than a conventional flat electrode.

SEM analysis of the nanotubes revealed that they were hollow in morphology, and that their lengths ranged from $\sim 2 - 5 \mu\text{m}$. Calculation of the mass of gold deposited showed that less gold was deposited for the nanotubes than for the nanowires. This correlates with the SEM analysis that showed that the nanotubes are shorter in length than the nanowires.

Voltammetry in acidic solution showed a well resolved redox couple for gold oxide formation and reduction, indicating that the nanotubes retained their electrocatalytic activity following adsorption to an electrode surface.

The capacitance values of the nanotubes were larger than those of the gold nanowires. This may be due to the increased active surface area of the tubes (i.e. the inner walls) compared to the solid nanowires.

A template approach to deposition of nanowires and nanotubes ensures that nanostructures of uniform length and diameter can be easily fabricated using metal salt solutions. The increased active surface area owing to the inner walls of the nanotubes may contribute an enhanced electrocatalytic signal over the solid nanowires, which would be useful in a biosensor and could amplify the signal


generated by a low concentration of target analyte. By orienting the nanotubes in an upright, ordered fashion on an electrode surface, these hollow nanotubes could give a higher signal than that of a nanoparticle of similar radius, but would occupy the same space on the electrode surface. This is a major advantage over the use of nanoparticles in the detection of low concentrations of analyte, dramatically improving sensitivity without the need for target amplification, and without compromising the number of biomarkers that can be detected.

3.5 References

- ¹J. Perez-Juste, I. Pastoriza-Santos, L. M. Liz-Marzan and P. Mulvaney, *Coord. Chem. Rev.*, 2005, **249**, 1870-1901.
- ²P. Livi, K. Bedner, A. Tarasov, M. Wipf, Y. Chen, C. Schoenenberger and A. Hierlemann, *Sensors and Actuators B-Chemical*, 2013, **179**, 293-300.
- ³Y. Lu, M. Yang, F. Qu, G. Shen and R. Yu, *Bioelectrochemistry*, 2007, **71**, 211-216.
- ⁴A. Mulchandani and N. V. Myung, *Curr. Opin. Biotechnol.*, 2011, **22**, 502-508.
- ⁵S. Roy and Z. Gao, *Nano Today*, 2009, **4**, 318-334.
- ⁶M. Xu, F. Yang, Y. Yuan, Q. Guo, B. Ren, J. Yao and R. Gu, *J. Colloid Interface Sci.*, 2013, **407**, 60-66.
- ⁷Z. Wen, M. Cheng, J. Sun and L. Wang, *Electrochim. Acta*, 2010, **56**, 372-375.
- ⁸N. Du, X. Fan, J. Yu, H. Zhang and D. Yang, *Electrochemistry Communications*, 2011, **13**, 1443-1446.
- ⁹Y. Yang, F. Liu, T. Li, Y. Chen, Y. Wu and M. Kong, *Scr. Mater.*, 2012, **66**, 495-498.
- ¹⁰I. Hwang, Y. Kim, S. Kim, B. Ju and J. Lee, *Sensors and Actuators B-Chemical*, 2009, **136**, 224-229.
- ¹¹Y. H. X. Duan , in *Semiconductor Nanomaterials for Flexible Technologies*, ed. Y. Sun, J.A. Rogers, William Andrew Publishing, Oxford, 2010, pp. 27-66.
- ¹²C.N.R. Rao, S.R.C. Vivekchand, A. Govindaraj, in: *Comprehensive Nanoscience and Technology*, ed. D.L.A.D.S.P. Wiederrecht, Academic Press, Amsterdam, 2011, pp. 289-314.
- ¹³Z. Liu, S. Z. El Abedin, M. S. Ghazvini and F. Endres, *Physical Chemistry Chemical Physics*, 2013, **15**, 11362-11367.

- ¹⁴ G.C. Hadjipanayis and Richard W. Siegel, *Nanophase Materials: Synthesis - Properties - Applications (NATO Science Series E: Applied Sciences, Volume 260)*, Kluwer Academic, 1994. p.260.
- ¹⁵ M. Moskovits, *Rev. Mod. Phys.*, 1985, **57**, 783-826.
- ¹⁶ S. Kivelson and A. J. Heeger, *Synth. Met.*, 1988, **22**, 371-384.
- ¹⁷ C. R. Martin, *Science*, 1994, **266**, 1961-1966.
- ¹⁸ C. R. Martin, *Acc. Chem. Res.*, 1995, **28**, 61-68.
- ¹⁹ C P Bean, *US Pat.*, 83095, 1969.
- ²⁰ G E Possin, *Rev. Sci. Instrum.*, 1970, **41**, 772
- ²¹ W D Willaims and N Giordano, *Rev. Sci. Instrum.*, 1984, **55**, 410.
- ²² R M Penner and C R Martin, *Anal. Chem.*, 1987, **59**, 2625.
- ²³ J. W. Liu and Y. Lu, *J. Am. Chem. Soc.*, 2003, **125**, 6642-6643.
- ²⁴ S. Kidambi, J. H. Dai, J. Li and M. L. Bruening, *J. Am. Chem. Soc.*, 2004, **126**, 2658-2659.
- ²⁵ M. Zayats, R. Baron, I. Popov and I. Willner, *Nano Letters*, 2005, **5**, 21-25.
- ²⁶ D. Suzuki and H. Kawaguchi, *Langmuir*, 2005, **21**, 8175-8179.
- ²⁷ N. Zhou, J. Wang, T. Chen, Z. Yu and G. Li, *Anal. Chem.*, 2006, **78**, 5227-5230.
- ²⁸ K. Dawson, J. Strutwolf, G. Herzog, D. W. M. Arrigan, A. J. Quinn and A. O'Riordan, *Electrochemical Nano/bio Sensors 2*, 2010, **28**, 29-37.
- ²⁹ B. J. Seddon, H. H. Girault, M. J. Eddowes, W. Peng and Z. Zhao, *J. Chem. Soc. , Faraday Trans.*, 1991, **87**, 2603-2606.
- ³⁰ M. Toimil-Molaes, *Beilstein Journal of Nanotechnology*, 2012, **3**, 860-883.
- ³¹ *Isopore™ Membrane Filters - Millipore*. www.millipore.com
- ³² M. V. Mirkin and S. Amemiya, *Nanoelectrochemistry*, CRC Press, Florida, 2015, pp. 370-371.

- ³³ L. Philippe, N. Kacem and J. Michler, *J. Phys. Chem. C*, 2007, **111**, 5229-5235.
- ³⁴ S. Valizadeh, J. M. George, P. Leisner and L. Hultman, *Electrochim. Acta*, 2001, **47**, 865-874.
- ³⁵ M. B. Hariri, A. Dolati and R. S. Moakhar, *Journal of The Electrochemical Society*, 2013, **160**, D279-D288.
- ³⁶ I. U. Schuchert, M. E. Toimil-Molares, D. Dobrev, J. Vetter, R. Neumann and M. Martin, *J. Electrochem. Soc.*, 2003, **150**, C189-C194.
- ³⁷ M. Motoyama, Y. Fukunaka, T. Sakka and Y. H. Ogata, *Electrochim. Acta*, 2007, **53**, 205-212.
- ³⁸ C. Schonenberger, B. M. I. vanderZande, L. G. J. Fokkink, M. Henny, C. Schmid, M. Kruger, A. Bachtold, R. Huber, H. Birk and U. Staufer, *J Phys Chem B*, 1997, **101**, 5497-5505.
- ³⁹ A. J. Bard and L. R. Faulkner, *Electrochemical methods: fundamentals and applications*, Wiley, New York, 1980. p.808.
- ⁴⁰ J. C. Hoogvliet, M. Dijkma, B. Kamp and W. P. van Bennekom, *Anal. Chem.*, 2000, **72**, 2016-2021.
- ⁴¹ Analytical Sciences Digital Library. *Analytical Chemistry: The Basic Concepts*. [Online] Available from: http://www.asdlib.org/onlineArticles/ecourseware/Kelly_Potentiometry/PDF-2-DoubleLayer.pdf (accessed 04 May 2012)
- ⁴² A. J. Bard and L. R. Faulkner, *Electrochemical methods: fundamentals and applications*, Wiley, New York, 1980. pp. 12.
- ⁴³ P. Forrer, F. Schlottig, H. Siegenthaler and M. Textor, *J. Appl. Electrochem.*, 2000, **30**, 533-541.



4. SYNTHESIS AND CHARACTERISATION OF GOLD:COPPER CORE:SHELL NANOWIRES

4.1 Introduction

Core:shell nanostructures can be broadly defined as nanostructures comprising a core comprised of one material, and a shell comprised of a different material. These can consist of a wide range of different combinations in close interaction, including inorganic:inorganic, inorganic:organic, organic:inorganic, and organic:organic materials. The choice of shell material of the core:shell nanostructure is generally strongly dependent on the end application and use.

Core:shell nanoparticles have been gaining in popularity over the last twenty years, and the focus of bimetallic core:shell nanoparticles has been mostly on electrocatalytic particles for oxygen reduction,^{1,2,3} methanol oxidation,⁴ and hydrogen oxidation,⁵ for use in fuel cells.

Due to the synergetic effect, bimetallic core:shell nanoparticles show better catalytic activities compared with single pure metallic nanoparticles.⁶ This effect may also be seen in bimetallic core:shell nanowires.

In recent years, there has been some interest in the area of core:shell nanowires, but most of the literature centres around carbon nanotubes decorated with metals⁷, metal oxide core:shell nanostructures⁸, or on metal:polymer core:shell wires⁹.

Core:shell nanostructures have been synthesised in a variety of ways, including electroless deposition¹⁰, photolithography¹¹, electrodeposition¹², pulsed laser deposition¹³, and sol-gel processes¹⁴. In most cases, the core is deposited first, and the shell is then deposited. In this work, the shell is deposited first, which is then filled with a solid core.

A variety of templates have been utilised in the core:shell nanowire deposition process, including mesoporous silica,^{15,16} viruses,¹⁰ self-assembled peptide nanowires,¹⁷ and polymer brushes.¹⁸

Electrochemical deposition of materials through templates assembled on an electrode surface has a number of significant advantages. With the template approach, one is able to prepare mono-disperse rods and tubules of controlled diameter. Electrodeposition offers the extra advantage of being able to control the length of the deposited structures by varying the deposition times. The use of the

polycarbonate membrane allows the template to be easily removed following deposition of the nanostructures by dissolution in organic solvent such as dichloromethane, without damage to the nanostructures themselves.

The overall objective of the project is to develop an electrochemical DNA biosensor for the detection of a specific DNA sequence, using electrochemically grown nanomaterials. The material synthesised in this chapter were gold:copper core:shell nanowires. The methods that are required for achieving this are explained in this chapter. Gold:copper core shell nanowires have been electrodeposited and their electrochemical and Raman properties probed. First, hollow copper nanotubes, 3.0 ± 0.5 μm long, with a uniform inner diameter of 147 ± 22 nm, were electrodeposited within the pores of a track etched polycarbonate membrane filter. Second, gold was then electrodeposited within these copper cylinders to yield the gold-copper core-shell nanowires. These core:shell nanowires had diameters of 161 ± 14 nm and lengths of 3.0 ± 1.0 μm . EDX spectroscopy confirmed the composition of the nanowires after each deposition step. The nanowires were shown to exhibit useful Raman properties due to the SERS effect of the gold core.

4.2 Results and Discussion

4.2.1 Substrate used as template for nanostructure deposition

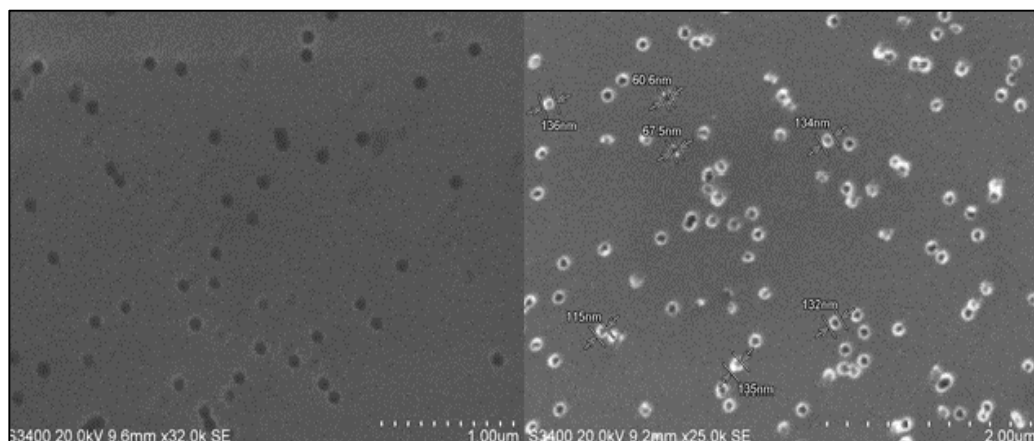


Figure 4.1: SEM images of a commercial PC membrane. A 20 nm thick gold layer has been sputtered on the membrane surface and the membrane has been mounted on a carbon tab for SEM analysis. Accelerating voltage is 20 kV.

A commercially available polycarbonate membrane (shown in Figure 4.1) was used as a template for the deposition of the nanowires. The pore size is specified as 100 nm²⁵, and SEM analysis showed the size of the pores to be 100 ± 20 nm. The pore-density according to manufacturer²⁵ is 6×10^8 pores/cm². The surface of the membrane was sputtered with a layer of gold ~ 300 nm thick to create electrical contact with the working electrode during the electrodeposition process.

Polycarbonate membrane was used as they are easily available, have high pore density, and are easy to remove after deposition of the nanostructure by dissolution in organic solvent such as dichloromethane, which causes minimal damage to the deposited nanowires.



Figure 4.2: *Image of membrane following sputter coating with a ~300 nm thick layer of gold before electrodeposition. Membrane was sputtered for 18 mins at a sputtering voltage of 2 kV and a plasma current of 20 mA. (Membrane is mounted on an aluminium stub and adhered with a carbon tab for sputtering).*

4.2.2 Galvanostatic deposition of copper

The objective of this experiment was to synthesise copper nanostructures within the pores of the polycarbonate membrane.

Examination of the literature suggested that use of a highly concentrated CuSO_4 electrolyte in acidic solution would yield single crystalline solid copper nanowires. A 0.2 M solution of CuSO_4 in 0.1 M H_2SO_4 with a pH of 3 was used as deposition solution. A wide range of deposition potentials and currents have been reported in the literature, so copper was galvanostatically deposited at +0.02A.¹⁹

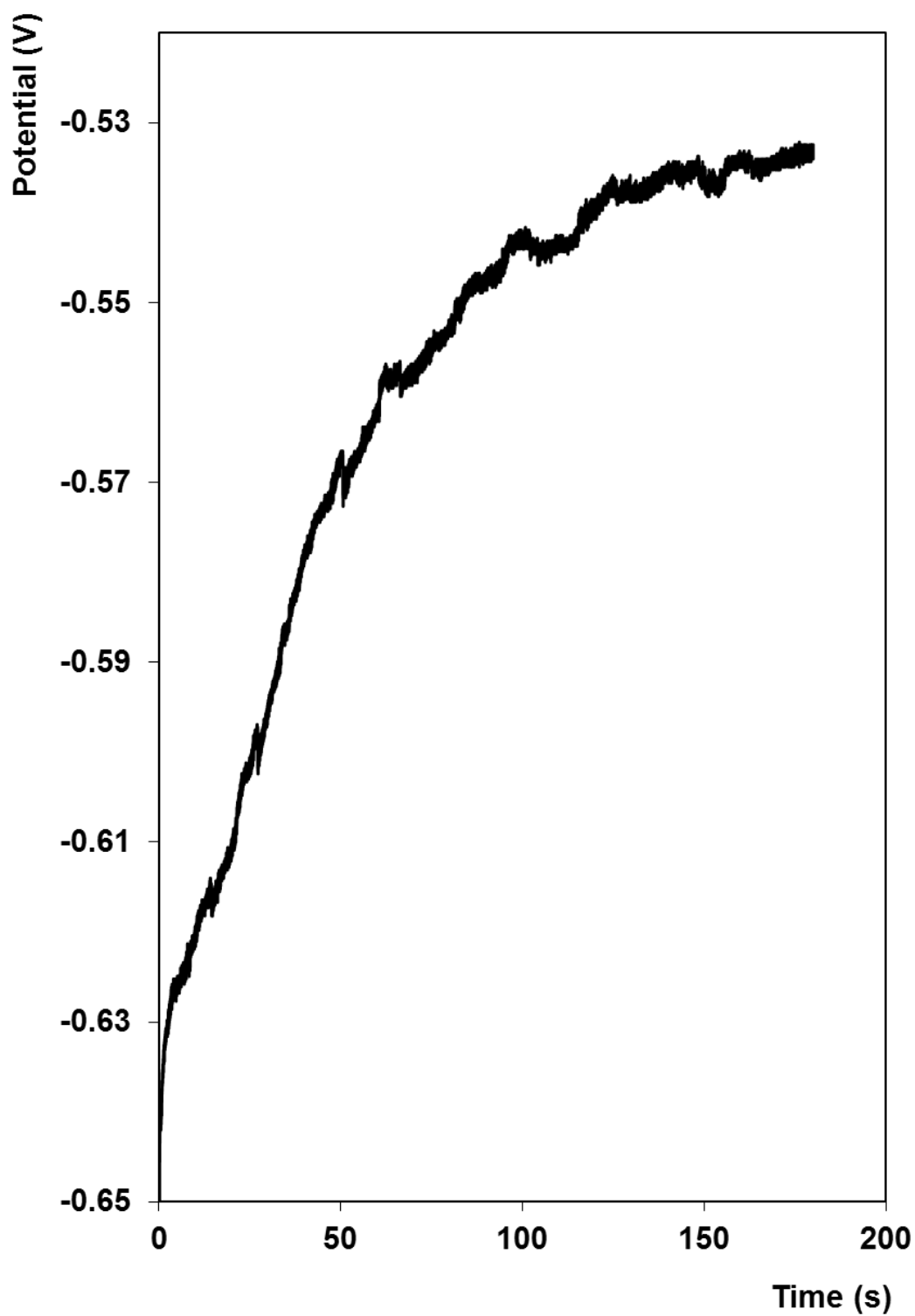


Figure 4.3: *Potential – time transient showing growth of copper nanotubes through the pores of a polycarbonate membrane mounted on FDTO glass. A fixed current of +0.02 A vs. Ag/AgCl in 3 M KCl was applied for 180 seconds.*

Figure 4.3 shows the potential-time transient of the deposition of copper nanotubes through the pores of the polycarbonate membrane. As the current is fixed in this deposition process, the potential varies, going from more negative to less negative as the copper is deposited. When a constant current is applied to the system, the current is used for (1) charging the double layer capacitance up to the potential at which the electrode reaction can proceed with a measureable rate, and (2) electrode reaction.²⁰ The steady current applied to the electrode causes the CuSO₄ to be reduced at a constant rate. The potential of the electrode moves to values characteristic of the couple, and varies with time as the Cu²⁺/CuSO₄ concentration changes at the electrode surface. Eventually, diffusion can no longer supply enough CuSO₄ to provide the required current and the potential should shift toward more negative values until a new, second reduction process can begin.³⁷ As this feature is not observed in this deposition, it is inferred that the concentration of Cu ions at the electrode surface has not been depleted, and the applied current can still be maintained.

Since the electrodeposition of copper from CuSO₄-H₂SO₄ solutions involves two electron transfers, two chronopotentiometric waves might be expected, one for each charge transfer. However, since Cu⁺ is much more easily reduced than Cu²⁺ in CuSO₄-H₂SO₄ solutions, only one wave (corresponding to the overall two-electron transfer) is observed, as indicated in Figure 4.3. This indicates that the process is irreversible.^{21, 22}

The mass of copper deposited was calculated using Faraday's law:

$$\text{Mass of deposited gold} = \frac{1}{F} \times \frac{Q \cdot M}{n} \quad \text{Equation 4.1}$$

Where F is Faradays constant (96485 Cmol⁻¹), Q is the charge passed (C), M is the molecular weight of Cu (gmol⁻¹) and n is the number of electrons passed (in this case, 2). Q is 3.6 C. (0.02 A x 180 seconds = 3.6 C)

So the previous equation becomes:

$$m = \frac{1}{96485 \text{ C/mol}} \times \frac{3.6 \text{ C} \times 63.5 \text{ g/mol}}{2} = 1.185 \times 10^{-3} \text{ g of copper deposited}$$

This equates to 1.865×10^{-5} moles of Cu deposited onto the entire electrode surface in this deposition time. Within the membrane, this equates to 6.014×10^{-15} moles of copper deposited as nanostructures.

$$\text{Pore density of membrane} = 1.27 \times 10^{10} \text{ pores/cm}^2$$

$$\text{Area of membrane} = 1.33 \text{ cm}^2$$

$$\text{Moles of copper deposited} = 6.045 \times 10^{-15} \text{ moles}$$

$$1.27 \times 10^{10} \text{ cm}^{-2} \times 1.33 \text{ cm}^2 \times 6.045 \times 10^{-15} \text{ mol} \times 96485 \text{ C/mol}$$

$$= 9.87 \text{ C required to fill the entire pore length}$$

The 3.6 C passed during the deposition implies that the formed nanostructures will be shorter than the 25 μm thickness of the membrane.

The formed copper nanostructures were analysed using SEM in order to determine their morphology and dimensions.

4.2.3 SEM analysis following copper deposition

SEM was used to determine whether the structures formed were hollow nanotubes or solid nanowires, and to determine an approximate length and diameter.

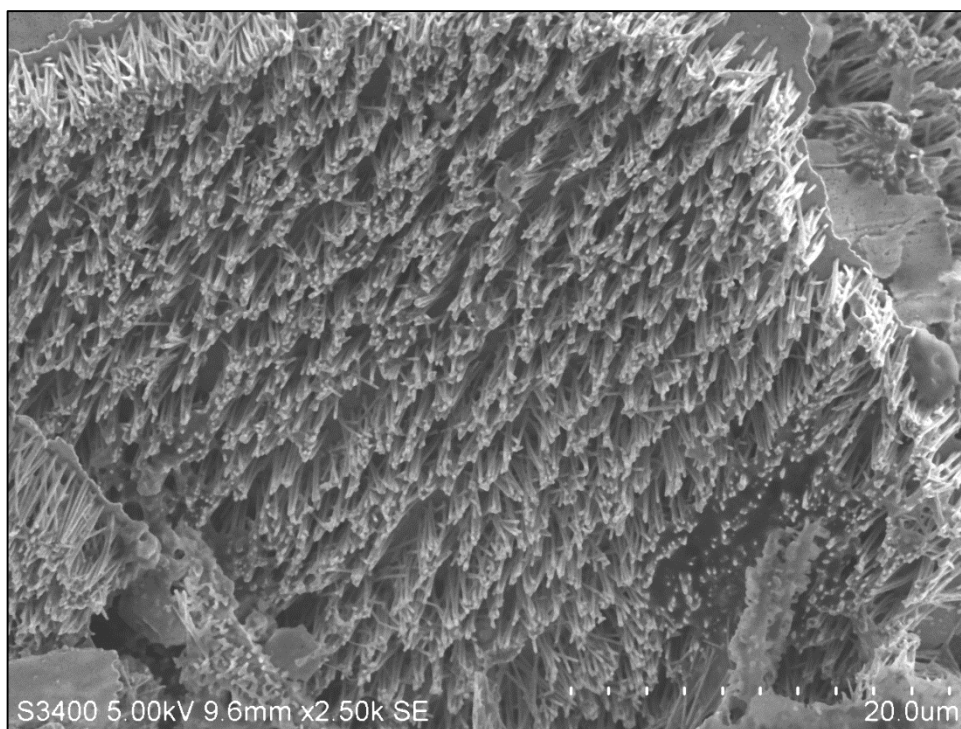


Figure 4.4: *SEM analysis of deposited nanostructures following deposition of copper for 3minutes; the polycarbonate membrane was dissolved in dichloromethane. This solution was not sonicated, but centrifuged for 60 seconds before 20 μ L was dropcast onto carbon tab for analysis.*

As this suspension was not sonicated, the sputtered gold layer is still mostly intact, and, as can be seen, the nanotubes are protruding from this sputtered gold primer layer.



Figure 4.5: SEM analysis of 20 μL drop cast Cu nanotubes placed on carbon tab for analysis (after dissolution of the membrane in dichloromethane, and sonication to remove PC membrane and sputtered gold layer)

Figure 4.5 above shows an SEM micrograph of dropcast copper nanotubes after removal of the polycarbonate membrane and suspension in dichloromethane. The solution was then sonicated for ten minutes. The hollow nature of the tubes is observed on the objects that are marked with red arrows.

SEM analysis of these deposits revealed that some hollow nanotubes were formed. There are several hypothesised reasons for this. During the deposition of the conductive gold layer onto the polycarbonate membrane, the metal diffuses into the pore walls, which leads to preferential electrodeposition of metal on the walls, which forms tubes instead of solid wires.²³ It is also hypothesised that hydrogen gas evolution from the surface of the working electrode during deposition could also be responsible for the formation of hollow tubes rather than solid nanowires. A suggested mechanism for this is that for horizontally positioned membranes, the generated hydrogen gas finds a path from the growing electrode surface through the pore centre to the pore mouth, and subsequently blocks the deposition in its path, and shields the centre of the nanopore.²⁴

While the resolution of these images could be improved, there are several hollow structures observed in the sample. Higher resolution imaging of the formed structures was performed and is shown in Figure 4.11.

SEM characterisation showed that the diameters of the nanotubes are 147 nm (± 22 nm), which implies that the pore size of the membrane increased slightly ($\sim 30\%$) as the copper tubes were deposited. Some reasons for this are discussed later in the chapter.

The length of the hollow copper nanotubes is approx. 3.2 ± 0.1 μm , from SEM micrographs obtained. According to the manufacturer specifications, the thickness of the polycarbonate membranes was $25 \mu\text{m}^{25}$, so a length of 3 μm wire would indicate that the metal deposition did not fill the entire pore length, and that longer deposition times would likely give longer nanotubes.

The charge required to fill the length of the membranes is 9.87 C, which would correspond to a wire length of 25 μm . The total charge passed in the Cu deposition is 3.6 C, which is 36% of the charge needed to fill the membrane. Based on passing 36% of the charge needed to fill the pores, and assuming 100% Faradaic efficiency, the Cu nanotubes should be ~ 9 μm long. The shorter length of the nanotubes may be due to a number of reasons:

1. Faradaic efficiency is less than 100%
2. Not all of the pores are filled during the deposition process
3. The pores are filled non-uniformly during deposition

A simple pre-electrodeposition pore-wetting step can help to control whether electrodeposition occurs in all of the pores at the same time. If the membrane is immersed in deionised water under ultrasonic agitation for 2 minutes before mounting to the working electrode, this step ensures homogenous growth over the whole area exposed to the electrolyte.³⁰

The length of the wires can be controlled during potentiostatic growth while monitoring the current-time transient. The transient for electrodeposition of nanowire arrays into the pores of a polycarbonate membrane can be divided into four stages.^{26,29} In stage I, the cathodic current increases immediately after $t = 0$,

then decreases abruptly before $t = 20$ s. This is defined as stage I, in which metal wires are “hatched” in the pores of the membrane. Stage II extends to approx. $t = 260$ s, in which the pores become completely filled. The current profile is mostly steady during stage II. A current increase corresponds to the transition to stage III, in which the effective surface area of the electrode increases because the electrodeposited wires emerge from the top of the membrane and growth commences over the top of the whole membrane. Finally, in stage IV, an electrodeposited film outside the top surface of the membrane is developed. All four stages are shown in Figure 4.6.

Hollow nanotubes have a potentially higher electrocatalytically active surface area than a solid nanowire. The inside of the hollow nanotube could be filled with another metal, or the inner walls could be functionalised with metal nanoparticles which are catalytically active. Having a bimetallic nanostructure could prove useful in electrochemical biosensing applications.

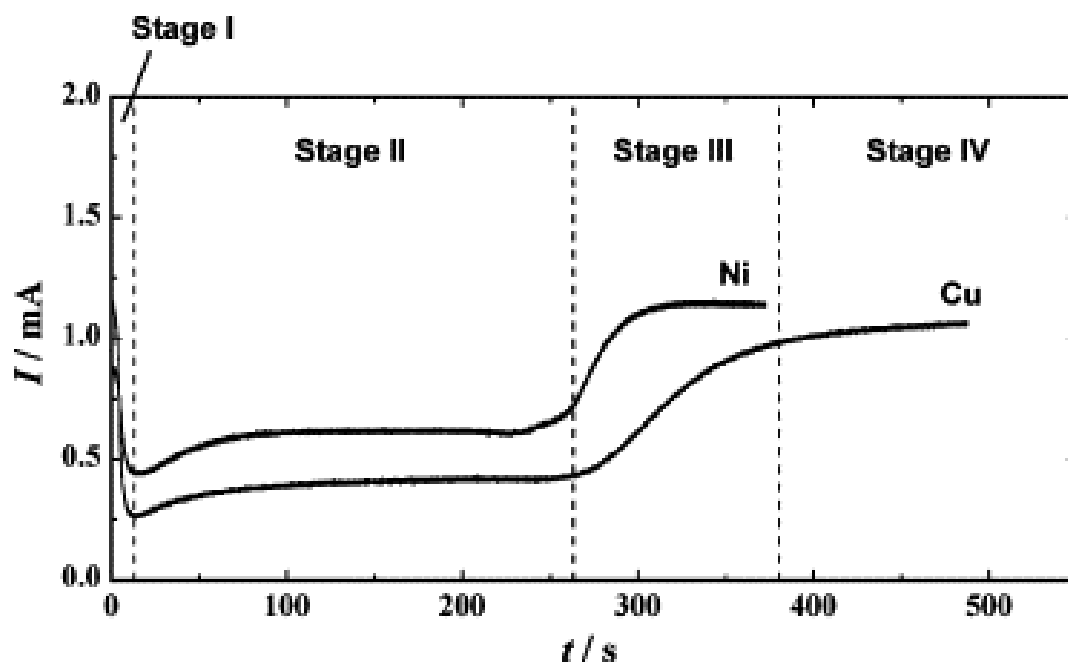


Figure 4.6: Electrochemical reduction current as a function of time t for the potentiostatic deposition of Ni and Cu in pores of polycarbonate membrane. Pore size: 200nm; deposition solution: $0.60 \text{ mol L}^{-1} \text{ CuSO}_4$, $5 \times 10^{-3} \text{ mol L}^{-1} \text{ H}_2\text{SO}_4$; deposition method: potentiostatic, potential not quoted. The schematics display three different stages of growth process: Stage I: metal wires grow in the pores; Stage II: the pores are completely filled; Stage III: growth commences over the whole membrane surface; Stage IV: an electrodeposited film of metal outside the membrane surface is further developed. Figure reproduced from M. Motoyama, Y. Fukunaka, T. Sakka and Y. H. Ogata, *Electrochim. Acta*, 2007, **53**, 205-212]

4.2.4 Potentiostatic deposition of gold

Following deposition of copper, gold was electrochemically deposited from a 30 mM solution of HAuCl_4 made up in 0.1M KCl at a potential of -0.273 V vs. Ag/AgCl in 3 M KCl for 3 minutes^{27, 28}.

Figure 3 shows the current-time transient of for the deposition of gold (following deposition of copper) under potentiostatic conditions.

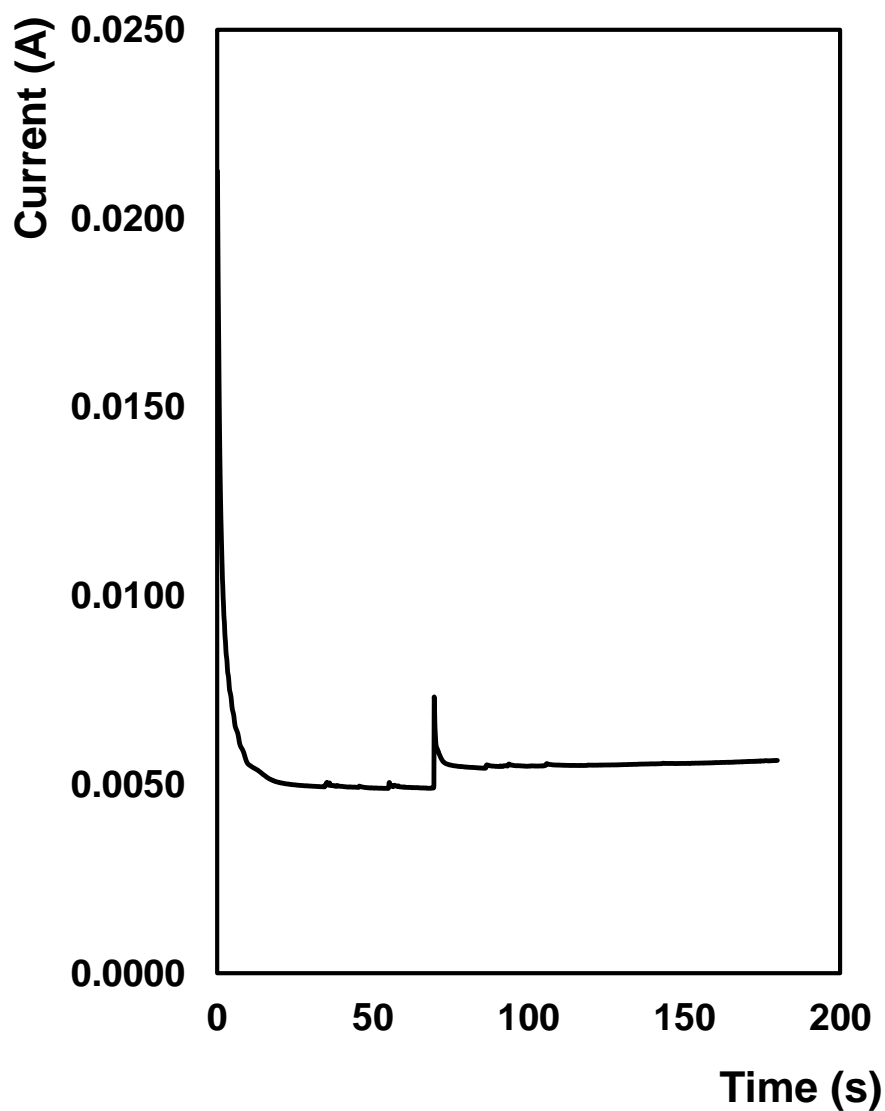


Figure 4.7: Current-time transient for growth of gold nanowires through a porous polycarbonate membrane mounted on FDTO following previous deposition of copper in the same membrane. The potential applied was -0.273 V vs. Ag/AgCl in 3 M KCl for 180 seconds.

Figure 4.7 shows the current-time transient for the deposition of gold nanowires through the pores of a polycarbonate membrane. The first region is a current spike immediately at the beginning of the transient which quickly depletes once nucleation of the metal ions immediately at the electrode surface occurs. The second region is the decay of the current to slightly decreasing, which corresponds to the gold depositing into the pores. At approximately 75s a small current spike occurs in the transient, which then decays rapidly and the current returns to a steady state, although the current is now higher than it was before the spike. Generally, a current spike such as this would be characteristic of the metal deposition having reached the top of the pore walls, and the beginning of hemispherical “cap” deposition on the top of the wires. However, no evidence of this was found during SEM analysis, and this sort of cap growth would generally occur after much longer deposition times. The current increase would generally be much larger than the spike observed in Figure 4.7. SEM analysis of the copper wires revealed that their lengths are approximately $3.0 \pm 0.1 \mu\text{m}$, which is much shorter than the length of the pore itself, which is $\sim 25 \mu\text{m}$ according to the manufacturer.

The cause of this current spike is unknown, as it does not seem to be related to any reactions pertaining to the deposition of the metal within the pores.

Generally, the recorded I-t curve during Au deposition reveals four different stages: 1) initially, the current decreases due to a limited mass transport. 2) The metal film grows in the pores and a slight increase in current is observed as the distance to the pore opening becomes smaller. If the deposition time were increased, the transient would show the current increasing until 3) the pores are filled to the top, and at the membrane surface cap formation associated with three-dimensional deposition is observed. Thereafter, 4) the hemispheric caps originating from each nanowire form a coherent, planar layer that expands until it covers the entire surface of the membrane. Thus, the effective cathode area increases and a rapid increase of the deposition current can be observed.

By observing the current-time transient during electrodeposition, the growth of the nanowires can be stopped at the desired stage, resulting in nanowires that are shorter than the thickness of the membrane template, nanowires that have

hemispherical “caps” on top, or nanowires that have a uniform film covering their entire surface.

In this case, as only two stages are shown in the transient, it can be assumed that the wires deposited will be shorter than the thickness of the membrane, and will have no hemispherical caps. This was confirmed by SEM analysis of the deposited wires.

This can also be determined by monitoring the charge passed during deposition of the metal. As previously calculated, a charge of 9.6 C would be required to deposit wires that would fill the entire length of the pore. As seen in Figure 4.8, the charge passed during the deposition of the gold nanowires is 9.985×10^{-1} C, which is much less than that required to fill the pores. Thus, it is expected that the lengths of the nanostructures formed will be less than the 25 μm membrane thickness.

4.2.5 Mass of deposited gold

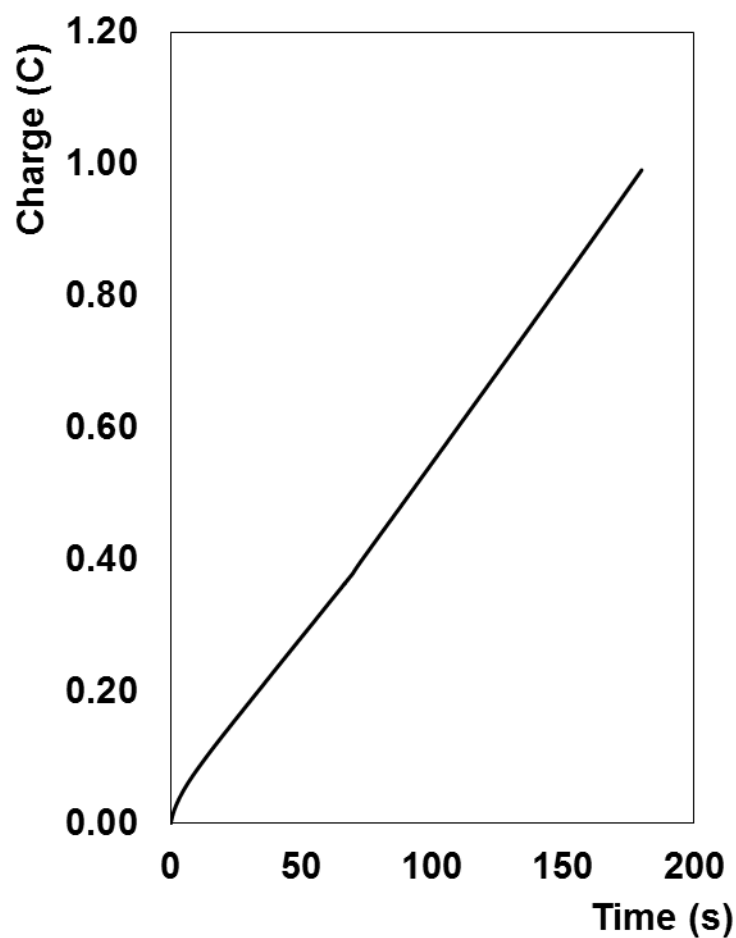


Figure 4.8: *The integrated curve of the current vs. time transient to provide information on the charge passed during Au deposition. The charge passed was 9.985×10^{-1} C.*

The mass of gold was calculated from Faraday's Law, Equation 3.1.

From Figure 4.8, the total charge transferred, Q is 9.985×10^{-1} C;

So the equation becomes:

$$m = \frac{1}{96485 \text{ C/mol}} \times \frac{9.985 \times 10^{-1} \text{ C} \times 196 \text{ g/mol}}{3} = 6.761 \times 10^{-4} \text{ g of gold deposited.}$$

According to the above calculations, there was less gold deposited than copper. These results may seem to correlate with the FE-SEM images (Figure 4.12) which show some nanotubes not completely filled following Au deposition, and with the current-time transient, which does not show the sharp increase in current characteristic of the filling and capping of pores during the deposition process.

4.2.6 SEM analysis following gold deposition

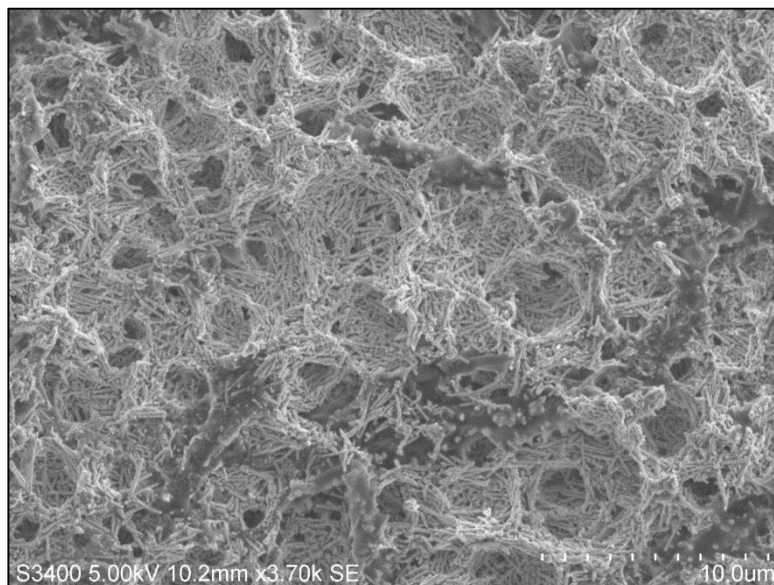


Figure 4.9: SEM image of Au:Cu nanowires dropcast from suspension onto a carbon tab for analysis. (After dissolution of the membrane in dichloromethane, and sonication to remove PC membrane and sputtered gold layer). Accelerating voltage is 5 kV.

Figure 4.9 shows a sample of nanowires in which gold has been electrodeposited at a potential of -0.273 V vs. Ag/AgCl in 3 M KCl for 3 minutes, following copper deposition through the pores of the polycarbonate membrane.



Figure 4.10: SEM images of *Cu:Au nanowires from suspension, dropcast onto a carbon tab. (Following dissolution of the membrane in dichloromethane, and sonication to remove PC membrane and sputtered gold layer). The accelerating voltage was 5kV.*

The average diameters and lengths of the core:shell nanowires are about $161 \text{ nm} \pm 14 \text{ nm}$ and $3 \text{ } \mu\text{m} \pm 0.1 \text{ } \mu\text{m}$, respectively. The measured diameter of the obtained solid nanowires is larger than the pore diameter of polycarbonate membrane, ($100 \text{ nm} \pm 20 \text{ nm}$), and approx. 8% larger than that of the hollow copper nanotubes ($147 \text{ nm} \pm 22 \text{ nm}$) however the wire length remains largely consistent with the lengths of the wires following Cu deposition only. This is interesting as it implies that the gold deposited has not filled the pores of the polycarbonate membrane above where the copper deposition ended, but have instead deposited inside the hollow walls of the copper tubes, creating solid nanowires composed of a copper shell and a gold core, rather than a “striped” nanotube/wire consisting of half copper and half gold. This increase in nanowire diameter is evidence of the pore widening process occurring during the deposition of nanowires.²⁹

There are two possible reasons for the increased diameter:

1. The wires may not be cylindrical, but rather wider in the middle than at the ends,
- or
2. The pores widen during growth.

This latter scenario can originate during metal deposition, if the metal not only grows strictly along the pore axis, but also to a certain degree radially, which exerts pressure on the polycarbonate membrane, causing a widening of the pores.³⁰

A study of nanowires of several metals deposited in the pores of track-etch membranes by Schönenberger et al.³⁰, discovered that the pores in the template are not the same diameter all the way through, but instead have a maximum diameter along the middle of the pore, and are narrower at the top and bottom of the pore. For several suppliers and several pore sizes, it was found that the middle section of the pore can be wider by up to a factor of three.

They have proposed that the pore widening effect is a consequence of proximity exposure. If secondary electrons are generated isotropically at each point along the ion track in the membrane, any point in the vicinity of the track, but sufficiently inside the membrane, receives exposure from secondary electrons generated above and below this point. This is different for a point close to the surface of the membrane. At the top surface, impinging secondary electrons can only originate from below this point, since the impacting ion moves through a vacuum from above. For this reason, proximity exposure is reduced by a factor of 2 close to the membrane surface. If etched, the pore will develop a smaller diameter at the top and bottom of the membrane compared to regions inside.

SEM analysis of the as synthesised core:shell nanowires was performed in order to determine an average diameter. The nanowires were measured from images, some of which had nanowires which were oriented standing up as in Figure 4.5, so that the top of the wire was measured; and some of which had nanowires which were lying flat, as in Figure 4.10, so that the diameter was measured somewhere in the middle of the wire. If the pore diameters differed between the top and middle of the membrane, this might account for the increase in diameter of the synthesised wires compared to the measured diameters of the pores. The diameters of the pores were only measured at the top of the membrane as that was all that was accessible. There are also inherent limitations in the use of SEM to determine the dimensions of these nanostructures. A more accurate representation of the nanowire lengths and diameters could have been obtained by analysing a cross section of the membrane under TEM prior to dissolution.

4.2.7 Fe-SEM analysis

As the Hitachi S3400N scanning electron microscope was not sufficiently high resolution to image the inner diameters of the hollow nanotubes, it was decided to image using an Oxford INCA high resolution field emission scanning electron microscope. The images obtained allowed the inner diameter of the hollow nanotubes to be measured and an average diameter of $58 \text{ nm} \pm 4.5 \text{ nm}$ was calculated.

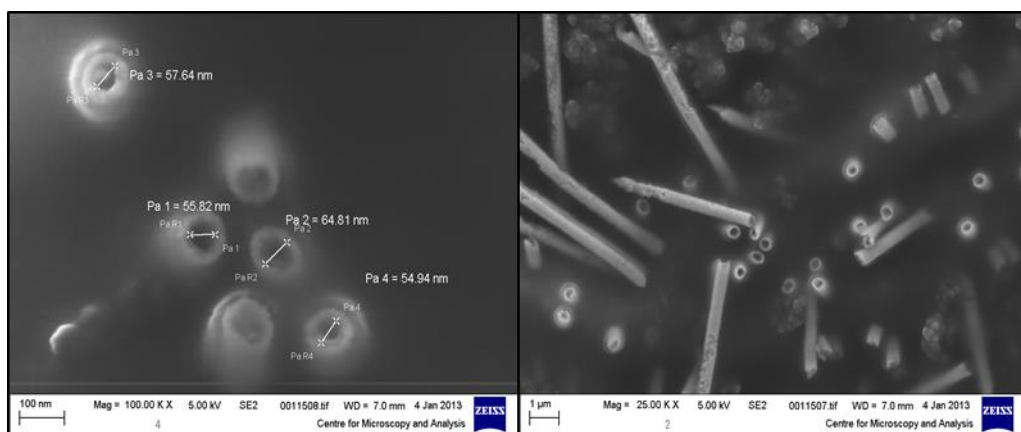


Figure 4.11: *High resolution images of hollow copper nanotubes following release from the polycarbonate membrane, suspension in dichloromethane and dropcasting onto planar gold slides. Inner diameter was shown to be $58 \text{ nm} \pm 4.5 \text{ nm}$. Accelerating voltage was 5 kV. (Imaged by Dr Elaine Spain)*

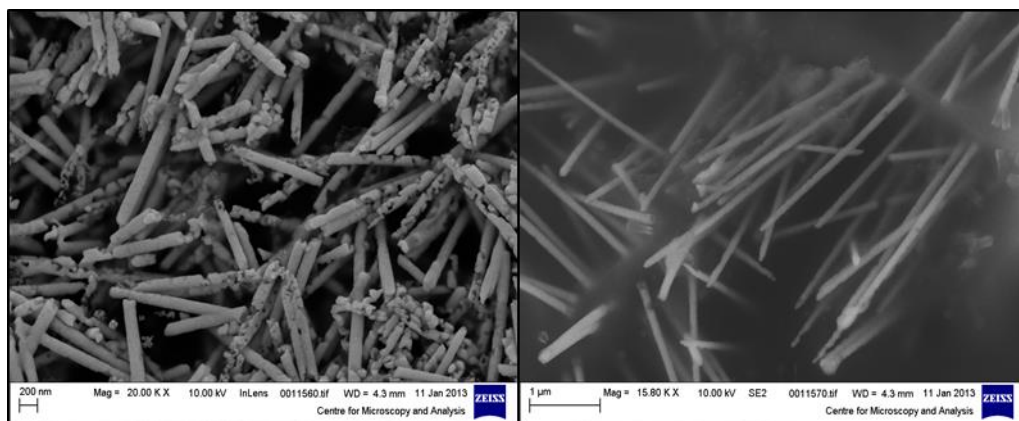


Figure 4.12: *High resolution image of gold:copper core:shell nanotubes following release from membrane, suspension and dropcasting. Accelerating voltage was 10 kV. (Imaged by Dr Elaine Spain)*

Figure 4.12 above shows the high resolution SEM image of the solid gold:copper core:shell nanowires after both metals have been deposited and the wires have been released from the membrane. These wires are shown to be mostly solid, as opposed to the hollow copper tubes seen in Figure 4.11. This confirms the theory that the gold was deposited inside the hollow copper walls of the tubules, and not inside the sputtered walls of the polycarbonate membrane not filled with copper tubules. From the current-time transient, Figure 4.7, it can be seen that the current decreases sharply at the beginning of the process, attributed to the creation of the depletion layer, followed by growth inside the channels with almost constant growth rate. If the material were to reach the top of the membrane and start to deposit caps on top, a sharp current increase would be observed for this process³¹. As this sharp increase is not observed, it is likely that the deposition of the material did completely fill the channels and begin to deposit caps along the top. This also makes it likely that not all of the nanotubes were completely filled with gold.

4.2.8 EDX spectroscopy

EDX spectroscopy was used to confirm the presence of the copper in a 500 μL sample of the nanotubes and both copper and gold in a 500 μL sample of the core:shell nanowires.

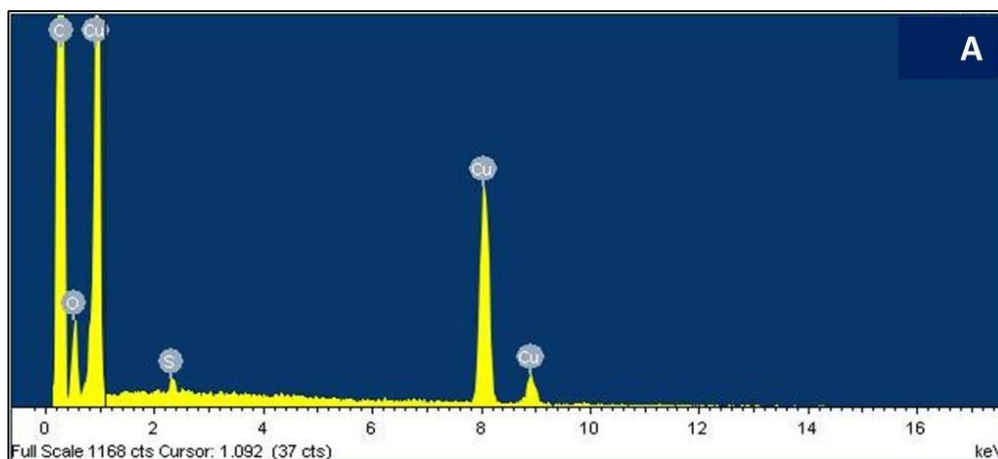


Figure 4.13: *EDX spectrum of hollow Cu nanotubes following release from the polycarbonate membrane, suspension in dichloromethane, and dropcasting onto carbon tabs for analysis. The spot size used was 100 nm. (Spectrum acquired by Dr Elaine Spain)*

Energy dispersive X-ray (EDX) analysis was performed along the length of an individual copper nanotube (A) following complete dissolution of PC template, suspension and drop casting on to carbon tabs. The EDX reveals Cu with high purity (95 at.% weight).

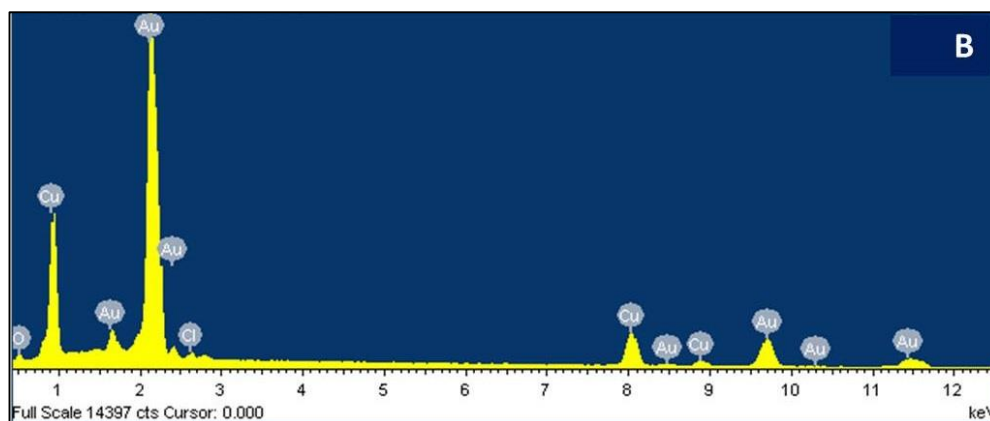


Figure 4.14: *EDX Spectrum of Au:Cu nanowires following release from the polycarbonate membrane, suspension in dichloromethane, and dropcasting onto carbon tabs for analysis. The spectrum was acquired from the length of the nanowire. The spot size used was 300 nm.(Spectrum acquired by Dr Elaine Spain)*

Figure 4.14 illustrates an EDX spectrum of the top end of the gold-copper core-shell nanowires. The EDX spectrum exhibits a strong peak corresponding to elemental gold (77 at.% weight), confirming the nature of the core of the metallic wires present, while other weak peaks of Cu (4.6 % weight) observed are attributed to of the copper shell of the wire.

4.2.9 Cyclic Voltammetry

Figure 4.15 illustrates cyclic voltammograms for the 1 cm × 1 cm FDTO electrode with a bare polycarbonate membrane, and before and after deposition of the copper nanotubes array within the pores of a PC membrane on FDTO, in a deoxygenated 0.1 M H₂SO₄ solution at a scan rate of 100 mVs⁻¹. Typically, oxide films on copper are composed of both cuprous oxide (Cu₂O) and/or cupric oxide (CuO).^{32,33} After the deposition of copper, (dotted line) a well-defined redox couple was obtained with a cathodic peak and anodic peak at -0.377 V and 0.235 V vs. Ag/AgCl in 3 M KCl, respectively. According to earlier literature reports, these redox peaks are attributed to the formation of CuO.³² The oxidation peak is due to the formation of Cu oxide overlayer and the peak at -0.377 V is its subsequent reduction.

The solid line voltammogram in Figure 4.15 illustrates the cyclic voltammogram following gold deposition through the hollow copper tubes, and shows a well resolved cathodic peak at 0.151 V representing the reduction of gold oxide.³⁴ The voltammetric currents measured in the anodic region are significantly higher after the deposition of gold, indicating a convolution from the copper and gold oxide formation. Moreover, the copper reduction peak is shifted +0.1685 V after the electrodeposition of Au. This positive shift may be due to the fact that it is harder to form the oxide on the copper in the presence of Au, suggesting a lower electron density of Cu in the presence of Au.

Another explanation for this redox shift is due to the IR drop. The IR drop is the voltage drop across the cell during passage of current due to the internal resistance of the cell.³⁵ The major effects of IR drop in cyclic voltammetry include shift in peak potential, decrease in magnitude of current, and increase in peak separation.³⁶ The IR drop can be minimised by using a three-electrode system (as was used in this work). The reference electrode tip should be in close proximity to the working electrode surface. In the three electrode set up, the working electrode and the reference electrode are positioned beside each other, with the counter electrode on the other side of the reference electrode.

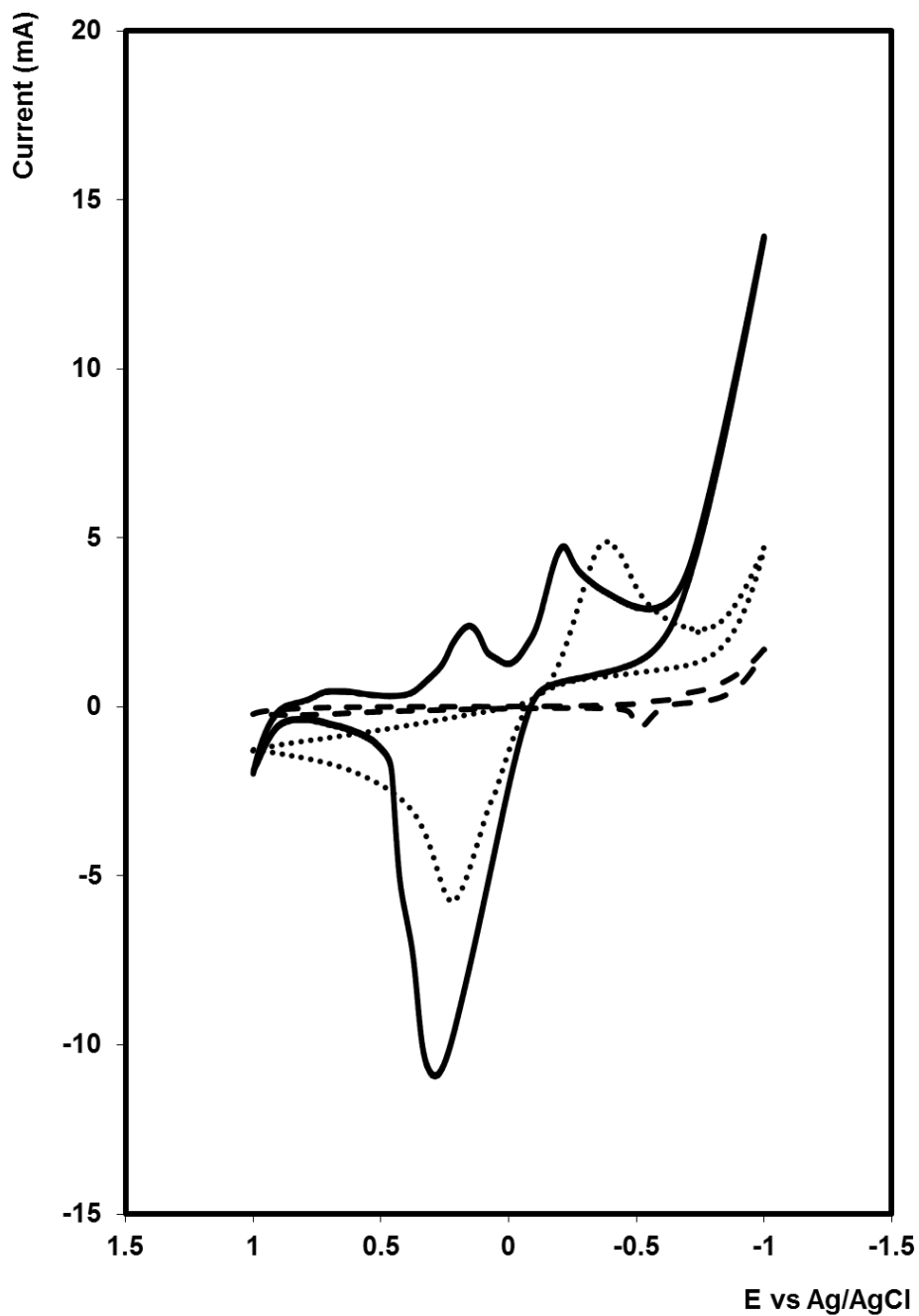


Figure 4.15: Cyclic voltammogram of a 1 cm^2 FDTO electrode modified with a PC template decorated with a conductive 300 nm Au back layer (dashed line), after electrodeposition of the copper (dotted line), and after deposition of the gold (solid line). The supporting electrolyte is 0.1 M H_2SO_4 and the scan rate is 100 mV s^{-1} . The reference electrode is Ag/AgCl in 3 M KCl. The sixth scan is presented.

The nanotubes were released from the PC membrane and suspended in a solution of dichloromethane. The nanotubes were then dropcast on a bare gold electrode and fixed with 2.5 % glutaraldehyde, before being characterised using cyclic voltammetry.

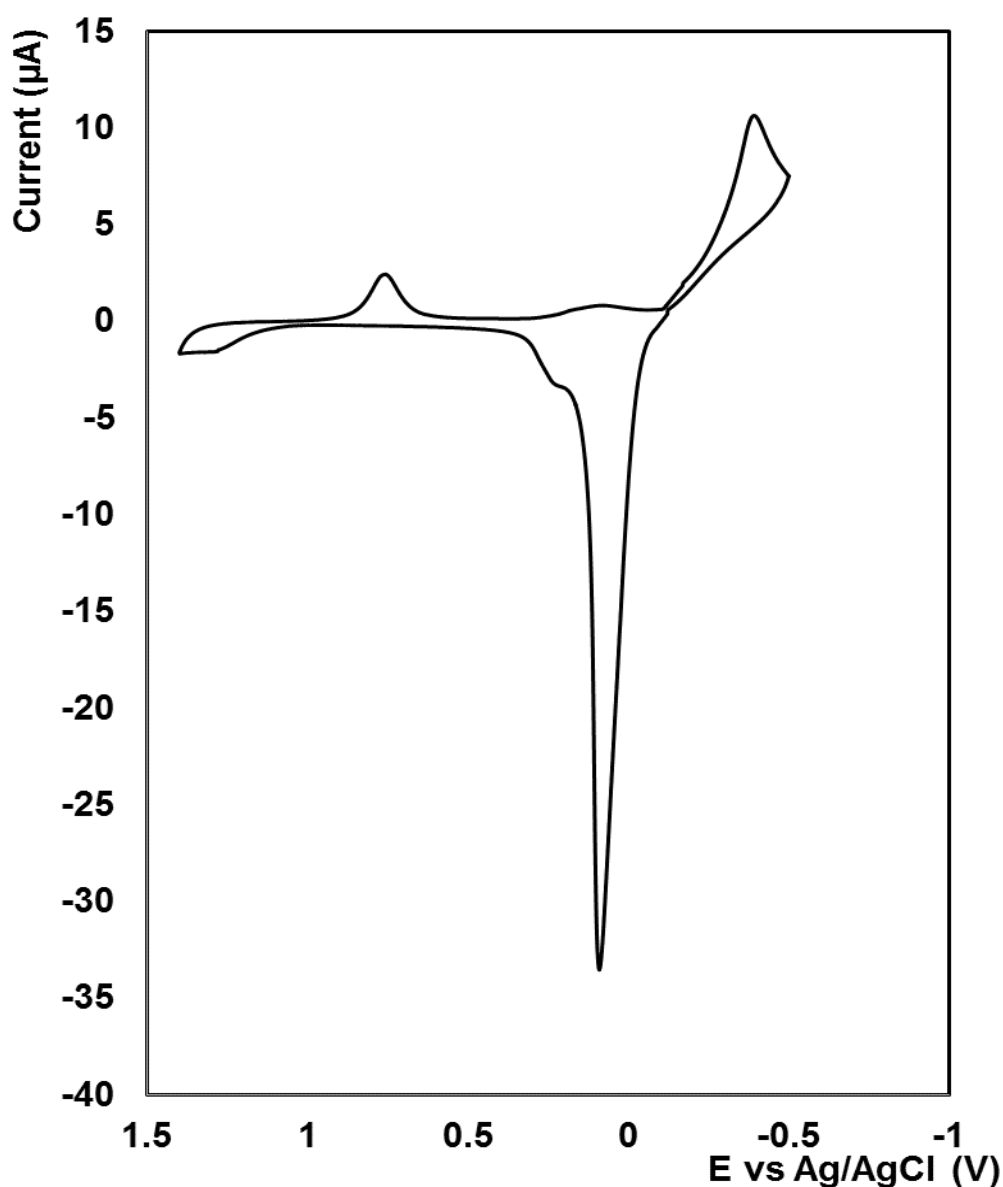


Figure 4.16: *Au electrode modified with hollow Cu nanotubes after removal of the polycarbonate membrane and suspension in dichloromethane. The nanowires are then dropcast onto the bare 2 mm diameter electrode surface and fixed with 2.5 % glutaraldehyde. The supporting electrolyte is 0.1 M H₂SO₄ and the scan rate is 100 mV s⁻¹. The reference electrode is Ag/AgCl in 3 M KCl. The sixth scan is presented.*

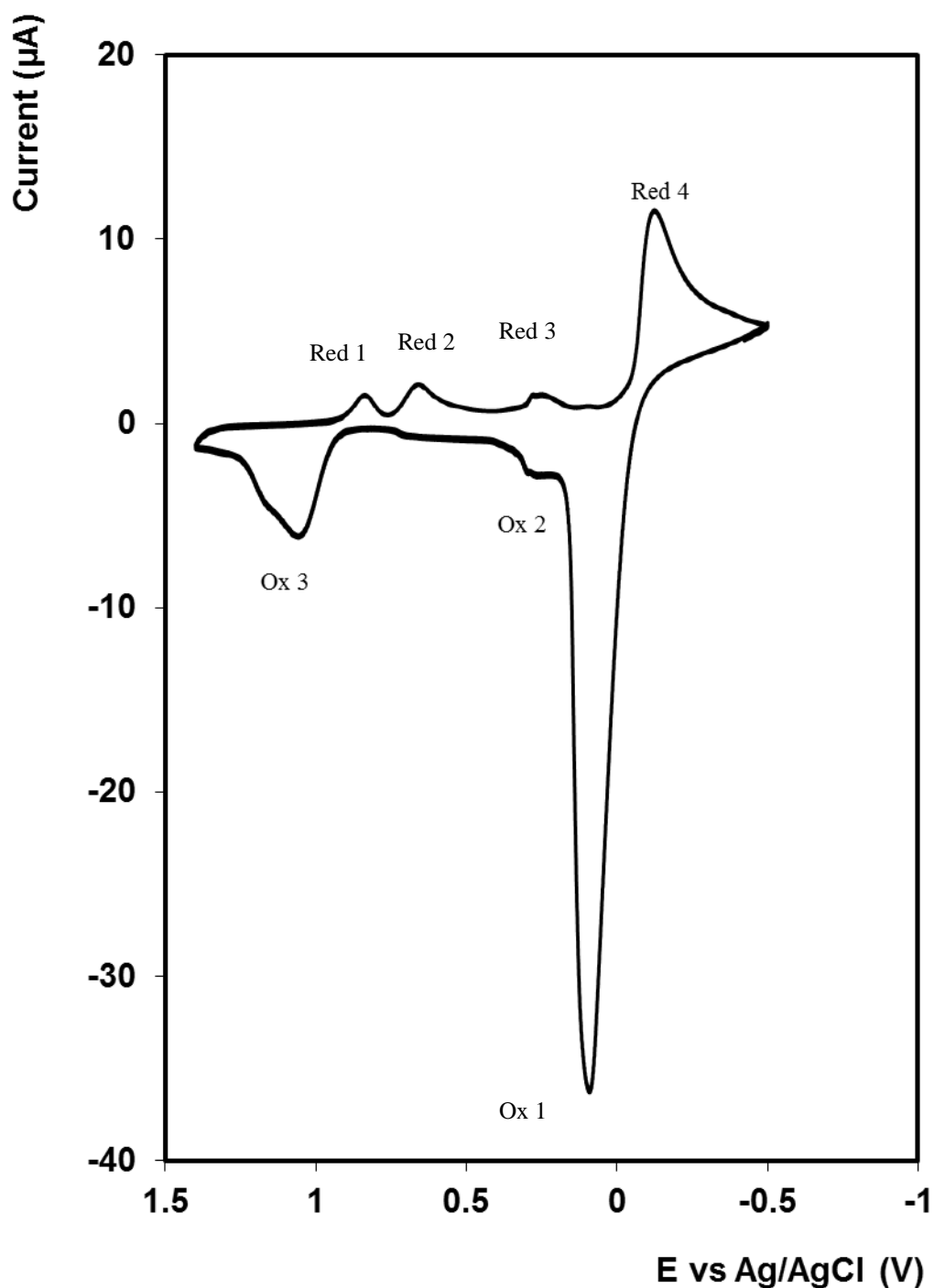


Figure 4.17: *Au electrode modified with Au:Cu core:shell nanowires after removal of the polycarbonate membrane and suspension in dichloromethane. The nanowires are then dropcast onto the bare 2 mm diameter electrode surface and fixed with 2.5 % glutaraldehyde. The supporting electrolyte is 0.1 M H₂SO₄ and the scan rate is 100 mV s⁻¹. The reference electrode is Ag/AgCl in 3 M KCl. The sixth scan is presented.*

Figure 4.16 illustrates the cyclic voltammogram of the copper nanotubes which were drop cast and allowed to dry on to a 2 mm diameter gold disc electrode and then cycled in 0.1 M H_2SO_4 from -0.5 V to 1.5 V to identify the different potentials of oxidation. Two oxidation peaks are observed at +0.095 V and +0.247 V for CuO and Cu_2O , respectively.³⁷ The peak at -0.378 V is due to the subsequent reduction of the Cu oxide. There is also a very weak peak at +0.253 V which may also correspond to reduction of Cu (II) to Cu (I). The anodic peak at +1.323 V and the reduction peak centred at approximately +0.77 V correspond to the gold oxide formation and the gold oxide reduction peak of the underlying gold disc electrode.³⁷

Figure 4.17 displays three oxidation peaks and four reduction peaks for the released gold:copper nanowires. During the positive sweep, the copper is oxidised into CuO with a well resolved peak +0.081 V. The Ox 2 peak at approximately +0.286 V might be due to the oxidation of CuO into Cu (III) to form Cu_2O_3 .³⁷ The low conductivity of this oxide results in a much smaller peak than that observed for CuO at +0.081 V (Ox 1). The oxidation peak (Ox 3) at +1.064 V represents gold oxide formation of the underlying gold disc electrode, with a small shoulder observed which could indicate oxidation of the core of the gold nanowires. In the negative sweep, the peak centred at approximately +0.84 V (Red 4) corresponds to the gold oxide reduction peak. There is a peak at +0.662 V (Red 3) which corresponds to the reduction of Cu_2O_3 (Cu III) to Cu_2O (Cu II). Further reduction of copper is perceived with a weak peak at +0.258 V (Red 2) and a sharp peak at -0.124 V (Red 1) which represent the reduction of Cu (II) to Cu (I) and Cu (I) to Cu^0 , respectively.

The ratio of the areas associated with the gold and copper oxide formation peaks is approximately 1:20 which is somewhat lower than the ratio of 1:45 expected based on the diameter and lengths of the core-shell nanowire determined from SEM. Again, this result most likely arises from incomplete copper oxide formation at this scan rate due to slow formation kinetics when the nanowires are bound within the template. Once the nanowires have been released, the gold oxide formation/reduction process occurs in two distinct processes. Gold oxide formation (on both the underlying electrode, and the core of the nanowires) occurs

at a less positive potential once released, while the two peaks associated with reduction occur at potentials that are more and less positive than that observed prior to release. These results suggest that the thermodynamics of oxide formation/reduction are sensitive to the microenvironment.

4.2.10 Raman Spectroscopy

Surface Enhanced Raman Spectroscopy (SERS) is a Raman Spectroscopic (RS) technique that provides greatly enhanced Raman signal from Raman-active analyte molecules that have been adsorbed onto nanostructured metal surfaces. Increases in the intensity of Raman signal have been regularly observed on the order of 10^4 - 10^6 , and can be as high as 10^8 and 10^{14} for some systems.^{38, 39} The importance of SERS is that it is both surface selective and highly sensitive whereas RS is neither. RS is ineffective for surface studies because the photons of the incident laser light simply propagate through the bulk and the signal from the bulk overwhelms any Raman signal from the analytes at the surface. SERS selectivity of surface signal results from the presence of surface enhancement (SE) mechanisms only at the surface. Thus, the surface signal overwhelms the bulk signal, making bulk subtraction unnecessary.

The exact mechanism of the enhancement effect of SERS is still a matter of debate in the literature. There are two primary theories, electromagnetic theory and charge-transfer theory. The electromagnetic theory proposes the excitation of localised surface plasmons, while the chemical theory proposes the formation of charge-transfer complexes. The chemical theory applies only for species that have formed a chemical bond with the surface, so it cannot explain the observed signal enhancement in all cases, whereas the electromagnetic theory can apply even in those cases where the specimen is physisorbed only to the surface.

Electromagnetic theory: The increase in intensity of the Raman signal for adsorbates on particular surfaces occurs because of an enhancement in the electric field provided by the surface. When the incident light in the experiment strikes the surface, localised surface plasmons are excited. In order for scattering to occur, the plasmon oscillations must be perpendicular to the surface; if they are in-plane with the surface, no scattering will occur. It is because of this requirement that roughened surfaces or arrangements of nanoparticles are typically employed in SERS experiments as these surfaces provide an area on which these localized collective oscillations can occur.⁴⁰

The choice of surface metal is also dictated by the plasmon resonance frequency. Visible and near-infrared radiation (NIR) are used to excite Raman modes. Silver and gold are typical metals for SERS experiments because their plasmon resonance frequencies fall within these wavelength ranges, providing maximal enhancement for visible and NIR light. Copper's absorption spectrum also falls within the range acceptable for SERS experiments.⁴¹ Platinum and palladium nanostructures also display plasmon resonance within visible and NIR frequencies.⁴²

Chemical theory: While the electromagnetic theory of enhancement can be applied regardless of the molecule being studied, it does not fully explain the magnitude of the enhancement observed in many systems. For many molecules, often those with a lone pair of electrons, in which the molecules can bond to the surface, a different enhancement mechanism that does not involve surface plasmons has been described. This chemical mechanism involves charge transfer between the chemisorbed species and the metal surface. The chemical mechanism only applies in specific cases and probably occurs in concert with the electromagnetic mechanism.^{43, 44}

During the late 1970's and early 1980's it was recognised that a few noble metals, mainly Ag, Au, and Cu, would provide a large SERS enhancement, provided the metal surface roughness or colloid size were of the order of a few tens of nanometres. In the 1980's, a strategy based on "borrowing SERS" was proposed, either by depositing SERS-active metals on non SERS-active substrates, or by depositing non-SERS active materials over SERS-active substrates.

The approach of "borrowing SERS activity" was first proposed by Van Duyne et al. in 1983 to obtain Raman signals of molecular species adsorbed on non-SERS-active materials such as n-GaAs electrodes through electrodepositing a discontinuous SERS-active overlayer of Ag.⁴⁵ This approach is to employ the long-range effect of the strong electromagnetic field created by the SERS-active Ag to enhance the Raman scattering of adsorbates at the semiconductor nearby. This configuration has a limitation for studying surface-adsorption, which requires that the surface species can be adsorbed at the non-SERS-active substrate, but it has been shown that most molecules prefer to adsorb at the SERS-active sites.

The most effective and feasible way to borrow SERS activity is to coat with an ultrathin film of other materials completely on SERS-active substrates of Ag, as done by the Fleischmann group,^{46,47} and on Au, by the Weaver group.^{48,49} The essential notion rests on the expectation from electromagnetic theories that the enhancement effect should occur for molecules located close to (within 1-10 nm) SERS-active nanoparticles, or nanostructured surfaces.^{50,51} With the aid of the long range effect of the enormous electromagnetic enhancement created by the high SERS-active substrate underneath, the Raman enhancement can be engendered even for molecules spatially separated from the substrate.⁵²

The strong electromagnetic field will be diminished exponentially with increasing film thickness, therefore the film has to be ultra-thin, normally a few atomic layers.

The copper nanotubes and core:shell nanowires were immersed in a solution of $[\text{Ru}(\text{bpy})_2(\text{Qbpy})]^{2+}$ dye for two days and drop cast onto ITO glass slides for characterisation using Raman spectroscopy. The presence of gold in the nanowires may create a SERS effect, giving rise to a higher intensity compared to the pure copper nanotubes.

The lone pair in the nitrogen atoms in the pyridine groups gives a strong bond between the Au core and the dye molecules, as opposed to the copper shell.⁵³ Coupled with the SERS effect due to the gold, there should be a significant enhancement of the Ru dye modes when bound to the core:shell nanowires compared to their intensity when bound to the hollow copper nanotubes. The Raman spectra of both are shown in Figure 4.18.

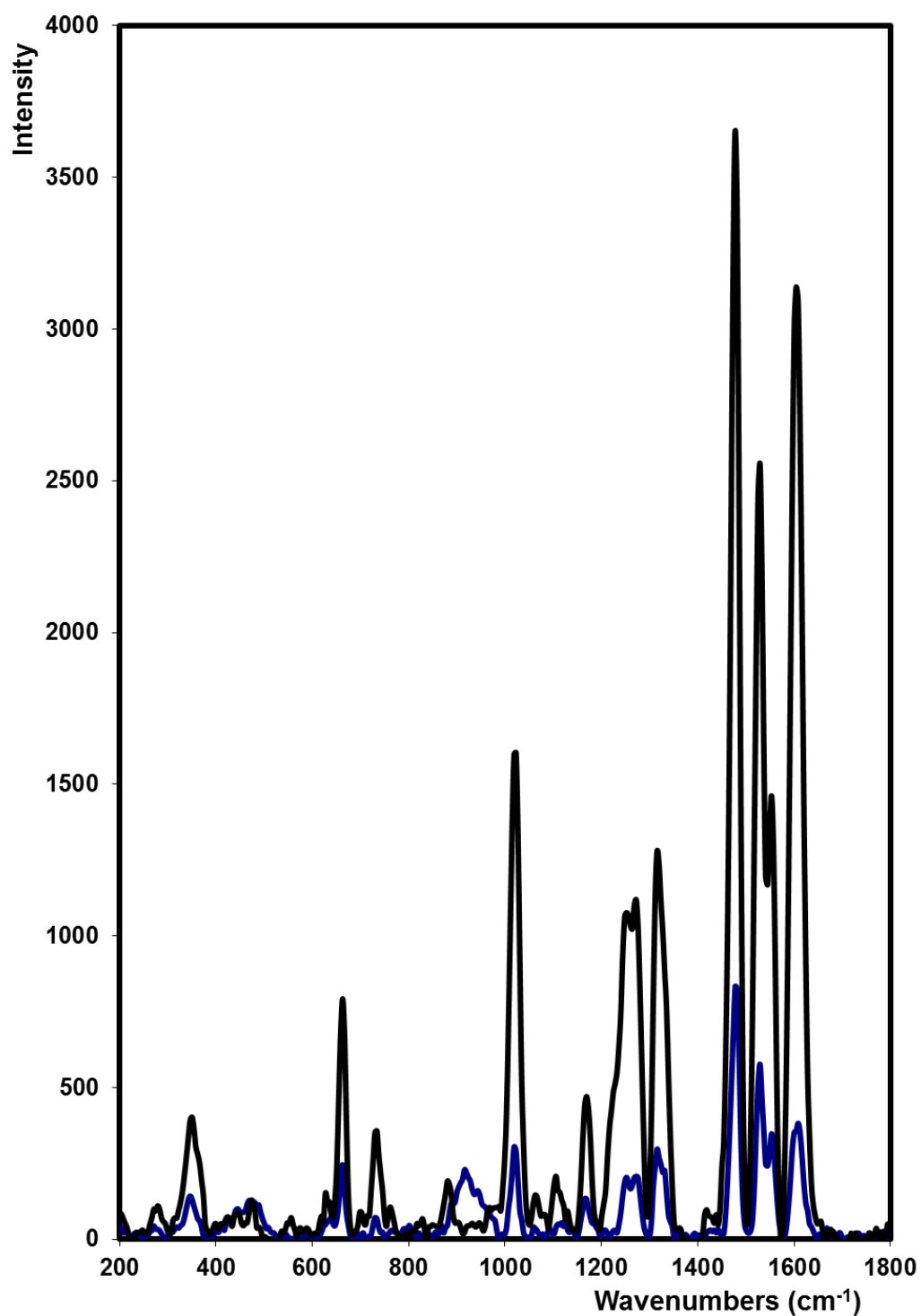


Figure 4.18: Raman spectra of the copper nanotube array (blue) and the Cu:Au core:shell nanowire array (black). The excitation wavelength was 488 nm. The nanowires were immersed in a 1 μ M solution of $[\text{Ru}(\text{bpy})_2(\text{Qbpy})]^{2+}$ dye dissolved in 40:60 ethanol and DI H_2O for 2 days and dropcast onto planar ITO glass for Raman analysis.

In the spectrum of the hollow Cu nanotubes, three peaks located at around 279, 346, 650 cm^{-1} are observed. Both the weak peak at 279 cm^{-1} and the strong peak at 346 cm^{-1} are ascribed to CuO, indicating the formation of an oxide on the surface.⁵⁴ The peak centred at 650 cm^{-1} is believed to be contributed by several Cu_2O related sub-peaks such as 590, 631 and 658 cm^{-1} .^{54, 55} An intense feature at 1018 cm^{-1} and weaker bands between 698 and 757 cm^{-1} are attributed to aromatic ring C–C modes of the $[\text{Ru}(\text{bpy})_2(\text{Qbpy})]^{2+}$. C–H deformation modes are observed around 1308 and 1272 cm^{-1} . The peaks observed at 1632, 1596, 1549, 1521 and 1481 cm^{-1} are attributed to pyridine C–C stretching modes.⁵⁶ A moderately intense feature around 1169 cm^{-1} is attributed to a coupled C–H bend and ring stretching mode.⁵⁷ The broadenings and downshifts of the Raman peaks are mainly attributed to the quantum confinement effect of CuO nanotubes.⁵⁸ The quantum confinement effect can be observed once the diameter of the material is of the same magnitude as the wavelength of the electron wave function.⁵⁹ A particle behaves as if it were free when the confining dimension is large compared to the wavelength of the particle. During this state, the bandgap remains at its original energy due to a continuous energy state. However, as the confining dimension decreases and reaches a certain limit, typically in nanoscale, the energy spectrum turns to discrete. As a result, the bandgap becomes size dependent. This ultimately results in a blue shift in optical illumination as the size of the particles decreases.

The SEM images indicate that the prepared Cu nanotubes have diameters of 50-70 nm, with average lengths of up to 3 μm , so that the length is larger than the diameter, which means that the quantum confinement effect mainly occurs along the diameter direction of the Cu nanotubes.⁵⁸ In contrast, following deposition of the gold inside the hollow Cu tubes, the intensity of the CuO related peaks at 358 and 658 cm^{-1} both become relatively stronger. Overall, the intensity of the Au:Cu core:shell wires is approximately four times greater than the intensity of just the hollow Cu tubes. The features associated with CuO at both 358 and 658 cm^{-1} are present both before and after gold deposition. Thus, it can also be concluded that both CuO and Cu_2O exist in the sample before and after gold deposition. The presence of the gold core inside the nanotube has served to create an enhancement of the Raman signal of these peaks.

4.3 Conclusion

In summary, a templated electrodeposition strategy has been developed and shown to be an efficient route to creating gold-copper core-shell nanowires. Prior to their release from the polycarbonate template, the nanotubes exist as a highly aligned array with uniform diameters (147 ± 22 nm) along the entire lengths of the wires (3.0 ± 0.5 μ m). The shell thickness is approx. 44.5 ± 5 nm.

Following deposition of gold through the hollow copper tube, the nanowires have uniform diameters of 161 ± 20 nm, with lengths of 3.0 ± 0.1 μ m. These differences in diameter and length are not statistically significant, but represent the challenges in fabrication of fully uniform nanowires using polycarbonate membranes as templates. Polycarbonate membranes may be subject to distortion during the deposition process, due to their malleable nature, and so the nanowires formed may have diameters that are larger than the original pore size. In addition, it has been shown previously that some polycarbonate membranes do not have uniform pore diameters throughout the length of the pore, and that the diameters can increase by as much as a factor of 3 in the middle of the membrane as compared to the ends.

The nanowires were characterised using voltammetry in acidic solution, showing well resolved redox couples for both copper and gold.

Resonance Raman spectroscopy was performed on both the hollow copper nanotubes and the core:shell nanowires, following functionalisation with a Ruthenium dye. The gold core shows a four-fold enhancement of features associated with this dye.

Use of these core:shell structures in a biosensing assay could improve sensitivity over traditional PCR and fluorescent labelled methods. The presence of a second metal on the wire could open up the possibility of a multiplexed assay capable of detecting several DNA sequences at once just by tuning the potentials for each metal. For example, by selectively stripping the copper shell following a DNA sandwich assay, the LOD of this type of assay could be as low as 1 nM of target DNA. .

Using this approach, as few as 300 hybridisation events could be detected. This would greatly enhance the sensitivity of the biosensor, which means that the target DNA strand could be detected at low concentrations typically seen early in the disease.

The approach developed lends itself to multiplexing since the potential at which the shell is stripped depends on the metal used. This approach is also advantageous in that it removes the need to add an additional reagent, i.e. H_2O_2 in the electrocatalysis assay.


4.4 References

- ¹ H. Yang, *Angewandte Chemie International Edition*, 2011, **50**, 2674-2676.
- ² J. Luo, L. Wang, D. Mott, P. N. Njoki, Y. Lin, T. He, Z. Xu, B. N. Wanjana, I. S. Lim and C. Zhong, *Adv Mater*, 2008, **20**, 4342-4347.
- ³ C. J. Zhong and M. M. Maye, *Adv Mater*, 2001, **13**, 1507-1511.
- ⁴ J. Zeng, J. Yang, J. Y. Lee and W. Zhou, *J Phys Chem B*, 2006, **110**, 24606-24611.
- ⁵ Z. Liu, G. Jackson and B. Eichhorn, *Angewandte Chemie International Edition*, 2010, **49**, 3173-3176.
- ⁶ R. Ghosh Chaudhuri and S. Paria, *Chem. Rev.*, 2012, **112**, 2373-2433.
- ⁷ Q. Liu, R. Zou, Y. Bando, D. Golberg and J. Hu, *Progress in Materials Science*, 2015, **70**, 1-49.
- ⁸ S. Han, C. Li, Z. Liu, B. Lei, D. Zhang, W. Jin, X. Liu, T. Tang and C. Zhou, *Nano Lett.*, 2004, **4**, 1241-1246.
- ⁹ Z. Deng, S. Pal, A. Samanta, H. Yan and Y. Liu, *Chem. Sci.*, 2013, **4**, 2234-2240.
- ¹⁰ J. H. Joo, J. F. Hodelin, E. L. Hu and E. D. Haberer, *Mater Lett*, 2012, **89**, 347-350.
- ¹¹ W. Yan, J. Y. Kim, W. Xing, K. C. Donovan, T. Ayvazian and R. M. Penner, *Chem. Mater.*, 2012, **24**, 2382-2390.
- ¹² D. Shi, J. Chen, S. Riaz, W. Zhou and X. Han, *Nanotechnology*, 2012, **23**, 305601.
- ¹³ G. Sahu, K. Wang, S. W. Gordon, W. Zhou and M. A. Tarr, *Rsc Advances*, 2012, **2**, 3791-3800.

- ¹⁴ M. Liu, X. Li, H. Imrane, Y. Chen, T. Goodrich, Z. Cai, K. S. Ziemer, J. Y. Huang and N. X. Sun, *Appl. Phys. Lett.*, 2007, **90**, 152501.
- ¹⁵ H. Kim and J. Cho, *Nano Lett.*, 2008, **8**, 3688-3691.
- ¹⁶ Y. Wu, T. Livneh, Y. X. Zhang, G. Cheng, J. Wang, J. Tang, M. Moskovits and G. D. Stucky, *Nano Lett.*, 2004, **4**, 2337-2342.
- ¹⁷ J. Ryu and C. Park, *Angewandte Chemie International Edition*, 2009, **48**, 4820-4823.
- ¹⁸ M. Zhang, M. Drechsler and A. H. E. Müller, *Chem. Mater.*, 2004, **16**, 537-543.
- ¹⁹ R. Inguanta, S. Piazza and C. Sunseri, *Appl. Surf. Sci.*, 2009, **255**, 8816-8823.
- ²⁰ M. Paunovic and M. Schlesinger, *Fundamentals of electrochemical deposition*, Wiley, New York, 1998, pp 102.
- ²¹ E. Mattsson and J. O. Bockris, *Transactions of the Faraday Society*, 1959, **55**, 1586-1601.
- ²² J. O. Bockris and M. Enyo, *Transactions of the Faraday Society*, 1962, **58**, 1187.
- ²³ C. Huang and Y. Hao, *Nanotechnology*, 2009, **20**, 445607
- ²⁴ D. M. Davis and E. J. Podlaha, *Electrochemical and Solid State Letters*, 2005, **8**, D1-D4.
- ²⁵ *Isopore™ Membrane Filters - Millipore*. www.millipore.com
- ²⁶ M. Motoyama, Y. Fukunaka, T. Sakka and Y. H. Ogata, *Electrochim. Acta*, 2007, **53**, 205-212.
- ²⁷ E. Spain, R. Kojima, R. B. Kaner, G. G. Wallace, J. O'Grady, K. Lacey, T. Barry, T. E. Keyes and R. J. Forster, *Biosensors and Bioelectronics*, 2011, **26**, 2613-2618.
- ²⁸ E. Spain, B. Miner, T. E. Keyes and R. J. Forster, *Chemical Communications*, 2012, **48**, 838-840.

- ²⁹ M. Proenca, C. Sousa, J. Ventura, M. Vazquez and J. Araujo, *Nanoscale Research Letters*, 2012, **7**, 280.
- ³⁰ C. Schonenberger, B. M. I. vanderZande, L. G. J. Fokkink, M. Henny, C. Schmid, M. Kruger, A. Bachtold, R. Huber, H. Birk and U. Staufer, *J Phys Chem B*, 1997, **101**, 5497-5505.
- ³¹ M. E. Toimil-Molares, *Beilstein Journal of Nanotechnology*, 2012, **3**, 860-883.
- ³² J. Juodkazytė, B. Šebeka, I. Savickaja, A. Selskis, V. Jasulaitienė and P. Kalinauskas, *Electrochim. Acta*, 2013, **98**, 109-115.
- ³³ B. D. Yuhas and P. Yang, *J. Am. Chem. Soc.*, 2009, **131**, 3756-3761.
- ³⁴ W. Ma, Y. Ying, L. Qin, Z. Gu, H. Zhou, D. Li, T. C. Sutherland, H. Chen and Y. Long, *Nat. Protocols*, 2013, **8**, 439-450.
- ³⁵ *Solution in drop definition / electrochemistry dictionary*
- ³⁶ D. Britz, *J Electroanal Chem*, 1978, **88**, 309-352.
- ³⁷ A. J. Bard and L. R. Faulkner, *Electrochemical methods: fundamentals and applications*, Wiley, New York, 1980. p.808.
- ³⁸ K. Kneipp, H. Kneipp, I. Itzkan, R. R. Dasari and M. S. Feld, *Chem. Rev.*, 1999, **99**, 2957-2976.
- ³⁹ M. Moskovits, *Reviews of Modern Physics*, 1985, **57**, 783-826.
- ⁴⁰ E. Smith and G. Dent, *Modern Raman Spectroscopy: A Practical Approach*. Wiley, New York, 2005.
- ⁴¹ J. A. Creighton and D. G. Eadon, *J. Chem. Soc. , Faraday Trans.*, 1991, **87**, 3881-3891
- ⁴² C. Langhammer, Z. Yuan, I. ZoriÄ† and B. Kasemo, *Nano Lett.*, 2006, **6**, 833-838

- ⁴³ J. R. Lombardi, R. L. Birke, T. Lu and J. Xu, *J. Chem. Phys.*, 1986, **84**, 4174-4180
- ⁴⁴ J. R. Lombardi and R. L. Birke, *J. Phys. Chem. C*, 2008, **112**, 5605-5617
- ⁴⁵ R. P. Van Duyne and J. P. Haushalter, *J. Phys. Chem.*, 1983, **87**, 2999-3003.
- ⁴⁶ M. Fleischmann, Z. Q. Tian and L. J. Li, *J Electroanal Chem*, 1987, **217**, 397-410.
- ⁴⁷ G. Mengoli, M. M. Musiani, M. Fleischmann, B. Mao and Z. Q. Tian, *Electrochim. Acta*, 1987, **32**, 1239-1245.
- ⁴⁸ L. W. H. Leung and M. J. Weaver, *J Electroanal Chem*, 1987, **217**, 367-384.
- ⁴⁹ L. W. H. Leung and M. J. Weaver, *J. Am. Chem. Soc.*, 1987, **109**, 5113-5119.
- ⁵⁰ P. K. Aravind, A. Nitzan and H. Metiu, *Surf. Sci.*, 1981, **110**, 189-204.
- ⁵¹ A. Nitzan and L. E. Brus, *J. Chem. Phys.*, 1981, **75**, 2205-2214.
- ⁵² Z. Tian, B. Ren, J. Li and Z. Yang, *Chem. Commun.*, 2007, , 3514-3534.
- ⁵³ S. Zhao, X. Tian, J. Liu, Y. Ren and J. Wang, *Journal of Molecular Modeling*, 2014, **20**, 2467.
- ⁵⁴ Z. H. Gan, G. Q. Yu, B. K. Tay, C. M. Tan, Z. W. Zhao and Y. Q. Fu, *Journal of Physics D-Applied Physics*, 2004, **37**, 81-85.
- ⁵⁵ Y. S. Gong, C. P. Lee and C. K. Yang, *J. Appl. Phys.*, 1995, **77**, 5422-5425.
- ⁵⁶ B. S. Yadav, I. Ali, P. Kumar and P. Yadav, *Indian Journal of Pure & Applied Physics*, 2007, **45**, 979-983.
- ⁵⁷ C. T. Mallon, E. Spain, T. E. Keyes and R. J. Forster, *Chemical Communications*, 2013, **49**, 1380-1382.
- ⁵⁸ A. S. Ethiraj and D. J. Kang, *Nanoscale Research Letters*, 2012, **7**, 70.
- ⁵⁹ M. Cahay, *Quantum Confinement VI: Nanostructured Materials and Devices: Proceedings of the International Symposium*. The Electrochemical Society. New Jersey, 2001.



5. DETECTION OF NUCLEIC ACIDS USING FUNCTIONALISED GOLD NANOWIRES, NANOTUBES, AND GOLD:COPPER CORE:SHELL NANOWIRES

5.1 Introduction

DNA and RNA can be important biomarkers of disease, i.e. they can be found in body fluids or tissue when disease is present. As the number of deaths attributed to diseases such as cancer increase year on year, a strong emphasis is now being placed on the development of point of care devices which can determine the concentration of these biomarkers in blood, serum, saliva, urine or other sample matrices.¹

A number of illnesses have been characterised by the presence of specific DNA and RNA sequences, upregulated proteins, antibodies etc. in blood and tissue samples, for example peptic ulcer disease,² hepatitis,³ a number of cancers including breast, liver and pancreatic,^{4,5,6} and many other diseases. The target DNA of interest in this work is the gram-positive bacterium *Staphylococcus aureus*, which is responsible for mastitis in cows, and a range of illnesses, from minor skin infections, such as pimples, impetigo, boils (furuncles), cellulitis folliculitis, carbuncles⁷, scalded skin syndrome⁹, and abscesses, to life-threatening diseases such as pneumonia⁷, meningitis⁸, endocarditis⁹, toxic shock syndrome (TSS)¹⁰, bacteraemia, and sepsis¹¹ in humans. Methicillin-resistant *S. aureus*, abbreviated MRSA, is one of a number of strains of *S. aureus* which have become resistant to most antibiotics.¹²

Mastitis occurs when white blood cells (leucocytes), are released into the mammary gland, usually in response to an invasion of bacteria of the teat canal. Milk-secreting tissue and various ducts throughout the mammary gland are damaged due to toxins from the bacteria. Mastitis can cause a decline in potassium and lactoferrin. It also results in decreased casein, the major protein in milk. As most calcium in milk is associated with casein, the disruption of casein synthesis contributes to lowered calcium in milk. The milk protein continues to undergo further deterioration during processing and storage. Milk from cows with mastitis also has a higher somatic cell count. Generally speaking, the higher the somatic cell count, the lower the milk quality.¹³

The most obvious symptoms of clinical mastitis in cattle are abnormalities in:

- The udder such as swelling, heat, hardness, redness, or pain; and
- The milk such as a watery appearance, flakes, clots, or pus.¹⁴

Current somatic cell counts (SCC) and alternative methods for detection of mastitis include:¹⁵

- California mastitis test (CMT)

This assay indirectly measures the SCC in milk samples. A bromocresol-purple-containing detergent is used to break down the cell membrane of somatic cells, and the subsequent release and aggregation of nucleic acid forms a gel-like matrix with a viscosity that is proportional to the leukocyte number.

- Portachek

This assay uses an esterase-catalysed enzymatic reaction to determine the SCC in milk.

- Fossomatic SCC

This counter operates on the principle of optical fluorescence. Ethidium bromide penetrates and intercalates with nuclear DNA, and the fluorescent signal generated is used to estimate the SCC in milk. Ethidium bromide is thought to act as a mutagen because it intercalates double stranded DNA.¹⁶

- Delaval cell counter

This counter operates on the principle of optical fluorescence, whereby propidium iodide is used to stain nuclear DNA to estimate the SCC in milk. Propidium iodide is a mutagen and is a respiratory irritant.¹⁷

- Electrical conductivity (EC) test

This test measures the increase in conductance in milk caused by the elevation in levels of ions such as sodium, potassium, calcium, magnesium and chloride during inflammation.

- Culture tests

Laboratory-based tests use selective culture to identify different microorganisms involved in causing mastitis.

- pH test

The rise in milk pH, due to mastitis, is detected using bromothymol blue.

- Enzymes

Assays are used to detect enzymes, such as N-acetyl- β -D-glucosaminidase (NAGase) and lactate dehydrogenase (LDH).

These assays are used to detect mastitis when it has already contaminated the milk produced by the cow. By developing an assay to detect the mastitis DNA when present in low concentrations (perhaps before symptoms have manifested), the treatment could begin earlier and this may prevent the symptoms occurring and prevent loss of income to the farmer due to spoiled milk.

Additionally, some of these assays require use of reagents which are toxic or mutagenic, which is not ideal.

Presently, the detection of DNA relies on methods such as polymerase chain reaction (PCR), gel electrophoresis and southern blotting.¹⁸ These methods are labour intensive, expensive, require large amounts of expensive equipment, have low sensitivity, and are time consuming. As biomarkers associated with disease tend to be present in very low concentrations in the blood (e.g. picomolar), a detection method must be ultra-sensitive and have a very low limit of detection. One of the challenges in creating an electrochemical detection platform is amplifying the signal associated with the biorecognition events so that it can be easily detected.

With the development of ultrasensitive electrochemical biosensors, and the need for miniaturisation of these sensors, nanomaterials have been drawing considerable attentions, due to their unique size and properties.^{19,20}

In particular, noble metal nanostructures have gained special interest because of their conductivity, optical properties and biocompatibility as high surface-to-volume ratio and high heat transfer (thermal conductivity).^{21,22} Amongst them, copper-based nanoparticles are of great interest due to their low toxicity, low cost and easy availability, and because they possess properties similar to that of other metallic nanoparticles.²³ Gold nanoparticles can act as conductor centres, and can facilitate electron transfer.

Since the discovery of carbon nanotubes, other one-dimensional nanostructures such as nanotubes, nanowires and nanorods have been the focus of some investigations. Nanowires have a number of unique physical and electronic properties that are different from those of spherical nanoparticles,²⁴ which makes them ideal for use in an electrochemical biosensor.

In this work, the objective is to increase the sensitivity of nucleic acid detection through the use of nanowires that amplify the signal generated by a single target binding event. This is in contrast to current gold standard nucleic acid detection strategies such as Polymerase Chain Reaction (PCR), or Nucleic Acid Sequence Based Amplification (NASBA), which amplify the target nucleic acid itself. The use of the nanowire is advantageous in that it provides significantly higher surface area than a nanoparticle, which is useful for generating a larger electrocatalytic current.

The core:shell nanowire could also be used to generate an alternative signal that can be measured, for example through thiol bond reduction or sacrificial metal oxidation which is important for multi analyte detection.

The advantage of this approach is that it does not require amplification of the target nucleic acid, making it easier to incorporate into a point-of-care device that is user-friendly.

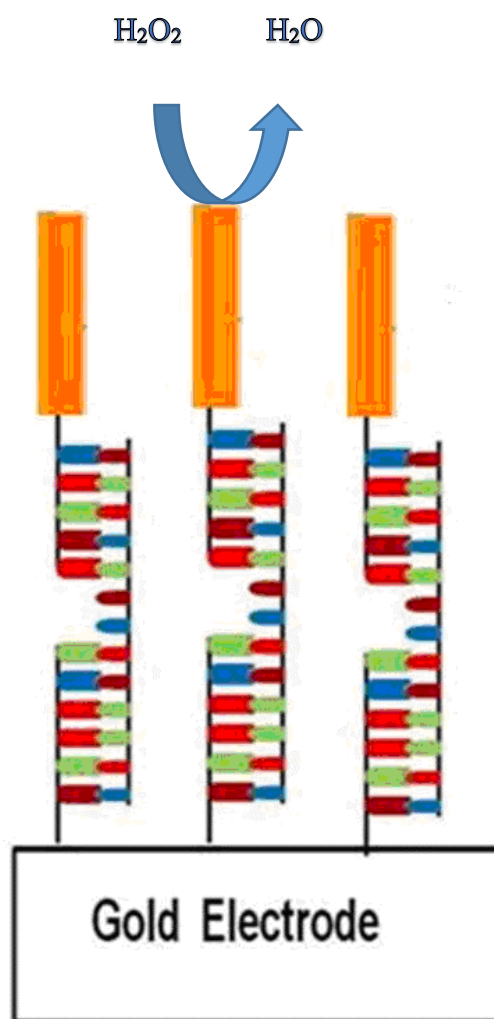
5.2 Results and Discussion

5.2.1 Application of gold nanowires to label-free, amplification free, detection of target DNA

The ability of the regioselectively modified solid nanowires to detect DNA specifically associated with *S. aureus* mastitis was investigated. Nanowires confined on the electrode surface by capture-target- hybridisation are capable of electrocatalysing the reduction of hydrogen peroxide generating a current whose magnitude is directly proportional to the concentration of target pathogen DNA. The target DNA concentration was determined by measuring the difference in the electrocatalytic reduction current at the gold nanowires/tubes, Δi , before and after the addition of 200 μM hydrogen peroxide to a solution of deoxygenated 0.01 M H_2SO_4 .

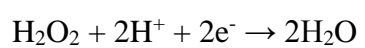
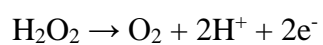
Scheme 5.1 shows the fully hybridised electrode, to which gold nanowires or nanotubes are adhered via complementary DNA hybridisation. The presence of the nanowires is due to the presence of the target strand of DNA, and the number of nanowires present should correspond to the concentration of target DNA present on the electrode surface.

A fixed potential is applied to the electrode, and as there are no redox processes occurring on gold at this potential, the current will decay to almost zero. An injection of 200 μM H_2O_2 is then added to the solution, and the current response increases dramatically. The current response is due to the reduction of the added hydrogen peroxide by the gold nanowires.



Scheme 5.1: *Schematic diagram of Au nanowire modified gold electrode, hybridised with capture, target and probe DNA*

The reaction proceeds as follows:



Equation 5.1

5.2.1.1 Characterisation of gold nanowire/nanotube biosensor response

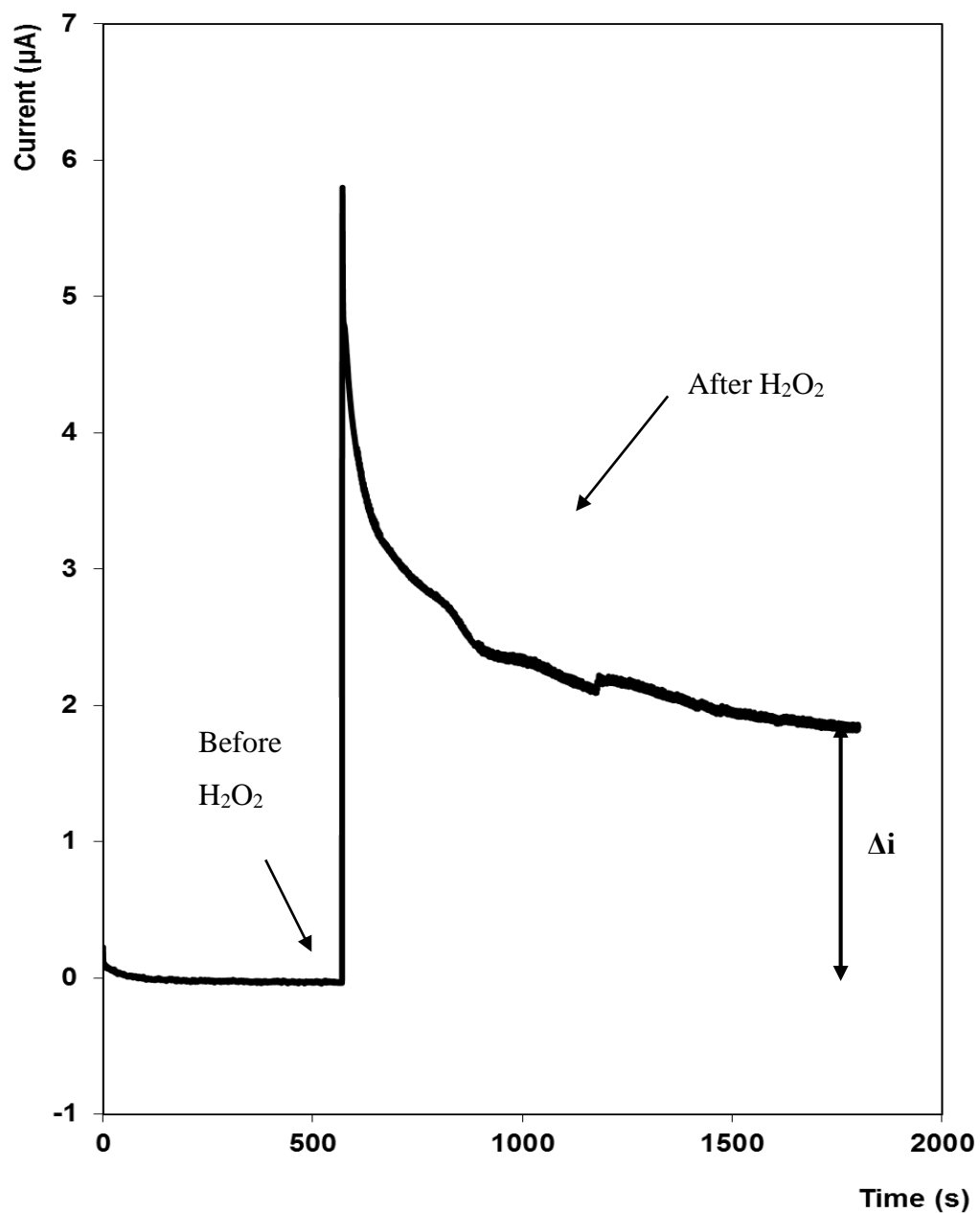
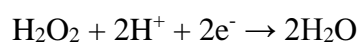
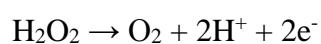


Figure 5.1: Current-time transient showing response of solid Au nanowires to addition of 200 μM of 30% wt. Hydrogen Peroxide. The supporting electrolyte was 0.01 M H_2SO_4 , and the applied potential was -0.1 V. vs. Ag/AgCl in 3 M KCl. The target DNA concentration was 10 aM.

As illustrated in Figure 5.1, the initial current detected in aqueous sulphuric acid in the absence of any deliberately added peroxide was measured for approximately ten minutes. When 200 μM of H_2O_2 was added to 0.01 M H_2SO_4 , the current rapidly increased due to the catalytic reduction of the hydrogen peroxide by the gold nanowires.

The reaction proceeds as follows:



Equation 5.2

5.2.1.2 Calibration plot for gold nanowire response

Using a concentration range of target DNA from 1 μM to 1 aM the electrocatalytic properties of the solid gold nanowires towards H_2O_2 was investigated. The calibration plot is shown in Figure 5.2.

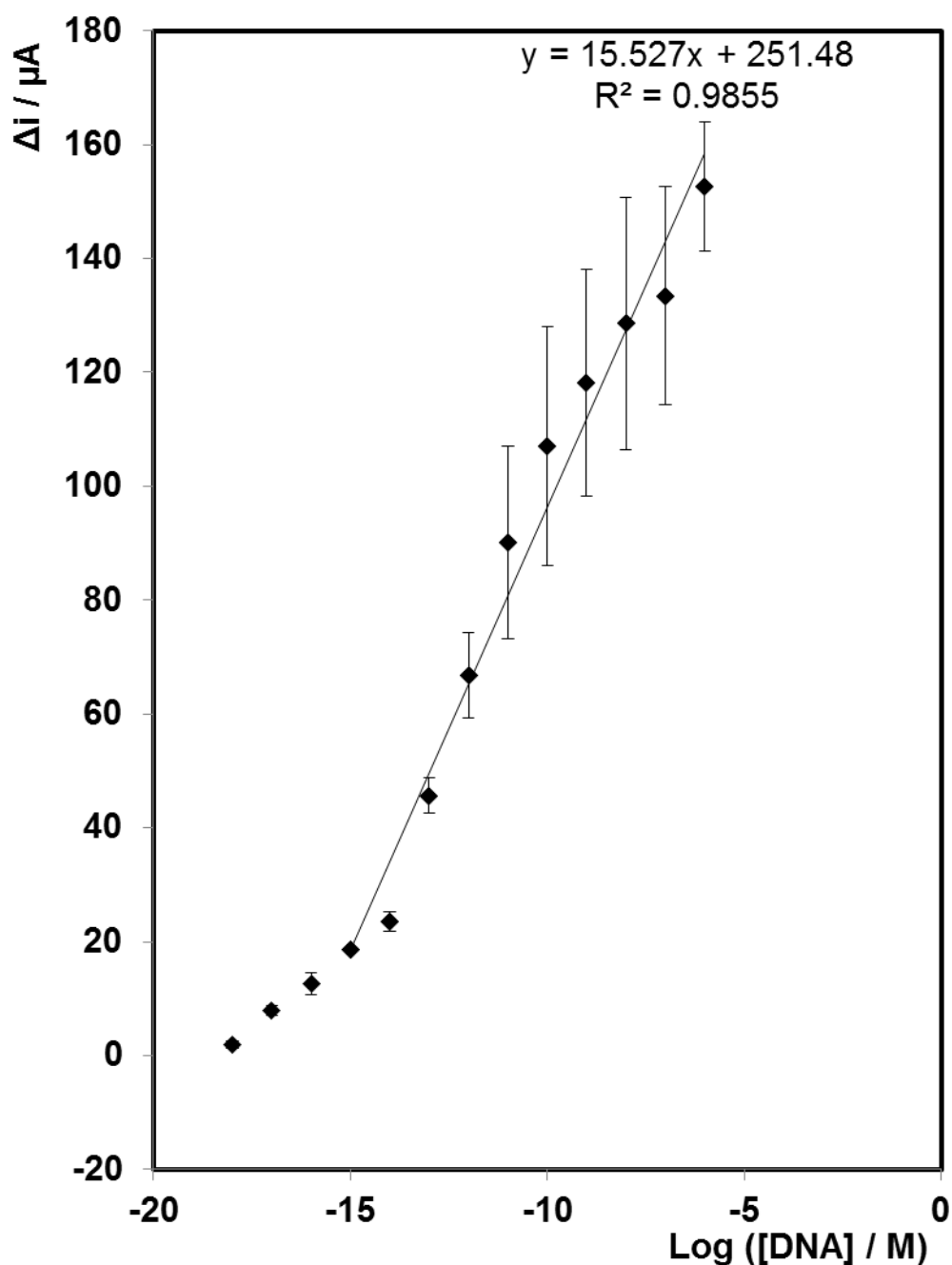


Figure 5.2: Calibration curve for the electrochemical detection of target DNA range 1 μM to 1 aM on a 2 mm diameter bare electrode following hybridisation with probe DNA that is labelled with solid gold nanowires. The supporting electrolyte is 0.01M H_2SO_4 . The detection potential is -0.1 V vs. Ag/AgCl in 3 M KCl. The concentration of H_2O_2 added is 200 μM . Where error bars are not visible, they are smaller than or the same size as the size of the symbol. In this experiment, $n = 3$ different batches of gold nanowires.

Figure 5.2 shows the dependence of Δi on the concentration of target strand DNA where the electrocatalytic Au nanowires are functionalised with probe strand DNA. The electrocatalytic current observed at these decorated nanowires is acceptably linear for target DNA concentrations from 1 fM to 1 μ M.

The sensitivity of the assay involving solid Au nanowire-labelled probe strands is 15.5 μ A dec⁻¹, over ten times greater than the 1.32 μ A dec⁻¹ of the platinum nanoparticles reported previously.²⁵ This dramatically higher sensitivity and wide linear dynamic range indicates that the nanowires retain both their electrocatalytic and DNA binding capabilities.

Table 5.1: *Response of electrode to different concentrations of target DNA for solid gold nanowires.*

Concentration (M)	Log DNA	Average Δi (μ A)	Standard Deviation
1.00E-18	-18	1.89	0.61
1.00E-17	-17	7.91	0.86
1.00E-16	-16	12.57	1.96
1.00E-15	-15	18.56	0.46
1.00E-14	-14	23.52	1.67
1.00E-13	-13	45.69	3.15
1.00E-12	-12	66.74	7.55
1.00E-11	-11	90.08	16.88
1.00E-10	-10	107.02	20.98
1.00E-09	-9	118.23	19.92
1.00E-08	-8	128.56	22.16
1.00E-07	-7	133.46	19.11
1.00E-06	-6	152.63	11.41

5.2.2 Application of hollow gold nanotubes to label-free, amplification-free detection of target DNA

Depending on the rate of peroxide diffusion into and through the nanotubes compared to the rate of electrolysis at their surface, the additional surface area of the nanotube compared to the nanowire could amplify the current associated with individual DNA hybridisation events. It is hoped that the current associated with these hollow nanotubes would be greatly increased when compared to the solid gold nanowires, which would make them an attractive nanomaterial for incorporation to an electrochemical nucleic acid detection device.

This biosensor was characterised in the same way as for the solid gold nanowires.

5.2.2.1 Calibration plot for gold nanotube response

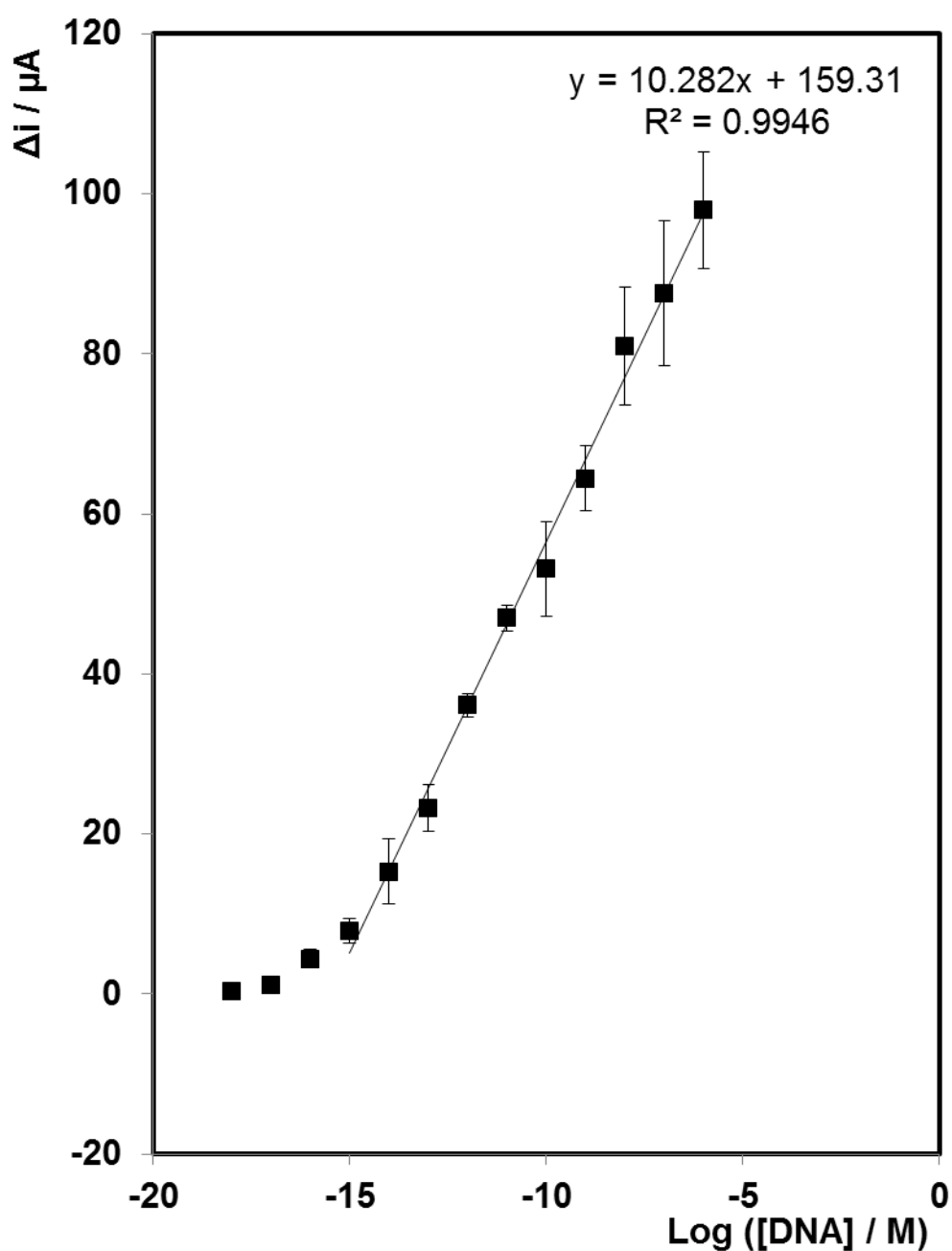


Figure 5.3: Calibration curve for the electrochemical detection of target DNA range 1 μM to 1 aM on a 2 mm diameter bare electrode following hybridisation with probe DNA that is labelled with hollow gold nanotubes. The supporting electrolyte is 0.01M H_2SO_4 . The detection potential is -0.1 V vs. Ag/AgCl in 3 M KCl. The concentration of H_2O_2 added is 200 μM . Where error bars are not visible, they are smaller than, or the same size as the size of the symbol. In this experiment, $n = 3$ different batches of gold nanotubes.

Table 5.2: *Response of electrode to different concentrations of target DNA for hollow gold nanotube-labelled probe strand.*

Concentration (M)	Log DNA	Average Δi (μA)	Standard deviation
1.00E-18	-18	0.41	0.39
1.00E-17	-17	1.16	0.21
1.00E-16	-16	4.43	1.21
1.00E-15	-15	7.89	1.50
1.00E-14	-14	15.33	4.00
1.00E-13	-13	23.18	2.93
1.00E-12	-12	36.06	1.49
1.00E-11	-11	46.98	1.64
1.00E-10	-10	53.10	5.95
1.00E-09	-9	64.43	4.09
1.00E-08	-8	80.99	7.40
1.00E-07	-7	87.53	9.04
1.00E-06	-6	97.99	7.28

The sensitivity observed for the nanotubes, $10.2 \mu A \text{ dec}^{-1}$, is approximately 35% less than that observed for the solid nanowire-labelled DNA. This result is significant since the total area of the nanotube is approximately twice that of the nanowire which might be expected to lead to an enhanced current for the nanotube. However, the nanotube is uniformly functionalised with capture strand DNA which most likely impedes access of the peroxide to the nanotube surface. The higher current suggests that the regioselectively modified nanowires are more catalytically active, i.e., physically separating the molecular recognition and electrocatalytic detection functions produces a more sensitive assay.

Significantly, the Limit of Quantitation, LOQ, is 1 fM for both nanostructures which is approximately four orders of magnitude lower than that reported previously using platinum nanoparticles.²⁵ The low LOQ reflects the relatively large current generated by a single hybridisation event, i.e., the electrocatalytic current per nanowire is large. Theory²⁶ suggests that the diffusion limited current for a single solid nanowire is approximately 70 pA. Therefore, there are approximately 250,000 nanowires immobilised at the LOQ for the regioselectively modified nanowires and a maximum of approximately 3% of the electrode surface is covered even if all of the nanowires lie flat on the electrode surface. The wide dynamic range arises because the area occupied by each nanowire is small, of the order of 3 nm² even when lying flat on the electrode surface, and the association constant is relatively low since the targets are short, meaning that even for micro molar concentrations of target, only about 30% of the electrode is covered with nanowires.

For the electrocatalytic nanowires and nanotubes reported here, the dynamic range is very wide, approximately 10 orders of magnitude.

5.2.2.2 Control Study

A study was carried out where the probe strand was unlabelled, and the catalytic current measured arises due to the underlying modified gold electrode (shown along with data for nanowire-labelled and nanotube-labelled probe strands in Figure 5.4). As expected, where the probe strand is not labelled, its hybridisation with the target does not produce any measurable current. The sensitivity of the 2 mm gold disc electrode following hybridisation of the DNA where the probe DNA strand is unlabelled is $0.0795 \mu\text{A dec}^{-1}$, reflecting the poor electrocatalytic properties of the DNA modified gold electrode. These low currents in the absence of gold nanowire/tube labels indicate that the background current associated with direct reduction of hydrogen peroxide at the underlying electrode is low. This result is significant as the magnitude of this background current directly influences the limit of detection.

Table 5.3: *Response of bare gold electrode to target DNA for unlabelled probe strand DNA*

Concentration (M)	Log DNA	Average Δi (μA)	Standard Deviation
1.00E-18	-18	0.95	0.0146
1.00E-17	-17	1.00	0.0147
1.00E-16	-16	1.08	0.0180
1.00E-15	-15	1.22	0.0185
1.00E-14	-14	1.21	0.0217
1.00E-13	-13	1.19	0.0178
1.00E-12	-12	1.40	0.0276
1.00E-11	-11	1.18	0.0175
1.00E-10	-10	1.49	0.0305
1.00E-09	-9	1.84	0.0359
1.00E-08	-8	1.64	0.0351
1.00E-07	-7	1.96	0.0397
1.00E-06	-6	1.78	0.0396

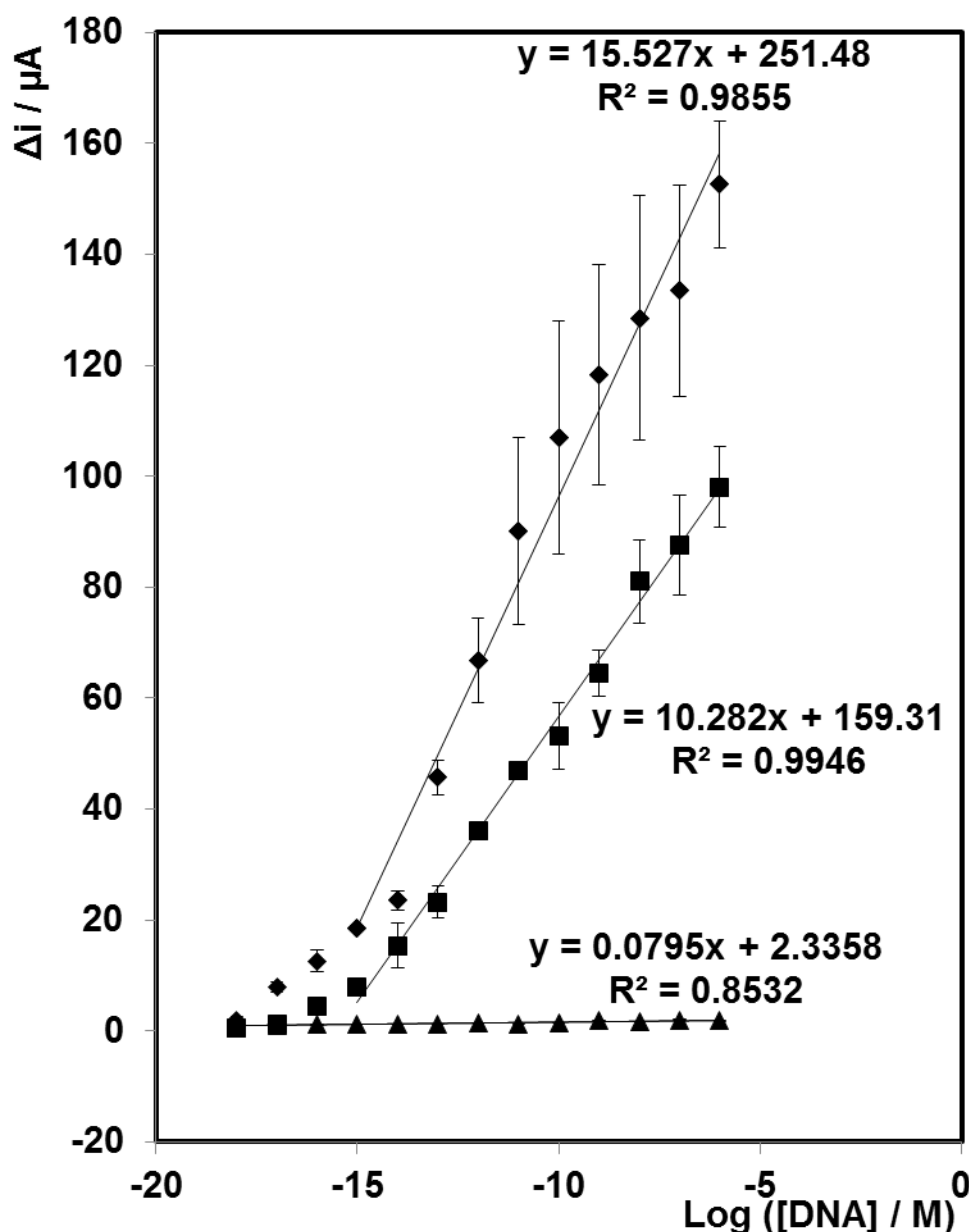


Figure 5.4: Calibration plots for the electrochemical detection of *Staph. Aureus* mastitis DNA on a 2 mm radius electrode modified with capture strand DNA following hybridization with the target DNA and gold nanowires regioselectively modified with probe strand DNA (♦) and uniformly decorated nanotubes (■). A control experiment showing the response of the electrode where the probe strand is not labelled is also shown (▲). The supporting electrolyte is 0.01M H_2SO_4 . The detection potential is -0.1 V vs. Ag/AgCl in 3 M KCl. The concentration of peroxide added was 200 μM . Where error bars are not visible, they are smaller than, or comparable to, the size of the symbols.

For both the gold nanowires and nanotubes, the current increases linearly with increasing DNA concentration, from approximately 1 fM to 10 μ M. This performance compares favourably with other more challenging detection strategies. For example, Cho et al.²⁷ have reported a linear range of 10 pM to 1 nM of target DNA concentration where the conductivity of the bound nanowires is measured. Other high sensitivity approaches rely on amplification of the target, e.g., Russell et al. have detected a target DNA concentration of 66 fM by using rolling circle amplified DNA which has been metallised to form gold nanowires.²⁸

It is important to note that the data presented in Figure 5.4 represent the average and standard deviations of three independently synthesised nanowires rather than the results of repeated assays using a single batch of wires. Figure 5.5 shows the calibration data for each of three individual batches of nanowires. The calibration curves are linear for $-15 < \log [\text{DNA}] < -9$ with acceptable correlation coefficients, $R^2 = 0.9973, 0.9947$ and 0.9917 . However, the absolute calibration sensitivities (slopes) vary between nanowire batches with values of 25.0 ± 0.6 , 22.9 ± 0.8 and $13.7 \pm 0.7 \mu\text{A dec}^{-1}$ being observed. Therefore, while the calibration sensitivity is reproducible within a single batch of nanowires ($<5\%$), achieving a good reproducibility between batches is challenging. These inter-batch deviations may arise from differences in wire length, e.g., due to wires breaking during removal from the template, or from differences in pore wetting during wire deposition.

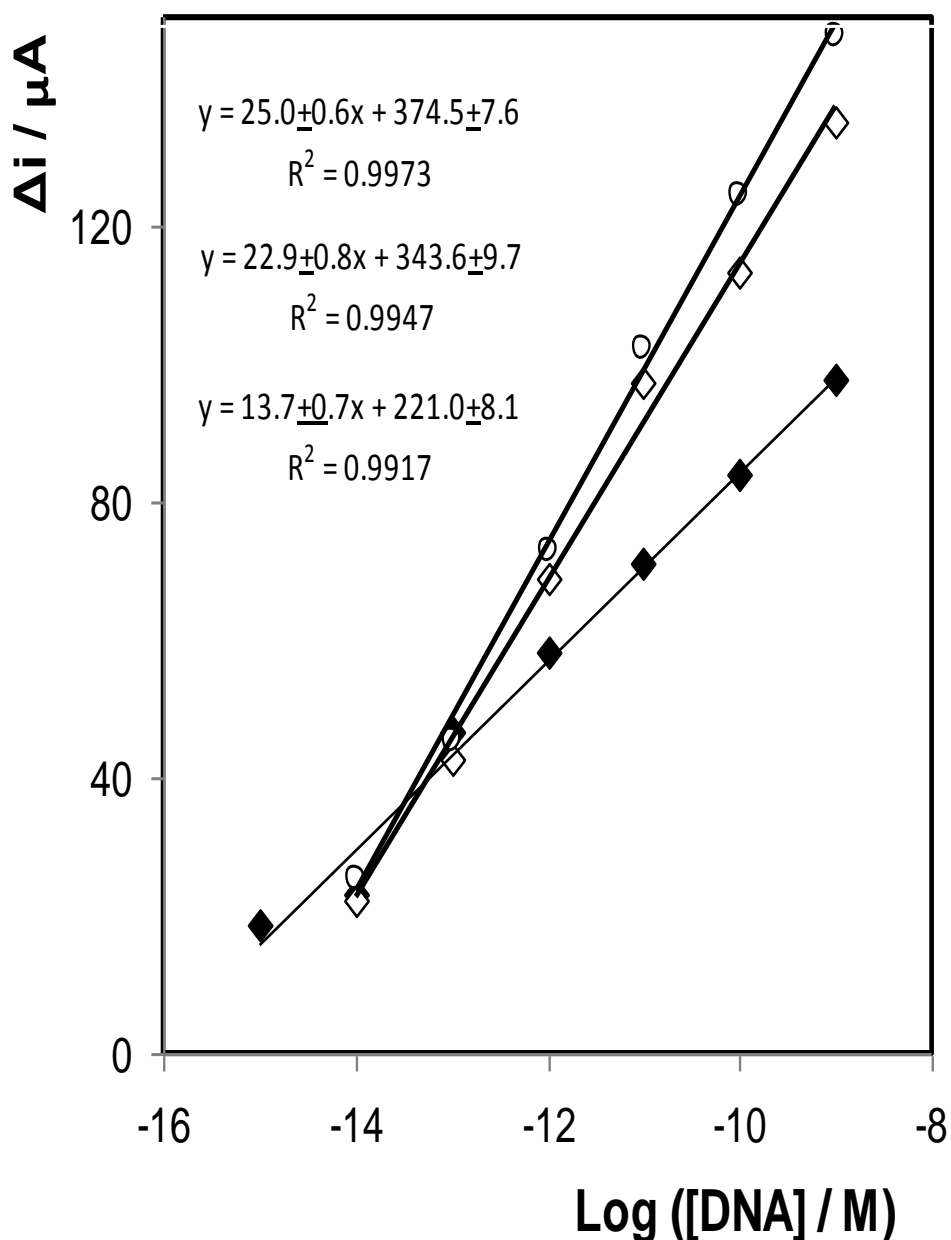


Figure 5.5: Calibration plots for the electrochemical detection of *Staph. Aureus* mastitis DNA on a 2 mm radius electrode modified with capture strand DNA following hybridization with the target DNA and gold nanowires regioselectively modified with probe strand DNA for each of three individual batches of nanowires. The concentration of H_2O_2 added was 200 μM . The calibration curves are linear for $-15 < \log [DNA] < -9$ with acceptable correlation coefficients, $R^2=0.9973$, 0.9947 and 0.9917. The concentration of hydrogen peroxide is 200 μM .

5.2.3 Selectivity of the assay using 1 Mismatch target DNA

5.2.3.1 1 Base Mismatch

The assay was carried out as before, using a target strand of DNA with a single base mismatch from that of the *S. Aureus* DNA used previously, and the solid gold nanowires as electrocatalytic label. The target strand sequence used was: 5'-TGC-TAA-ACA-CTG-CCG-TTT-GAA-GTC-TGT-TTA-AAA-GAA-ACT-TA-3', where the A base marked in red is the mismatch. This strand of DNA (containing this specific mismatch) is not known to be present in a pathogenic organism. This mismatch was chosen to determine whether the assay could distinguish between the target mastitis DNA, and other strands of DNA that were similar in composition, but which contain a single base difference.

All results generated for this assay by Dr Elaine Spain.

DNA concentration (M)	Log DNA concentration (M)	Δi (A)
1.00E-06	-6	5.83E-05
1.00E-07	-7	4.48E-05
1.00E-08	-8	4.67E-05
1.00E-09	-9	3.89E-05
1.00E-10	-10	3.46E-05
1.00E-11	-11	2.73E-05
1.00E-12	-12	2.6E-05
1.00E-13	-13	2.21E-05
1.00E-14	-14	1.92E-05
1.00E-15	-15	1.63E-05
1.00E-16	-16	1.53E-05
1.00E-17	-17	9.67E-06
1.00E-18	-18	5.37E-06

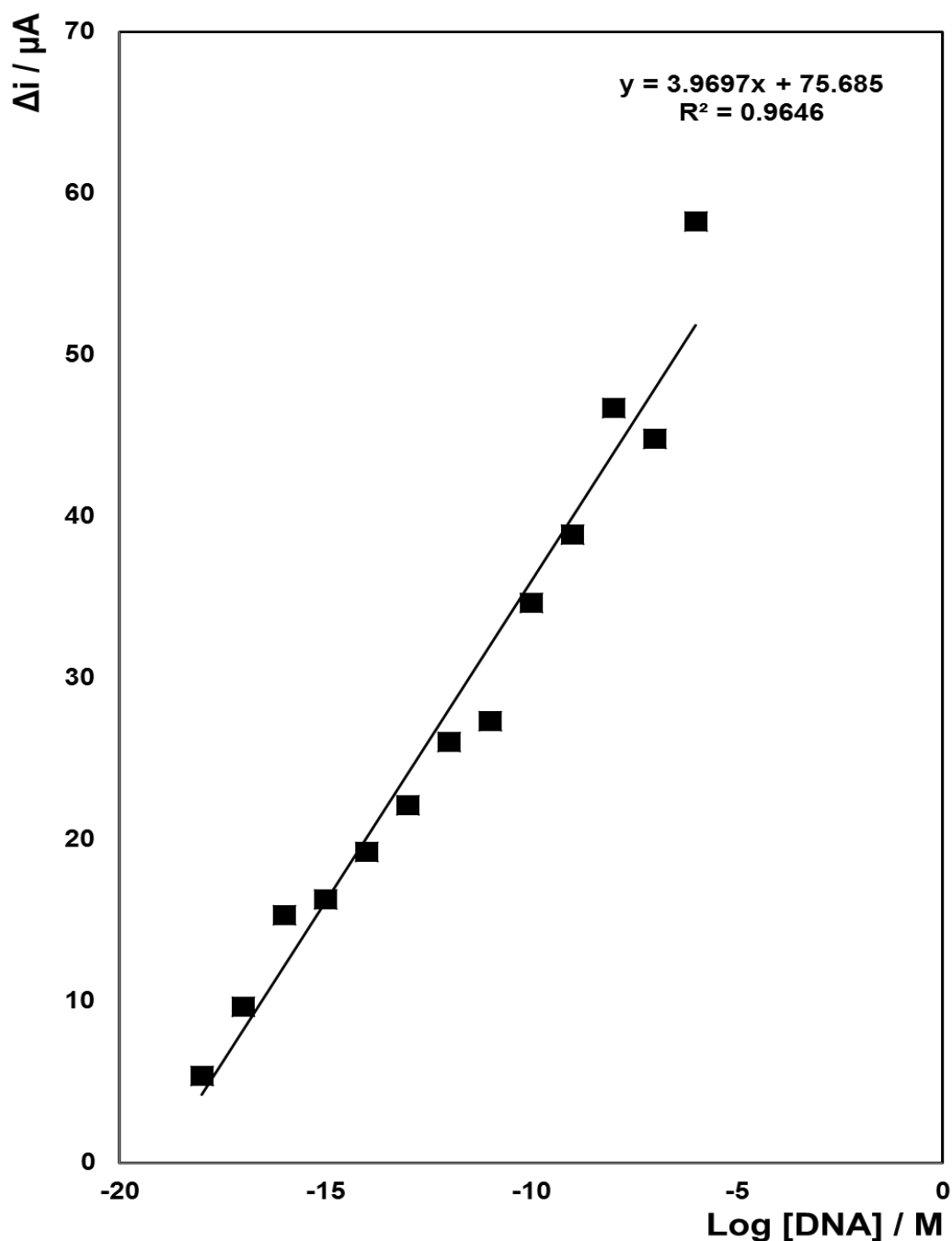


Figure 5.6: Calibration plots for the electrochemical detection of *Staph. Aureus* mastitis DNA on a 2 mm radius electrode modified with capture strand DNA following hybridization with the target DNA that contains a 1 base mismatch, and gold nanowires regioselectively modified with probe strand DNA. The supporting electrolyte is 0.01M H_2SO_4 . The detection potential is -0.1 V vs. Ag/AgCl in 3 M KCl. The concentration of peroxide added was 200 μM . $n = 1$ for this experiment.

The response of this assay to the 1-base mismatch DNA is linear over the range of concentrations from 1 μ M to 1 nM, with a linear regression coefficient of 0.9646. This linear regression value shows an acceptable linearity, and is only slightly lower than that of the fully complementary assay. Moreover, the slope of this assay is not the same as for the fully complementary DNA strand.

The magnitude of the current generated has also decreased, and is over 2.5 times lower than the maximum current generated for the fully complementary electrode. This implies that the assay in its current form should be sensitive enough to discriminate between a fully complementary DNA strand, and one containing a single base mismatch.

The sensitivity of the assay is reduced by approximately 75% compared to the assay using the fully complementary target DNA strand. These results are quite promising, indicating that the numbers of target strands containing just one base different from the strand of interest that bind to the capture strand is very low.

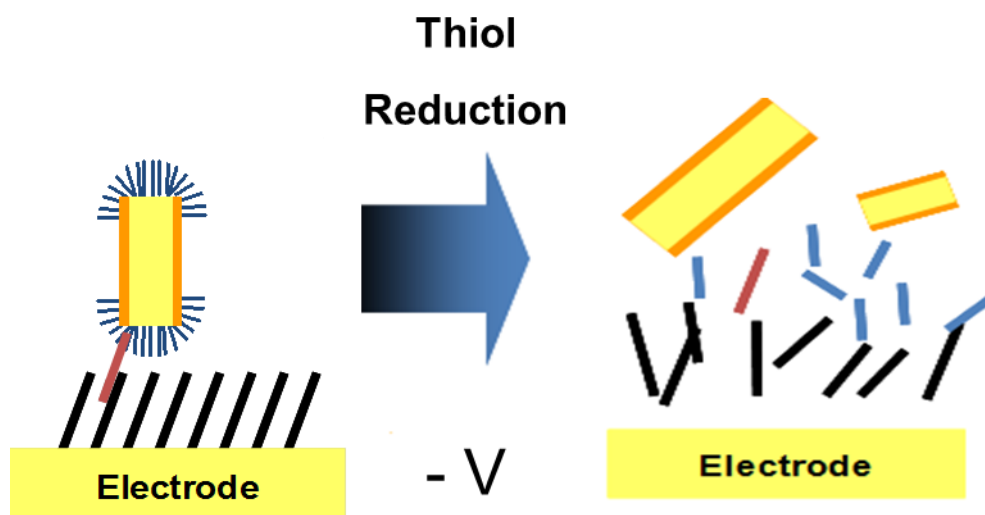
5.2.4 Application of gold:copper core:shell nanowires to label-free, amplification-free detection of target DNA

Previously, electro-catalytically active metal nanoparticles have been used in detection of DNA at attomolar concentrations.²⁵ Metal nanowires also possess these electrocatalytic properties, but, by utilising their higher surface-to-volume ratio, the signal generated by the nanowires can be larger than the signal due to nanoparticles. If one assumes that the nanowires are adhered to an electrode surface via DNA hybridisation in a dense, close packed monolayer, the area of the wires that is in contact with the electrode is equivalent to the area of a disc, while the walls of the wire are standing upright and free from probe strands of DNA. This means that this clean metal surface is available to utilise in generating a signal due to a hybridisation event. This higher surface to volume ratio could generate a greatly enhanced signal due to a comparable number of hybridisation events to an electrode modified with nanoparticles.

5.2.4.1 Characterisation of core:shell nanowire biosensor response

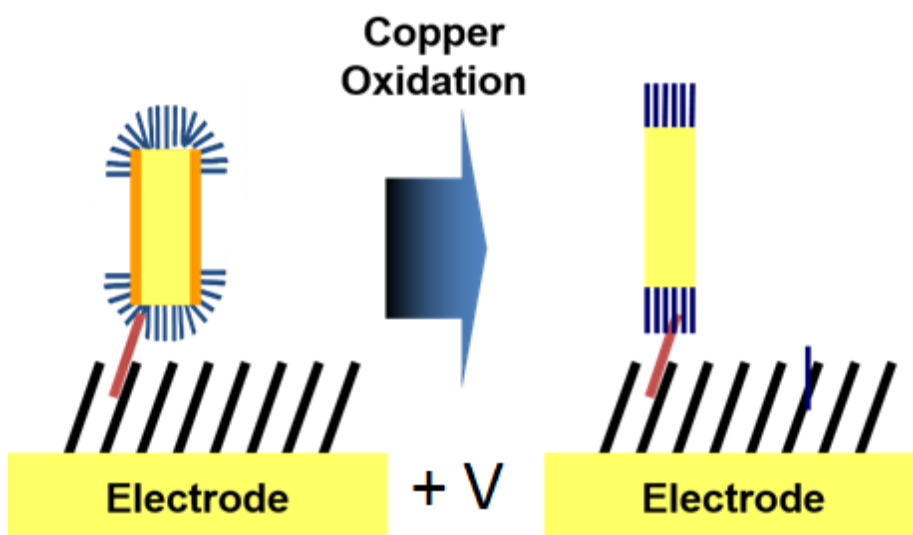
The gold:copper core:shell nanowires have been applied to the detection of DNA. The core:shell nanowires can be functionalised with a thiolated DNA probe strand that is complementary to a section of the target before the wires are released from the template. Given the significantly higher propensity for thiol adsorption on gold rather than copper the thiolated probe is likely to be predominantly bound to gold. By depositing a DNA capture layer on an electrode whose sequence is complementary to the remaining section of the target, the core-shell nanowires can be confined on the electrode surface through DNA hybridisation in a sandwich assay. Once confined, two approaches were utilised to detect the target DNA concentration.

1. The thiol bonds were selectively reduced by applying a negative potential for a fixed time, giving an amplified current/charge response to binding events. The target DNA concentration was determined by measuring the charge corresponding to the oxidation of the copper shell before selective reduction of the thiol bonds between the probe and nanowire, and between the capture strand and underlying electrode. Theoretically, there should be no copper left on the surface of the electrode as all of the nanowires have been freed into solution. Voltammetry of the electrode after the reduction step will confirm if the nanowires have been removed, as there should be no redox couple for copper oxidation and reduction present after removal of the nanowires. This approach allows a correlation between charge corresponding to copper oxidation and no. of nanowires bound to the surface of the electrode, which in turn corresponds to concentration of target DNA present.



Scheme 5.2: *Detection of target DNA approach 1: Selective reduction of thiol bonds to release nanowires into solution. In the above figure, the probe strand is shown in blue, the target DNA strand is shown in red, and the capture strand in black. Following application of a negative potential, the thiol bonds has been selectively reduced, and the DNA strands separated from the electrode and nanowire surfaces, and are now suspended in solution. The nanowires are no longer adhered to the surface of the electrode via the DNA hybridisation.*

2. The copper shell of the core:shell nanowire was selectively oxidised into solution by applying a positive potential for a fixed time. The distinct advantage of the core shell structure is that because the gold is not oxidised, it is possible for the nanowire to remain on the surface of the electrode throughout the amplified detection step which would not be possible with a pure copper nanowire. The target DNA concentration can be determined by measuring the charge corresponding to the oxidation of the copper shell before and after selective oxidation of the copper shell.



Scheme 5.3: *Detection of target DNA approach 2: Selective oxidation of copper shell into solution. In the above figure, the probe strand is shown in blue, the target DNA strand is shown in red, and the capture strand in black. Following application of a suitable positive potential, the copper shell of the nanowire should be removed into solution, leaving the nanowire still adhered to the electrode surface via the probe DNA strands on the gold core.*

5.2.4.2 Theoretical charge produced by selective oxidation of copper shell

From SEM images:

Average wire length: $3\mu\text{m}$

Average diameter of wire: 161nm (Au + Cu)

Total volume of wire: $\pi r^2 h$

$$= (\pi) (80.5 \times 10^{-7} \text{cm})^2 (3 \times 10^{-4} \text{cm})$$

$$= 6.1 \times 10^{-14} \text{cm}^3$$

Volume of Au tube only:

Average diameter of inner tube: 58nm

$$= (\pi) (29 \times 10^{-7} \text{cm})^2 (3 \times 10^{-4} \text{cm})$$

$$= 7.9 \times 10^{-15} \text{cm}^3$$

$$6.1 \times 10^{-14} \text{cm}^3 - 7.9 \times 10^{-15} \text{cm}^3$$

$$= 5.31 \times 10^{-14} \text{cm}^3 \text{ (volume of copper only)}$$

$$5.31 \times 10^{-14} / 7.11 \text{ (molar volume of copper)}$$

$$= 7.5 \times 10^{-15} \text{ moles of copper}$$

$$7.5 \times 10^{-15} \text{ moles} \times 96485 \text{ C/mol} = 7.2 \times 10^{-10} \text{C (per nanowire)}$$

Area of 2mm disc electrode: 0.0314cm^2

$$\text{Area of 1 NW} = 2 \times 10^{-10} \text{cm}^2$$

No. of NWs per electrode (assuming the nanowires are confined to the surface via DNA strands that orient the wires upright in a closely packed layer) = $0.0314 / 2 \times 10^{-10}$

$$= 1.49 \times 10^8 \text{ NWs/electrode}$$

$$1.49 \times 10^8 \text{ NWs} \times 7.2 \times 10^{-10} \text{C} = 10534 \times 10^{-6} \text{C}.$$

This corresponds to a theoretical maximum charge of 0.01C, assuming the electrode is totally covered with nanowires, and assuming all of the copper layer is removed from the gold:copper core:shell nanowire.

Comparatively, previous assays involving the electrocatalysis of hydrogen peroxide using DNA functionalised nanoparticles have yielded a max current of 8×10^{-6} A.²⁵ Converting this to charge in a (for example) ten second response time, this becomes 8×10^{-5} C. The concentration of target DNA would need to be 0.1 mM in order to generate this amount of charge through electrocatalysis.

The theoretical charge produced from this strategy is almost three orders of magnitude larger than from the electrocatalysis strategy. An amplification in signal of this magnitude, could it be achieved in practice, would allow for even small concentrations of DNA corresponding to single binding events to be detected.

In addition, the approach described above is advantageous over electrocatalysis as it does not require the addition of an additional reagent, i.e. hydrogen peroxide. This reduces the number of steps required to generate a result, which simplifies the use of the device for the end user.

5.2.4.3 Theoretical charge produced by reduction of thiol bonds

1. Cleaving bonds between DNA and electrode surface

The charge produced from the reduction of thiol bonds is calculated using the surface coverage of a close-packed monolayer of DNA (i.e. the capture strand DNA on the Au electrode surface).

$$\Gamma_{\text{DNA}} = 3 \times 10^{13} \text{ molecules/cm}^2 \text{ }^{29}$$

$$\frac{3 \times 10^{13}}{6.013 \times 10^{23}} = 4.981 \times 10^{-11} \text{ mol /cm}^2$$

$$\text{Area of 2mm disc electrode} = 0.0314 \text{ cm}^2$$

$$\Gamma = \frac{Q}{nFA}$$

$$4.981 \times 10^{-11} = \frac{Q}{(1)(96485)(0.0314)}$$

$$Q = 1.5 \times 10^{-7} \text{ C}$$

2. Cleaving bonds between probe strand DNA and nanowire surface

$$\text{Area of 1NW} = \pi r^2 = \pi (80.5 \times 10^{-7})^2$$

$$= 2.01 \times 10^{-10} \text{ cm}^2$$

$$1/2.01 \times 10^{-10} = 4.9 \times 10^9 \text{ nanowires per cm}^2$$

$$\text{Area of 2mm disc electrode} = 0.0314 \text{ cm}^2$$

$$= 4.9 \times 10^9 \times 0.0314 \text{ cm}^2 = 1.54 \times 10^8 \text{ nanowires on disc electrode surface}$$

$$\text{Fill factor for hexagonal close packing } 0.74 \text{ }^{30}$$

$$0.74 \times 1.54 \times 10^8 = 1.14 \times 10^8 \text{ NWs in hexagonal close packed layer on disc electrode}$$

$$1.14 \times 10^8 \times 2.01 \times 10^{-10} \text{ cm}^2 = 0.023 \text{ cm}^2$$

$$\Gamma = \frac{Q}{nFA}$$

$$4.981 \times 10^{-11} = \frac{Q}{(1)(96485)(0.023)} \quad Q = 1.1 \times 10^{-7} \text{ C, assuming full surface coverage}$$

of electrode with nanowires.

Total Q from reduction of both sets of thiol bonds: $2.6 \times 10^{-7} \text{ C}$.

Although the theoretical charge produced from this strategy is similar to the charge produced in an electrocatalysis assay, it provides an alternative, reagent-free method of determining target DNA concentration.

5.2.4.4 Selective reduction of thiol bonds

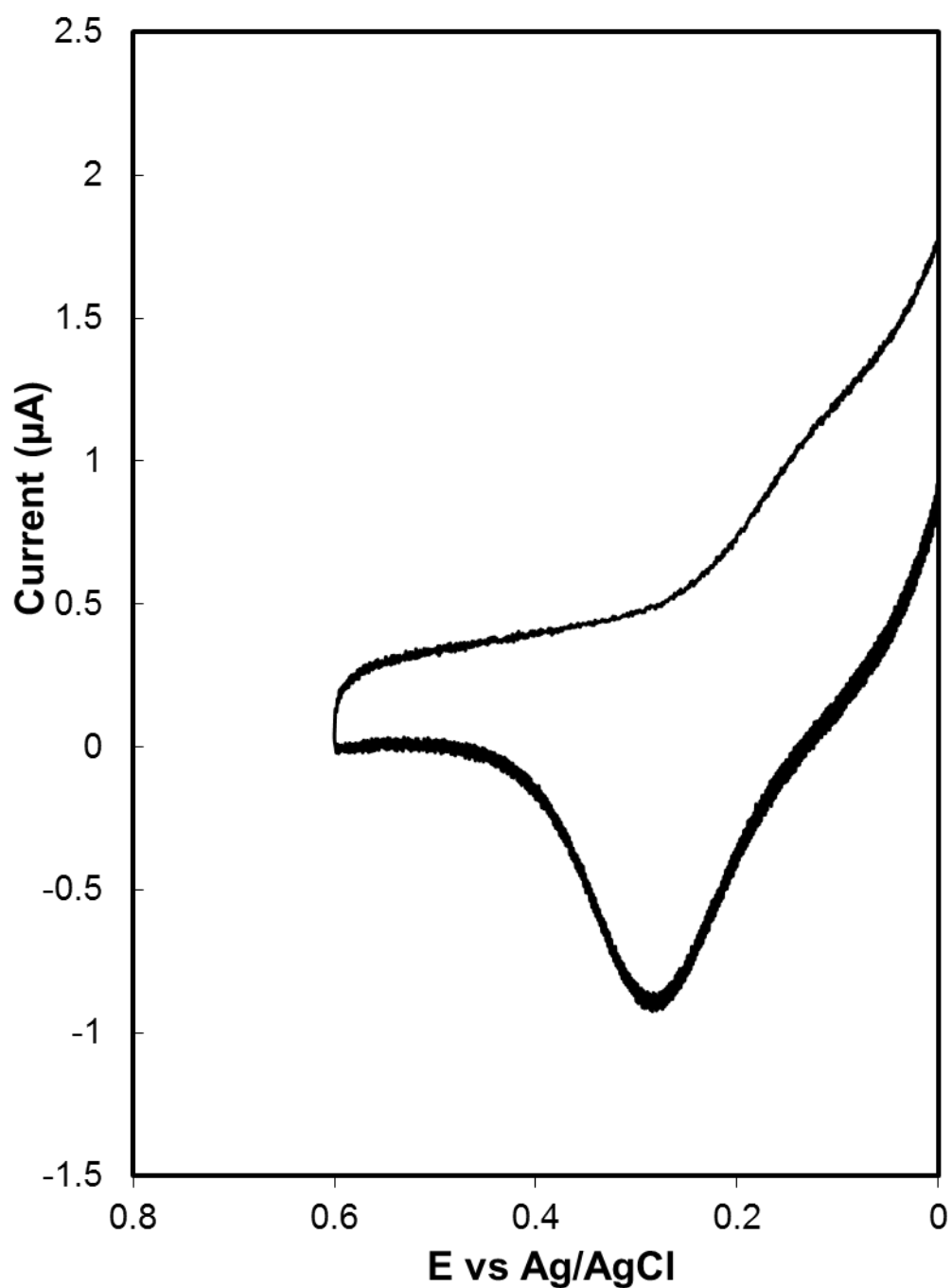


Figure 5.7: Cyclic voltammogram of a 2 mm diameter gold disc electrode after modification with capture strand DNA and hybridization with the target and core-shell nanowires labelled probe sequence where the target strand concentration is 100 μM . the supporting electrolyte was 0.01 M H_2SO_4 . The scan rate is 100 mVs^{-1} .

Figure 5.7 shows a cyclic voltammogram of a 2mm gold disc electrode which has been modified with capture strand DNA, which has been hybridised with target DNA, which has then been hybridised with core:shell nanowire labelled probe DNA. In contrast to Figure 4.17, the size of the oxidation and reduction peaks are greatly reduced. Both peaks have been shifted. The Cu (I) to Cu⁰ reduction peak seen at -0.124V in Figure 4.17 has been shifted to +0.104 V vs. Ag/AgCl in 3 M KCl in Figure 5.7, following decoration of the nanowires with probe DNA. The reduction of the area of this Cu (I) reduction peak may indicate that there are problems or difficulties in reducing the Cu (I) after modification with DNA.

There is also a shift in the potential of the oxidation peak from +0.081V in Figure 4.17 to +0.274 V vs. Ag/AgCl in Figure 5.7. The reduction in area of this peak indicates that it is more difficult to form this oxide following nanowire decoration with DNA, but there is still some oxide being formed on the shell of the nanowires.

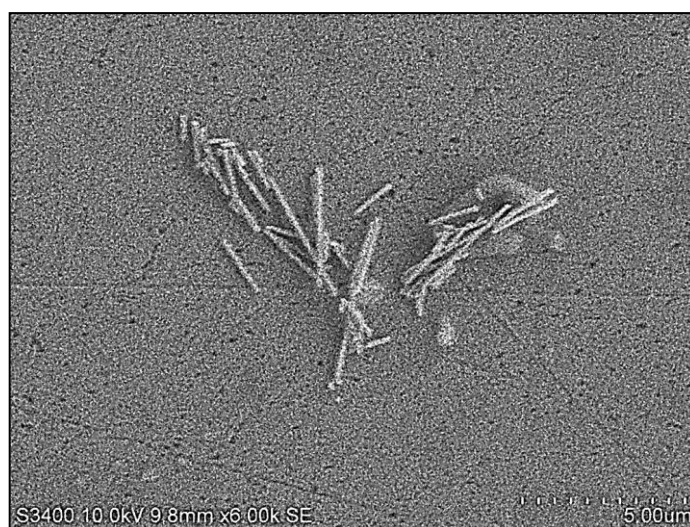


Figure 5.8: SEM image of nanowires bound to the electrode surface via the DNA hybridisation. This image was captured before the reduction of thiol bonds. The target DNA concentration is 10nM and the accelerating voltage is 10kV.

The thiol bonds were reduced by applying a fixed potential -0.3 V vs. Ag/AgCl in 3 M KCl for ten minutes. As can be seen in Figure 5.9, after a potential of -0.3 V is applied, both the copper oxidation and reduction peaks are greatly reduced.

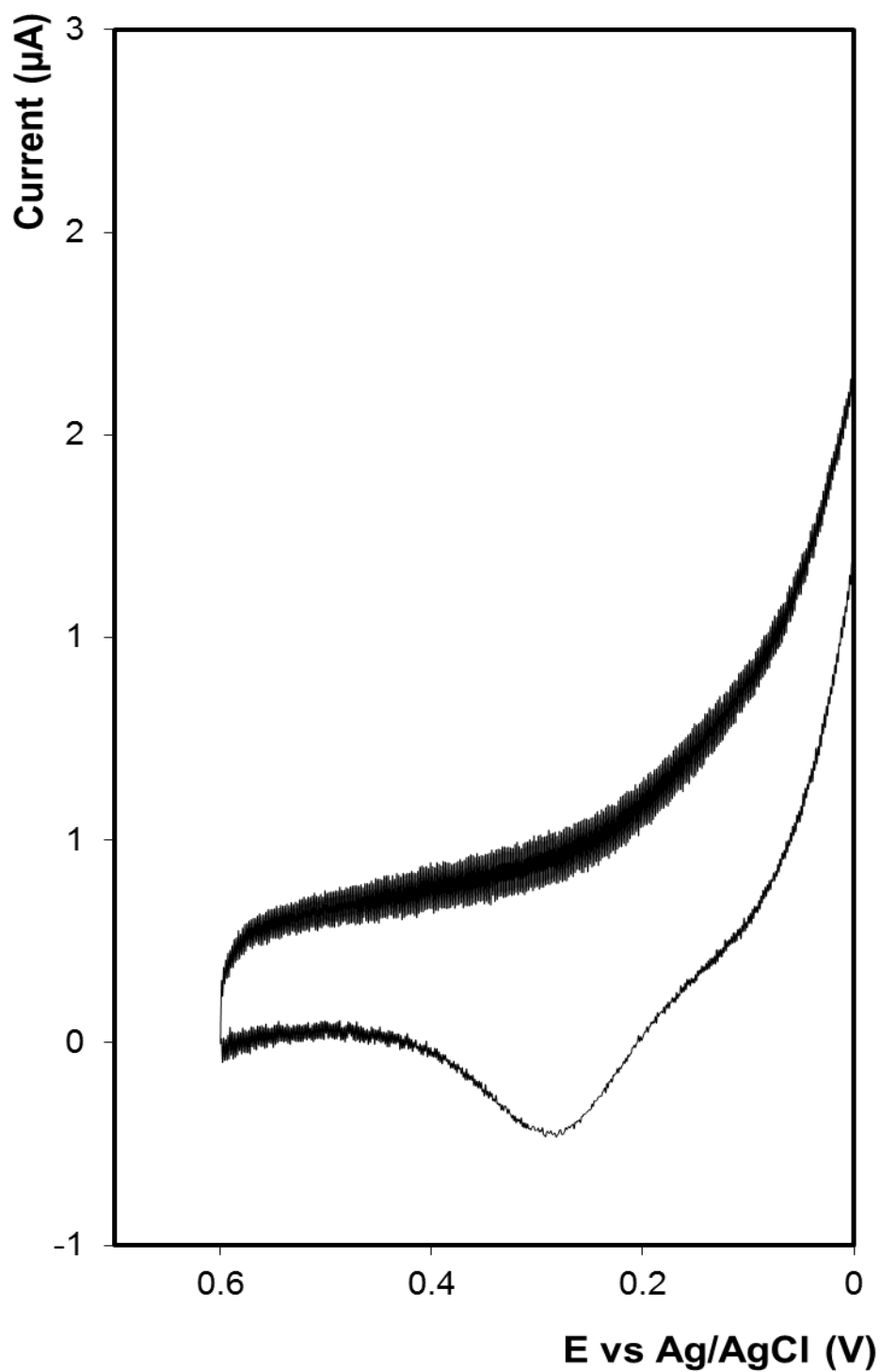


Figure 5.9: Cyclic voltammogram of a 2 mm diameter gold disc after the thiol bonds have been reduced from the nanowires and electrode. The supporting electrolyte is 0.01 M H_2SO_4 . The scan rate is 100mVs^{-1} . The reference electrode was Ag/AgCl in 3 M KCl.

SEM imaging showed that most of the nanowires were removed from the surface of the electrode following application of a negative potential for ten minutes.

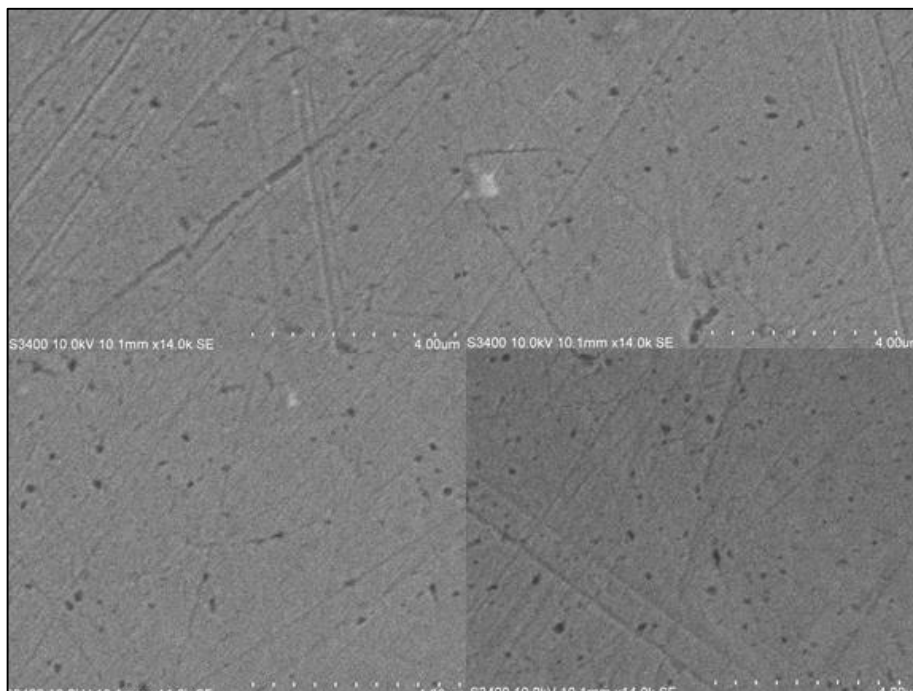
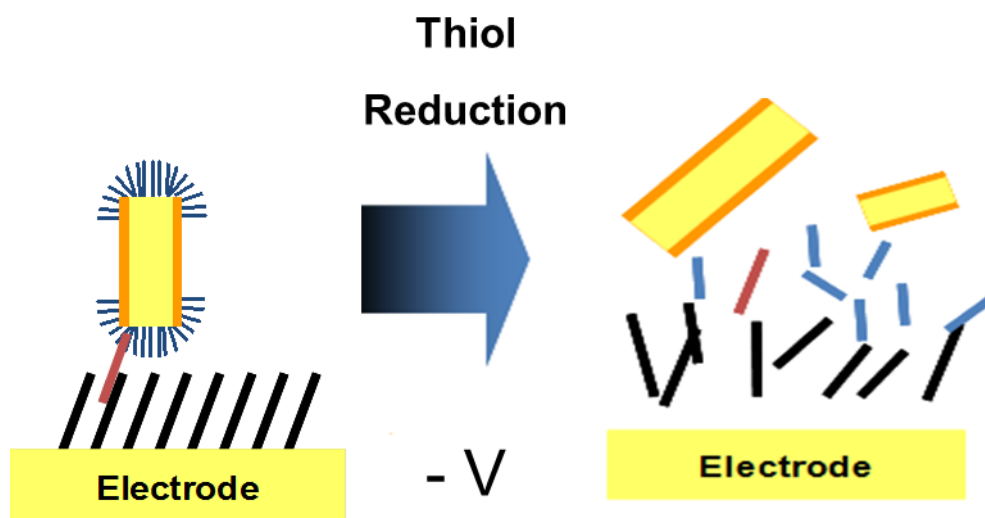


Figure 5.10: SEM images of DNA modified electrode surface following reduction of thiol bonds between nanowire and probe strand DNA. The accelerating voltage was 10kV.

While SEM imaging shows that most of the nanowires have been removed from the electrode surface, the voltammetry shows that a peak indicative of copper oxidation is still present at +0.280 V vs. Ag/AgCl in 3 M KCl. This peak was later determined to be as a result of macroscopic imperfections in the surface of the electrodes used, due to vigorous mechanical polishing during previous use. The electrodes were cycled in acidic electrolyte and the charge due to these imperfections was recorded for each electrode. This value was then subtracted from the charge values when the nanowires were present. This correction was performed on all data from Figure 5.10 to Figure 5.14.

5.2.5 Detection of DNA Approach 1 – Reduction of thiol bonds



Scheme 5.4: Schematic diagram of reduction of thiol bonds in order to detect DNA without need for target amplification. In the above figure, the probe strand is shown in blue, the target DNA strand is shown in red, and the capture strand in black.

The experiment was carried out with concentrations of target DNA ranging from 100 μ M to 1 nM.

The nanotube/DNA modified electrode was cycled six times in 0.1 M H_2SO_4 between $-0.2 \text{ V} \rightarrow 0.6 \text{ V}$ vs. Ag/AgCl in 3 M KCl. The area of the peak due to oxidation of copper was recorded, which corresponds to charge passed due to the copper. The presence of the copper peak indicates that nanowires have been adhered to the electrode surface via the complementary binding of the capture, target, and probe ssDNA strands.

The modified electrode was cycled again under the same conditions after the reduction of the thiol bonds, and a perceived copper oxidation peak was present in the voltammogram at a potential of $+0.280 \text{ V}$ vs. Ag/AgCl in 3 M KCl. The presence of this copper oxidation peak indicated that some population of the

nanowires remained on the surface of the electrode due to incomplete reduction of the thiol bonds. However, SEM imaging showed that all of the nanowires had been removed from the surface of the electrode. Voltammetry of the electrodes following removal of any residual DNA and mechanical polishing revealed that this peak was present even when the electrode was “cleaned”, indicating the presence of surface imperfections such as scratches arising from abrasive polishing, and wear and tear from use. The area of this residual peak was recorded, and subtracted from the values pertaining to the copper oxidation.

A curve of $\log [\text{DNA}]$ vs. difference in charge (before and after thiol reduction) was plotted to determine if there was a linear response between the target DNA concentration and the charge passed due to thiol bond reduction.

Table 5.4: *Average values for background corrected difference in charge, and the corresponding standard deviations*

Concentration DNA	Log DNA	Average difference in charge (μC)	Standard deviation
1.00E-4	-4	0.50	0.021
1.00E-5	-5	0.46	0.002
1.00E-6	-6	0.34	0.023
1.00E-7	-7	0.27	0.029
1.00E-8	-8	0.20	0.019
1.00E-9	-9	0.15	0.052

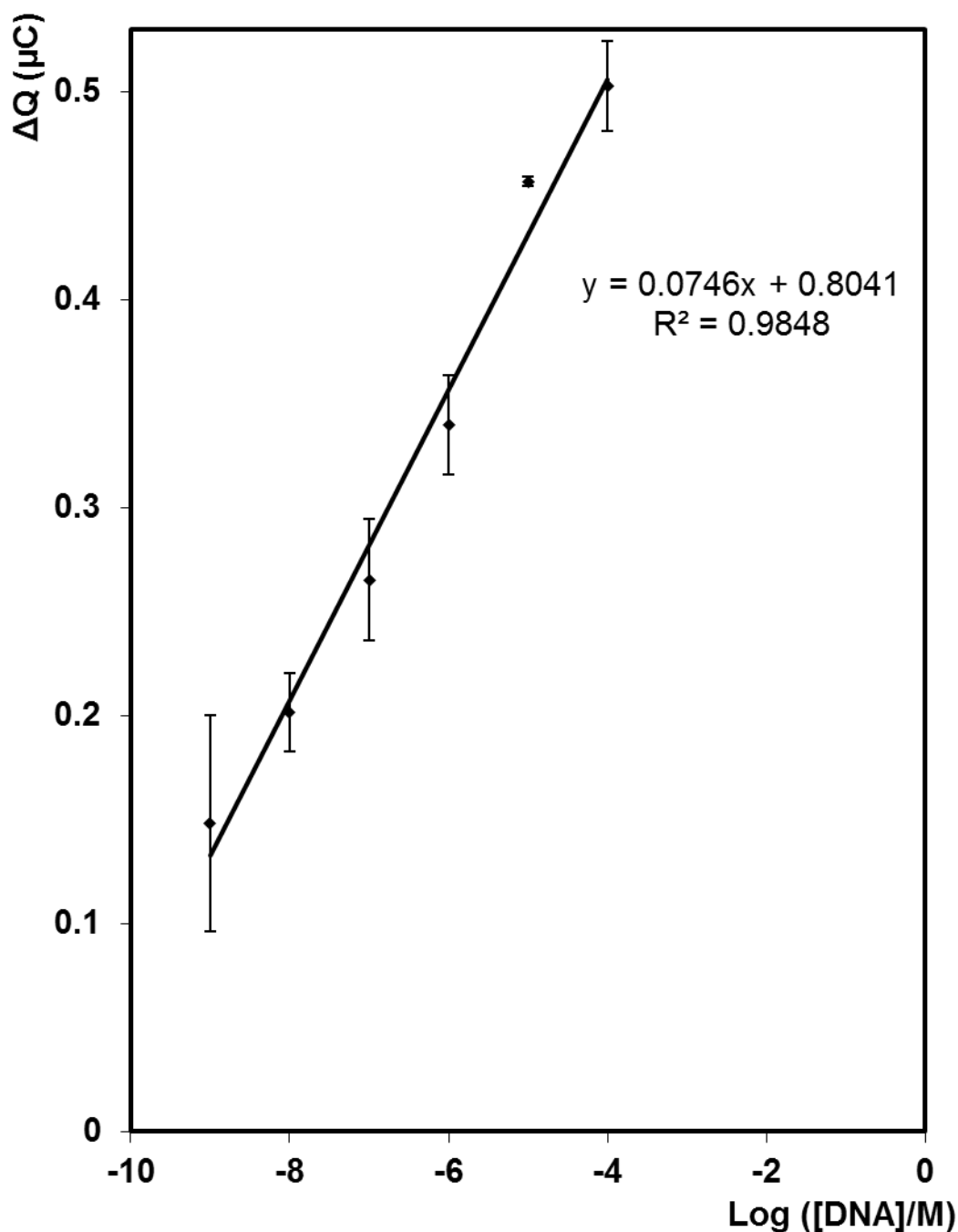
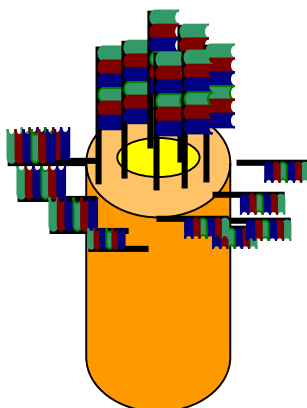


Figure 5.11: Calibration curve for the electrochemical detection of *Staph. Aureus mastitis* DNA on a 2 mm diameter bare electrode following hybridisation with probe DNA that is labelled with core:shell nanowires. ΔQ represents the difference in charge before and after the reduction of thiol bonds. Where error bars are not visible, they are smaller than, or comparable to, the size of the symbols. In this case, $n=3$ different batches of nanowires. The supporting electrolyte is 0.01 M H_2SO_4 and the scan rate is 100 mVs^{-1} .

An acceptably linear response is observed for concentrations of sequence-specific DNA from *S. aureus* from 1 nM to 100 μ M. The dynamic range of 5 orders of magnitude makes the detection strategy appealing for situations, e.g., infection, where the target concentration can vary widely. The maximum charge associated with this strategy has been shown to be $\sim 0.5 \times 10^{-6}$ C at a target DNA concentration of 100 μ M, which is 48% larger than the theoretical charge calculated from reduction of thiol bonds between capture strand and electrode surface plus probe strand and nanowire surface, assuming the thiol bonds were only present on the end of the nanowire. The fact that the actual charge response is larger than the theoretical charge may be due to a number of reasons.

1. The probe DNA has “leaked” into the polycarbonate membrane and has attached to a certain fraction of the walls of the nanowire, and the reduction of these extra thiol bonds is contributing some charge to the system. This would result in a nanowire that looks something like this:



Scheme 5.5: Schematic image of nanowire with probe strand decoration on a certain percentage of the walls of wire as well as the bottom of the wire

2. The large background charge associated with the underlying electrode has not fully been accounted for, and is actually contributing much more to the measured charge, possibly due to some other process occurring at the electrode surface. This is highly unlikely, because there are no known gold faradaic processes occurring at the potential that the thiols were reduced at, and gold is not active at the potential range that the area of the copper peak is measured.

3. The calculations also assume that one nanowire is immobilised by one target strand, while in reality, it is more likely to be 5-10 target strands immobilising one nanowire.

The leakage of the probe nanowire is most likely to be the cause of the extra charge.

The sensitivity of the assay is $0.0746 \mu\text{C dec}^{-1}$. The expected slope could be determined from the association constant of the target strand to probe strand, providing the concentration of probe strand on the surface of the nanowire and the concentration of the target-probe hybrid could be calculated. As the association constant³⁴ is large for the probe-target hybrid, 3.34×10^{22} , one would assume that the sensitivity of this approach would be very high.

5.2.5.1 Control Study

A control study was carried out in the absence of target *S. aureus* DNA. Core shell nanotubes were labelled with probe DNA as above, and a separate bare gold electrode was functionalised with a monolayer of capture strand DNA. This electrode was then immersed in a solution of probe-labelled nanotubes. This was repeated on 6 bare gold electrodes to probe the extent of non-specific adsorption.

In the absence of target DNA, the sequences of the probe strand and capture strand DNA are non-complementary to each other, and so ideally no binding should occur, which means that there should be no nanowires present on the surface of the electrode. In order to determine this, the electrode was cycled in 0.01 M H₂SO₄ from -0.2 → 0.6 V vs. Ag/AgCl in 3 M KCl, with a scan rate of 100 mVs⁻¹. The absence of a copper oxidation peak at approximately 0.235 V vs. Ag/AgCl in 3 M KCl and its corresponding reduction peak would confirm that no measurable non-specific binding of the probe and capture DNA has occurred.

As shown in Figure 5.12, there is no copper oxidation peak at approximately 0.23 V, which is what was expected. The absence of target DNA means that there should be no core:shell nanowires are present on the surface of the electrode, as the probe DNA sequence is only complementary to the sequence of the target DNA. The charge passed in the region where a copper oxidation peak would be expected in the voltammogram below is -2.788×10^{-9} C, a value that is three orders of magnitude lower than the charge passed when the target DNA is present. There is still some charge being passed, due to the possibility that a small number of non-specific binding events have occurred on the electrode surface.

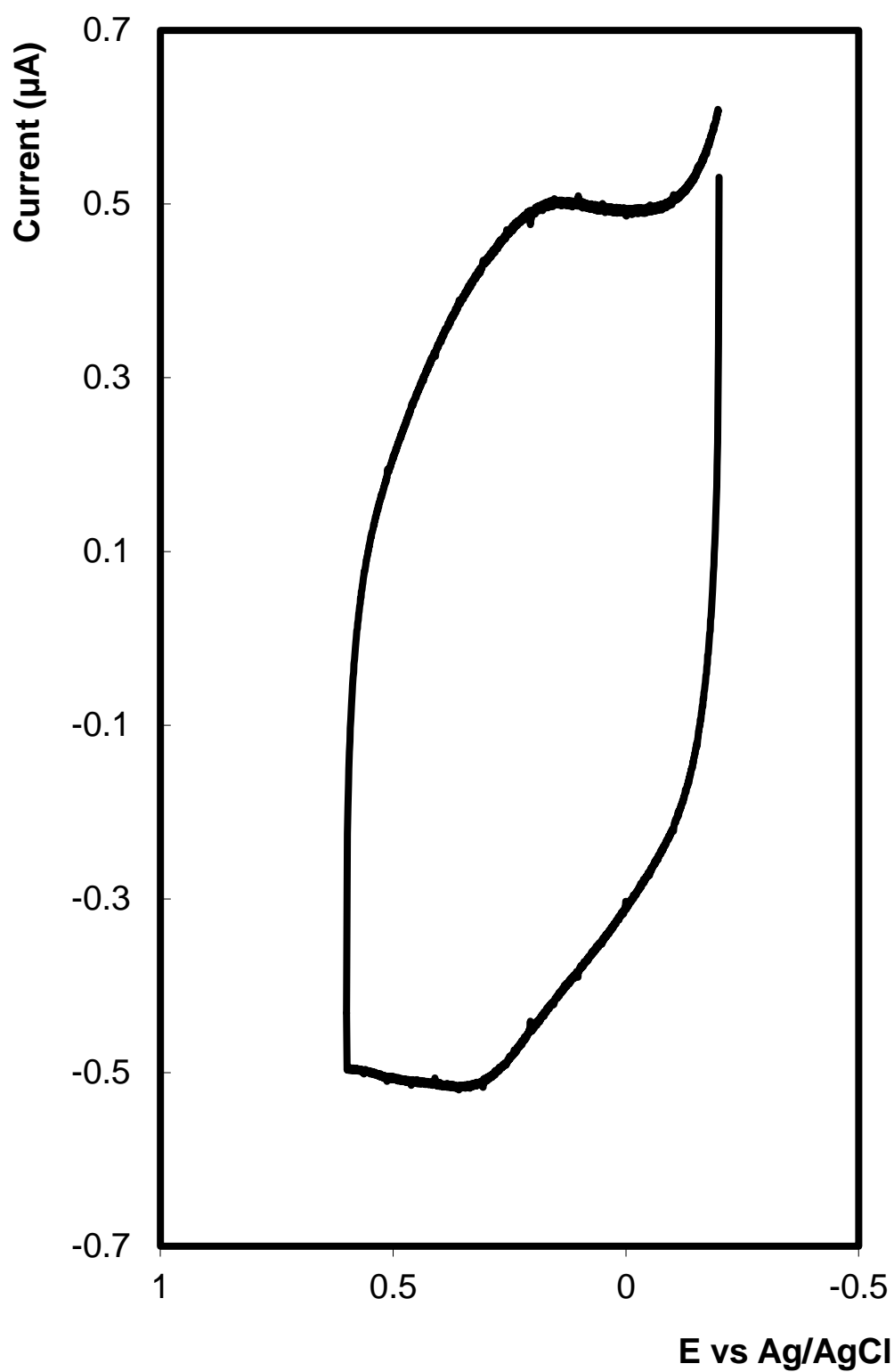


Figure 5.12: Cyclic Voltammogram of bare gold electrode modified with a monolayer of capture strand DNA and nanotube-labelled probe DNA. The supporting electrolyte is 0.01 M H₂SO₄ and the scan rate is 100mVs⁻¹

Table 5.5: *Charge passed by DNA functionalised electrode in the absence of target DNA*

Electrode No:	Charge passed	μC
1	8.49E-08	0.08
2	8.26E-08	0.08
3	8.01E-08	0.08
4	8.82E-08	0.09
5	8.07E-08	0.08
6	8.65E-08	0.09

As can be seen in Table 5.5, in the absence of target DNA the amount of charge passed is close to zero. This allows us to assume that there are very few, if any, core:shell nanowires present on the electrode surface. Any nanowires that are present are there because there may be some non-specific binding between the probe DNA strand and the capture DNA strand. However, the number of these non-specific binding events is very low, and as we see, there are a comparable number of these events occurring on each electrode.

The value of 0.08 μC passed represents a decrease of ~72% compared to the charge passed when for example, 100 μM of target DNA is present (charge passed is 0.5 μC at 100 μM DNA concentration).

These results show that the system will not give a response in the absence of target DNA, meaning that the number of non-specific binding events between the capture and probe strands of DNA is very low.

5.2.6 Selectivity of the Assay using 1 and 3 Base Mismatched target DNA

5.2.6.1 1 Base Mismatch

The assay was carried out as before, using a target strand of DNA with a single base mismatch from that of the *S. Aureus* DNA used previously. The target strand sequence used was: 5'-TGC-TAA-ACA-CTG-CCG-TTT-GAA-GTC-TGT-TTA-**A**AA-GAA-ACT-TA-3', where the A base marked in red is the mismatch. This strand of DNA (containing this specific mismatch) is not known to be present in a pathogenic organism. This mismatch was chosen to determine whether the assay could distinguish between the target mastitis DNA, and other strands of DNA that were similar in composition, but which contain a single base difference.

Table 5.6: Assay results for target DNA containing a single base mismatch

Concentration DNA (M)	Log [DNA]	Run 1 (μC)	Run 2 (μC)	Run 3 (μC)	Average (μC)	Standard Deviation
1.00E-4	-4	0.1198	0.3017	0.4370	0.2859	0.0957
1.00E-5	-5	0.1191	0.2685	0.3650	0.2508	0.0682
1.00E-6	-6	0.1122	0.2715	0.3399	0.2412	0.0483
1.00E-7	-7	0.1119	0.2516	0.2485	0.2034	0.0809
1.00E-8	-8	0.1117	0.1763	0.1700	0.1527	0.0356
1.00E-9	-9	0.1117	0.1350	0.0845	0.1104	0.0358

A graph of these average charges vs. log DNA concentration was plotted and is shown in Figure 5.13.

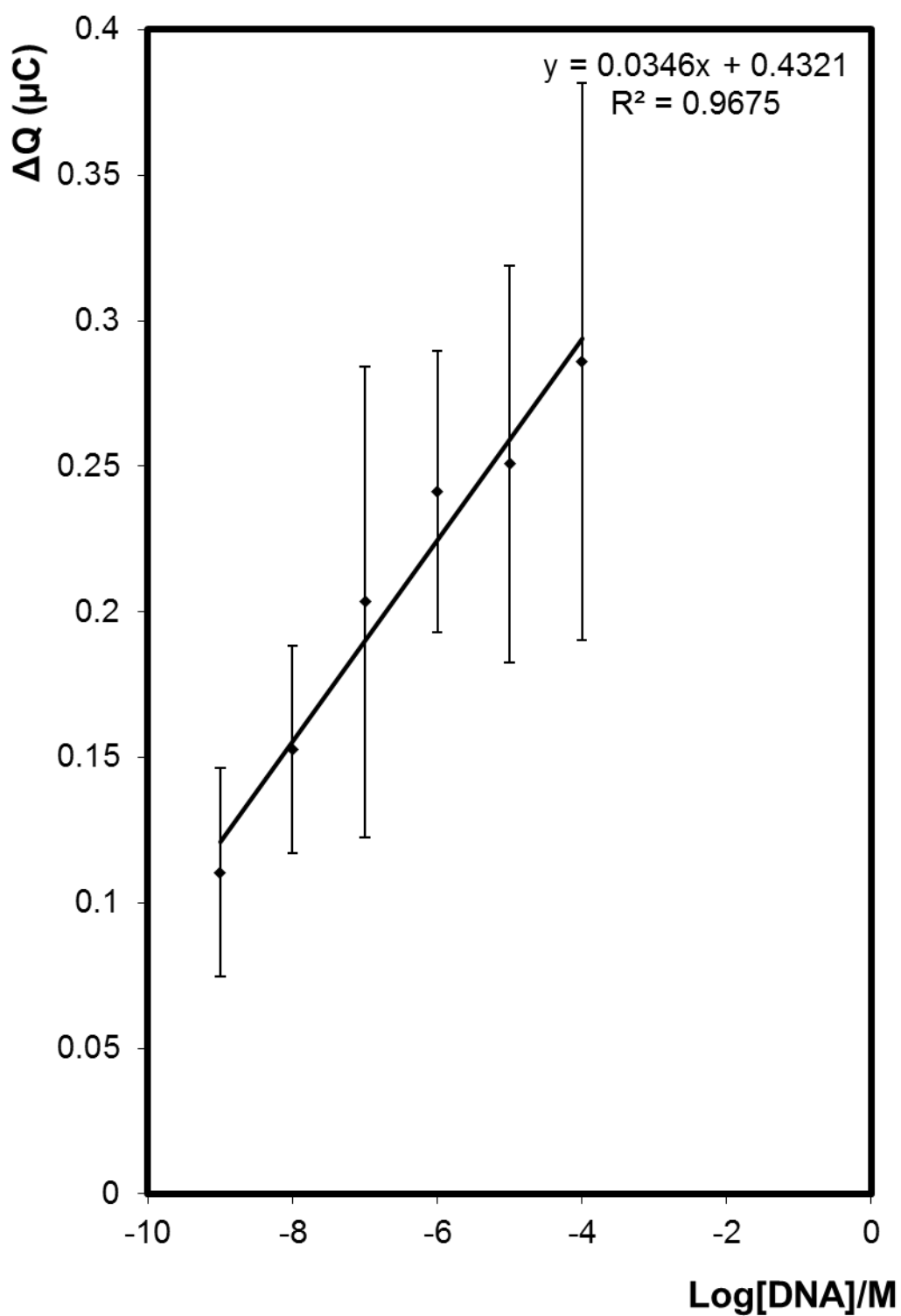


Figure 5.13: Calibration curve for the electrochemical detection of target DNA containing a 1 base mismatch on a 2 mm diameter bare electrode following hybridisation with probe DNA that is labelled with core:shell nanotubes. The supporting electrolyte is 0.01M H_2SO_4 .

The response of this assay to the 1-base mismatch DNA is linear over the range of concentrations from 100 μM to 1 nM, with a linear regression coefficient of 0.9675. This linear regression value shows an acceptable linearity, but is significantly worse than that observed for the fully complementary assay. Moreover, the slope of this assay is not the same as for the fully complementary DNA strand, see Figure 5.11. However, the magnitude of the charge is almost the same as that observed for the fully complementary DNA strand. This implies that the assay in its current form may not be sensitive enough to discriminate between a fully complementary DNA strand, and one containing a single base mismatch.

The sensitivity of the assay is reduced by approximately 40% compared to the assay using the fully complementary target DNA strand. From the calculated association constants, a decrease of 41% sensitivity was expected. However, the similar magnitude of the charge for both the mismatched and fully complementary DNA confirms that this assay may have problems discriminating between similar stands of DNA.

This assay has also been shown to be irreproducible, which would be a problem in application to real samples in a clinical setting. The standard deviation values for some DNA concentrations in this assay are quite large, in particular for the 100 μM concentration. As the hybridisation times have been optimised to ensure saturation of each surface, the standard deviation values for this assay are not due to differences in the number of DNA strands bound to the electrode surface. The large deviations may arise from numbers of nanowires on the surface of the electrode, due to different levels of non-fully complementary binding between the probe DNA and the mismatched target DNA.

Other possible causes include charge associated with electrode imperfections, or non-removal of all nanowires from electrode surface following thiol reduction.

5.2.6.2 3 Base Mismatch

This assay was then repeated using a target strand of DNA that contained three base mismatches. The sequence of this strand was: 5'-TGC-TAA-ACA-CTG-CCG-CTT-GAA-GTC-TGT-TTA-**GAT**-GAA-ATA-TA-3', where the GAT bases in red are the mismatched bases. This strand of DNA belongs to *Staphylococcus epidermidis*, a common strain of *S. aureus* that is present on the skin and in the mucosal flora of humans.³¹ It is not normally pathogenic, but patients with compromised immune systems can be at risk of developing a hospital acquired infection.³² As this strand of DNA is so commonly found in humans, there is a high chance of this strand of DNA being present in a sample of blood taken for *S. aureus* testing. It has also been known to give a positive result for mastitis.³³

Table 5.7: Assay results for target DNA containing three base mismatches

Concentration DNA (M)	Log [DNA]	Run 1 (μC)	Run 2 (μC)	Run 3 (μC)	Average (μC)	Standard Deviation
1.00E-4	-4	0.1741	0.23	0.228	0.2107	0.0317
1.00E-5	-5	0.1735	0.215	0.2118	0.2001	0.0231
1.00E-6	-6	0.1726	0.198	0.2021	0.1909	0.0160
1.00E-7	-7	0.1718	0.16	0.1868	0.1729	0.0134
1.00E-8	-8	0.1707	0.14	0.166	0.1589	0.0165
1.00E-9	-9	0.1698	0.12	0.1474	0.1457	0.0249

A graph of these average charges vs. log DNA concentration was plotted and is shown in Figure 5.14.

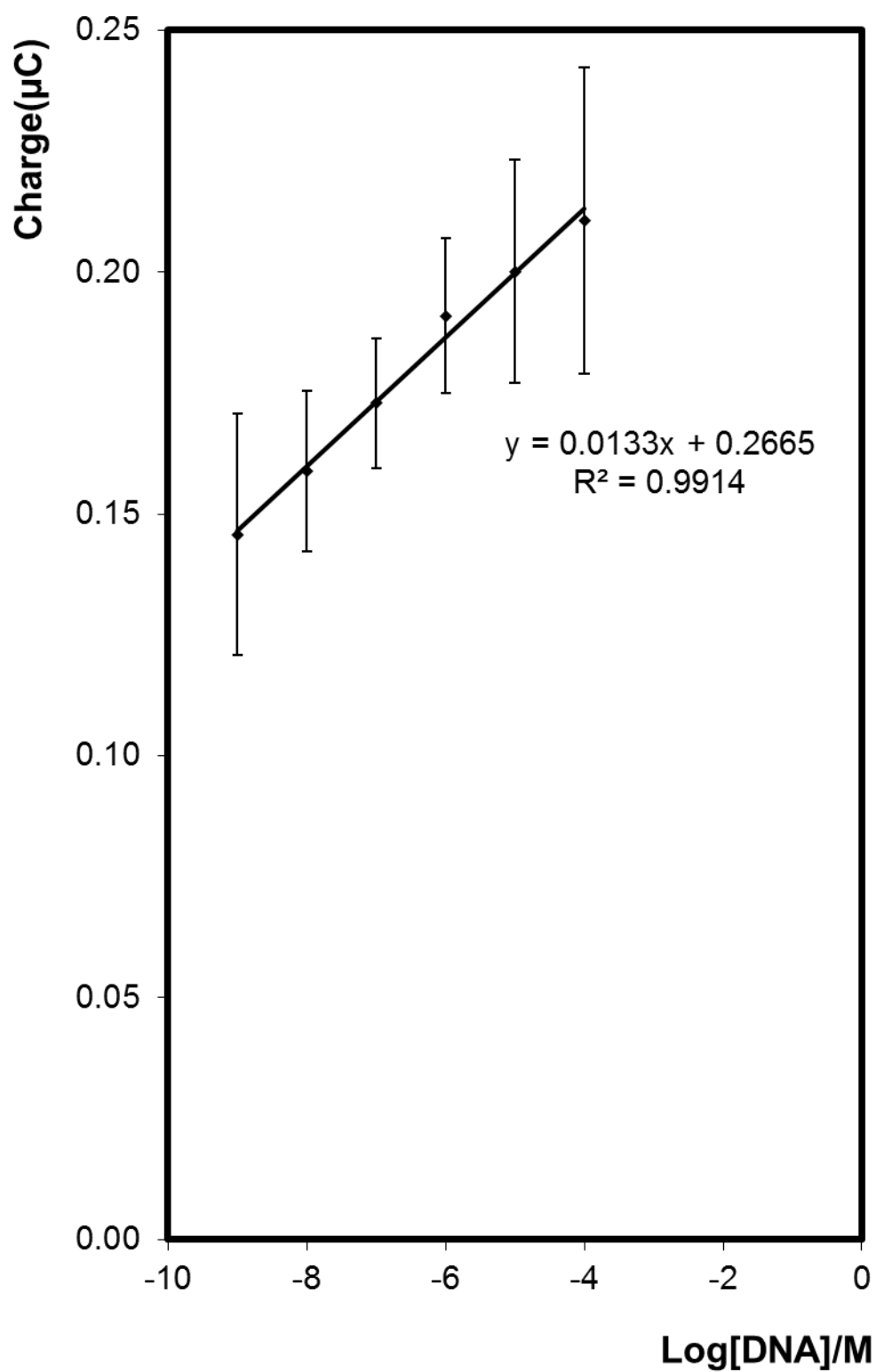


Figure 5.14: Calibration curve for the electrochemical detection of target DNA containing 3 base mismatch on a 2 mm diameter bare electrode following hybridisation with probe DNA that is labelled with core:shell nanotubes. The supporting electrolyte is 0.01M H_2SO_4 .

A linear relationship was fit to this data, as this is the expected response, however the reproducibility of the data is such that it cannot discriminate between target concentrations of 1×10^{-6} M and 1×10^{-7} M.

The response of this assay to the 3 base mismatch DNA is linear over the range of concentrations from 100 μ M to 1 nM as it was in both the fully complementary assay and the one base mismatch assay. The slope of close to zero indicates that this assay has extremely low sensitivity, and there is no difference in the charge passed when the concentration of 3 base mismatched DNA strands is systematically varied. The change in charge between the lowest and higher concentration is so low (0.07C over six orders of magnitude of DNA concentration), which implies that this approach will give approx. the same response regardless of the actual concentration of the mismatched DNA present in the sample. This shows that this assay is highly selective for the fully complementary target DNA strand, and that the concentration of a 3 base mismatched ssDNA strand in the sample will not impact the charge. However, there is a large background charge associated with this assay whose source is difficult to identify.

Statistically, the slope is indistinguishable from zero, which implies that the sensitivity of this assay is very low. The association constant³⁴ for the fully complementary target sequence for the probe strand is $\sim 2 \times 10^{55}$, while the association constant³⁴ for the three base mismatch target strand is $\sim 7.86 \times 10^{11}$. These values are calculated based on complementary base pairing between most bases. The actual association constant may be higher due to the presence of more complementary base pairs than were used to calculate this value.³⁴

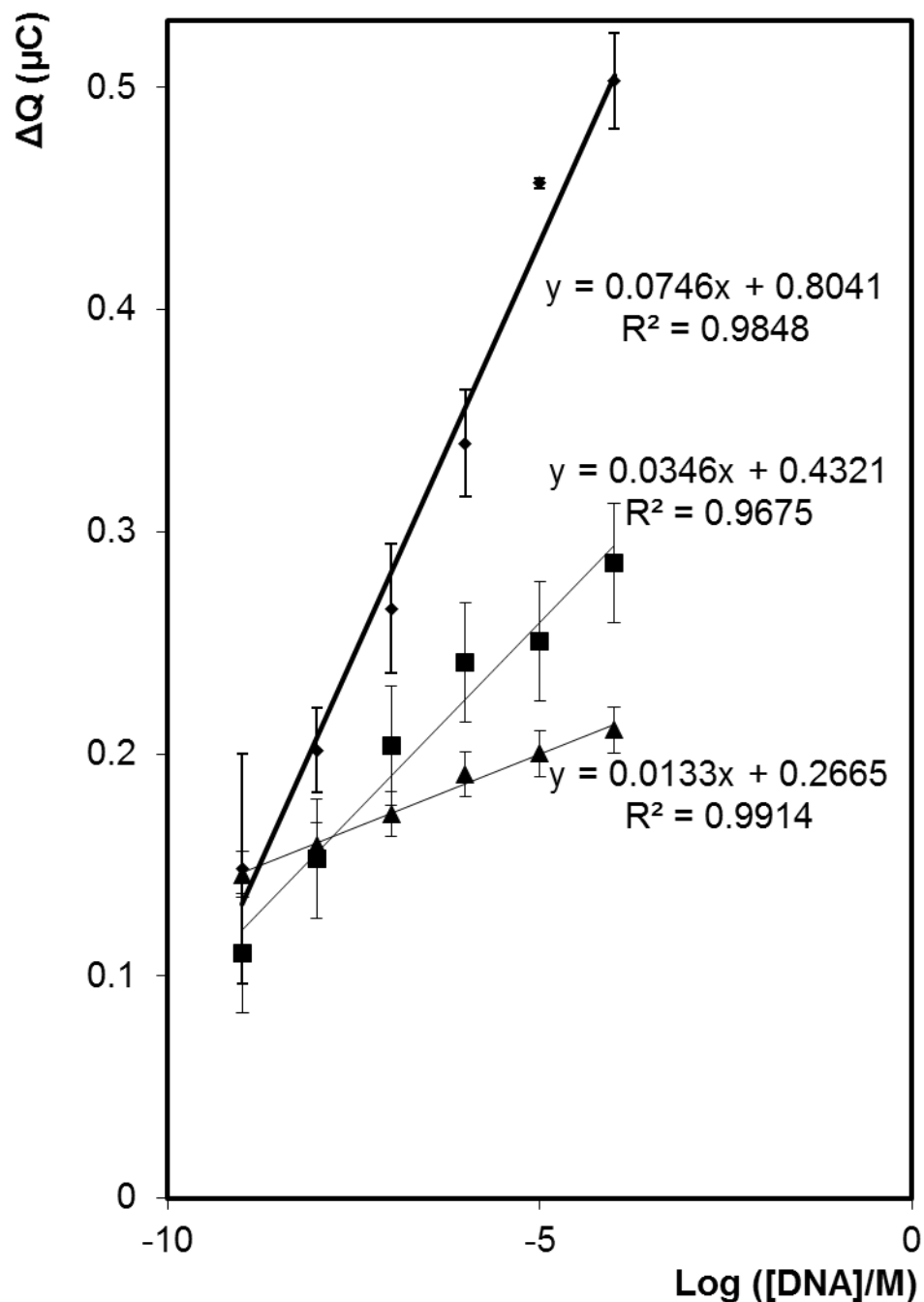


Figure 5.15: Electrochemical detection of sequence-specific *Staphylococcus Aureus* pathogen DNA concentration; (\blacklozenge) represents a fully complementary target DNA sequence; (\blacksquare) represents target DNA containing a single base mismatch; (\blacktriangle) represents target DNA containing 3 base mismatches. The Y axis is the difference in charge before and after reduction of thiol bonds. Where error bars are not visible, they are smaller than, or comparable to, the size of the symbols. In this experiment, $n = 3$ for different batches of nanowires.

A comparison plot of the response of the assay to fully complementary target DNA, single base mismatch DNA and three base mismatch DNA is presented in Figure 5.15.

As shown, the reproducibility of the assay is very poor. The deviations within the assay may be due to the poor control over how many nanowires can be synthesised per template, and possible loss of nanowires during the template removal steps. There is also the possibility of variations in the numbers of probe strands binding to the mismatched DNA from run to run.

The overlap in charge passed at low (1nM) concentration of target DNA between all three assays suggests that this concentration of DNA may be the lower limit of detection for this thiol reduction approach. This is a relatively disappointing result in terms of low-concentration detection, as DNA is normally present in whole blood samples at around fM (10^{-15}) concentrations.³⁵ While the DNA concentration may be increased in blood samples of patients infected with a disease, this lower limit of detection is not sensitive enough to detect the presence of the pathogen early in infection.

5.2.7 Detection of DNA Approach 2 – Selective oxidation of copper shell

Assuming that one target strand of DNA immobilises one probe-decorated nanowire, there will be a signal generated that is associated with that single binding event. A large charge will be associated with the removal of the entire copper shell. The volume of the copper shell is $4.297 \times 10^{-14} \text{ cm}^3$; and dividing by the molar volume of copper 7.11 mol/cm^3 , gives 6.045×10^{-15} moles of copper available to remove from each nanowire. Each mole corresponds to 96485 C, so the charge per nanowire will be $5.83 \times 10^{-10} \text{ C}$. The maximum number of nanowires that could be present on a 2mm diameter gold disc electrode is 1.49×10^8 wires, with a charge of $5.83 \times 10^{-10} \text{ C/wire}$ gives a potential maximum charge of 0.086 C, or 86867 μC . A charge this large represents a massive amplification in the analytical signal, which would improve the sensitivity of the assay even at low concentrations of target DNA.

The electrode was functionalised with capture strand and target strand as before, which was then hybridised with nanowire-labelled probe strand. This DNA-nanowire modified electrode was cycled in 0.01 M H_2SO_4 to confirm the presence of nanowires by measuring the charge associated with the copper oxidation peak.

SEM imaging was used to confirm that the nanowires were confined to the electrode surface via the DNA hybridisation.



Figure 5.16: SEM image of probe DNA labelled nanowires confined to the surface of a gold electrode functionalised with capture and *InM* target DNA containing a 1 base mismatch via DNA hybridisation. Accelerating voltage is 10kV.

A positive potential of +0.3 V vs. Ag/AgCl in 3 M KCl was applied to the electrode, initially for ten minutes, in order to determine whether the copper shell could be removed into solution.

SEM characterisation showed that the nanowires were still confined to the surface of the electrode. The resolution of the SEM was such that it could not be confirmed whether a small monolayer of the copper shell had been removed during this ten minute oxidation step. The presence of nanowires after ten minutes confirmed that the thiol bonds between the DNA and the nanowire were not disturbed by the applied potential.



Figure 5.17: SEM images of probe-labelled nanowires confined to electrode surface of a gold electrode functionalised with capture DNA and 1nM target DNA containing a 1 base mismatch via DNA hybridisation following copper shell oxidation at +0.3 V vs. Ag/AgCl in 3 M KCl for ten minutes. The accelerating voltage is 10kV.

Following oxidation of copper for ten minutes, it is clear that the nanowires are still on the surface of the electrode.

The oxidation of copper was performed again for a longer period of time to determine whether all of the copper shell could be removed. This time the positive potential was applied for five hours. The potential is chosen so that oxidation of copper occurs, but as no redox processes are known to occur on gold at this potential, it should not affect the remaining gold core of the nanowire.

By monitoring the charge as the oxidation was occurring, it should be possible to pinpoint when the last of the copper shell was fully oxidised from the nanowire surface.

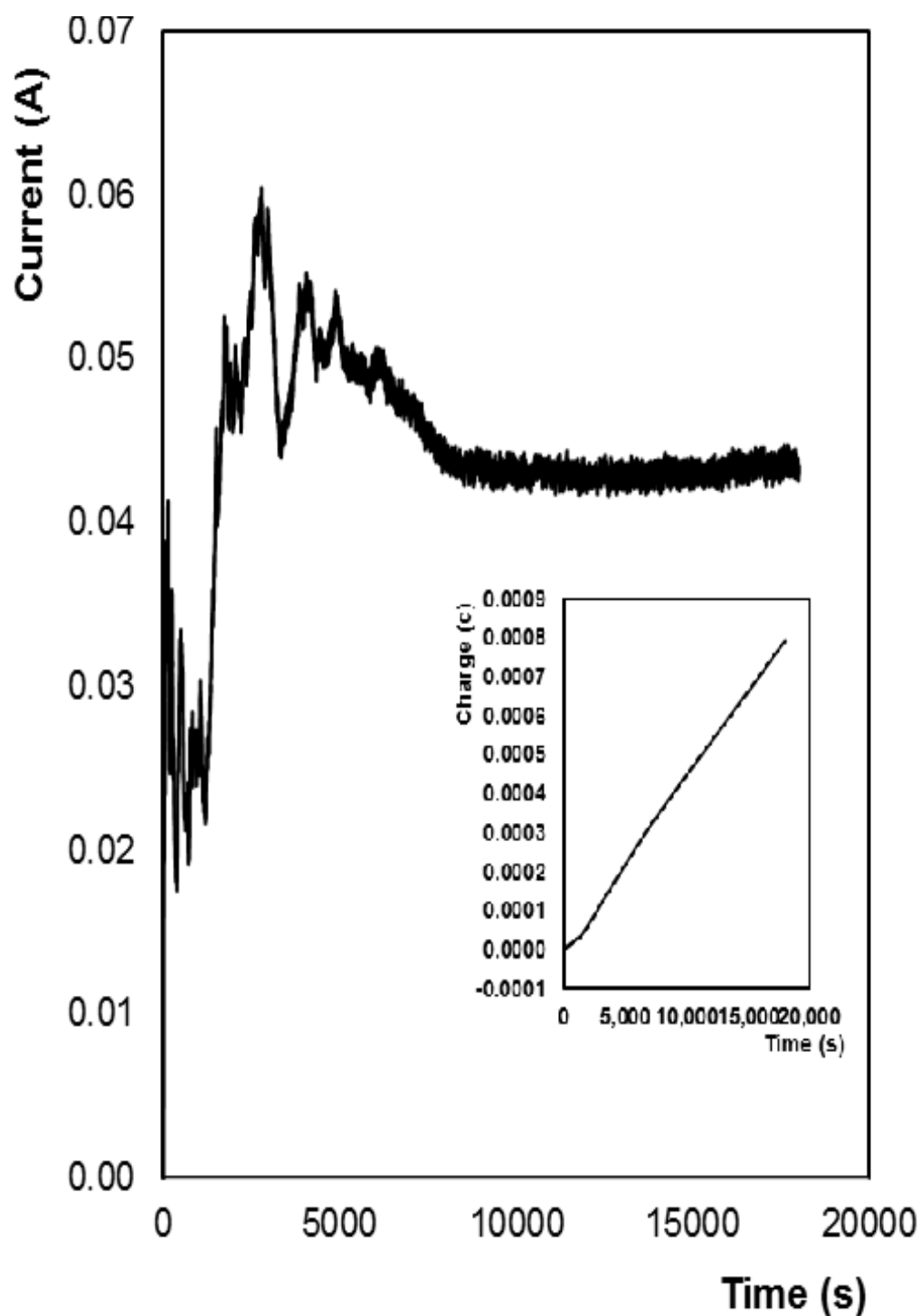


Figure 5.18: Current-time transient for selective oxidation of copper shell of core:shell nanowire at a fixed potential of +0.3 V vs. Ag/AgCl in 3 M KCl for 5 hours in 0.1M H_2SO_4 . Inset: Charge vs. Time transient following selective oxidation of copper shell at fixed potential of 0.3 V vs. Ag/AgCl in 3 M KCl for 5 hours.

This transient shape is as it was expected, i.e. that the current initially increases as the copper is oxidised, and then gradually decreases and plateaus off as all of the available copper is fully.

It was expected that after all of the copper was removed from the shell of the nanowire that the charge would reach a point where an oxidation current would not be observed, as no processes were occurring on the surface of the gold core at this potential, and all of the copper would be oxidised. As can be seen in the charge time transient, inset of Figure 5.18, the charge continues to increase steadily over the five hours. It was expected that as the copper shell was oxidised at the surface of the nanowire, the charge would begin increase more slowly, and then plateau off or start to decrease as the copper was fully oxidised.

SEM imaging was performed on the electrode surface to try to determine if the copper had indeed been removed from the nanowire surface.

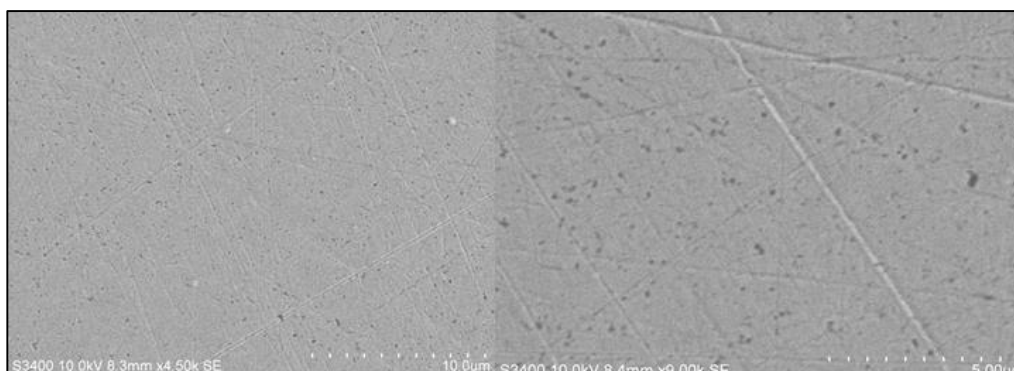


Figure 5.19: SEM images of electrode surface following oxidation of copper shell from nanowire surface for five hours at +0.3V. The accelerating voltage is 10kV.

As can be seen from the images above, it appears that most, if not all, of the nanowires have been removed from the surface of the electrode. This result is somewhat unexpected, as the potential applied is one that is not in the region where it will induce reduction or oxidation of the gold nanowire, and should not induce removal of thiol bonds from the nanowires or the electrode surface.

It appears that the charge increases steadily until approximately 1600 seconds before increasing more rapidly. This may be the point at which the nanowires are removed from the surface of the electrode, and due to some background process occurring at the electrode surface, the charge continues to increase indefinitely.

As it was not possible to measure the charge associated with the oxidation of the copper shell, it was not possible to equate the charge to a concentration of target DNA present on the surface of the electrode. Because of the unknown background process occurring in this experiment it is not possible to construct a calibration curve for this assay.

Future work on this assay could include EDX characterisation of the nanowires after oxidation of copper for short times to identify the time point at which the copper has been fully removed from the nanowire surface.

5.3 Conclusion

In conclusion, gold nanowires and nanotubes were created by electrodeposition within the pores of a track etched polycarbonate membrane. Prior to their release from the membrane, the nanowires exist in a highly aligned array with diameters of 70 ± 20 nm and length of 7.1 ± 2.7 nm.

The top end of the gold nanowires was selectively functionalised with probe DNA complementary to that specifically found within *S. aureus* mastitis. Significantly, the DNA modified nanowires can be released by dissolving the template with dichloromethane without damaging the adsorbed DNA. In a DNA sandwich assay, the current associated with reduction of hydrogen peroxide at the gold nanowires varies linearly with the concentration for target concentrations between 1 fM and 10 μ M. The sensitivity of the assay decreases by approximately a factor of 1.5 when gold nanotubes that are uniformly decorated with probe strand DNA are used suggesting that access of the peroxide to the gold surface influences the current observed.

Significantly, the limit of quantitation is 1 fM, and aM concentrations of DNA can be detected. The dynamic range is very wide, 10 orders of magnitude, reflecting the relatively larger current generated by a single nanowire, its small footprint, relatively large (0.03 cm^2) working electrode area and a relatively low association constant.

While the calibration sensitivity is reproducible within a single batch of nanowires (<5%), achieving a good reproducibility between batches is challenging. These inter-batch deviations most likely arise from differences in wire length, e.g., due to wires breaking during removal from the template, or due to differences in pore-density between membranes used as templates.

The excellent electrocatalytic activity of the modified gold electrode towards hydrogen peroxide meant that the electrode could be served as a new biosensing platform that would provide operational access to a great deal of DNA. The application of the nanowires to the reduction of hydrogen peroxide also served to prove that the surface of the nanowires can be functionalised using 5' thiolated DNA, which can be used to detect pathogenic DNA. Moreover, the good

biocompatibility and large surface area of gold nanowires make them ideal for adsorption of DNA, and other biomarkers such as enzymes, proteins and RNA.

While this work succeeded in developing a functioning biosensor, there are some further experiments that would need to be performed before successful application to a commercial biosensing platform, as well as some batch to batch variability issues which could be improved by changing the template used to either anodic alumina, or by creating a template using photolithographic methods.

In addition, a templated electrodeposition strategy has shown to be an efficient route to creating gold-copper core-shell nanowires. Prior to their release from the polycarbonate template, the nanowires exist as a highly aligned array with uniform diameters (147 ± 22 nm) along the entire lengths of the wires (3.2 ± 0.1 μ m). The shell thickness is approx. 44.5 ± 5 nm.

By reducing the thiol bonds between the DNA and the electrode following a DNA sandwich assay, the concentration of DNA from the pathogen *Staph. Aureus* can be detected at nanomolar concentrations. The charge generated from this approach was found to be 0.5 μ C at the highest concentration of target DNA, which is much lower than previous methods of DNA detection using catalytic metal nanowires and nanoparticles. This charge is larger than expected assuming the probe DNA was hybridised only to the bottom of the nanowire, so it is assumed that some leakage of the probe DNA occurred, and probe strands are decorating some percentage of the outer wall of the nanowire. The sensitivity of the assay was much lower than expected, which may be due to a number of factors:

1. Binding of a nanowire-labelled probe strand blocks a certain percentage of target strands in close proximity from hybridisation with a separate nanowire. (Due to steric issues with the large surface area of the nanowire, it may be possible that not all of the target DNA is being hybridised with probe at all).
2. The calculations in this work assume that the nanowires are vertically aligned in a dense close-packed layer following target-probe hybridisation. As the nanowires are so large, they may actually be too heavy to be held upright by the dsDNA, and may actually be lying on the surface of the electrode. This may then cause several

target strands to be blocked off from hybridisation with the probe DNA, which may mean that the concentration of DNA that is being detected is actually much lower than the concentration present on the electrode surface.

This assay has shown to be selective towards ssDNA strands containing a 1 and 3 base mismatch to the target DNA. However, there appears to be a large background charge contributing to the overall measurement in the assay, and it is not known where this contribution is coming from.

Additionally, the reproducibility of the assay is very poor. The deviations within the assay may be due to poor control over how many nanowires can be synthesised per template, and possible loss of nanowires during the template removal steps. There is also the possibility of variations in the numbers of probe strands binding to the mismatched DNA from run to run.

The overlap in charge passed at the lowest (1nM) concentration of target DNA between all three assays suggests that this concentration of DNA may be the lower limit of detection for this thiol reduction approach. This is a relatively disappointing result in terms of low-concentration detection, as DNA is normally present in whole blood samples at around fM (10^{-15}) concentrations.³⁶

The sacrificial “stripping” of the outer metal shell of the nanowire has been identified as an alternative detection strategy for nucleic acid detection, which is important for application in a multiplexed assay. Use of this method could allow for several types of target DNA to be detected in a single assay just by manipulating the properties of different metals. The charge associated with the removal of the entire copper shell is $\sim 86000 \mu\text{C}$, which represents a massive amplification in signal over previous electrocatalysis assays. Unfortunately, a sufficient oxidation time could not be identified that allowed just the copper shell of the nanowire to be removed. After five hours, the entire nanowire was removed from the surface of the electrode. Investigation of the current-time transient and the charge-time transient identified an unknown background process that is occurring that is not fully understood at this time.

The ability to produce oxides at a controlled surface coverage on the copper nanowires makes them useful for electronics applications where the gold

conducting core and semiconducting copper oxide shell open up some interesting new possibilities.

5.4 References

- ¹ V. Gubala, L. F. Harris, A. J. Ricco, M. X. Tan and D. E. Williams, *Anal. Chem.*, 2012, **84**, 487-515.
- ² M. Hammar, T. Tyszkiewicz, T. Wadstrom and P. W. Otoole, *J. Clin. Microbiol.*, 1992, **30**, 54-58.
- ³ H. Okamoto, Y. Sugiyama, S. Okada, K. Kurai, Y. Akahane, Y. Sugai, T. Tanaka, K. Sato, F. Tsuda, Y. Miyakawa and M. Mayumi, *J. Gen. Virol.*, 1992, **73**, 673-679.
- ⁴ O. Zach, H. Kasparu, O. Krieger, W. Hehenwarter, M. Girschikofsky and D. Lutz, *Journal of Clinical Oncology*, 1999, **17**, 2015-2019.
- ⁵ M. Esteller, M. Sanchez-Cespedes, R. Rosell, D. Sidransky, S. B. Baylin and J. G. Herman, *Cancer Res.*, 1999, **59**, 67-70.
- ⁶ R. Ashida, K. Yamao, N. Mizuno, T. Sawaki, A. Arakawa, *Gastrointestinal Endoscopy*, 2010, **71**, .AB221-222.
- ⁷ G. Lina, Y. Piémont, F. Godail-Gamot, M. Bes, M. Peter, V. Gauduchon, F. Vandenesch and J. Etienne, *Clinical Infectious Diseases*, 1999, **29**, 1128-1132.
- ⁸ L. S. Schlesinger, S. C. Ross and D. R. Schaberg, *Medicine*, 1987, **66**, 148-156.
- ⁹ K. Becker, A. W. Friedrich, G. Lubritz, M. Weilert, G. Peters and C. von Eiff, *J. Clin. Microbiol.*, 2003, **41**, 1434-1439.
- ¹⁰ S. Jarraud, M. A. Peyrat, A. Lim, A. Tristan, M. Bes, C. Mougel, J. Etienne, F. Vandenesch, M. Bonneville and G. Lina, *Journal of Immunology*, 2001, **166**, 669-677.
- ¹¹ F. D. Lowy, *N. Engl. J. Med.*, 1998, **339**, 2026-2027.

- ¹² S.C. Nickerson, W.E. Owens, R.L. Boddie. *Journal of Dairy Science*, 1995, **78**, 1607-1618.
- ¹³ Nickerson SC. International Symposium on Bovine Mastitis. Indianapolis, IN, September, 1990. 82–91.
- ¹⁴ *Symptoms of mastitis* <http://www.dairyco.org.uk/technical-information/animal-health-welfare/mastitis/symptoms-of-mastitis/> (accessed May 2015)
- ¹⁵ C. Viguier, S. Arora, N. Gilmartin, K. Welbeck and R. O’Kennedy, *Trends Biotechnol.*, 2009, **27**, 486-493.
- ¹⁶ M. J. Waring, *J. Mol. Biol.*, 1965, **13**, 269-282.
- ¹⁷ *Propidium iodide* / Sigma-Aldrich (accessed May 2015)
- ¹⁸ I. Ghosh, C. I. Stains, A. T. Ooi and D. J. Segal, *Molecular Biosystems*, 2006, **2**, 551-560.
- ¹⁹ J. W. Liu and Y. Lu, *J. Am. Chem. Soc.*, 2003, **125**, 6642-6643.
- ²⁰ S. Kidambi, J. H. Dai, J. Li and M. L. Bruening, *J. Am. Chem. Soc.*, 2004, **126**, 2658-2659.
- ²¹ Z M. Zayats, R. Baron, I. Popov and I. Willner, *Nano Letters*, 2005, **5**, 21-25.
- ²² D. Suzuki and H. Kawaguchi, *Langmuir*, 2005, **21**, 8175-8179.
- ²³ A. Umer, S. Naveed, N. Ramzan and M. S. Rafique, *Nano*, 2012, **07**, 1230005.
- ²⁴ J. Wang, *Analyst*, 2005, **130**, 421-426.
- ²⁵ E. Spain, E. Brennan, H. McArdle, T. E. Keyes and R. J. Forster, *Anal. Chem.*, 2012, **84**, 6471-6476.
- ²⁶ M. Moskovits, *Reviews of Modern Physics*, 1985, **57**, 783-826.
- ²⁷ H. Cho, S. K. Kim, Y. Jung, J. Jung and B. H. Chung, *Chemical Communications*, 2011, **47**, 5756-5758.

- ²⁸ C. Russell, K. Welch, J. Jarvius, Y. Cai, R. Brucas, F. Nikolajeff, P. Svedlindh and M. Nilsson, *ACS Nano*, 2014, **8**, 1147-1153.
- ²⁹ A. W. Peterson, R. J. Heaton and R. M. Georgiadis, *Nucleic Acids Res.*, 2001, **29**.
- ³⁰ Structures of Metals: Close packing,
www.seas.upenn.edu/~chem101/sschem/metallicsolids.html (accessed September 2013)
- ³¹ P. D. Fey and M. E. Olson, *Future Microbiology*, 2010, **5**, 917-933.
- ³² W. Levinson, *Review of Medical Microbiology and Immunology* (11th ed.) McGraw-Hill. New York, 2001. Pp. 94–99.
- ³³ S. Pyorala and S. Taponen, *Vet. Microbiol.*, 2009, **134**, 3-8.
- ³⁴ PrimerQuest® program, IDT, Coralville, USA.
<http://www.idtdna.com/Scitools>. (accessed May 2015)
- ³⁵ A. V. Cherepanova, S. N. Tamkovich, O. E. Bryzgunova, V. V. Vlassov and P. P. Laktionov, *Ann. N. Y. Acad. Sci.*, 2008, **1137**, 218-221.
- ³⁶ A. V. Cherepanova, S. N. Tamkovich, O. E. Bryzgunova, V. V. Vlassov and P. P. Laktionov, *Ann. N. Y. Acad. Sci.*, 2008, **1137**, 218-221.



6. CONCLUSIONS AND FUTURE WORK

6.1 Summary

This thesis focuses on the synthesis of nanowires and nanotubes via a templated electrodeposition approach, and the application of these nanomaterials to the detection of ss-DNA associated with the pathogen *S. aureus mastitis*.

As the concentrations of biomarkers such as ss-DNA are extremely low at the early stages of any disease, an increased sensitivity and lower limits of detection are essential for successful detection. Biosensors are promising devices which are superior to traditional analytical detection techniques due to their fast response time, portability, ease of use, and specificity. It is expected that these devices will have a major role in the field of self-care or point-of-care in the near future. Thus, this work is focussed on improving the sensitivity of DNA biosensors through the use of metal nanomaterials.

Following chapters that review the current templates and synthesis methods used to deposit nanowires and present the experimental strategies employed, Chapter 3 reported on the synthesis and characterisation of gold nanowires and nanotubes. A range of deposition times were investigated, and it was found that the length of the nanowires increased with increasing deposition time, confirming that in electrodeposition of nanowires and nanotubes, the length is controlled by how long the potential is applied for. The standard deviations of the lengths of the deposited nanowires were fairly large, which suggests that although the lengths of the wires are determined by the deposition time, there may be large variations in the lengths of wires deposited from batch to batch; as although the available surface area of membrane, solution concentration and volume, and deposition time can be controlled, there can be large variations in the charge passed during deposition due to factors controlled by the potentiostat, and issues with the electrodes used. The lengths of the nanotubes were shown to be shorter than the lengths of the nanowires, which correlated with the amount of charge passed during the deposition of nanotubes being lower than that passed during deposition of nanowires, indicating that less metal had been deposited.

SEM characterisation revealed that the wires/tubes were cylindrical in shape, and had relatively uniform diameters, 118 ± 20 nm. SEM also revealed that the nanowires/tubes retained their characteristic shape even after removal from the template.

The inner wall of the nanotubes was identified as having the potential to create a higher electrochemical surface area than the solid nanowires, depending on the rate of diffusion of electrolyte inside the hollow tubes.

In Chapter 4, the same template electrodeposition strategy was employed in order to synthesise gold:copper core:shell nanowires. Initially, hollow copper nanotubes were deposited, then later filled with solid gold nanowires to create a fully solid core:shell structure. These nanowires were characterised using a range of microscopic and spectroscopic techniques, as well as voltammetrically. The core:shell nanowires had relatively uniform diameters of 161 ± 22 nm. The core:shell structures also retained their characteristic shape after removal of the membrane template. The diameters of the core:shell wires were somewhat larger than those of the gold nanowires and nanotubes, which may suggest that pore-widening occurs during deposition, or that the pores of the membranes have non-uniform channel diameters throughout their lengths. This non-uniform diameter phenomenon has been observed previously. The lengths of the core:shell nanowires were relatively constant at 3.0 ± 0.1 μm after both copper and gold deposition, suggesting that the gold did not deposit above the copper in the pore channel, but rather diffuse down to the bottom of the pore and fill the hollow copper tube deposited previously.

The fact that the diameters of the nanowires/tubes and the core:shell nanowires were different may indicate that a polycarbonate membrane may not be the best template to use if uniformity in the structure of the nanowire is required. AAO templates have been shown to have a uniform diameter throughout the length of the channel, however it is much more difficult to remove the nanowires from the AAO template following deposition, and structural damage may occur.

These discrepancies in the diameters of the nanowires are problematic in terms of their application in a sensing assay.

In Chapter 5, the gold nanowires and nanotubes, and the core:shell nanowires were applied to the detection of ss-DNA using three different approaches.

Firstly, the gold nanowires and nanotubes were utilised in an electrocatalytic detection strategy, which utilised the ability of the nano gold surface to catalyse hydrogen peroxide.

The current associated with the reduction of H_2O_2 at the surface of the nanowire is directly proportional to the number of nanowires/nanotubes on the surface of the electrode, which in turn is proportional to the concentration of target pathogen DNA. The target DNA concentration was determined by measuring the difference in the electrocatalytic reduction current at the gold nanowires/tubes, Δi , before and after the addition of 200 μM hydrogen peroxide to a solution of 0.01 M H_2SO_4 . For both the gold nanowires and nanotubes, the current was shown to increase linearly with increasing DNA concentration, from approximately 1 fM to 10 μM . The Limit of Quantitation, LOQ, is 1 fM for both kinds of nanostructure indicating that low concentrations of the target can be detected using this electrocatalytic approach. Significantly, the sensitivity observed for the nanowires, 15.5 $\mu\text{A dec}^{-1}$, is approximately 35% higher than that observed for the nanotubes. Moreover, the currents observed are consistently larger for the nanowires. This result is significant since the total area of the nanotube is approximately twice that of the nanowire which might be expected to lead to an enhanced current for the nanotube. However, the nanotube is uniformly functionalised with capture strand DNA which most likely impedes access of the peroxide to the nanotube surface. The higher current suggests that the regioselectively modified nanowires are more catalytically active, i.e., physically separating the molecular recognition and electrocatalytic detection functions produces a more sensitive assay.

The results of the assay were produced using the average and standard deviations of independently synthesised batches of nanowires, rather than the results of repeated assays using a single batch of wires. An investigation into the inter-batch

variation was carried out. The calibration curves are linear for $-15 < \log [\text{DNA}] < -9$ with acceptable correlation coefficients, $R^2 = 0.9973, 0.9947$ and 0.9917 . However, the absolute calibration sensitivities (slopes) vary between nanowire batches, with values of 25.0 ± 0.6 , 22.9 ± 0.8 and $13.7 \pm 0.7 \mu\text{A dec}^{-1}$ being observed. Therefore, while the calibration sensitivity is reproducible within a single batch of nanowires ($<5\%$), achieving a good reproducibility between batches has proven challenging. This is generally due to the use of polycarbonate membranes as templates, issues with the reproducibility of the available surface area for deposition, batch-to-batch variations of pore density, pore diameter, and pore thickness between membranes, and other instrumental issues. The template issues could be removed with the development of a reusable template with defined channel heights and diameters, however, the template would have to be robust enough to allow the nanowires to be removed without deformation of either the wires, or the template itself.

The gold:copper core:shell nanowires were also used to detect the ss-DNA of the pathogen *S. aureus*. In this case, there were two detection strategies identified:

1. Reduction of the thiol bonds between the capture and electrode, and between the probe and nanowire. By measuring the charge associated with the number of nanowires present on the electrode surface, the concentration of target DNA on the electrode surface could be measured. The greater the target DNA concentration, the greater the number of wires on the surface, and the larger the charge generated.
2. Oxidisation of the outer copper layer of the nanowire. The advantage of the core shell structure is that because the gold is not oxidised, it is possible for the nanowire to remain on the surface of the electrode throughout the amplified detection step which would not be possible with a pure copper nanowire.

Both of these strategies were expected to yield theoretical maximum charges of $0.26 \mu\text{C}$ and 0.01 C respectively, in comparison to an expected maximum charge of $8 \times 10^{-5} \text{ C}$ for an electrocatalysis assay in a ten second response time.

The thiol reduction assay produced an acceptably linear response for the target DNA sequence for concentrations from 1 nM to 100 μ M. This is a dynamic range of 5 orders of magnitude which is impressive, however the lower limit of detection of 1 nM is not quite sensitive enough to be able to detect DNA at the low concentrations that would be present at the early stages of disease, (normally pM concentrations in whole blood).

The maximum charge produced during the thiol reduction assay was 0.5 μ C at a target DNA concentration of 100 μ M, a value that is 48% larger than the theoretical maximum calculated assuming thiol bonds were present at the ends of the nanowire only. It was assumed that “leakage” of the probe DNA during nanowire functionalisation could have led to the walls of the nanowire having probe strands attached as well as the ends of the wire, which would lead to there being more thiol bonds reduced. Despite the extra charge being produced in this assay, the charge produced was not as large as the electrocatalysis assay, and the dynamic range was not as wide. The limit of detection was also lower, which is problematic in terms of sensitivity. This assay proved to have good selectivity towards the target DNA as compared to variations of the target sequence containing a 1 and 3 base mismatch.

The copper oxidation strategy proved to be unsuccessful, as a potential could not be identified that removed the copper only. After five hours the nanowires were completely removed from the nanowire surface, which was unexpected as there are no known faradaic processes for gold occurring at this potential.

Overall this thesis has identified that template electrodeposition is a successful strategy for fabrication of nanowires and nanotubes, however some challenges still remain with regards to the control of the dimensions of these structures, and the reproducibility of these properties from batch to batch.

Gold nanowires and nanotubes used in an electrocatalytic detection system are highly sensitive over a wide range of target DNA concentrations, and offer a large signal enhancement over that of a planar gold electrode. Again, issues with inter batch variations make these nanostructures less attractive for incorporation into a biosensor device than perhaps nanoparticles, which can be uniformly synthesised.

Future work on the development of a biosensor using nanowires could include development of a reusable template for nanowire synthesis, and comparison with commercially available nanowires. Additionally, more repeats of the assay using the 1 base mismatch target DNA should be carried out, as well as an investigation of the performance using the 3 base mismatch DNA. Following identification of the best performing nanowires, (template deposited or commercially available), interference studies should be carried out, in order to determine the effects of common interferences found in blood or other bio fluids on the performance of the assay. These could include molecules such as ascorbic acid, acetaminophen, and proteins. Further study could be done on the hybridisation times of the DNA strands, in order to see if they can be reduced, which would reduce the turnaround time of this assay.

The core:shell nanowires have proved to be less sensitive than the gold nanowires, and present their own set of challenges in terms of identification of an oxidising potential for the outer shell, and the large background that is present in the mismatch selectivity assays. These core:shell nanowires also suffer from the same inter batch variation issues as the gold nanowires and nanotubes, so perhaps future work could include fabrication of a robust, reusable template, which would greatly reduce these inter batch variations in length and diameter.

The core:shell nanowires would be a lot more difficult to incorporate into a biosensor in their current form. As the aim of this work was to produce an assay capable of detecting target DNA at very low concentrations, it would be more prudent to pursue the incorporation of the gold nanostructures into a functioning biosensor. The dynamic range of the core:shell assay was much narrower than that of the gold nanostructures, and the LOD was 1 nM, which is unfortunately not sensitive enough to detect the pM concentrations of DNA that would normally be

present in blood. In addition, gold nanowires are available commercially, and these should be relatively uniform in length and diameter. If a suitable reusable and reproducible template is not identified, the use of these uniform commercially available nanowires is one possible solution.

The systems described in this work do not lend themselves to incorporation into a multiplexed approach at this stage, but with further study, it may be possible to detect a second target DNA strand on the same nanowire by another means, such as incorporation of a fluorescent labelled enzyme or dye.